# 3D-Silicon and Passive CMOS Sensors for Pixel Detectors in High Radiation Environments

**Dissertation**
**zur**
**Erlangung des Doktorgrades (Dr. rer. nat.)**
**der**
**Mathematisch-Naturwissenschaftlichen Fakultät**
**der**
**Rheinischen Friedrich-Wilhelms-Universität Bonn**

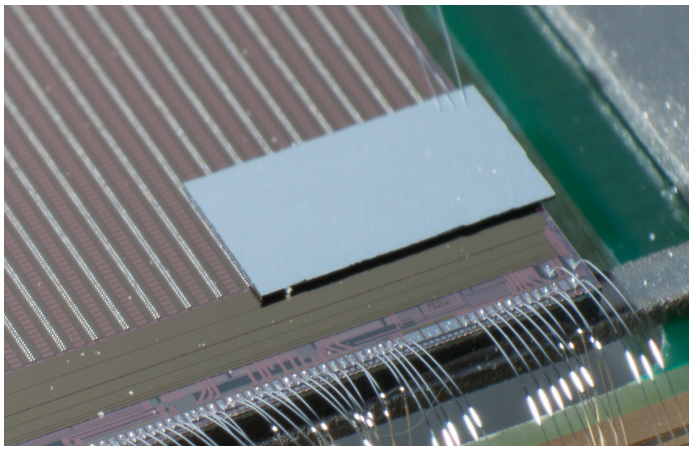

vorgelegt von
David-Leon Pohl
aus
Herne

Bonn 2020

Cover picture: A small prototype of a passive CMOS sensor connected to the larger pixel readout-chip using bump bonding (*background*). Wire-bond connections of the readout chip to the support PCB are visible (*foreground*).

Angefertigt mit Genehmigung der Mathematisch-Naturwissenschaftlichen Fakultät
der Rheinischen Friedrich-Wilhelms-Universität Bonn

1.Gutachter: Prof. Dr. Norbert Wermes
2.Gutachter: Prof. Dr. Klaus Desch

Tag der Promotion: 08.01.2020
Erscheinungsjahr: 2020

## Abstract

The future upgrade of the Large Hadron Collider to the High-Luminosity LHC demands new pixel detectors that can operate in environments with exceptionally high radiation. This requires investigations into new radiation-tolerant sensor technologies and readout electronics, and the advancement of radiation-damage models. In this work, planar- and 3D-silicon sensors from the latest upgrade of the ATLAS pixel detector (IBL) and novel passive CMOS sensors are characterized after high levels of irradiation. New measurement techniques for the readout chip (ATLAS FE-I4) enabled precise charge-collection efficiency studies with highly segmented silicon sensors and the extraction of radiation-damage model parameters. A dedicated simulation, based on a model with just 2 parameters, successfully describes the dependence of charge collection on sensor voltage up to a fluence of $5 \times 10^{15}\,\mathrm{n_{eq}\,cm^{-2}}$ NIEL. The life-time of charge-carriers in silicon at $5 \times 10^{15}\,\mathrm{n_{eq}\,cm^{-2}}$ NIEL is determined to be $0.75 \pm 0.08\,\mathrm{ns}$. At $7 \times 10^{15}\,\mathrm{n_{eq}\,cm^{-2}}$, charge-collection efficiency is about 50% for 3D- and 250 µm planar-silicon sensor designs. The 3D-silicon sensors demonstrate a much lower power consumption (15%), which is an important advantage for their potential usage in the innermost layer of the future pixel detector. For the outer pixel layer, which has relaxed requirements for radiation-tolerance ($1 \times 10^{15}\,\mathrm{n_{eq}\,cm^{-2}}$), a novel prototype of a planar silicon sensor is characterized. Since the sensor implantations are produced using a 150 nm CMOS process from LFoundry, they are termed *passive CMOS* sensors. A detailed study with respect to crucial sensor parameters, such as bulk resistivity ($> 2\,\mathrm{k\Omega\,cm}$), capacitance (105 fF), and detection efficiency ($> 99\,\%$) reveals similar performance to current ATLAS planar-silicon sensors. Additionally, resistor biasing of pixels, a feature available in the CMOS process, enhances the detection efficiency by approximately 1%. Driven by these promising results, the option to use passive CMOS sensors for the future ATLAS pixel detector is actively pursued.

# Contents

# 1 Introduction

## 1.1 Motivation

A major quest of mankind is to understand the universe we live in. Logically, this quest leads to questions about the nature of the universe and its constituents. Modern particle physics pursues these questions by investigating the fundamental structures of matter, called particles. Their properties and interactions are investigated in colliders where particles are accelerated and brought to collision. The particles created in such collisions primarily have short life-times and give insight about their components and the fundamental forces involved. Particle reactions that probe and refine modern theories and predictions are extremely rare and require recording of many particle reactions.

For example, in the recent discovery of the Higgs particle in the world's largest collider, the Large Hadron Collider (LHC) at the European Center for Nuclear Research (CERN), more than 1 Billion proton collisions were needed to produce one Higgs particle. In order to record these reactions fast and highly sensitive particle detectors that can cope with extreme particle rates are needed. Furthermore, the proton energy and collision rate at the LHC are increased successively with a major upgrade in 2025, to increase discovery potential and measurement precision. Therefore, the ever-increasing requirements for the detectors demand continuous detector research and development.

The ATLAS[1] detector located at the LHC is the particle detector of the ATLAS experiment. It is designed as a multi-purpose detector consisting of multiple specialized sub-detectors that determine particle properties like charge, energy, and momentum. Arguably, the most complex sub-detector is the pixel detector that contributes to particle vertex and track reconstruction with high resolution space points. The development of the ATLAS pixel detector is mainly driven by the rapid progress made in the solid-state industry. The ever-decreasing feature-sizes of CMOS processes allow for more sophisticated, fast, and granulated readout electronics. Electrical interconnection techniques, wafer processes, and new high-voltage CMOS processes made available to the community enable conceptual advancement. New lightweight materials and cooling- and powering concepts drive the developments for the pixel detector services and support structures. Many synergies with the solid-state industry exist, allowing to use common design and production tools for electrical and mechanical engineering. Nevertheless, the unique conditions at the ATLAS experiment demand farther-reaching research to archive the required readout speed, low mass, and radiation-hard pixel-detector designs. This is approached via the development of software tools that aid detector

[1] **A** **T**oroidal **L**HC **A**pparatu**S**

design, measurements on prototypes allowing successive improvements, and the advancements of models that describe the physical processes involved during particle detection. Designing a pixel detector, starting from the definition of requirements, followed by a prototyping phase, and finally the production, is complex and requires a large research collaboration. The international research collaboration involved in the development of the ATLAS pixel detector comprises more than 20 institutes based in over 5 countries.

The content presented in this thesis focuses on novel radiation-hard pixel sensors for the ATLAS pixel detector layers. With the latest upgrade of the ATLAS pixel detector in 2014 (IBL), so called 3D pixel sensors found their first application in high-energy particle physics. In comparison to the common planar sensors, they have a smaller distance between biasing and readout electrode, making them more radiation hard. A detailed comparison of the charge-collection efficiency between planar and 3D sensors as a function of radiation and bias voltage using data from measurements and simulation is presented here (Chapter 5). Important steps like the development of charge reconstruction methods for pixel detectors using the ATLAS FE-I4 (Chapter 3) and accompanying simulations to extract radiation-damage model parameters at high fluences up to $5 \times 10^{15}\,\mathrm{n_{eq}\,cm^{-2}}$ are presented in dedicated sections.

For the outer layers of the future ATLAS hybrid pixel detector the utilization of a CMOS process for a planar sensor is a promising option. These sensors are termed passive CMOS sensors, since they do not incorporate active amplification. Such sensors can profit from CMOS process features allowing for design improvements and production optimizations. A first prototype design is investigated in Chapter 6 regarding all crucial sensor parameters.

## 1.2 The ATLAS experiment at the LHC

### 1.2.1 The Large Hadron Collider

The Large Hadron Collider (LHC [EB08]) is the largest and most powerful particle collider to date. It is located in a tunnel beneath the France–Switzerland border at the European Center for Nuclear Research (CERN) near Geneva (Figure 1.1). The LHC is a circular collider with two

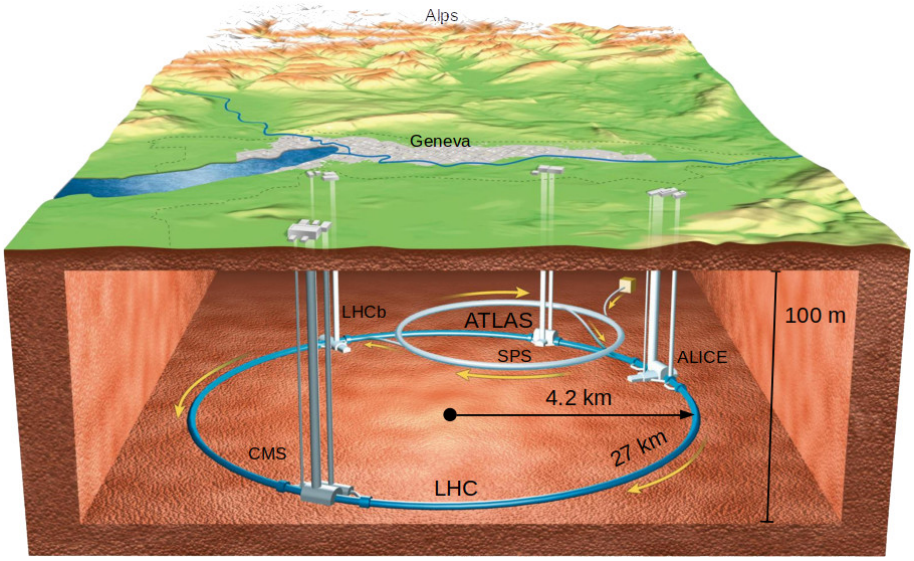


Figure 1.1: The Large Hadron Collider with its four experiments: ATLAS, CMS, LHCb, and ALICE.

counter-circulating particle beams. The benefit of the circular concept is that particles can pass the acceleration chain several times to gain energy and the increased probability that particles participate in a collision due to multiple passes. Charged particles with large masses are favored in circular colliders, due to their energy loss from synchrotron radiation that scales with the fourth power of the mass $m_0$:

$$\Delta E \propto \frac{1}{\rho^2} \frac{E^4}{m_0^4} \tag{1.1}$$

$\rho$ is the radius of the circular path.
At the LHC, protons and heavy ions are used. Since the maximum achievable energy scales with the radius of the collider, the LHC has an eponymously large radius of 4.25 km archiving a maximum collision energy of 14 TeV. Another reason for the large radius is the high magnetic field strength required to keep the particle on track. The Lorentz force generated by 8.4 T strong superconducting dipole magnets operated at 1.4 K is needed to balance the centripetal force:

$$\rho = \frac{p}{q\,B} \tag{1.2}$$

$p$ is the particle momentum, $q$ the charge and $B$ the magnetic field strength.
The main physics program at the LHC focuses on proton-proton collisions (p-p). Since protons are no fundamental particles, their constituents (gluons and quarks) interact at a fraction of the proton energy leading to a large energy regime that is covered without accelerator adjustments. The proton beam consists of 7.5 cm long packages with about $1 \times 10^{11}$ protons each, called bunches. Up to 2808 equally spaced bunches are stored in the ring at a gap of about 7.5 m. The ultra-relativistic proton bunches move almost at the speed of light leading to proton collisions in the detector every 25 ns [Ben+04, p. 5][G+17, p. 8]. The corresponding collision frequency of 40 MHz is also called *bunch crossing frequency*. Since bunch collisions are independent of each other one summarizes all particle interactions within one bunch collision to an *event*. The reconstruction of particle properties happens on a per-event basis. The event-rate dictates the time-stamping precision of the particle detectors that is needed to distinguish different events. It also determines the required sensitivity time-windows and granularity of the sub-detectors, to avoid information merging of neighboring events. The proton collision rate $\dot{N}$ depends on the cross sections $\sigma_i$ of all processes involved and the *instantaneous luminosity* $\mathcal{L}$:

$$\dot{N} = \sum_i \sigma_i \cdot \mathcal{L} \tag{1.3}$$

The luminosity quantifies the performance of a particle accelerator and defined as:

$$\mathcal{L} = \frac{f N^2}{4\pi\sigma_x\sigma_y} \tag{1.4}$$

With the revolution frequency $f$ of $N$ counter-rotating particles in each beam and $\sigma_{x,y}$ is a measure for the beam size. The *integrated luminosity* is often used to describe the total data delivered and is calculated by integration of Equation (1.4):

$$\mathcal{L}_{\text{int}} = \int \mathcal{L}\, dt \tag{1.5}$$

The sensitivity and measurement error for the observation of a particle reaction or -property depends on the total number of observations. The statistical measurement error approximately scales with:

$$\sigma_{\text{stat}} \propto \frac{1}{\sqrt{N}}$$

and thus halves when the sample size is quadrupled. The systematic error profits from larger sample sizes, too. High-statistic control samples allow for a better understanding of the detector response and description of physical backgrounds. Furthermore, large statistics allow hard data cuts to select more clean and well-understood events [GA00, p. 2]. A way to increase the integrated luminosity and therefore measurement precision is to increase the measurement time and the instantaneous Luminosity $\mathcal{L}$. Consequently, the LHC follows an upgrade schedule to increase its instantaneous luminosity about every 3 - 5 years (Figure 1.2). After an initial ramp up of beam energy and luminosity in the first run period in 2011 and 2012, the nominal peak luminosity of

$\mathcal{L} = 1 \times 10^{34}\,\mathrm{cm}^{-2}\,\mathrm{s}^{-1}$ has been reached in 2016.


Figure 1.2: Upgrade schedule of the LHC for increased beam energy and luminosity. The total data collected for the different run periods is given by the integrated luminosity (Equation (1.5)) in inverse femto barn ($1\,\mathrm{fb} = 1 \times 10^{-24}\,\mathrm{cm}^2$). Long shutdown periods of about 2 years are used to upgrade the particle detectors at the LHC.

Two main challenges for the detectors arise from a luminosity increase:

1. An increase of the *instantaneous* luminosity leads to more interactions per bunch crossing, which leads to more instantaneous particles in the detector and therefore to a higher occupancy. Figure 1.3 shows the increase of the (inelastic) interactions per bunch over the last years. After the next major upgrade in 2026, about 200 primary interactions are expected.

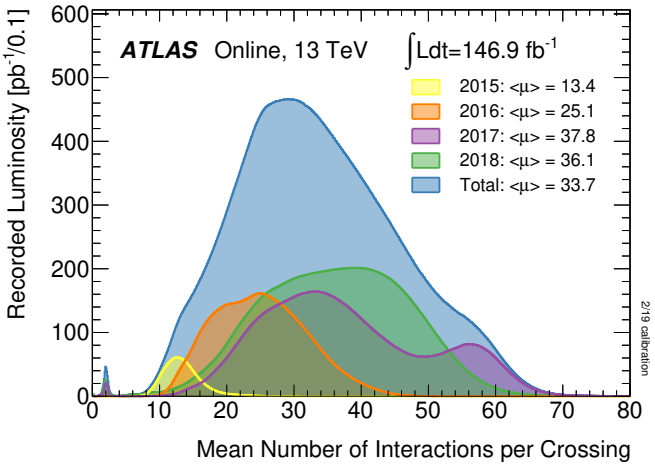


Figure 1.3: Interactions per bunch crossing during stable beam conditions for different run periods. Calculated from the per bunch instantaneous luminosity assuming a value for the total p-p inelastic cross section (e.g. 80 mb at 13 TeV) using the integral of Equation (1.3). Mean interactions $\mu$ are stated for each year. [ATLa]

For the tracking detectors, this requires a finer granularity and a larger data bandwidth.

2. An increase of the *integrated* luminosity leads to more radiation damage in the detectors,

requiring new radiation-tolerant detector designs. Investigations into radiation-hard sensors for pixel detectors are the main topic of this study and introduced in Chapter 5 and Chapter 6.

For the next major upgrade of the LHC to the so-called High-Luminosity LHC (HL-LHC), luminosity leveling will be exploited to keep the instantaneous luminosity constant [G+17, p. 6]. This allows to reach higher integrated luminosities in a shorter period, while preventing for detectors unfavorably high instantaneous luminosities.

### 1.2.2 The ATLAS detector

The ATLAS[2] detector has a length of 45 m and a diameter of 25 m making it the largest particle detector to date. It consists of many sub-detectors that utilize a wide range of particle detection techniques to allow the reconstruction of the particle properties like mass, momentum, position, charge, and decay length . The sub-detectors are symmetrically arranged in multiple layers around the collision point, also called interaction point (*IP*). As depicted in Figure 1.4, one can differen-

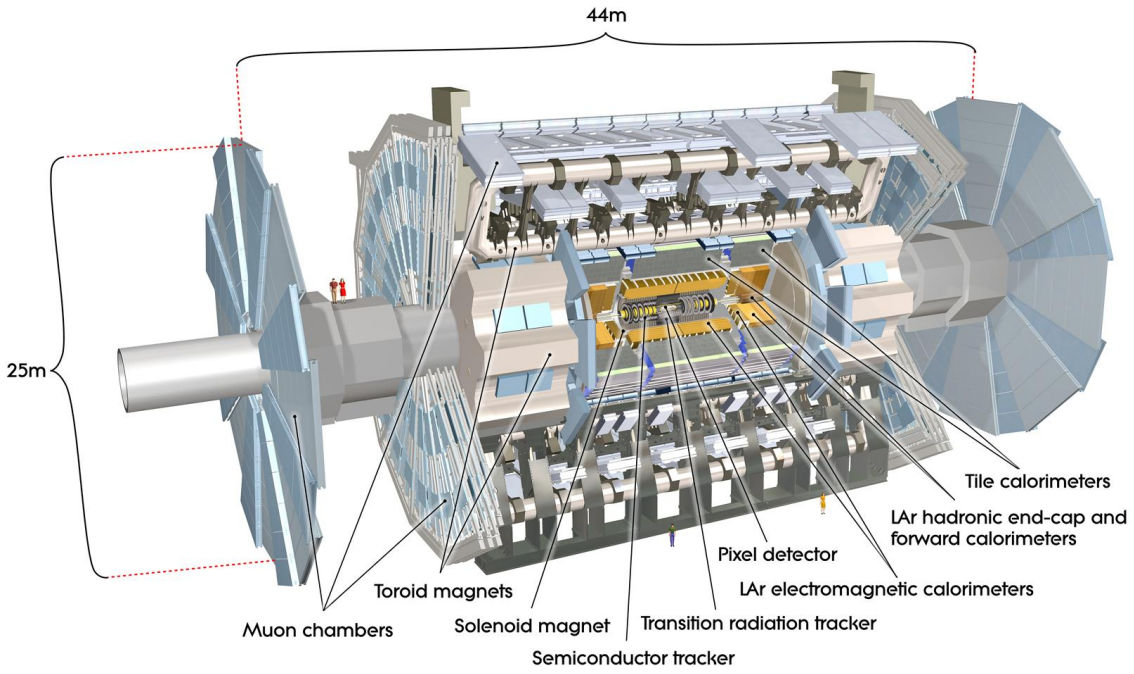


Figure 1.4: Layout of the ATLAS detector. Computer generated image with two people as a scaling reference. [Peq08a]

tiate between a barrel region with a cylindrical layout that surrounds the central beam pipe and perpendicular disc layers in the forward respectively backward region. A slice of the barrel region showing the different sub-detectors and particle types that interact with it is shown in Figure 1.5. One can group the sub-detectors into 3 groups following the particle path starting at the interaction

[2] **A** **T**oroidal **L**HC **A**pparatu**S**

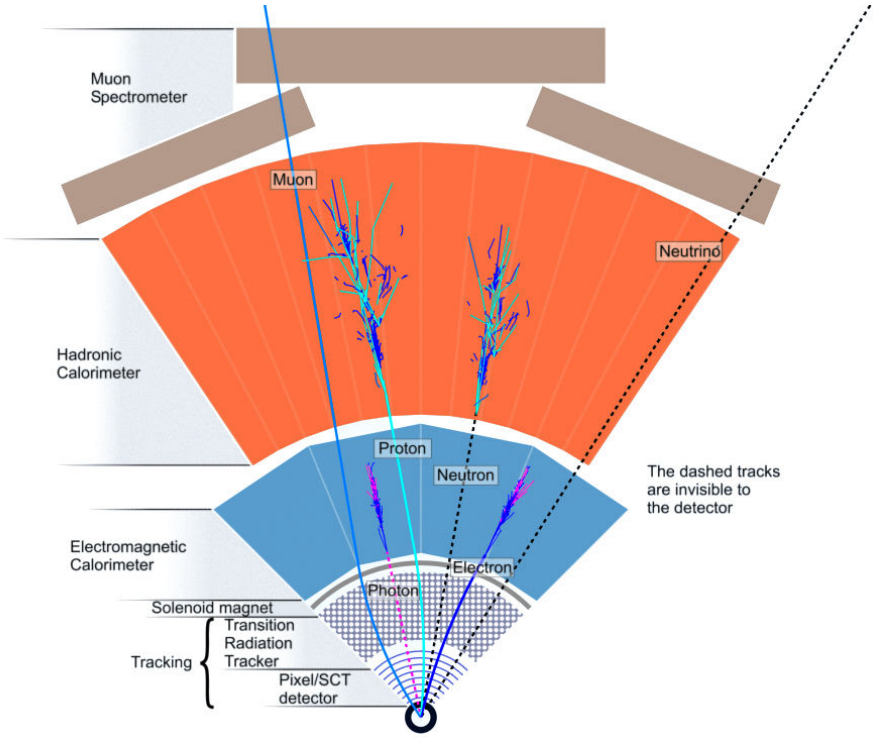


Figure 1.5: Cross section of the ATLAS detector barrel and the signatures of particles in the 3 subsystems for tracking, calorimetry, and muon spectrometry. Based on [Peq08b].

point:

- Inner tracker: The inner tracking detector (*ITk*) measures the trajectories of all charged particles (short: tracks). It is immersed in a 2 T magnetic field parallel to the beam axis to allow the determination of particle momenta by their track curvature. In addition, the primary vertex of the proton collision is reconstructed from the tracks, as-well-as secondary vertices from long-lived particles that decay within the tracker volume. From a displacement of the secondary vertex to the primary interaction, particles that decay via the weak interaction can be identified, making the inner tracker also an important contributor to particle identification. The vertex resolution is mostly determined by the four pixel detector layers. An introduction to the ATLAS pixel detector is given in Section 2.3. Following the pixel detectors are 4 layers of silicon strip detectors (*SCT*) and a transition radiation tracker (*TRT*) with 12 $m^3$ volume. Depending on the distance to the interaction point the granularity of these detectors are scaled. Closest to the interaction point is the pixel detector with about 92 M sensitive segments (pixels), followed by the SCT and TRT with 6 M, respectively 0.35 M.

- Calorimeters: The calorimeters used in the ATLAS detector are segmented sampling calorimeters to measure the total energy of particles together with their coarse location. They consist of alternating layers of absorber material and active detector layers. The detector layers measure the cascade of secondary particles (so called particle showers) from the energy

loss of the primary particle in the absorber material. Depending on the choise of the absorber material, absorber thickness, and position the particle either interact mainly by electromagnetic interaction or via nuclear interactions. The calorimetry system in ATLAS consists of an electromagnetic calorimeters ($ECAL$) to measures the energy of electrons and photons followed by a hadronic calorimeter ($HCAL$) for particles that are made of quarks (hadrons).

- Muon spectrometer: Muons are the only charged particles that are not stopped in the preceding detectors. Due to their clean and unique signature, they help to select events with physical interactions of interest. Therefore, the muon spectrometer has trigger chambers that are optimized for fast readout and high-precision tracking chambers to allow determination of momentum and charge through their track curvature in an auxiliary 4 T toroid magnetic field.

# 2 Pixel detectors in High Energy Physics

This chapter describes how pixel detectors work and presents the theoretical models that describe the detection process in chronological order. The first section introduces the interactions of particles with pixel sensors, which lead to free charge carriers in silicon. Subsequently, movement of the charge carriers is considered, and the resulting detectable signal is derived. Alongside, the designs of pixel sensors and their requirements for their application in high-energy physics are motivated. With a review of current radiation-damage models in Section 2.2, focus is placed on radiation damage in silicon sensors, as this damage leads to unique requirements and operational parameters. The models presented in the first two sections are used in the simulations of Chapter 3 and Chapter 5 to describe measurement data and extract sensor parameters. References to use cases are given at appropriate places. The chapter concludes with a description of the ATLAS pixel detector. In particular, the latest upgrade of the pixel detector (IBL, Section 2.3.1) is presented, since its sensors and the new readout electronic are used for the measurements in Chapter 5 and Chapter 6.

## 2.1 Signal generation and detection

Particles and radiation are detected through their interaction with matter. The part of a detector where particle interactions create a measurable signal is termed *sensor*. These interactions depend on particle type, particle energy, and sensor material. They decrease the kinetic energy (*energy loss*) and change the particle's direction (*multiple scattering*).

### 2.1.1 Energy deposition in silicon sensors

For the energies used in this study, the energy loss of charged particles is mainly dealt by inelastic scattering at shell electrons of the silicon atoms, leading to ionization and excitation. The resulting (quasi-) free charge carriers in the sensor can then be measured to detect the initial particle. Scattering at electrons is a discrete statistical process of single collisions creating fluctuations in the energy loss that leads to a broadening of the energy-loss distribution depending on sensor material and thickness. For the *average* energy loss per unit path-length Bethe derived a formula from quantum mechanical calculations. It describes the energy loss for relativistic particles ($\beta\gamma = 0.1 \ldots 500$) with a mass larger then the electron mass ($M \gg m_\mathrm{e}$) accurately to a few percent [Tan+18, p. 447]:

$$\left\langle -\frac{dE}{dx} \right\rangle = 4\pi\, r_e^2\, n\, m_\mathrm{e} {c_0}^2 \frac{z^2}{\beta^2} \left[ \frac{1}{2} \ln \frac{2\, m_\mathrm{e} \beta^2 \gamma^2\, W_\mathrm{max}}{I^2} - \beta^2 - \frac{\delta}{2} \right] \tag{2.1}$$

with:

| | |
|---|---|
| $c_0$, $v$ | Speed of light and particle speed |
| $m_\mathrm{e}$, $r_e$ | Electron mass and classical electron radius $r_e = e^2/\left(4\pi\,\epsilon_0\,m_\mathrm{e}\,{c_0}^2\right)$ |
| $n$ | Density of the scatterer, thus the electron density: $n = \frac{Z\rho}{A\,u}$ |
| | $Z$, $A$, $\rho$: Atomic number, mass number and mass density of the sensor material; for silicon $Z = 14$, $A = 28$, $\rho = 2.3290\,\mathrm{g\,cm^{-3}}$. $u$ is the atomic mass unit. Often the energy loss is given as *stopping power* when dividing by the material mass density: $\frac{1}{\rho}\frac{dE}{dx}$ in $\mathrm{MeV\,cm^{-2}\,g^{-1}}$. |
| $z$ | Charge of incident particle in $e$; usually $z = 1$ |
| $\beta$, $\gamma$ | Speed of incident particle given as the ratio to the speed of light $\beta = \frac{v}{c_0}$ and Lorentz factor $\gamma = \frac{1}{\sqrt{1-\beta^2}}$ |
| $W_\mathrm{max}$ | The maximum energy transfer in a knock-on collision: $W_\mathrm{max} \approx 2\,m_\mathrm{e}{c_0}^2(\beta\gamma)^2$ |
| $I$ | Mean ionization energy of the sensor material; for silicon $I = 173\,\mathrm{eV}$. |

Table 2.1: Variables and constants used to describe the energy loss of particles in silicon.

The term $\frac{\delta(\beta\gamma)}{2}$ describes the density correction. The rise of energy loss at higher velocities, due to the contribution of more distant collisions, is reduced by the polarization of the sensor material. The induced polarization depends on the materials density[1] and is parametrized for different energy ranges as [KW16, p. 38]

$$\delta(\beta\gamma) = \begin{cases} 2\,X\ln 10 + C_D & X \geq X_1 \\ 2\,X\ln 10 + C_D + a(X_1 - X)^k & X_0 \leq X < X_1 \\ \delta_0 10^{2(X-X_0)} & X < X_0 \end{cases} \tag{2.2}$$

with $X = \log(\beta\gamma)$ and for silicon $C_D = -4.4351$ [SBS84, p. 269]. When the condition $M \gg m_\mathrm{e}$ is not satisfied, as it is the case for electrons and positrons, a modified Bethe-Bloch formula has to be used [CW51, p. 356]. The modifications take into account that the incident particle is heavily deflected due to its comparable mass to the scatter particle and in case of electrons the quantum mechanical indistinguishability between both. For electrons the Bethe-Bloch formula becomes [Tan+18, p. 456]:

$$\left\langle -\frac{dE}{dx} \right\rangle = 4\pi\,r_e^2\,n\,m_\mathrm{e}{c_0}^2\,\frac{1}{\beta^2}\left[\frac{1}{2}\ln\frac{\tau^2+2}{2(I/(m_\mathrm{e}{c_0}^2)^2} + \frac{F(\tau)}{2} - \frac{\beta^2}{2} - \frac{\delta}{2}\right] \tag{2.3}$$

with the components as described before, $\tau = \gamma - 1$, and

$$F(\tau) = 1 + \frac{\frac{\tau^2}{8} - (2\tau+1)\ln 2}{(\tau+1)^2} \tag{2.4}$$

Figure 2.1 depicts the collision energy loss in silicon for heavy particles and electrons.

For light particles or highly relativistic particles ($\beta\gamma \gg 500$), the radiation energy-loss via Bremsstrahlung has to be considered as an additional contribution to the total energy loss. Since

[1] More information and tabulated values of different materials in [SBS84]

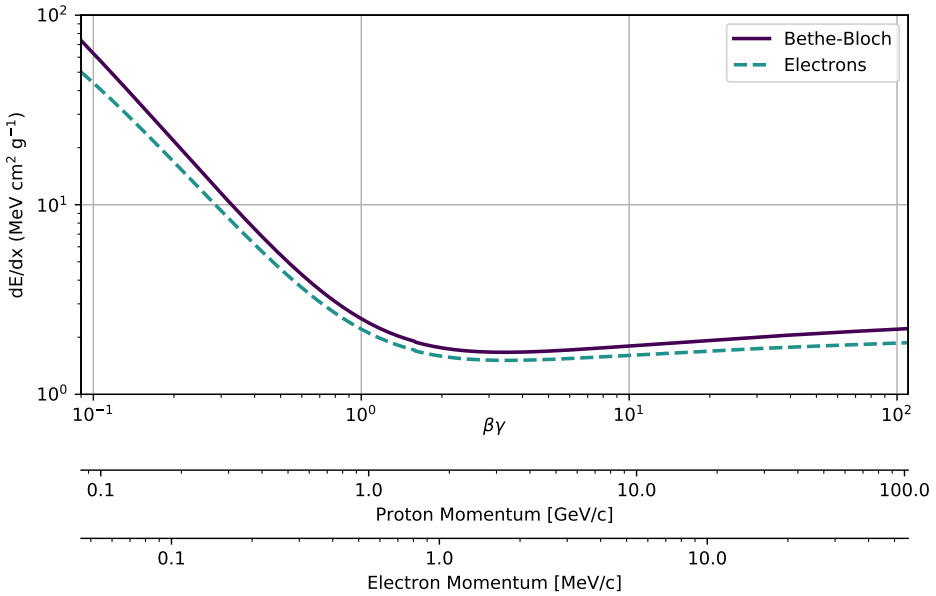


Figure 2.1: Collision energy-loss in silicon for heavy particles ($M \gg m_e$, *solid line*) and electrons (*dotted line*). The minimum-ionizing energy range for energies above $\beta\gamma \approx 2$ is visible. Equation (2.1) and Equation (2.3) are used. The values match for the depicted range within a few percent the output of the ESTAR, PSTAR programs [Ber+05], that take higher order corrections into account (e.g. shell-correction). Corresponding particle momenta are stated below.

the Bremsstrahlung cross section scales with the inverse square of the particle mass [Leo94, p. 35]:

$$\sigma \propto \left(\frac{e^2}{mc_0{}^2}\right)^2 \tag{2.5}$$

the contribution is only relevant for electrons, positrons, and highly energetic muons when considering the energy range of modern particle physics experiments. The critical energy $E_c$, defined as the energy where the collision energy-loss equals the radiation energy-loss by Bremsstrahlung [BGK14, p. 22], is reached in silicon at:

$$\frac{dE}{dx}_{\text{collision}}(E_c) = \frac{dE}{dx}_{\text{radiation}}(E_c) \tag{2.6}$$

$$\Rightarrow E_{c,\text{Si}} \approx 48\,\text{MeV} \text{ for electrons} \tag{2.7}$$

$$\wedge\ E_{c,\text{Si}} \approx 580\,\text{GeV} \text{ for muons} \tag{2.8}$$

The values are from [Ber+05][GMS01, p. 22]. For energies above $E_c$, the radiation loss dominates and the energy loss can be approximated as:

$$-\frac{dE}{dx}_{\text{radiation}} = \frac{1}{X_0}E \Rightarrow E(x) = E_0 \exp\left(-\frac{x}{X_0}\right) \tag{2.9}$$

where $X_0$ is the *radiation length*, a material characteristic that depends on its mass density. The radiation length describes the distance where an electron lost about 63% of its initial energy. When defining the requirements for a tracking detector, a fraction of the radiation length is often used as a quantifier for the allowed material budged, since formulas describing particle interactions with matter are often formulated in relation to the radiation length (e.g. multiple scattering, Equation (2.14); pair production, Equation (2.19)). The energy deposition via Bremsstrahlung creates a few high-energetic photons opposed to the quasi-continuous energy deposition along the particle path for collision energy-loss. Since the absorption probability of high energetic photons is small in thin silicon sensors (Section 2.1.1), Bremsstrahlung does not contribute to the *energy deposited* and thus to the charge signal available for particle detection. Another mechanism reducing the energy deposit are high energetic electrons ($\delta$-rays) that can occur by inelastic scattering at shell electrons. These electrons are not bound to their atom and perhaps escape the sensor volume before depositing their kinetic energy. Therefore, it is common to modify the Bethe-Bloch formula to restricts the maximum energy transfer $W$ in one collision, giving the restricted energy loss:

$$\left\langle -\frac{dE}{dx} \right\rangle = 4\pi\, r_e^2\, n\, m_\mathrm{e} {c_0}^2 \frac{z^2}{\beta^2} \left[ \frac{1}{2} \ln \frac{2\, m_\mathrm{e} \beta^2 \gamma^2\, W_\mathrm{upper}}{I^2} - \frac{\beta^2}{2} \left( 1 + \frac{W_\mathrm{upper}}{W_\mathrm{max}} \right) - \frac{\delta}{2} \right] \tag{2.10}$$

with $W_\mathrm{upper} = \min\left(W_\mathrm{cut}, W_\mathrm{max}\right)$. $W_\mathrm{cut}$ is the kinetic energy of an electron with a stopping range in the order of the sensor thickness [Bak+87, p. 679]. For cut values $W_\mathrm{cut}$ that approach the maximum energy transfer $W_\mathrm{max}$, this equation reduces to the Bethe-Bloch formula in Equation (2.1). The restricted energy loss, with $W_\mathrm{cut} = 10 \cdot \min\left(-\frac{dE}{dx}\right)$, is depicted in Figure 2.2 as dotted lines and shows a constant value for a large range of energies. The *energy deposit* for charged particles with an energy $\beta\gamma > 2$ is almost constant in the energy range of interest. Particles depositing an energy close to the minimum-ionizing energy-loss are called *minimum-ionizing particles* (short: MIP). The energy-loss distribution of MIPs is used to define the worst-case scenario where the detector has to be fully operational and the requirements like detection efficiency and readout speed are matched. For the measurements in Chapter 5 and Chapter 6, high energetic electrons and pions are used, that are considered minimum ionizing.

#### Energy-loss distribution

Energy loss due to collision with shell electrons is a discrete process and the energy deposit in a sensor consists of several separate collisions. For large numbers of collision, the total energy deposit in the sensor approximates the Gaussian distribution due to the central limit theorem. But for thin tracking detectors, such an approximation cannot be done and the distribution has a long tail towards higher energy-losses due to rare inelastic scatterings producing delta electrons. This makes the energy-loss distribution in thin sensors highly asymmetric with a long high energy tail that is defined by the ratio between average energy-loss and maximum energy-loss in a single collision $W_\mathrm{max}$. The average energy loss as given by Equation (2.10) is for practical applications ill-defined, since determining it requires detailed sampling of the tail of the energy-loss distribution [Tan+18, p. 450]. Therefore, the most probable value of the charge distribution (MPV) is a much more

stable quantity and is primarily used when quantifying energy depositions. For the description of charge deposition spectra in thin absorbers Landau calculated a distribution function given as a definite integral [Lan44]:

$$\frac{1}{\pi}\int_0^\infty e^{-u\ln u - u\,\lambda}\sin\pi u\,du \tag{2.11}$$

that can be used after appropriate scaling and shifting [KW16, p. 48]. The most probable energy loss can be written in similar notation as Equation (2.1):

$$-\frac{dE}{dx}_{\text{MPV}} = 4\pi\, r_e^2\, n\, m_\text{e} {c_0}^2 \frac{z^2}{\beta^2}\left[\frac{1}{2}\ln\left(\frac{2\,m_\text{e}\beta^2\gamma^2}{I^2}\frac{2\,\pi\, r_e^2\, m_e\, {c_0}^2\, n\, z}{\beta^2}\right) - \frac{\beta^2}{2} - \frac{\delta}{2}\right] \tag{2.12}$$

where the material distance $z = \rho \cdot d$ (sensor mass density $\cdot$ sensor thickness) introduces a dependence on the sensor thickness. Figure 2.2 shows the difference between average and most probable energy-deposition for a 200 µm silicon detector. The most propable energy deposit is considerable lower and therefore commonly used to define the operation point of the detector. For thin silicon

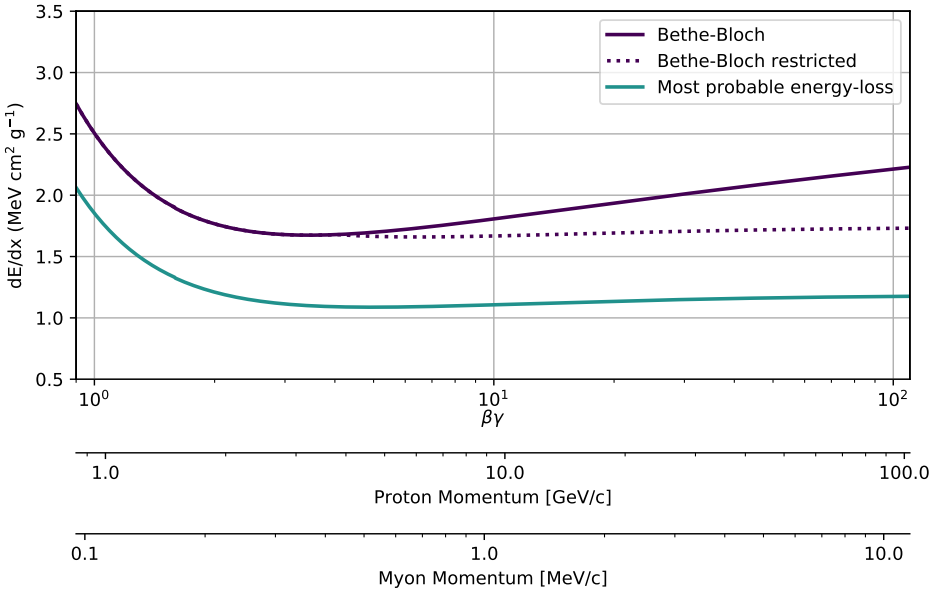


Figure 2.2: Average and most probable collision energy-loss in a 200 µm silicon sensor for heavy particles ($M \gg m_\text{e}$). Equation (2.1), Equation (2.10), and Equation (2.12) are used. Corresponding particle momenta are stated below.

sensors, the Landau distribution cannot be used to calculate the expected energy-deposition spectrum and more complex theories have been developed (e.g. [Apo+00]). Detailed discussions can be found in [Bic88] and [Bak+87, p. 688]. But for the *description* of energy-deposition spectra from MIPs a convolution of the Landau and a Gaussian distribution (Langau) is often sufficient (e.g. [Han+83; MPS11]). A comparison between a Langau fit and the measured energy deposit in a 230 µm thick silicon sensor is depicted in Figure 2.3. Despite the tail to the left due to charge sharing the distribution is well described by the Langau function. The MPVs of measured charge

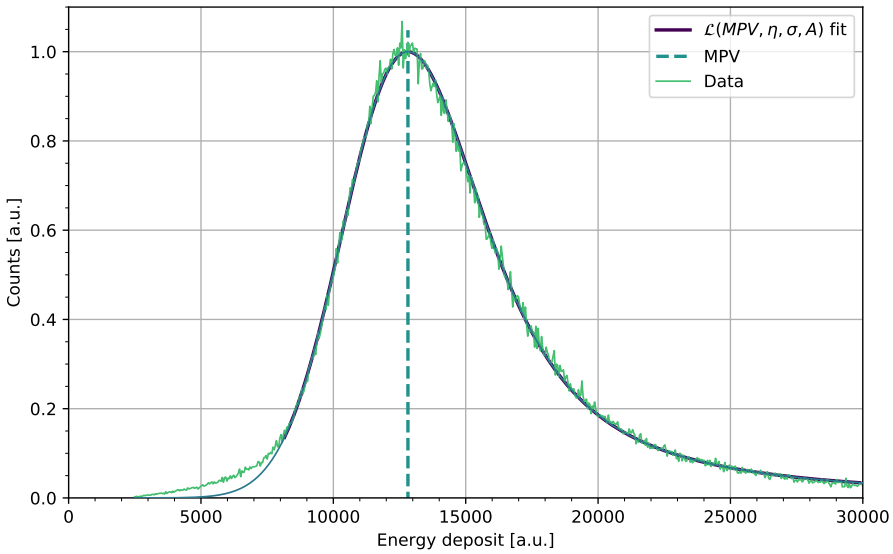


Figure 2.3: Langau fit to the single-pixel energy deposit of traversing $^{90}$Sr electrons. Fit range depicted by *solid dark line*. Detector noise is not subtracted and increases the distribution width and MPV. Maximum measured energy deposit is restricted by readout chip (ATLAS FE-I4).

spectra is used in Chapter 5 and Chapter 6 to quantify sensor properties like charge-collection efficiency and bulk resistivity.

### Multiple scattering

In addition to the inelastic collisions with the shell electrons charged particles also undergo repeated elastic scatterings at the sensor nuclei. The scattering cross section for scattering off a single charged particle at the nuclei with charge number $Z$ is given by the Rutherford formula [Leo94, p. 41]:

$$\frac{d\sigma}{d\Theta} = Z^2 \, r_e \frac{mc}{\beta p} \frac{1}{4 \sin^4 (\theta/2))} \tag{2.13}$$

with the components as described in Table 2.1 and scattering angle $\theta$. In a pixel sensor multiple scatterings occur with most of the scatterings doing only small deflections due to the $1/\frac{1}{\sin^4(\theta/2))}$ dependence in Equation (2.13). For multiple collisions in the sensor with small deflections, the projected angular distribution can be approximated by a Gaussian distribution due to the central limit theorem. Rare large angle scatterings add tails to the Gaussian distribution and are better described by *Moliere's Theorie* [Mol47; Mol48]. But, for most practical applications, like track fitting, the Gaussian approximation is sufficient for silicon sensors of a few 100 µm thickness, since more then 99,9% of the scattering angles follow the normal distribution. The standard deviation $\theta_0$ of this distribution is described by the *Highland-Formula* [LD91, p. 10]:

$$\theta_0 = \frac{13.6\,\text{MeV}}{\beta c_0 p} \sqrt{\frac{x}{X_0}} \left[ 1 + 0.038 \ln \left( \frac{x}{X_0 \, \beta^2} \right) \right] \tag{2.14}$$

for a single charged particle after a path length $x$ at velocity $\beta c_0$ and momentum $p$ in a material with radiation length $X_0$.

Low energetic electrons are heavily deflected in silicon due to their low mass, a process that is better described by random walk than small-angle scattering. Consequently, the path length in the sensor largely varies and therefore the total energy deposit from collision energy-loss. This is exemplarily depicted in Figure 2.4 for $^{90}$Sr electrons in a 200 µm silicon sensor with an energy of a few MeV. Only about 40% traverse the silicon sensor and deposit energy following the Langau

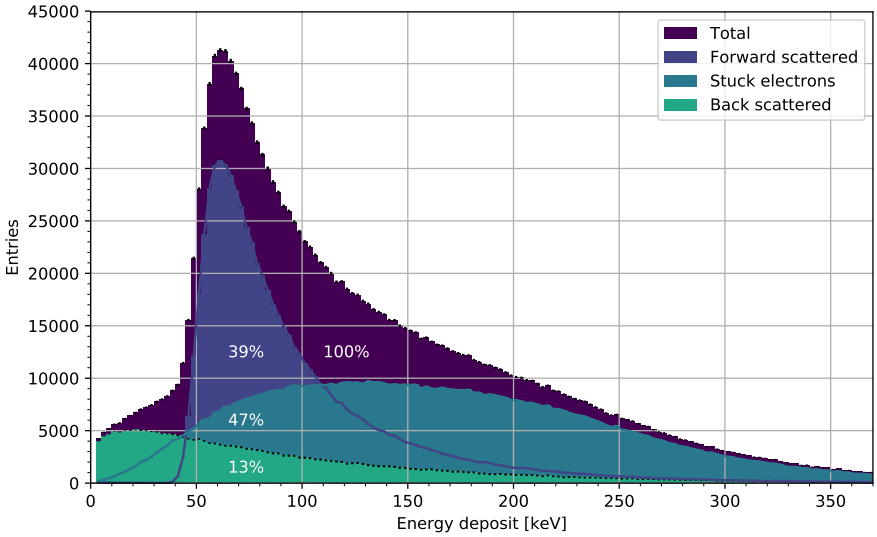


Figure 2.4: Deposited energy of $^{90}$Sr electrons in a 200 µm silicon sensor. The contributions of traversing, backscattered and absorbed electrons are depicted separately. *SourceSim* simulation (Section 3.1.1).

distribution as introduced above (Section 2.1.1). Most electrons are either fully absorbed or even back scattered. For charge measurements with low energetic electron sources, the randomized path length has to be considered, especially when using single pixels that confine a small volume. A continuative discussion can be found in Section 3.1.2.

#### Energy deposition by photons

The energy loss of photons in the sensor is different from the energy loss of charged particles. A beam of photons (light) is primarily attenuated in intensity and not degraded in energy. The intensity $I$ of a photon beam decreases exponentially with the distance $x$ in the sensor:

$$I(x) = I_0 e^{-\mu x} \tag{2.15}$$

$I_0$ is the initial intensity and $\mu$ the attenuation coefficient. The reciprocal of the attenuation coefficient is also called *mean free path*

$$\lambda = \frac{1}{\mu} \tag{2.16}$$

and can be interpreted as the distance where the initial intensity is attenuated to 37% or where the probability of a photon interaction is $1 - 1/e = 63\%$. Interacting photons create mainly low-energetic electrons that in turn deposit their (primarily full) energy through ionization as described before. The attenuation coefficient depends on the sensor material and is mainly defined by three competing processes that have different cross sections $\sigma$, depending on the photon energy:

$$\mu(E) = \mu_{\text{Photo}} + \mu_{\text{Compton}} + \mu_{\text{Pair}} = \frac{\rho}{u\,A}\left(\sigma_{\text{Photo}} + \sigma_{\text{Compton}} + \sigma_{\text{Pair}}\right) \tag{2.17}$$

The variables are described in Table 2.1. The attenuation coefficient in silicon is depicted in Figure 2.5 for the three processes:

1. Photoelectric effect: a photon that interacts via the photoelectric effect is fully absorbed in the sensor and a free electron with the energy of the photon, reduced by the electron binding energy, is created. Since a well-defined energy is deposited, radioactive gamma sources with photon energies below 100 keV are commonly used for energy calibrations of silicon detectors. Such calibration for ATLAS IBL detector modules is presented in Section 5.3.3. The attenuation length in silicon for radioactive gamma sources varies from a few 10 µm to a few mm (Figure 2.6). As a consequence, low energetic photons (few keV) deposit their energy close to the sensor surface while the absorption and therefore detection of high energetic photons ($> 20$ keV) is largely suppressed. The repercussions for energy calibrations of pixel detectors are discussed in Section 5.3.3.

2. Compton scattering: Compton scattering describes elastic scattering at atomic electrons, where a part of the photons kinetic energy is transferred to the electron. The amount of

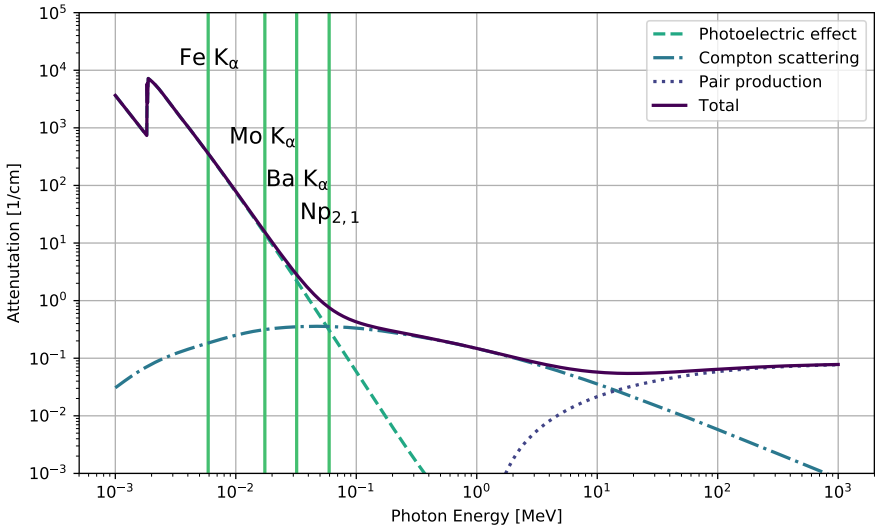


Figure 2.5: Attenuation in silicon for photons interacting via photoelectric effect, compton scattering, and pair production. Most probable photon energies of common gamma sources depicted as reference. Calculated from cross section data in [Ber+].

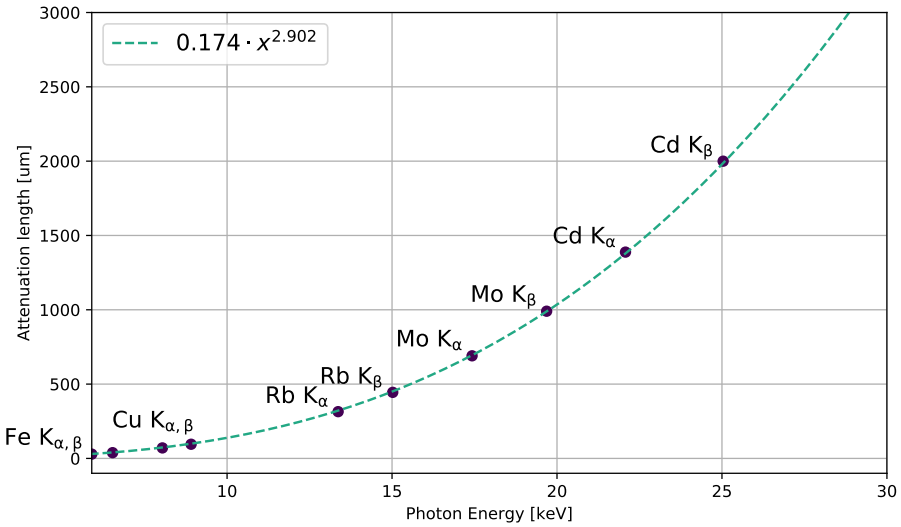


Figure 2.6: Attenuation length in silicon for photons interacting via the photoeffect. Photon-peak energies from sources depicted as reference with fit to data from [HGD93].

energy transferred ($E_\gamma$ - $E_{\gamma'}$) depends on the scattering angle $\theta$:

$$\frac{1}{E_{\gamma'}} - \frac{1}{E_\gamma} = \frac{1}{m_e\, c}\,(1 - \cos(\theta)) \tag{2.18}$$

Since the deflected photon is not necessarily absorbed in the sensor, a continuous energy-deposition spectrum arises from Compton scattering (*Compton continuum*). The maximum energy deposited is observed in spectra as the *Compton edge* that is defined by the maximum scattering angle of $\theta = 180°$.

3. Pair production: A photon with an energy above approximately twice the electron mass ($E \geq 2\, m_e = 1.022\,\text{MeV}$) can convert into an electron-positron pair when it is close to the silicon nucleus that must take some recoil to satisfy momentum conservation. For high energies above 10 MeV, pair production is the dominant mode of photon interaction in silicon. In the ATLAS experiment such energies are reached. But pair production is an unwanted process, since electron-positron pairs are difficult to track and a photon that converted in the inner tracking layers cannot be detected as such by the outer electromagnetic calorimeter. This imposes limitations on the total material budged of a pixel detector. Therefore, the total path-length $x$ in silicon should be low to reduce the probability of pair-production (Equation (2.15)). It also motivates the usage of low-density and light-weight materials for the pixel-detector services, that have large radiation length $X_0$, since the cross section for pair-production scales via [KW16, p. 86]:

$$\sigma_{\text{Pair}} \approx \frac{7}{9}\frac{1}{X_0}\frac{1}{n} \tag{2.19}$$

### 2.1.2 Charge carriers in silicon

Silicon atoms are arranged in a crystal lattice structure, creating a periodic potential. From the solution of the Schrödinger equation for electrons in a periodic potential follows that only certain energy ranges (*energy bands*) are allowed and that lightly bound electrons can be treated as quasi free particles [Ham01, 4ff][SN07, 12ff]. In silicon, as a semiconductor, the last two not fully occupied energy bands are separated by a forbidden energy region (*band gap*). These bands termed *valence* and *conduction band* are depicted in Figure 2.7. Only not fully occupied bands

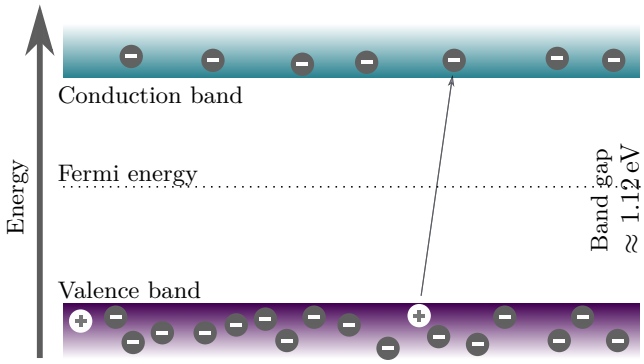


Figure 2.7: Electronic band structure in silicon with electrons and holes. Based on [SN07, p. 24].

have electrons that can take additional energy from an external electric field, thus contain drifting electrons and contribute to the silicon conductivity. For the evaluation of electrical properties, it is therefore sufficient to consider only these two bands. The description of charge-carrier transport is possible with classical formulas of motion, treating the electrons in these bands as free particles with different effective masses and mobilities [Ham01, p. 75]. By convention, missing electrons in the valence band are referred to as electron-holes (short: holes) and despite not being a physical particle, they are given a mass and a mobility. Both, electrons and holes, are the charge carriers in silicon. The mobility $\mu$ that relates the charge carrier drift velocity to the electric field $E$:

$$v_d = \mu E \tag{2.20}$$

can be described with the following function, that is determined from fits to data [Jac+77, p. 87]:

$$\mu(E,T) = \frac{v_m}{E_c} \frac{1}{\left[1 + \left(\frac{E}{E_c}\right)^{\beta}\right]^{\frac{1}{\beta}}} \tag{2.21}$$

with the temperature $T$ in Kelvin and:

| | Electron | Hole | Unit |
|---|---|---|---|
| $v_m$ | $1.53 \cdot 10^9 \cdot T^{-0.87}$ | $1.62 \cdot 10^8 \cdot T^{-0.52}$ | $\mathrm{cm\,s^{-1}}$ |
| $E_c$ | $1.01 \cdot T^{1.55}$ | $1.24 \cdot T^{1.68}$ | $\mathrm{V\,s^{-1}}$ |
| $\beta$ | $2.57 \cdot 10^{-2} \cdot T^{0.66}$ | $0.46 \cdot T^{0.17}$ | - |

Since the mobility itself decreases with the electric field strength, a saturation of drift velocity above $50\,\mathrm{kV\,cm^{-1}}$ can be observed. This value corresponds approximately to a bias voltage of 1000 V applied to 200 µm thick sensors; a value that is reached in the ATLAS pixel detector at the end of runtime (Figure 2.8). At common bias voltages and sensor thicknesses, the drift time of electrons through the sensor bulk is in the order of nanoseconds and for holes about 45 % longer.

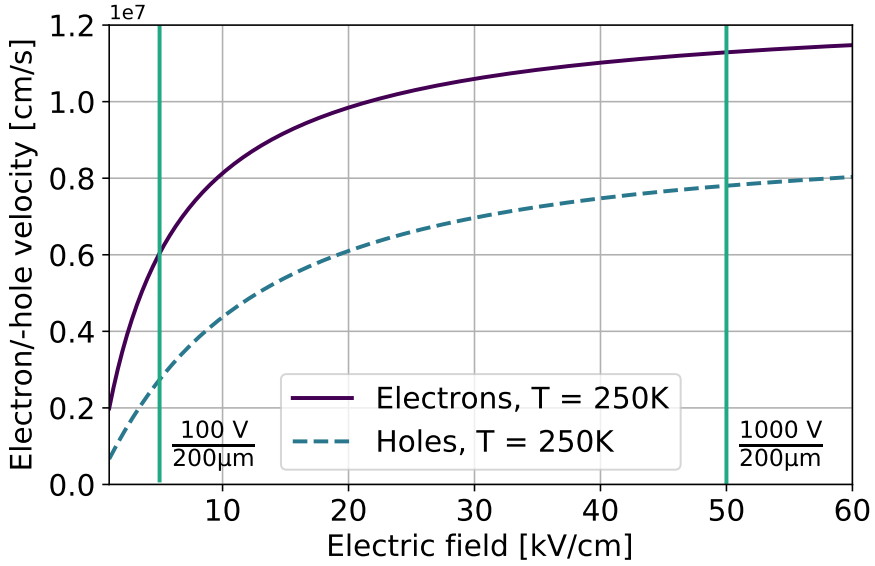


Figure 2.8: Charge carrier velocities in silicon as a function of the electrical field strength at different temperatures (Equation (2.21)). Two field strengths that occur in the ATLAS IBL pixel layer at beginning (*left*) and end (*right*) of the operation period are depicted.

Energy deposit by ionizing radiation, as introduced in the preceding section, creates electrons and holes in equal amount due to charge conservation. These are called electron-hole pairs (*e-h pair*). The energy needed to create one e-h pair in silicon depends on the band gap energy and therefore on temperature. A slight dependence on the ionizing particle type is also observed [ER65, p. 2089]. The exact value has changed in the course of history, mainly due to better experimental setups. For photons and electrons at room temperature ($T = 300\,\mathrm{K}$), the mean energy $w$ in silicon is about [Sch+00]:

$$w = 3.65\ \mathrm{eV/e-h} \tag{2.22}$$

For the most probable number of e-h pairs for a MIP traversing a 200 µm silicon sensor, as used in this study, follows with Equation (2.12):

$$N_{\mathrm{e-h}} = \frac{\frac{dE}{dx}\,\mathrm{MPV}}{w} \cdot 200\,\mu\mathrm{m} \approx 13870 \tag{2.23}$$

The recombination of an electron in the conduction band requires the lattice to take some momen-

tum (*indirect semiconductor*) making the life times of charge carriers orders of magnitude larger then their drift times in thin sensors. The recombination is mainly dealt by crystal defects (e.g. impurity atoms) and discussed within the scope of radiation damage in Section 2.2. In silicon with low impurity concentrations life times above a few 100 µs have be observed [Sch97, p. 167]. In intrinsic silicon, i.e. silicon with no impurity atoms, the number of holes and electrons is the same. The free charge-carrier concentration $n_i$ can be calculated by integration of their density $n(E)$ over the conduction band energies. $n(E)$ is given by the density of states $N(E)$ times the occupation probability $F(E)$:

$$n_i = \int_{E_c}^{\infty} n(E)\, dE = \int_{E_c}^{\infty} N(E)F(E)\, dE \tag{2.24}$$

Electrons follow the Pauli exclusion principle and the occupation propability is consequently given by the Fermi-Dirac distribution:

$$F(E) = \frac{1}{1 + e^{\frac{E-E_F}{k_b T}}} \tag{2.25}$$

$E_F$ is the Fermi energy where the occupation probability is 50 %. In intrinsic silicon it is located in the center of the band gap (Figure 2.7). Evaluation of Equation (2.24) leads to [SL12, pp. 34-36]:

$$n_i = \sqrt{N_C\, N_V} e^{-\frac{E_g}{2\, k_B\, T}} \tag{2.26}$$

with the band gap energy in silicon of $E_g \approx 1.12\,\text{eV}$ and the effective density of states in the valence and conduction band $N_V, N_C \propto T^{\frac{3}{2}}$. Due to the strong dependence of the free charge-carrier concentration $n_i$ on temperature, semiconductors show a drastic change in the current density:

$$J = e\, n_i\, (v_e + v_h) = e\, n_i\, (\mu_e + \mu_h)\; E \tag{2.27}$$

and therefore in the resistivity:

$$\rho = \frac{E}{J} = \frac{1}{e\, n_i\, (\mu_e + \mu_h)} \tag{2.28}$$

with temperature. Intrinsic semiconductors are non-conductive at absolute zero and show a large resistivity decrease with increasing temperatures.

### 2.1.3 The p-n junction for particle detection

Impurity atoms (dopants) are added to the silicon lattice to steer its electrical characteristics. This process is called doping. For n-type doping, elements from the fifth group of the periodic table (e.g. phosphorus) are used. These elements, referred to as donors, add lightly bound electrons to the silicon. For p-type doping elements from the third group (e.g. boron) are used introducing lightly bound holes (acceptors). They are lightly bound (*shallow dopants*), since the energy levels in the band gap are very close to the conduction and valence band, respectively (Figure 2.9). Therefore, at room temperature they are practically fully ionized. As the charge-carrier concentration of intrinsic silicon is much lower ($\mathcal{O}(10^{10})\,\text{cm}^{-3}$ at room temperature), the dopant concentration

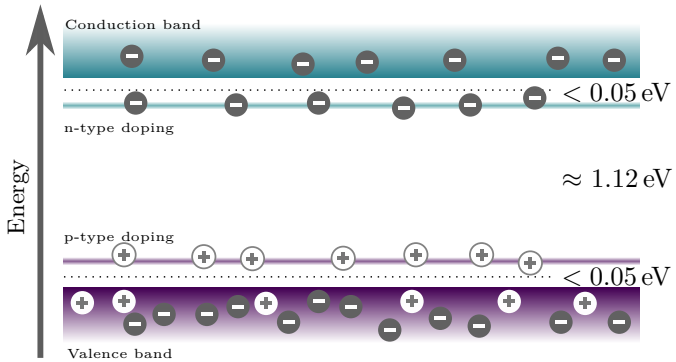


Figure 2.9: Electronic band structure for n- and p-type silicon. The Fermi level (*dotted line*) is located between the additional energy level and the conduction/valence band for n-type/p-type doping. Based on [SN07, p. 24].

$N_D/N_A$ defines the resistivity of the n-type/p-type silicon bulk (Equation (2.28)):

$$\rho_{\mathrm{n-type}} \approx \frac{1}{e\, N_D\, \mu_e} \qquad \rho_{\mathrm{p-type}} \approx \frac{1}{e\, N_A\, \mu_h} \tag{2.29}$$

Depending on the application, doping concentrations between $1 \times 10^{12}\,\mathrm{cm}^{-3} - 1 \times 10^{18}\,\mathrm{cm}^{-3}$ are used. For CMOS circuits, where high conductivities are important, the doping concentration is high ($\mathcal{O}(10^{18})\,\mathrm{cm}^{-3}$). In silicon sensors for particle detection a high resistive silicon bulk, thus low doping concentrations, are usually preferred ($1 \times 10^{12}\,\mathrm{cm}^{-3} - 1 \times 10^{14}\,\mathrm{cm}^{-3}$). In contrast to intrinsic silicon one type of charge carriers can dominate the conductivity after doping. To differentiate them one uses the terms *majority* and *minority* charge carrier for electrons or holes.

When n- and p-type silicon is brought into thermal contact, an interface called *p-n junction* is created (Figure 2.10). The free majority charge carriers in the contact region recombine and create a zone depleted of free charge carriers (*depletion zone*). As a consequence, the immovable dopants in the depletion zone are ionized and create *space charge*. The resulting electric field counteracts the diffusion of charge carriers until a thermal equilibrium is reached. The field can be calculated from space charge $\rho(x)$ using the one dimensional Maxwell equation:

$$\frac{d}{dx} E(x) = \frac{1}{\epsilon_s} \rho(x) \tag{2.30}$$

$$\Rightarrow E(x) = \begin{cases} -e\frac{N_A}{\epsilon_s}\,(x + x_p) & -x_p \leq x \leq 0 \\ e\frac{N_D}{\epsilon_s}\,(x - x_n) & 0 \leq x \leq x_n \end{cases} \tag{2.31}$$

with permittivity of silicon ($\epsilon_s$) and depletion zone width $x_p$, $x_n$ in the p- and n-type region. The emerging potential over the space charge region is called *build-in voltage*. It depends on the difference of the Fermi-levels in the n- and p-type region and is in shallow doped silicon about

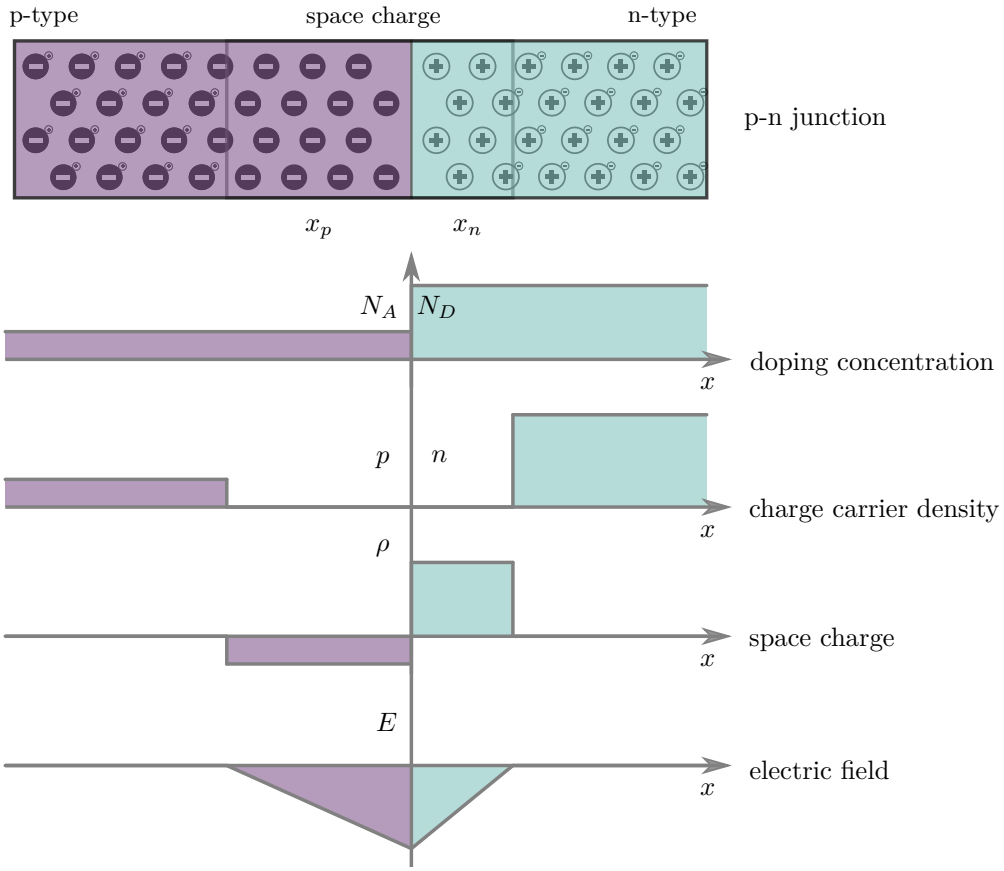


Figure 2.10: Abrupt p-n junction with corresponding doping concentration, free charge-carrier concentration, space charge, and electric field. Adapted from [KW16, p. 291].

0.6 V – 0.8 V. The relation of the build in voltage to the depletion width is:

$$V_{\mathrm{bi}}(x) = \int_{-x_p}^{x_n} E(x)\,dx = \frac{e}{2\,\epsilon_s}\left(N_A\,x_p^2 + N_D\,x_n^2\right) \tag{2.32}$$

$$\Rightarrow x_p = \sqrt{\frac{2\,\epsilon_s}{e}\frac{N_D}{N_A\,(N_D+N_A)}V_{\mathrm{bi}}} \quad \wedge \quad x_n = \sqrt{\frac{2\,\epsilon_s}{e}\frac{N_A}{N_D\,(N_D+N_A)}V_{\mathrm{bi}}} \tag{2.33}$$

The ratio of the depletion widths is consequently given by the ratio of doping concentrations:

$$\frac{x_p}{x_n} = \frac{N_D}{N_A} \tag{2.34}$$

In silicon sensors the n- and p-doping concentrations are orders of magnitude different, a property that is only slightly depicted in Figure 2.10 for better visualization. One type of silicon is highly doped ($> 1 \times 10^{18}\,\mathrm{cm}^{-3}$) for high conductivities and to help creating the metal-semiconductor contact that is needed to amplify the charge signal with readout electronics. This localized highly doped silicon (*implantation*, denoted with $n^+$, $p^+$) is called *readout electrode* and is with a few

µm usually very thin. In contrast, the silicon bulk has a much lower doping concentration ($\approx 1 \times 10^{12}\,\mathrm{cm}^{-3}$). Using Equation (2.34), one can therefore approximate the depletion zone width $d$ using the bulk doping concentration only:

$$d \approx \sqrt{\frac{2\,\epsilon_s}{e}\frac{V_{\mathrm{bi}}}{N_{\mathrm{eff}}}} \tag{2.35}$$

$N_{\mathrm{eff}}$ is the *effective doping concentration* that is used to describe the (unsigned) space charge concentration of the bulk. Generally, it equals the doping concentration $N_{\mathrm{D}}$ or $N_{\mathrm{A}}$. The definition becomes more useful when several electrically active impurity levels are present, for example after irradiation (Section 2.2), or if partially compensating p- and n-type doping concentrations exist. The depletion zone width is with conventional doping concentrations in the order of a few 10 µm only, thus much smaller than the sensor thickness. To increase the depletion zone, an external reverse bias voltage $V_{\mathrm{bias}}$ is applied (positive at the n-side and negative at the p-side) that pulls the free charge carriers out of the sensor bulk. The potential difference over the junction is then $V = V_{\mathrm{bias}} + V_{\mathrm{bi}}$. Since bias voltage is generally at least one order of magnitude larger than the build-in voltage, one can approximate the depletion width by:

$$d \approx \sqrt{\frac{2\,\epsilon_s}{e}\frac{V_{\mathrm{bias}} + V_{\mathrm{bi}}}{N_{\mathrm{eff}}}} \underset{V_{\mathrm{bias}} \gg V_{\mathrm{bi}}}{\approx} \sqrt{\frac{2\,\epsilon_s}{e}}\sqrt{\frac{V_{\mathrm{bias}}}{N_{\mathrm{eff}}}} \tag{2.36}$$

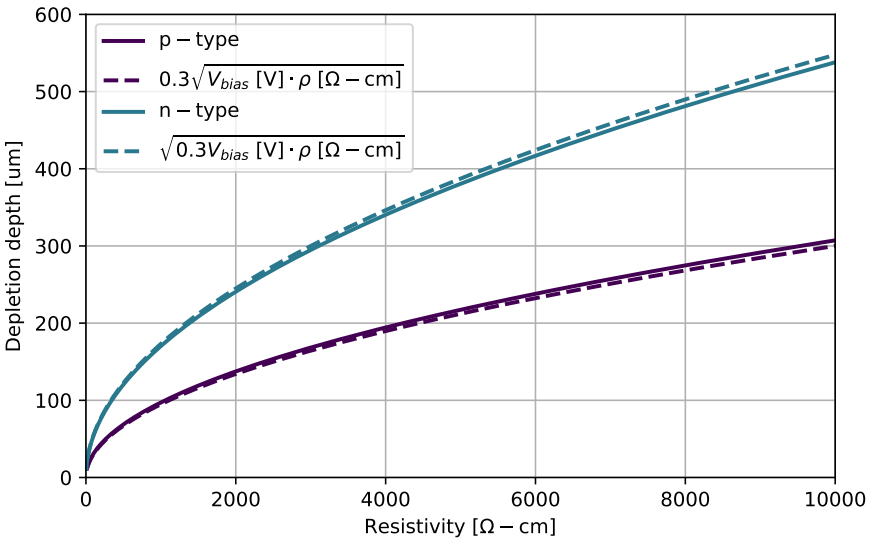


Figure 2.11: Depletion depth in a silicon sensor as a function of bulk resistivity for n- and p-type bulk. Evaluation for a bias voltage of $V_{\mathrm{bias}} = 100\,\mathrm{V}$ at $T = 300\,\mathrm{K}$. Approximation Equation (2.37) and Equation (2.38) depicted for comparison.

When using silicon for fast radiation detectors, large depletion regions are preferred with high electrical field strengths that allow for quick charge collection and reduced trapping probabilities after irradiation (Section 2.2). The benefit of charge collection in a depleted p-n junction is that high voltages can be applied to achieve such high field strengths, while keeping the leakage current low due to the low free charge-carrier concentration. High leakage current must be avoided since it is a substantial contributor to electronic noise when amplifying the charge signal. From Equation (2.36) and Equation (2.29) follows that detectors with high resistive silicon bulks and sensor designs allowing high bias voltages are more suitable. During nominal operation a bias voltage exceeding the depletion voltage is usually applied to ensure fast charge collection over the sensor thickness. The following approximation formulas for the depletion zone width can be derived from Equation (2.36) and Equation (2.29) and are depicted in Figure 2.8:

$$d \approx 0.3\sqrt{V_{bias}\ [\mathrm{V}] \cdot \rho\ [\Omega - \mathrm{cm}]} \qquad \text{p-type bulk} \tag{2.37}$$

$$d \approx \sqrt{0.3 \cdot V_{bias}\ [\mathrm{V}] \cdot \rho\ [\Omega - \mathrm{cm}]} \qquad \text{n-type bulk} \tag{2.38}$$

An application of Equation (2.37) can be found in Chapter 6, where the silicon bulk resistivity of new sensor prototypes is determined from the depletion width.

### 2.1.4 Charge signal in a pixel detector

The readout implantation in a pixel sensor is segmented to allow independent charge detection for each pixel. In the common planar design, each pixel has a thin implantation at the sensor readout surface. Such sensors are referred to as *planar* pixel sensors. For large readout electrodes, that take a large fraction of the sensor surface (few 10%), the electrical field is well approximated by the assumption of no gaps between the implantations. This effectively neglects any fraction of the electrical field parallel to the sensor surface and the perpendicular field simply equals the field of one p-n junction as introduced in Equation (2.31). When defining the z-direction perpendicular to the sensor surface, it follows for the electric fields and potentials in such a idealized pixel sensor:

$$\Phi_z(z) = \begin{cases} \frac{\rho}{2\epsilon} z^2 - \frac{\rho}{\epsilon} z_{\mathrm{dep}} z \\ V_{\mathrm{bias}} \\ \frac{\rho}{2\epsilon} z^2 - \frac{\rho}{2\epsilon} d \left( \frac{z_{\mathrm{dep}}^2}{d^2} + 1 \right) z \end{cases} \qquad \vec{E}(z)\,\vec{e}_z = \begin{cases} \frac{\rho}{\epsilon} z_{\mathrm{dep}} - \frac{\rho}{\epsilon} z & z_{\mathrm{dep}} \leq d, z \leq z_{\mathrm{dep}} \\ 0 & z_{\mathrm{dep}} \leq d, z > z_{\mathrm{dep}} \\ \frac{\rho}{2\epsilon} d \left( \frac{z_{\mathrm{dep}}^2}{d^2} + 1 \right) - \frac{\rho}{\epsilon} z & z_{\mathrm{dep}} > d \end{cases} \tag{2.39}$$

The three cases differentiate between a fully depleted sensor ($z_{\mathrm{dep}} > D$) and a partially depleted sensor with depletion zone edge at $z_{\mathrm{dep}} = \sqrt{\frac{2\epsilon}{\rho} V_{\mathrm{bias}}}$. Figure 2.12 depicts such a pixel detector, with n-type readout electrodes and p-type bulk[2]. Doping concentration and bias voltage are chosen in a way, that the sensor is not fully depleted and the depletion zone extends about 160 µm into the bulk.

[2] Numerical solutions to more realistic electrode configurations are depicted in Figure 5.2 of Section 5.1.1.

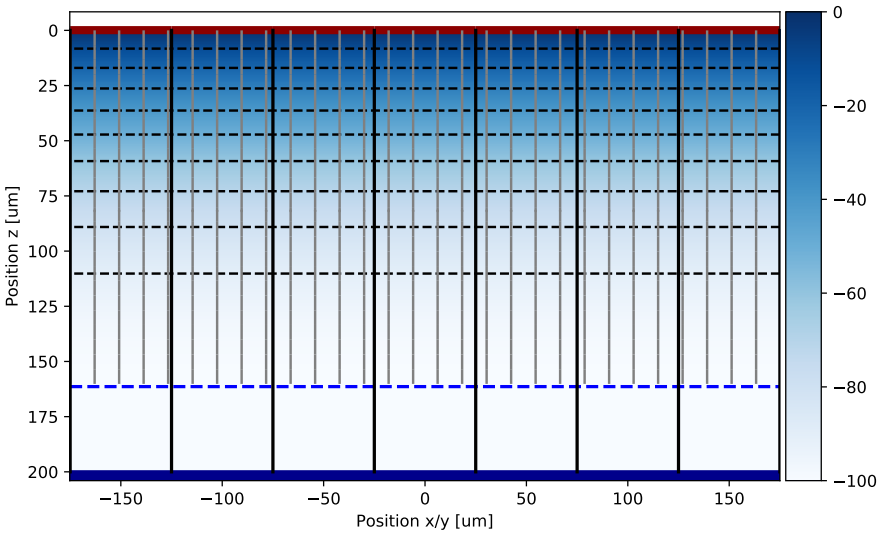


Figure 2.12: Side view of a p-type pixel sensor with 50 µm pixels. N-type readout electrodes depicted in *red* and backside $p+$ bias implantation in *blue*. Potential (*color scale*) and electric field (*grey lines*) depicted as given by Equation (2.39). Pixel dimensions (*black lines*) and equipotential lines (*dotted black*) shown. Doping concentration ($\rho = 5 \times 10^{12}\,\mathrm{cm}^{-3}$) and bias voltage ($V_{\mathrm{bias}} = 100\,\mathrm{V}$) create a depletion zone that extends about 160 µm into the bulk (*dotted blue line*).

Ionizing radiation creates electron and holes that drift to the readout and biasing electrode, depending on the orientation of the electric field (Equation (2.21)). In this context, it is often referred to as *drift field*. The moving charge carriers induce a current on the readout electrodes, that are kept at a fixed potential. This current can be measured with dedicated electronics for each sensor pixel to enable localized detection of the ionizing particle. The induced current of one drifting charge carrier at $\vec{x}_q$ can be calculated in three steps, which are illustrated in the following with simplifying assumptions:

1. The static electric field of the charge carrier at the electrode location ($z = 0$) is calculated from the Maxwell equation:

$$\nabla \vec{E} = -\frac{q\delta(\vec{x} - \vec{x}_q)}{\epsilon_s} \tag{2.40}$$

with the boundary condition of a vanishing electric field components parallel to the bias and readout electrodes surfaces, that are idealized as conductors:

$$E_{x,y}(x, y, z = 0) = E_{x,y}(x, y, z = d) = 0$$

When the charge carrier is close to the readout electrode $z \ll d$, one can neglect the boundary

condition at the bias side and a solution can be found using a mirror charge at $-\vec{x}_q$:

$$\vec{E} = -\frac{q}{2\pi\,\epsilon_s}\frac{z_q}{\sqrt{x^2+y^2+z_q^2}^3}\,\vec{e}_z \tag{2.41}$$

2. The induced charge $\sigma$ on the readout surface is given by Gauss's law:

$$\int_V \frac{\rho}{\epsilon_s} = \oint_{\partial V} \vec{E}\cdot d\vec{A} \Rightarrow \sigma = \epsilon_s\,E_z = -\frac{q}{2\pi}\frac{z_q}{\sqrt{x^2+y^2+z_q^2}^3} \tag{2.42}$$

For the total induced charge on the electrode with width $w$ in x-direction follows:

$$Q = \int_{-\infty}^{\infty}\int_{-w/2+x_q}^{w/2+x_q} \sigma\,dx\,dy = -q\,\frac{1}{\pi}\left[\arctan\left(\frac{w/2+x_q}{z_q}\right) + \arctan\left(\frac{w/2-x_q}{z_q}\right)\right] \tag{2.43}$$

The x-origin is set to the pixel center. The electrode dimension in y is assumed large and approximated by infinity.

3. For the total induced current on the electrode by one drifting charge carrier follows under the assumption that the electrostatic field propagates instantaneously:

$$I(t) = -\frac{d}{dt}Q = -\frac{\partial Q}{\partial z_q}\,\frac{dz_q}{dt} = q\,\frac{2}{\pi}\left(\frac{w+2\,x_q}{(w+2\,x_q)^2+4\,z_q^2} + \frac{w-2\,x_q}{(w-2\,x_q)^2+4\,z_q^2}\right)\,v \tag{2.44}$$

Consequently, the induced charge depends on the drifting charge position and the induced current has an additional dependency on the drift velocity.

#### Weighting field formalism

The position dependent solution in Equation (2.43) can be interpreted as a potential and its derivation with respect to the z-direction in Equation (2.44) as the corresponding field component in z. That the coupling between moving charges to arbitrary electrode geometries can be generally described by a *weighting potential* $\Phi_w$ and a *weighting field* $\vec{E}_w = -\vec{\nabla}\Phi_w$ is known as the Shockley-Ramo theorem [Ram39, p. 585]:

$$I = q\,\vec{E}_w\cdot\vec{v} \tag{2.45}$$

$$Q = \int_{t_0}^{t_1} I(t)\,dt = q\,(\Phi_w(\vec{x}_0) - \Phi_w(\vec{x}_1)) \tag{2.46}$$

Where the weighting potential is the solution to Laplace's equation [He01, p. 252]:

$$\nabla^2\Phi_w = 0 \tag{2.47}$$

when applying a unit potential to the readout electrode and zero potential to all others. The weighting potential depends solely on the geometry of all electrodes at fixed potential and is also

valid in the presence of space charge and constant magnetic fields in the sensor [He01, 253ff]. When taking the backside bias electrode into account, in contrast to the previous calculation, one can derive the following analytical solution for a planar pixel sensor [SHS04, p. 555]:

$$\Phi_w = -\frac{1}{\pi}\left[\arctan\left(\tan\frac{\bar{z}}{2}\tanh\left(\frac{\bar{x}+\frac{\bar{w}}{2}}{2}\right)\right) - \arctan\left(\tan\frac{\bar{z}}{2}\tanh\left(\frac{\bar{x}-\frac{\bar{w}}{2}}{2}\right)\right)\right] \tag{2.48}$$

$$\vec{E}_{\mathrm{x/y,z}} = \frac{\sinh\frac{\bar{w}}{2}}{d\left(\cosh\left(\frac{\bar{w}}{2}-\bar{x}\right)+\cos\bar{z}\right)\left(\cosh\left(\frac{\bar{w}}{2}+\bar{x}\right)+\cos\bar{z}\right)}\begin{pmatrix}-\sin\bar{z}\sinh\bar{x}\\ \cosh\frac{\bar{w}}{2}+\cos\bar{z}\cosh\bar{x}\end{pmatrix} \tag{2.49}$$

$$\bar{x} = \frac{\pi\,x}{d} \quad \wedge \quad \bar{z} = \frac{\pi\,z}{d} - 1 \quad \wedge \quad \bar{w} = \frac{\pi\,w}{d}$$

The weighting potential and -field is depicted in Figure 2.13. The weighting field shows a steep rise

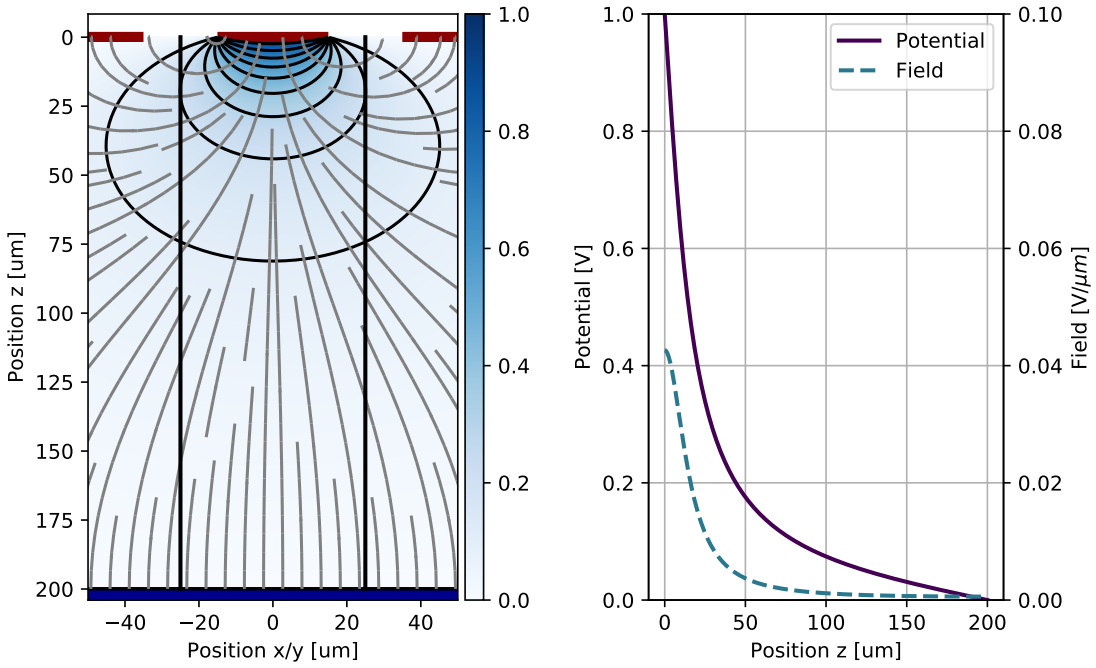


Figure 2.13: Weighting potential and weighting field of a planar pixel sensor with 200 µm thickness and 30 µm readout electrode width. *Left:* Two dimensional visualization. *Right:* Absolute field and potential at readout pixel center.

at the readout electrodes. The slope increases with the ratio of detector depth to readout electrode width ($d/w$). For large ratios, as they are present in the ATLAS pixel detector, charge carriers close to the electrode dominate the signal current. This dependence between e-h pair position and total charge induced is illustrated in Figure 2.14. Depending on the e-h pair position in the bulk, either the hole or electron contribution is higher. For a distribution of e-h pairs along the sensor depth, as it is the case for MIPs, the charge carrier type that is collected by the readout electrode dominates the charge signal. This can be seen in Figure 2.15 *left*, where electrons contribute 80% of the signal and are collected within 5 ns, whereas holes contribute only 20% and

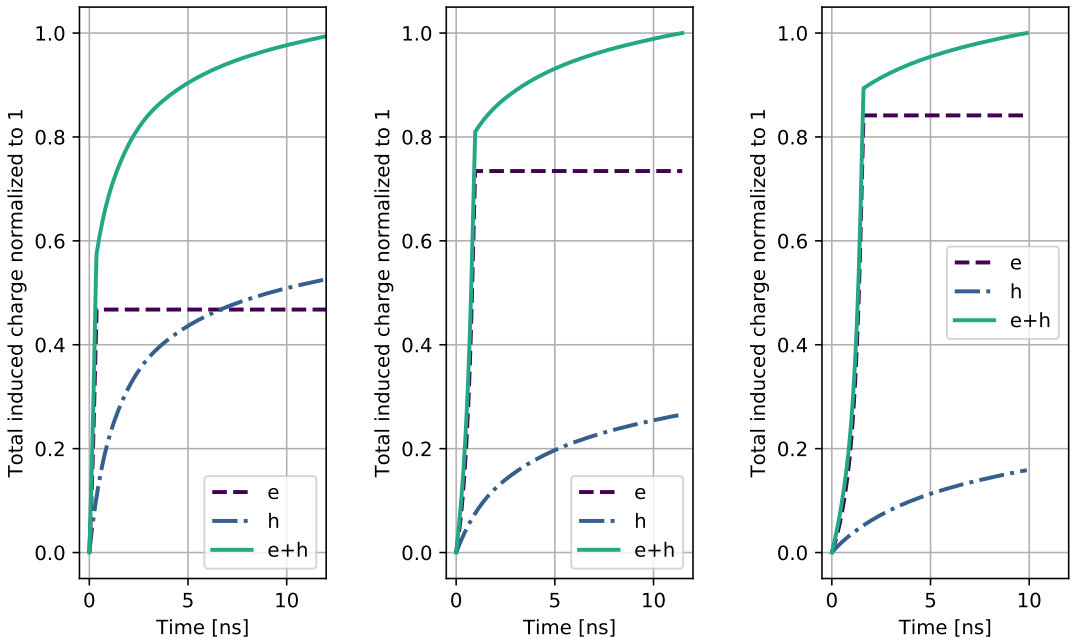


Figure 2.14: Total induced charge on the readout electrode of a planar pixel sensor for one drifting e-h pair. Different starting distances to readout electrode depicted: 40 µm (*left*), 100 µm (*center*), and 160 µm (*right*). Simulation parameters in Table 7.2.

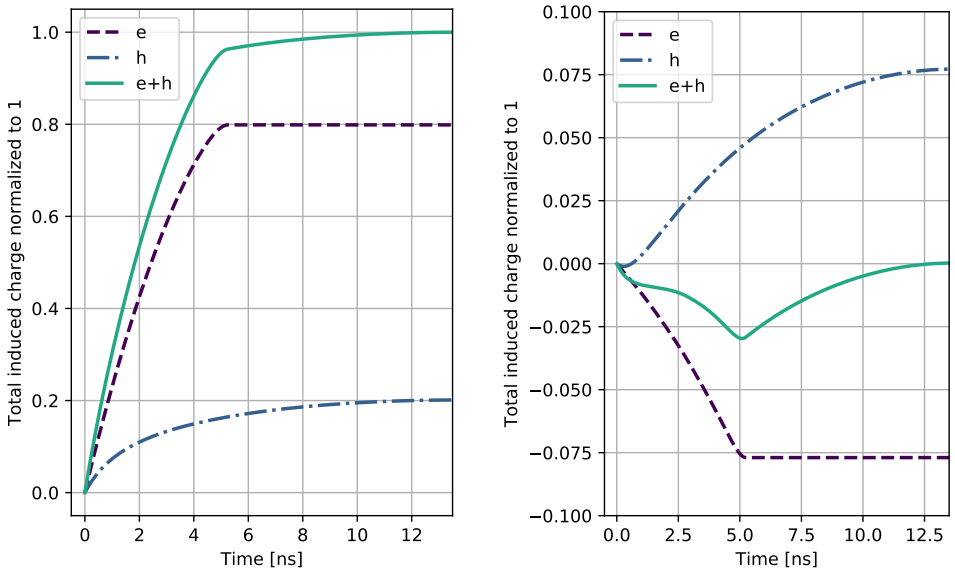


Figure 2.15: Total induced charge of e-h pairs from a minimum-ionizing particle in a planar pixel sensor. *Left:* perpendicular MIP track through the pixel center. *Right:* perpendicular MIP track through the neighboring pixel center. Simulation parameters in Table 7.2.

drift 3 times longer. Since the weighting field extends to neighboring pixels, these also see a signal current during drift. However, no net charge is deposited after the charge carriers have reached the electrode (Figure 2.15 *right*). With Equation (2.46) and Equation (2.20) one can express the signal current as a function of the weighting field, electrical field and charge-carrier mobility:

$$I(t) = q\,\vec{E}_w \cdot \vec{v} = q\,\mu_{\mathrm{e,h}}\,\vec{E}_w \cdot \vec{E}_d \tag{2.50}$$

For larger and faster signals, the collection of electrons with a higher mobility $\mu_\mathrm{e}$ is preferred and a depletion zone growing from the readout electrode side to maximize the $\vec{E}_w \cdot \vec{E}_d$ product. The faster drift velocity for electrons is also beneficial to minimize charge loss due to reduced charge carrier life-times after radiation damage in the sensor (Section 2.2). Consequently, radiation-hard silicon pixel sensors usually have an $n^+$ readout electrode for electron collection.

The convenient description of charge-carrier coupling to electrodes using the weighting field formalism also simplifies the calculation of induced currents. This is especially useful when more complex electrode geometries (e.g. large gap between readout electrodes or 3D pixel) are present that do not have analytical solutions. Instead of repeating the three steps depicted above at many points in time, it is sufficient to calculate a time independent weighting field once only. The weighting field formalism is also applied in the simulation of pixel detectors after irradiation in Chapter 5.

### 2.1.5 Charge cloud and charge sharing

Thus far, single e-h pairs were considered, that independently move through the bulk due to the drift field. In reality, ionizing radiation in silicon sensors creates large numbers of e-h pairs ($\mathcal{O}(1000)$), that interact with each other and move already by thermal energy without the need of an electric field. The movement of an ensemble of charge carriers, called *charge cloud*, is described by the continuity equation:

$$\frac{\partial \rho}{\partial t} = \underbrace{D\nabla^2\rho}_{\text{Diffusion}} - \underbrace{\mu\nabla\cdot\left(\rho\vec{E}\right)}_{\text{Repulsion and drift}} \tag{2.51}$$

with the charge cloud density-distribution $\rho$ and diffusion constant ($D$) given by Einstein's equation:

$$D = \mu\, k_B\, T/e \tag{2.52}$$

The first term in Equation (2.51) depicts diffusion due to density gradients and the second term movement due to an electric field. For low charge densities, as it is the case for MIPs and low energetic gamma-sources, repulsion can be neglected (see Section 3.1.1) and the solution to Equation (2.51) is:

$$\rho(\vec{r}, t) = \frac{N\,q}{\left(2\pi\sigma^2\right)^{3/2}} \exp\left(-\frac{\vec{r}^{\,2}}{2\sigma^2}\right) \tag{2.53}$$

with a time dependent Gaussian spread:

$$\sigma(t) = \sqrt{2\,D\,t} \tag{2.54}$$

The lateral expansion of the charge cloud while drifting through the sensor is one mechanism that is responsible for charge sharing between pixels. The evolution of the charge-cloud width is depicted in Figure 2.16. When neglecting plasma effects [TS67] and only considering the collected carrier

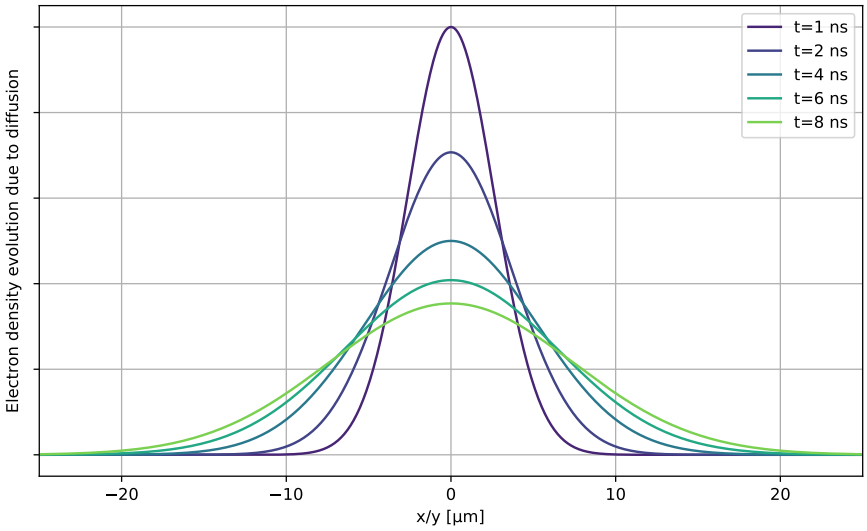


Figure 2.16: Time evolution of the electron charge-cloud density-distribution in silicon due to diffusion.

type, one can calculate the charge fraction induced on the readout electrode as a function of the primary charge deposition location $(x, y)$:

$$\begin{aligned} Q_{\text{frac}}(x, y, a, b, \sigma) &= \int\limits_{\text{pixel area}} \rho\left(\vec{r} - \vec{r}_{\mu}\right) d\vec{r} \\ &= \frac{1}{2\pi\sigma^2} \int\limits_{-a/2}^{a/2} \int\limits_{-b/2}^{b/2} \exp\left(-\frac{(x-\mu_x)^2 + (y-\mu_y)^2}{2\,\sigma^2}\right) d\mu_x\, d\mu_y \\ &= \frac{1}{4}\left(\operatorname{erf}\left(\frac{x+\frac{a}{2}}{\sqrt{2}\,\sigma}\right) - \operatorname{erf}\left(\frac{x-\frac{a}{2}}{\sqrt{2}\,\sigma}\right)\right) \\ &\quad \left(\operatorname{erf}\left(\frac{y+\frac{b}{2}}{\sqrt{2}\,\sigma}\right) - \operatorname{erf}\left(\frac{y-\frac{b}{2}}{\sqrt{2}\,\sigma}\right)\right) \end{aligned} \tag{2.55}$$

with pixel pitch in x ($a$), pixel pitch in y ($b$) and a charge-cloud width $\sigma$ after the drift. Figure 2.17 depicts $Q_{\text{frac}}$ for a pixel with ATLAS IBL geometry (50 µm x 250 µm) and a charge cloud size of 5 µm. The charge fraction within the pixel is mostly one and drops to 50% between pixels.

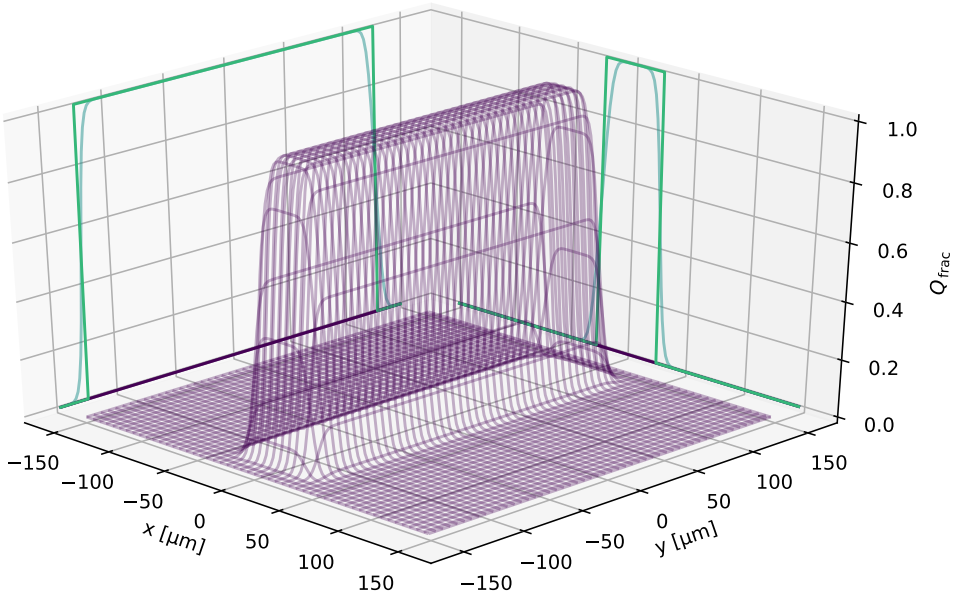


Figure 2.17: Charge in one 50 µm x 250 µm pixel given as a fraction. A charge-cloud width of 5 µm is assumed, corresponding to 200 µm drift at room temperature and a bias voltage of 90 V. Projections of the distribution (*dark*) and the pixel geometry (*light*) are shown at axis boundaries.

The mean charge fraction for one pixel, assuming a homogeneous irradiation within, is:

$$\begin{aligned}
\overline{Q}_{\text{frac}}(a,b,\sigma) = & \quad \frac{1}{ab}\int_{-a/2}^{a/2}\int_{-b/2}^{b/2} Q_{\text{frac}}(x,y,a,b,\sigma)\,dx\,dy \\
= & \quad \frac{1}{ab}\left(\sqrt{\frac{2}{\pi}}\sigma\left(1-\underbrace{\exp\left(-\frac{a^2}{2\sigma^2}\right)}_{\approx 0, a\gg\sigma}\right) - a\underbrace{\operatorname{erf}\left(\frac{a}{\sqrt{2}\sigma}\right)}_{\approx 1, a\gg\sigma}\right) \\
& \left(\sqrt{\frac{2}{\pi}}\sigma\left(1-\underbrace{\exp\left(-\frac{b^2}{2\sigma^2}\right)}_{\approx 0, b\gg\sigma}\right) - b\underbrace{\operatorname{erf}\left(\frac{b}{\sqrt{2}\sigma}\right)}_{\approx 1, b\gg\sigma}\right) \qquad (2.56) \\
\approx & \quad \frac{1}{ab}\left(a-\sqrt{\frac{2}{\pi}}\sigma\right)\left(b-\sqrt{\frac{2}{\pi}}\sigma\right) \qquad (2.57)
\end{aligned}$$

Approximation (2.56) assumes small charge clouds compared to the pixel pitch. This assumption is valid for common pixel pitches and charge clouds sizes at the ATLAS experiment (several 10 µm – 100 µm vs. a few µm). In the limiting case of no diffusion ($\sigma = 0$) charge sharing vanishes and is independent of the pixel pitch ($\overline{\text{Q}}_{\text{frac}} = 1$). When the brackets are multiplied out, one can see that charge sharing increases with $\frac{\sigma}{\text{pitch}_\text{x}} + \frac{\sigma}{\text{pitch}_\text{y}}$ and decreases with $\frac{\sigma^2}{\text{pitch}_\text{x}\cdot\text{pitch}_\text{y}}$. Thus, the

intuitive statement that for a given pixel area charge-sharing is mitigated best for square shaped pixels while an asymmetric aspect ratio enhances charge sharing becomes comprehensible. For the actual ATLAS pixel detector, charge sharing from diffusion of the charge cloud is negligible compared to other effects that dominate charge sharing like the track incident angle and the Lorentz drift. Using the pixel geometry of the ATLAS IBL and the values of Figure 2.17, with a relatively large charge cloud size of 5 µm, still yields above 90 % of the charge deposited in one pixel:

$$\overline{Q}_{\text{frac}}(a = 50\,\mu\text{m}, b = 250\,\mu\text{m}, \sigma = 5\,\mu\text{m}) \approx 91\,\%$$

But when measuring charge spectra of single pixels to deduce detector calibration constants or charge collection efficiencies, a loss of the *mean* charge per pixel of 9 % can be significant and is further discussed in Chapter 3.
To evaluate $\text{Q}_{\text{frac}}$ and $\overline{Q}_{\text{frac}}$ for a MIP or a photon depositing charge at a certain depth, the charge-cloud spread

$$\sigma(z) = \sqrt{2D\,t(z)}$$

has to be known. Knowledge of the drift time as a function of the initial charge-cloud position $t(z)$ requires knowledge of the electric field. For planar sensors, the electric field is given by Equation (2.39) and its z-component can be reformulated as:

$$E_{z\,\substack{\text{n-bulk}\\\text{p-bulk}}} = \mp\frac{2\,V_{\text{dep}}}{d^2}z - \frac{V_{\text{bias}} \mp V_{\text{dep}}}{d} \tag{2.58}$$

with sensor thickness (d) and full-depletion voltage ($V_{\text{dep}}$). With the relation between electric field and drift velocity ($v = \mu E$, (2.20)) at low electrical field strengths ($\mu \neq \mu(E)$) and after separation of variables and integration, one finds the drift time for a charge cloud at position $z$ within the sensor [Bel+83, p. 257]:

$$t(z)_{\substack{\text{n-bulk}\\\text{p-bulk}}} = \pm\frac{d^2}{2\,\mu\,V_{\text{dep}}}\ln\left(1 \pm \frac{2}{d}\frac{V_{\text{dep}}}{V_{\text{bias}} \mp V_{\text{dep}}}z\right) \tag{2.59}$$

The charge-cloud width in a planar sensor as a function of the initial charge-cloud position $z$ is consequently:

$$\sigma(z)_{\substack{\text{n-bulk}\\\text{p-bulk}}} = \sqrt{2\,D\,t(z)} \underset{\substack{(2.59)\\(2.52)}}{=} d\sqrt{\frac{k_B\,T}{e\,V_{\text{dep}}}}\sqrt{\pm\ln\left(1 \pm \frac{2}{d}\frac{V_{\text{dep}}}{V_{\text{bias}} \mp V_{\text{dep}}}z\right)} \tag{2.60}$$

When using high bias voltages ($V_{\text{bias}} \gg V_{\text{dep}}$), one can approximate the formulas with a first order Taylor series expansion:

$$t(z) = \frac{d}{\mu\,V_{\text{bias}}}\,z \qquad \wedge \qquad \sigma(z) = \sqrt{\frac{2\,k_B\,T\,d}{e\,V_{\text{bias}}}}\,z \tag{2.61}$$

These approximations are often sufficient, but fail when the bias voltage approaches the full-depletion voltage, as it is often present for low-resistive sensor materials and after radiation damage. This is exemplary depicted in Figure 2.18 by comparison to data. An application of the precise charge-sharing model can be found in Chapter 3, where measurements with pixel detectors are simulated.

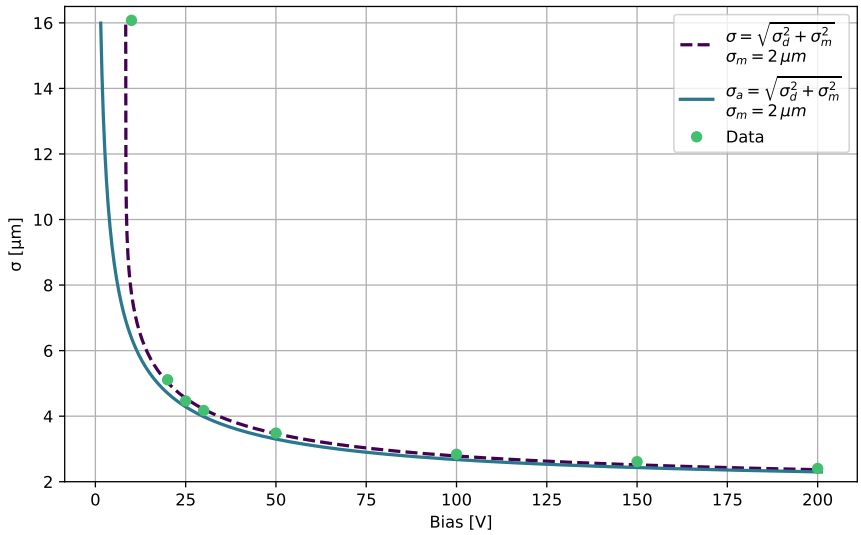


Figure 2.18: Charge-cloud width due to diffusion for different bias voltages. Full line shows Equation (2.61) and dotted line Equation (2.60). An additional contribution $\sigma_{\mathrm{m}}$ to the determined charge-cloud width is added, due to the finite laser spot size used in this measurement. Data from [Hir17].

## 2.2 Radiation damage

Particles do not only create the charge signal, as depicted in the preceding chapter, but can also irreversibly change the characteristics of the silicon. These changes usually lead to a degradation of detector properties and eventually render the detector non-functional. The silicon tracking detectors in the ATLAS experiment are closest to the interaction point and accumulate the largest particle flux of all sub-detectors. With each upgrade of the particle accelerator towards higher luminosities, this flux increases and thus the requirement to resist radiation, also called *radiation hardness*.

Radiation damage to silicon is classified into two categories:

1. Bulk damage from non-ionizing-energy-loss (NIEL) that mainly affects the sensor properties.

2. Surface and interface damage that scales with the total-ionizing dose (TID) and mainly affects readout electronics and sensor channel isolation.

The required radiation hardness for the ATLAS pixel detector increases from a NIEL of $1 \times 10^{15}\,\mathrm{n_{eq}\,cm^{-2}}$ and a TID of 500 kGy for the first version of the detector in operation since 2009 to about $15 \times 10^{15}\,\mathrm{n_{eq}\,cm^{-2}}$ and 7700 kGy in the future [ATL08, p. 4][col14, p. 8]. Great efforts have been put by many research groups to understand radiation damage in silicon and its repercussions for detector properties and -operation. A recent review of radiation damage at LHC conditions can be found for example in [Mol18].
The following sections summarize the changes to silicon from non-ionizing-energy-loss on microscopic level allowing a qualitative understanding of the changes of detector properties with irradiation. For the quantitative description, that is needed for detector operation, effective, simplified, and semi-empiric models are available, like the *NIEL scaling* and the *Hamburg model*. These models are introduced at the appropriate location.

### Bulk damage

Bulk damage is caused by displacement of silicon lattice atoms by high energetic electrons, hadrons, and photons. Depending on the energy of the dislocated primary-knock-on-atom (*PKA*), localized defects (*point defects*) or long-ranged defects with cascades of secondary interactions (*defect clusters*) are created [Lin03, p. 31]. The maximum energy transfer to the PKA is given by Equation (2.62) for the non-relativistic case (e.g. protons, neutrons) and Equation (2.63) for the relativistic case (e.g. electrons) [Har17, 138f]:

$$E_{\max} = 4E_{\mathrm{p}} \frac{m_{\mathrm{p}} m_{\mathrm{Si}}}{(m_{\mathrm{p}} + m_{\mathrm{Si}})^2} \qquad (2.62) \qquad\qquad E_{\max} = 2E_{\mathrm{e}} \frac{E_{\mathrm{e}} + 2m_{\mathrm{e}}c^2}{m_{\mathrm{Si}}c^2} \qquad (2.63)$$

The minimum energy transfer for the dislocation of an atom depends on the binding energy and is therefore a material property. In silicon at least 25 eV is needed for the dislocation of a PKA and at least 5 keV for the creation of defect clusters. Using Equation (2.63) this means that electrons need a kinetic energy of at least 225 keV (8 MeV) to create a point (cluster) defect, while neutrons and protons need only 185 eV (35 keV)[Har17, p. 139]. Consequently, the defect formation is energy and particle type dependent [Huh02, 204f].

With the displacement of lattice atoms vacancies and interstitials are formed. Vacancies are lattice sites which are unoccupied and interstitials are additional lattice sites in the lattice structure. The formation of di- and tri- vacancies and -interstitials is also common. These crystal defects can further react with the impurity atoms in the silicon (like oxygen, phosphorus and carbon) and form complex combinations. Common point defects are depicted in Figure 2.19. With temperature and time the defects can re-configure, break-up, recombine, and diffuse through the bulk. These processes are summarized by the term *annealing*. For detector operation, controlled annealing plays an important role in order to minimize the negative effects from radiation damage.

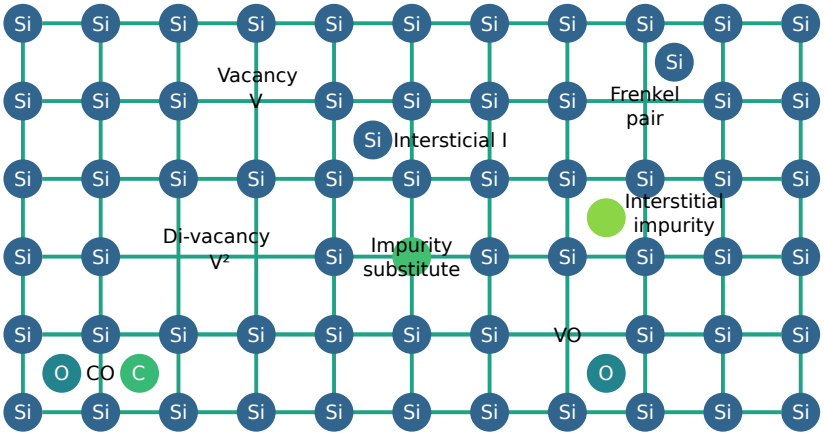


Figure 2.19: Displacements of silicon lattice atoms and arising point defects. Explanation of defects in text. Based on [Har17, p. 65].

### NIEL scaling

For practical applications, the defect formation arising from the different PKA energy distributions is neglected [Kra11, pp. 7.2-8] and radiation damage is assumed to depend only on the so-called displacement damage cross-section $D(E)$. This first-order approximation is also called NIEL-hypothesis (**N**on **I**onizing **E**nergy **L**oss) and is mainly motivated by the observation that many sensor properties scale with the NIEL fluence. This approximation has to be used with care, since an understanding at microscopic level why damage should scale with NIEL does not exist [Huh02, 204f] and prominent exceptions have been observed (e.g. [Kra+09]). Nevertheless, the NIEL scaling is essential for the assessment of the silicon sensor degradation with time during a planned experiment. It allows a reasonable prediction despite the unique particle composition, rates, and energy distributions in the experiment. Test measurements on-site with the same radiation background are usually not feasible. In the ATLAS experiment the radiation damage at the location of the pixel detector is mainly dealt by pions ($> 60$ %), followed by other charged hadrons and neutrons [Lin03, p. 33]. Since the displacement damage cross-section $D(E)$ for these particles at given energies are known, it is possible to scale the damage to a particle and energy independent quantity. The scale is commonly normalized to the damage of 1 MeV neutrons:

$$\kappa = \frac{\int D(E)\Phi(E)\,dE}{95\,\text{MeV mb} \cdot \Phi} \tag{2.64}$$

$\kappa$ is the damage factor and the denominator is the 1 MeV neutron equivalent dose (short: $\text{n}_{\text{eq}}\,\text{cm}^{-2}$). The expected NIEL value of the ATLAS experiment is calculated from simulations that describe the particle types and -energies and the expected integrated luminosity at the end of a run period [ATLb]. A practical application of the NIEL scaling can be found in Section 5.3.1, where sensors are irradiated with $3.5 \times 10^{15}$ mono-energetic 23 MeV-protons to get to a NIEL fluence of $7 \times 10^{15}\,\text{n}_{\text{eq}}\,\text{cm}^{-2}$ assuming a damage factor of $\kappa = 2$.

### Defect levels and sensor properties

Defects from radiation are uniformly distributed over the silicon bulk and add additional energy levels in the energy scheme of the semiconductor. For strong irradiation, the defect densities exceed the dopant density and drastically change the electrical characteristics of the silicon. Depending on the location of the defect levels within the band gap, one can differentiate three silicon sensor properties that are altered by radiation induced defects (Figure 2.20). A *qualitative* understanding

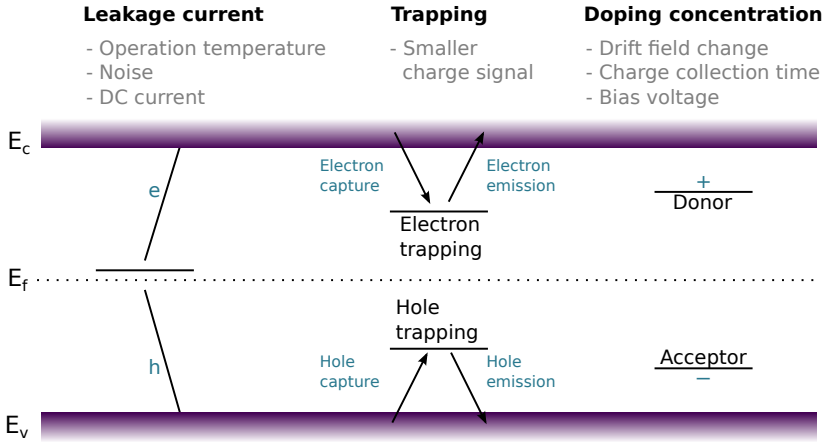


Figure 2.20: Additional energy levels due to bulk damage from radiation and its dominant repercussions on sensor properties (*dark font*). Impacts on detector operation are depicted in *grey font*. $E_\mathrm{c}$ / $E_\mathrm{v}$ denote the energy levels in the conduction / valence band. $E_\mathrm{f}$ is the Fermi level of intrinsic silicon. Based on [Har17, p. 66].

of defect properties can be reached with the assistance of the *Shockley-Read-Hall model*.

### Shockley-Read-Hall model

In low-doped silicon, as used for sensors, the generation and recombination of charge carriers via defects are dominant. The trap-assisted generation- and recombination-rates are described by the Shockley-Read-Hall model (*SRH*) [SR52]. The model assumes only defects with a single energy level that interact with charge carriers via four processes: *electron capture*, *electron emission*, *hole capture*, and *hole emission*. The system is at thermal equilibrium and consequently each capture process is balanced by its emission process. The trap occupation probability is given by the Fermi-Dirac distribution (Equation (2.25)):

$$f(E_\mathrm{t}) = \frac{1}{1 + e^{\frac{E_\mathrm{t} - E_\mathrm{f}}{k_\mathrm{B} T}}}$$

$E_\mathrm{t}$ is the trap activation energy, $E_\mathrm{f}$ the Fermi-Level, and $T$ the temperature. The equations for the four processes are:

- **Electron capture:** The probability per unit time that an electron is captured by an unoccupied localized state is called capture coefficient $c_\mathrm{n}$. It is defined by the product of the capture cross

section $\sigma_\mathrm{n}$ and the thermal velocity $v_\mathrm{th,e}$:

$$c_\mathrm{n} = v_\mathrm{th,e} \cdot \sigma_\mathrm{n}$$

The capture cross section $\sigma_\mathrm{n}$ describes the effectiveness of the defect in capturing electrons. Its value is usually determined experimentally by methods like Deep Level Transient Spectroscopy ($DLTS$) and Thermally Stimulated Current ($TSC$)[3]. For the total electron capture rate $r_\mathrm{e,c}$ follows:

$$r_\mathrm{e,c} = c_\mathrm{n} \cdot n \cdot N_\mathrm{t} \cdot (1 - f(E_\mathrm{t})) \tag{2.65}$$

$n$ is the free electron concentration, $N_t$ the defect concentration, and $1 - f(E_t)$ the probability that the trap is not already occupied. The product of defect concentration $N_t$ and vacant probability $1-f(E_t)$ can be interpreted as the effective defect concentration available for electron capture.

- **Electron emission:** The electron emission rate is defined by the probability that the trap is occupied by an electron $f(E_\mathrm{t})$, the trap concentration $N_\mathrm{t}$, and the emission probability $\epsilon_\mathrm{n}$:

$$r_\mathrm{e,e} = \epsilon_\mathrm{n} \cdot N_\mathrm{t} \cdot f(E_\mathrm{t})$$

At thermal equilibrium, the electron concentration in the conduction band does not change ($\frac{dn}{dt} = 0$) and the capture rate has to equal the emission rate: $r_\mathrm{e,c} = r_\mathrm{e,e}$. With this condition, one can determine the emission probability:

$$\epsilon_\mathrm{n} = c_\mathrm{n} \cdot n \cdot N_\mathrm{t} \cdot \frac{1 - f(E_\mathrm{t})}{f(E_\mathrm{t})} = c_\mathrm{n} \cdot n_\mathrm{i} \cdot \exp\left(\frac{E_\mathrm{t} - E_\mathrm{i}}{k_\mathrm{B} T}\right) \tag{2.66}$$

In the last step the free electron concentration $n$ is depicted by the intrinsic concentration $n_i$ and the intrinsic Fermi-Level $E_\mathrm{i}$: $n = n_\mathrm{i} \exp\left(\frac{E_\mathrm{t} - E_\mathrm{i}}{k_\mathrm{B} T}\right)$. For the electron emission rate follows:

$$r_\mathrm{e,e} = c_\mathrm{n} \cdot n_\mathrm{i} \cdot \exp\left(\frac{E_\mathrm{t} - E_\mathrm{i}}{k_\mathrm{B} T}\right) \cdot N_\mathrm{t} \cdot f(E_\mathrm{t})$$

- **Hole capture:** The hole capture rate can be calculated in analogy to the electron capture rate, but with inverted probabilities ($f_h(E_\mathrm{t}) = 1 - f_e(E_\mathrm{t})$):

$$r_\mathrm{h,c} = c_\mathrm{p} \cdot p \cdot N_\mathrm{t} \cdot f(E_\mathrm{t})$$

and the hole capture coefficient: $c_\mathrm{p} = v_\mathrm{th,h} \cdot \sigma_\mathrm{p}$.

- **Hole emission:** Thermal equilibrium condition ($r_\mathrm{h,c} = r_\mathrm{h,e}$) yields the hole emission rate,

[3] Introduction to methods for example in [Har17, p. 64].

similar to the electron emission:

$$r_{\mathrm{h,e}} = c_{\mathrm{p}} \cdot n_{\mathrm{i}} \cdot \exp\left(\frac{E_{\mathrm{i}} - E_{\mathrm{t}}}{k_{\mathrm{B}}T}\right) \cdot N_{\mathrm{t}} \cdot (1 - f(E_{\mathrm{t}}))$$

From these four processes, the probability that a trap is occupied by an electron can be calculated:

$$\begin{aligned} 0 \quad &= r_{\mathrm{e,c}} - r_{\mathrm{e,e}} = r_{\mathrm{h,c}} - r_{\mathrm{h,e}} \\ &\Rightarrow c_{\mathrm{n}} \cdot n \cdot N_{\mathrm{t}} \cdot (1 - f(E_{\mathrm{t}})) - c_{\mathrm{n}} \cdot n_{\mathrm{i}} \cdot N_{\mathrm{t}} \cdot e^{\frac{E_{\mathrm{t}} - E_{\mathrm{i}}}{k_{\mathrm{B}}T}} \cdot f(E_{\mathrm{t}}) \\ &= c_{\mathrm{p}} \cdot p \cdot N_{\mathrm{t}} \cdot f(E_{\mathrm{t}}) - c_{\mathrm{p}} \cdot n_{\mathrm{i}} \cdot N_{\mathrm{t}} \cdot e^{\frac{E_{\mathrm{i}} - E_{\mathrm{t}}}{k_{\mathrm{B}}T}} \cdot (1 - f(E_{\mathrm{t}})) \\ \Rightarrow f(E_{\mathrm{t}}) &= \frac{c_{\mathrm{p}} \cdot n_{\mathrm{i}} \cdot e^{\frac{E_{\mathrm{i}} - E_{\mathrm{t}}}{k_{\mathrm{B}}T}} + c_{\mathrm{n}} \cdot n}{c_{\mathrm{n}}\left(n + n_{\mathrm{i}} e^{\frac{E_{\mathrm{t}} - E_{\mathrm{i}}}{k_{\mathrm{B}}T}}\right) + c_{\mathrm{p}}\left(p + n_{\mathrm{i}} e^{\frac{E_{\mathrm{i}} - E_{\mathrm{t}}}{k_{\mathrm{B}}T}}\right)} \end{aligned} \tag{2.67}$$

Equation (2.67) can be rewritten for the occupation of acceptor and donor levels using the convention to define the trap energies relative to the intrinsic Fermi-level ($E_{\mathrm{A,D}} = E_{\mathrm{t_{A,D}}} - E_{\mathrm{i}}$)[Chi+05, p. 1070]:

$$f_{\mathrm{A}} = \frac{c_{\mathrm{p}} \cdot n_{\mathrm{i}} \cdot e^{-E_{\mathrm{A}}/k_{\mathrm{B}}T} + c_{\mathrm{n}} \cdot n}{c_{\mathrm{n}}\left(n + n_{\mathrm{i}} e^{E_{\mathrm{A}}/k_{\mathrm{B}}T}\right) + c_{\mathrm{p}}\left(p + n_{\mathrm{i}} e^{-E_{\mathrm{A}}/k_{\mathrm{B}}T}\right)} \quad f_{\mathrm{D}} = \frac{c_{\mathrm{n}} \cdot n_{\mathrm{i}} \cdot e^{E_{\mathrm{D}}/k_{\mathrm{B}}T} + c_{\mathrm{p}} \cdot p}{c_{\mathrm{n}}\left(n + n_{\mathrm{i}} e^{E_{\mathrm{D}}/k_{\mathrm{B}}T}\right) + c_{\mathrm{p}}\left(p + n_{\mathrm{i}} e^{-E_{\mathrm{D}}/k_{\mathrm{B}}T}\right)} \tag{2.68}$$

The SRH model is also successfully applied to non-equilibrium conditions. A non-equilibrium condition is present in the sensor under ionizing radiation that creates an excess of free charge carriers $\Delta n = \Delta p$. The consequential recombination rate $U = -\frac{\partial \Delta n}{dt} = -\frac{\partial \Delta p}{dt}$ towards equilibrium can be calculated from charge conservation, meaning that the net rate of electron capture equals the net rate of hole capture [MCK03, p. 232]:

$$\begin{aligned} U &= R - G = r_{\mathrm{e,c}} - r_{\mathrm{e,e}} = r_{\mathrm{h,c}} - r_{\mathrm{h,e}} \\ &= \frac{c_{\mathrm{p}} c_{\mathrm{p}} N_{\mathrm{t}} \left(pn - n_{\mathrm{i}}^2\right)}{c_{\mathrm{n}}\left(n + n_{\mathrm{i}} e^{\frac{E_{\mathrm{t}} - E_{\mathrm{i}}}{k_{\mathrm{B}}T}}\right) + c_{\mathrm{p}}\left(p + n_{\mathrm{i}} e^{\frac{E_{\mathrm{i}} - E_{\mathrm{t}}}{k_{\mathrm{B}}T}}\right)} = \frac{pn - n_{\mathrm{i}}^2}{\tau_{\mathrm{p}}\left(n + n_{\mathrm{i}} e^{\frac{E_{\mathrm{t}} - E_{\mathrm{i}}}{k_{\mathrm{B}}T}}\right) + \tau_{\mathrm{n}}\left(p + n_{\mathrm{i}} e^{\frac{E_{\mathrm{i}} - E_{\mathrm{t}}}{k_{\mathrm{B}}T}}\right)} \end{aligned} \tag{2.69}$$

with the life-times $\tau_{\mathrm{p,n}} = (N_{\mathrm{t}} c_{\mathrm{p,n}})^{-1}$. $U$ is positive for a net *recombination current* and negative for a net *generation current*.

The excess carrier life-time of a *low-level injection* can be calculated assuming that the extra injected electron and hole density is much less than the densities at thermal equilibrium: $\Delta n, \Delta p \ll n_0 + p_0$. With $\Delta n = n - n_0$, $\Delta p = p - p_0$ and $\Delta n = \Delta p$, it follows from Equation (2.69) [MCK03, p. 234]:

$$\frac{\partial \Delta n}{\partial t} \approx -\frac{(n_0 + p_0)\,\Delta n}{\tau_{\mathrm{p}}\left(n_0 + n_{\mathrm{i}} e^{\frac{E_{\mathrm{t}} - E_{\mathrm{i}}}{k_{\mathrm{B}}T}}\right) + \tau_{\mathrm{n}}\left(p_0 + n_{\mathrm{i}} e^{\frac{E_{\mathrm{i}} - E_{\mathrm{t}}}{k_{\mathrm{B}}T}}\right)} \propto -\Delta n \tag{2.70}$$

Thus, the decay of excess charge carriers follows an exponential law:

$$\Delta n(t) = \Delta n(0)\, e^{-\frac{t}{\tau}} \tag{2.71}$$

In the following the three main sensor parameters: *leakage current*, *trapping probability*, and *space charge* that are altered by irradiation induced defects are introduced. A comprehensive discussion of deep level defects in irradiated silicon, using the SRH model, can be found in [Lut96].

- **Leakage current:** Free electron-hole pairs from thermal generation current are separated by the electric field and give rise to the bulk leakage current. Bulk leakage current constitutes the main contribution to the sensor leakage current after irradiation. Assuming no recombination ($U = -G$) and a negligible free charge-carrier concentration in the depletion region ($n, p \approx 0$) one can estimate the generation current from a single defect using Equation (2.69):

$$G \approx \frac{n_\mathrm{i}^2}{\tau_\mathrm{p} n_\mathrm{i} e^{\frac{E_\mathrm{t}-E_\mathrm{i}}{k_\mathrm{B}T}} + \tau_\mathrm{n} n_\mathrm{i} e^{\frac{E_\mathrm{i}-E_\mathrm{t}}{k_\mathrm{B}T}}} \approx N_\mathrm{t} \frac{c\, n_\mathrm{i}}{2 \cosh\left(\frac{E_\mathrm{t}-E_\mathrm{i}}{k_\mathrm{B}T}\right)} \tag{2.72}$$

  In the last step equal hole and electron capture cross sections and thermal velocities are assumed ($c_\mathrm{n} = c_\mathrm{p} = c$) to better illustrate the interdependence of generation current and trap energy $E_\mathrm{t}$. Figure 2.21 depicts the current as a function of the energy level relative to the intrinsic Fermi energy $E_\mathrm{i}$. One can see that leakage current is mainly generated by traps that are located at the center of the band gap ($E_\mathrm{t} - E_\mathrm{i} \approx 0$). With irradiation, the trap density $N_\mathrm{t}$ increases and thereby the bulk leakage current. Irradiated sensors are therefore cooled to mitigate the current increase that in turn increases Shot noise and power consumption ($P = I_\mathrm{leak}\, V_\mathrm{bias}$). The temperature scaling of the leakage current can be calculated from Equation (2.72) using the temperature dependence of the intrinsic carrier concentration for a gap energy $E_\mathrm{g}$ (Equation (2.26), [Chi13, p. 2]):

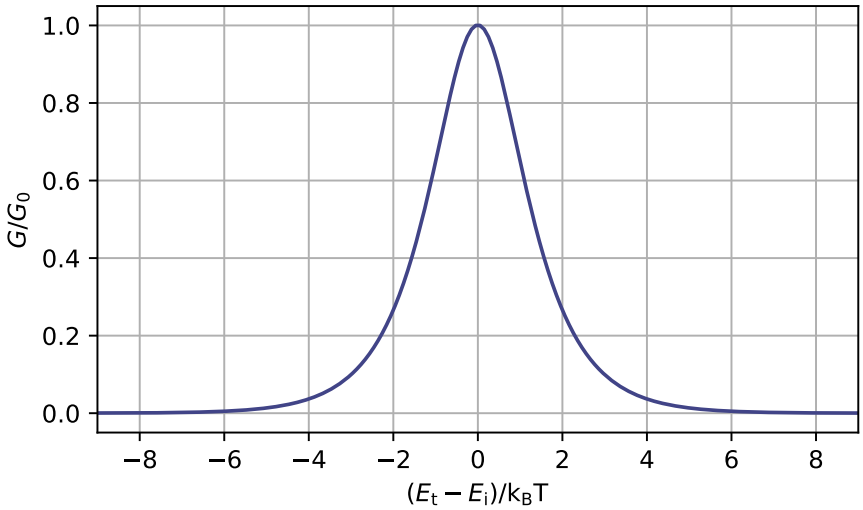


Figure 2.21: Generation current in the depletion region from a single trap with trap energy $E_\mathrm{t}$. Normalized to the maximum generation current $G_0$ at $E_\mathrm{t} = E_\mathrm{i}$.

$$n_\mathrm{i} \propto T^{\frac{3}{2}} e^{-\frac{E_\mathrm{g}}{2\,k_\mathrm{B}T}} \tag{2.73}$$

and the temperature dependence of the thermal velocity $v_{\mathrm{th}} \propto \sqrt{T}$. When the slight temperature dependence of the effective mass of the free charge carriers is neglected and the dependency of the generation current on defect energy is approximated by:

$$e^{\frac{\Delta E}{k_{\mathrm{B}} T}} + e^{-\frac{\Delta E}{k_{\mathrm{B}} T}} \underset{\Delta E / k_{\mathrm{B}} T > 1.5}{\approx} e^{\frac{\Delta E}{k_{\mathrm{B}} T}} \tag{2.74}$$

follows the commonly used formula for (bulk) leakage current scaling with temperature:

$$G(T) \propto T^2 e^{-\frac{E_{\mathrm{g}} + 2(E_{\mathrm{t}} - E_{\mathrm{i}})}{2 k_{\mathrm{B}} T}} = T^2 e^{-\frac{E_{\mathrm{eff}}}{2 k_{\mathrm{B}} T}} \tag{2.75}$$

The measured value of $E_{\mathrm{eff}}$ in irradiated silicon is $(1.214 \pm 0.014)\,\mathrm{eV}$ [Chi13, p. 21] which translates to a change of the leakage current of about 10 % per 1 °C in the temperature range of −20 °C to 20 °C. Increased leakage current is the first negative impact from irradiation for detector operation, since it prevents detector usage at room temperature. Active cooling is required to prevent *thermal runaway*, a situation in which leakage current increase is heating up the sensor, which in turn increases the leakage current. This self amplifying process eventually prohibits sensor operation.

The total bulk leakage current can be calculated from Equation (2.72) by adding the generation current density of all traps [Mol18, p. 1564]:

$$I_{\mathrm{leak}} = edA \sum_{i}^{\mathrm{defects}} G_{\mathrm{i}} \tag{2.76}$$

with elementary charge $e$ and the active sensor volume $d \cdot A$ (depletion width times area). In the first pixel layer of the future ATLAS pixel detector, the leakage current is a major challenge for planar sensors. With the nominal thickness $d = 150\,\mu\mathrm{m}$, the power budged cannot be satisfied. Therefore, a thinning to $d = 100\,\mu\mathrm{m}$ is considered [Col17, p. 103]; or the usage of 3D sensors that can be operated at much lower bias voltages.

Many measurements have revealed a linear scaling of the increase in bulk leakage current with the non-ionizing-energy-loss $\Phi_{\mathrm{eq}}$, which is independent of the bulk material (growth technique, doping concentration, impurity atoms) [Mol99, p. 105]:

$$\Delta I_{\mathrm{leak}} = ewA\,\alpha\,\Phi_{\mathrm{eq}} \tag{2.77}$$

The current related *damage factor* $\alpha$ decreases with time due to annealing. From fits to data, the following first order parametrization has been found to describe the annealing behavior at a given temperature $T$:

$$\alpha = \alpha_0(T) + \alpha_1 e^{-\frac{t}{\tau_I(T)}} - \alpha_2 \ln \frac{t}{t_0} \tag{2.78}$$

$\alpha_0$ is a temperature dependent offset and $\alpha_1$ scales the exponential reduction of leakage current that is likely related to defect dissociation. The last logarithmic term describes long term

annealing and is not based on a physical model[4]. With the common annealing procedure (80 min at 60 °C) the damage factor reduces by about 40 % to $(3.99 \pm 0.03) \times 10^{-17}\,\mathrm{A\,cm^{-1}}$. Leakage current annealing is also present in the ATLAS pixel detector during maintenance periods [Gor15, p. 5].

- **Trapping probability:** Due to trapping, the excess charge-carrier concentration from ionizing radiation reduces with time. It is assumed that the decay of the initial charge carriers $Q_0$ can be described by an exponential law as derived in Equation (2.71):

$$Q_{\mathrm{e/h}}(t) = Q_0\, e^{-\frac{t}{\tau_{\mathrm{e/h}}}} \tag{2.79}$$

The mean trapping probability $\frac{1}{\tau}$ of excess electrons and holes can be calculated from the SRH Equation (2.65) and Equation (2.66) assuming $\tau^{-1} = \frac{n}{r}$ [Kra11]:

$$\frac{1}{\tau_{\mathrm{e}}} = v_{\mathrm{th,e}} \cdot \sigma_{\mathrm{n}} \cdot N_{\mathrm{t}} \cdot (1 - f(E_{\mathrm{t}})) \qquad \frac{1}{\tau_{\mathrm{h}}} = v_{\mathrm{th,h}} \cdot \sigma_{\mathrm{p}} \cdot N_{\mathrm{t}} \cdot f(E_{\mathrm{t}}) \tag{2.80}$$

This equation is presumed to be valid also in the presence of an external electric field since the additional drift velocity $v_{\mathrm{d}}$ is negligible with respect to the thermal velocity $v_{\mathrm{th}}$. The trapping probability in the depletion region is consequently independent of the electric field or bias conditions[5]. From Equation (2.80) it is evident that electron and hole-trapping is more likely for trap levels in the upper ($f(E_{\mathrm{t}}) \approx 0$), respectively lower part ($f(E_{\mathrm{t}}) \approx 1$) of the band gap. For a change of the *measured* charge signal, not only the trapping probability has to be considered, but also the de-trapping time. To reduce the measured charge signal the de-trapping time has to be longer than the integration time of the readout electronics. Since multiple traps exist in irradiated silicon, an *effective trapping probability* is defined as follows:

$$\frac{1}{\tau_{\mathrm{eff,e}}} = v_{\mathrm{th,e}} \sum_{i}^{\mathrm{defects}} \sigma_{\mathrm{n,i}} \cdot N_{\mathrm{t,i}} \cdot (1 - f(E_{\mathrm{t,i}})) \qquad \frac{1}{\tau_{\mathrm{eff,h}}} = v_{\mathrm{th,h}} \sum_{i}^{\mathrm{defects}} \sigma_{\mathrm{p,i}} \cdot N_{\mathrm{t,i}} \cdot f(E_{\mathrm{t,i}}) \tag{2.81}$$

where $i$ runs over all traps with an emission time above the integration time of the readout electronics. Effective de-trapping times in irradiated silicon are in the order of microseconds whereas trapping times are in the order of nanoseconds [Kra+12]. The effective trapping probability has been found to scale linearly with the NIEL fluence $\Phi_{\mathrm{eq}}$[6]:

$$\frac{1}{\tau_{\mathrm{eff,e/h}}} = \beta_{\mathrm{e/h}} \Phi_{\mathrm{eq}} \tag{2.82}$$

The scaling factor $\beta_{\mathrm{e/h}}$ is independent of the silicon material, but shows a temperature dependence due to the temperature dependent parameters in Equation (2.81). From Equation (2.81)

[4] More information on the leakage current annealing parametrization and related defects can be found in [Mol+02].
[5] Exceptions from this assumption are reported in [Bea+99, p. 508], [Lan09, p. 73], and [Poh10, p. 40].
[6] An increase of the scaling factor by about 30 % for charged hadrons in comparison to neutrons is reported in [Kra+02a, p. 297].

a parametrization of the scaling factor with temperature can be derived [J W07, p. 2702]:

$$\beta_{\mathrm{e/h}}(T) = \beta_{\mathrm{e/h}}(T_0) \left( \frac{T}{T_0} \right)^{\kappa_{\mathrm{e/h}}} \tag{2.83}$$

$\kappa_{\mathrm{e/h}}$ is estimated from fits to data to be about -0.85 for electrons and -1.50 for holes. The scaling factor also changes with time due to annealing. But with the common annealing procedure to ensure beneficial annealing (80 min at 60 °C), the electron and hole trapping probabilities decrease, respectively increase by a few percent only [Kra+03, p. 441][Kra+02a, p. 303]. Figure 2.22 summarizes determined trapping probabilities after annealing using the transient-

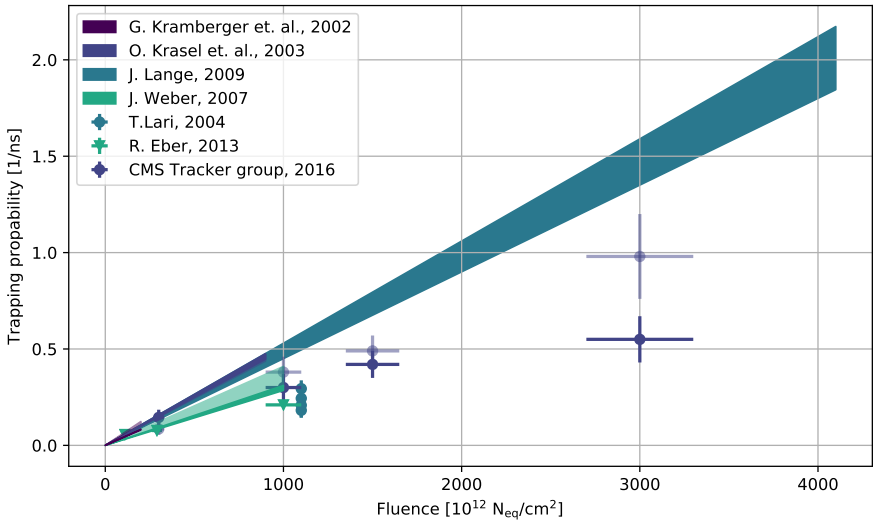


Figure 2.22: Trapping probabilities after irradiation and annealing from selected publications. Values determined separately for electrons and holes are distinguished using *dark* and *bright* colors. Areas are trapping probabilities measured with transient-current-technique published in [Kra+02a], [Kra+03], [Lan09], and [J W07]. The width of the area gives the $\pm\sigma$ confidence interval. Points are trapping probabilities from charge-collection efficiency measurements published in [Lar04], [Ebe13], and [Ada+16].

current-technique (*areas*) and charge-collection efficiency measurements (*points*). The trapping probabilities show a considerable spread. Most report a significant difference between electron and hole trapping probability (e.g. [Kra+02b, p. 649]), but exceptions exist where such a clean distinction is not found ([Kra+03, p. 3059]) or even the opposite is reported ([KLF93, p. 355]). A reason for the large deviations are simplified assumptions about the electrical field profile which have to be made to extract charge-carrier trapping. Especially, for irradiations above $1 \times 10^{15}\,\mathrm{n_{eq}\,cm^{-2}}$ the description of the field becomes difficult and published values are scarce. In Chapter 5 a study of charge-carrier trapping in 3D and planar pixel sensors is presented at fluencies in excess of $1 \times 10^{15}\,\mathrm{n_{eq}\,cm^{-2}}$.

- **Effective space charge:** The effective space charge density $\rho_{\text{eff}}$ determines the electrical field $\vec{E}$ in the sensor (Equation (2.31)):

$$\nabla \cdot \vec{E} = \frac{\rho_{\text{eff}}}{\epsilon_s} \tag{2.84}$$

with the permittivity of silicon $\epsilon_s$. The effective space charge $\rho_{\text{eff}}$ can be calculated as the sum of three contributions:

$$\rho_{\text{eff}} = \rho_{\text{dopants}} + \rho_{\text{defects}} + \rho(x)_{\text{free charge carriers}} \tag{2.85}$$

$\rho_{\text{dopants}}$ describes the fully ionized shallow defects from the initial doping and defines the material resistivity before irradiation. $\rho_{\text{defects}}$ is the space charge attributed to ionized defects in the silicon. It can be defined as:

$$\rho_{\text{defects}} = e \sum_{i}^{\text{defects}} (N_{\text{D,i}} f_{\text{D,i}} - N_{\text{A,i}} f_{\text{A,i}}) \tag{2.86}$$

with the elementary charge ($e$) and the donor and acceptor trapping state densities $N_{\text{D}}$, $N_{\text{A}}$. The trap occupation probabilities $f_{\text{D}}$, $f_{\text{A}}$ are given by Equation (2.68) and are largest for shallow donor and acceptor levels close to the conduction and the valence band, respectively. Consequently, mainly shallow defects from irradiation contribute to the change of space charge. Since the defect concentration is uniformly distributed in the silicon bulk, similar to the dopant concentration, one often uses the term *effective doping concentration* $N_{\text{eff}}$ synonymous with *effective space charge*. When neglecting the position dependent contribution in Equation (2.85), one can describe the full-depletion voltage by the effective doping concentration $\rho_{\text{eff}}$ and the thickness of the sensor $d$ (Equation (2.36)):

$$V_{\text{FD}} = e \frac{\rho_{\text{eff}}}{\epsilon_s} d^2 \tag{2.87}$$

The full-depletion voltage is a commonly used quantity to describe changes of the effective doping concentration with irradiation, as it directly relates to the necessary bias voltage during operation. The bias voltage has to be increased along with an increase of the doping concentration to minimize (or even prevent) an undepleted sensor region that does not contribute to charge collection[7]. However, many measurements with highly irradiated sensors suggest that the model of a localized and homogeneous space charge leading to a linear electric field is too simplistic. The effective space charge seems also affected by the free charge-carrier concentration from generation current that increases drastically with irradiation [EVL02]. Although the generation current density is constant over the bulk (Figure 2.23 a), the free charge-carrier densities are not (Figure 2.23 b). When the magnitude of free charge-carriers effects the occupation probability of the trapping centers, the trapping probability becomes position dependent and consequently the free electrons, respectively holes densities (Figure 2.23 c). The resulting effective doping concentration leads to a parabola shaped electrical field profile that one expects from a linearly graded p-n junction [SM 06, p. 92] with maxima at the sensor front- and back-

[7] The evolution of the full-depletion voltage of the ATLAS pixel detector is e.g. presented in [Ben+17].

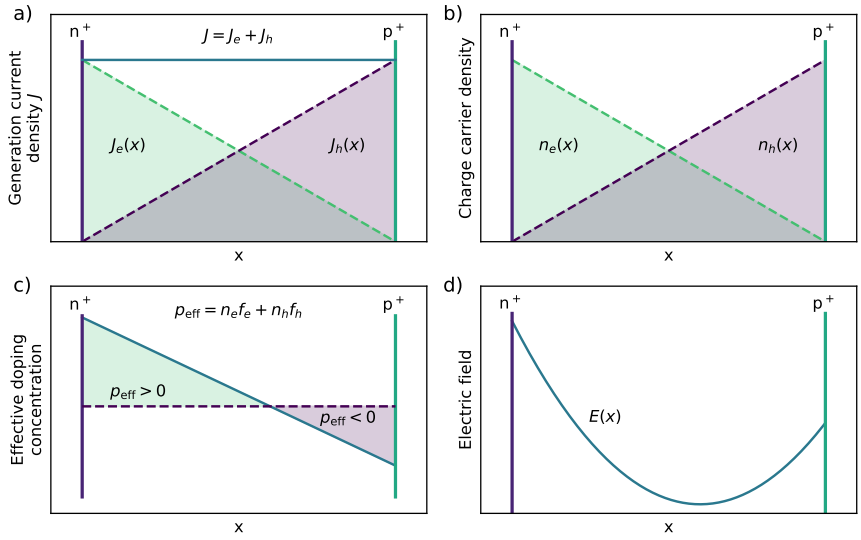


Figure 2.23: Model to explain the non-linear electrical field profile in the space charge region after heavy irradiation known as *double peak* or *double junction* effect. *a:* Uniform thermal generation current with non-uniform electron-, hole-current contribution. *b:* Free charge-carrier densities from generation current in the space charge region. *c:* Model: the occupation probability of irradiation induced trapping centers depends on the free charge carrier concentration. This makes trapping varyingly effective as a function of the position in the bulk, creating localized excess densities for electrons and holes. *d:* The electrical field shows a parabola shape with two peaks due to the variation of the effective space charge. Based on [EVL02, p. 558].

side (Figure 2.23 d). Therefore, this effect is often called *double peak* or *double junction* effect.

The evolution of effective space charge with radiation depends strongly on the bulk material and radiation type; a clear violation of the NIEL scaling hypothesis. N-type material *usually* shows a decrease of the effective doping concentration due to the compensation of the initial positive space charge from shallow dopants by defects introducing a negative space charge. This leads to space charge sign inversion (*SCSI*) at an irradiation corresponding to a few $1 \times 10^{13}\,\mathrm{n_{eq}\,cm^{-2}}$. During detector operation, the SCSI is observed as the point with the lowest bias voltage needed for full-depletion. The shares of uniform and non-uniform space charge in Equation (2.85) is also dependent on the radiation and determines how well the electric field can be approximated by a linear function. In [Ada+16, p. 5] very different field profiles are reported for irradiation of the same bulk material to a NIEL fluence of about $1 \times 10^{15}\,\mathrm{n_{eq}\,cm^{-2}}$ with 23 GeV protons and 23 MeV protons. Only the description of the results with 23 GeV protons needs a double-peaked electrical-field profile opposed to the irradiation with lower energetic 23 MeV protons, that are also used in this study. The electric field of the 23 MeV proton irradiation is well described by a uniform space charge distribution assuming a sufficient bias voltage. The linear electric field approximation is often still sufficient, since for high bias voltages the double peaked

profile often approximates the linear profile and a small peak at the backside of the sensor does not drastically change charge collection due to the low weighting potential at the backside of segmented sensors (Figure 2.13).

Another material- and radiation-dependent effect is acceptor and donor removal. It is caused by the deactivation of the shallow defects by radiation which nullifies the initial acceptors and donors contribution ($\rho_{\text{dopants}}$) to the space charge [Mol18, p. 7].

In order to describe the complex evolution of the effective doping concentration with irradiation and annealing an effective model has been developed. This model assumes a uniform effective doping concentration $\rho_{\text{eff}}$ and is often referred to as the *Hamburg model*. In this model the change of the effective doping concentration $\Delta\rho_{\text{eff}} = \rho_{\text{dopants}} - \rho_{\text{eff}}(t)$ is parametrized as:

$$\Delta\rho_{\text{eff}} = \rho_A(t) + \rho_C + \rho_Y(t) \tag{2.88}$$

$\rho_C$ defines the *stable damage* component that does not vary with time due to annealing. $\rho_A(t)$ depicts the *short term* annealing that is also called *beneficial annealing* since it decreases the doping concentration. $\rho_Y(t)$ is the *reverse annealing* component that increases with time. Reverse annealing is the reason why annealing time of sensors has to be limited, opposed to the changes in leakage current and charge-carrier trapping where annealing is only beneficial. In qualification tests, the common procedure is to anneal the sensor at 60 °C for 80 min to balance the beneficial and reverse annealing components. The parametrization of the three constitutions in Equation (2.88) is:

$$\begin{aligned} \rho_A(t) &= g_a \Phi_{\text{eq}} e^{-\frac{t}{\tau_a(T)}} \\ \rho_C &= \rho_{C,0}\left(1 - e^{-c\Phi_{\text{eq}}}\right) + g_c \Phi_{\text{eq}} \\ \rho_Y(t) &= g_y \Phi_{\text{eq}} \left(1 - e^{-\frac{t}{\tau_y(T)}}\right) \end{aligned} \tag{2.89}$$

The introduction rates $g_a$, $g_c$, and $g_y$ are usually extracted from fits to measurements of the full-depletion voltage with irradiation. A continuative discussion of the parameters can be found in [Mol18] and the references therein.

#### The role of measurements

Despite great efforts, the bulk damage mechanisms in silicon sensors are not fully understood and are currently investigated in the research collaboration RD50 [RD5]. Especially the connection between microscopic defects and macroscopic sensor properties is mostly understood at a qualitative level. Effective and simplified models have been developed to help understand and predict sensor properties with radiation like NIEL scaling, the Hamburg model, and TCAD models with effective trap levels. However, to gain descriptive and predictive power, these models usually have to be adjusted to the specific detector [Har17, p. 136]. This makes measurements of detector properties with radiation still a crucial part of the qualification procedure; especially when considering that with each tracking detector upgrade at the LHC usually a new world record of radiation hardness is required.

## 2.3 The ATLAS pixel detector

The initial ATLAS pixel detector was installed in 2007 and consists of three barrel layers and three forward and backward discs made of hybrid pixel detectors (Figure 2.24). Hybrid pixel detectors

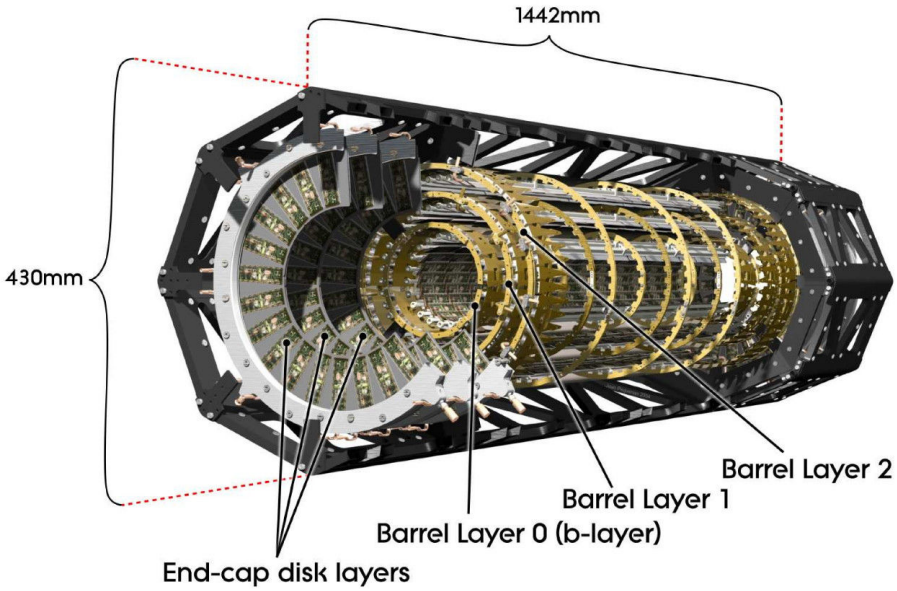


Figure 2.24: Layout of the ATLAS detector pixel detector. Computer generated image. From [ATL08, p. 5].

are a class of pixel detectors where sensor and readout electronics are produced separately and then electrically connected at pixel level. The benefit of such an approach is that both parts can be optimized independently according to requirements. Readout chips utilize radiation-hard CMOS processes with relatively small feature sizes, that enable the implementation of fast signal-amplification chains and complex digital logic for rapid data processing. Silicon sensors in high-energy physics, on the other side, are usually not produced in a CMOS process. High resistive silicon bulks are preferred with designs that sustain high bias voltages to allow for efficient charge collection after high levels of irradiation. The novelty of using a CMOS process also for the passive sensor of a hybrid pixel detector is discussed in Chapter 6. The disadvantage of the hybrid concept is the challenging and costly connection between sensor and readout. Additionally, limitations on the minimum thickness for both parts and for the minimum pixel pitch exist. In the ATLAS pixel detector an ohmic connection between each sensor pixel and readout pixel is realized by fine-pitch bump bonding. The components of such a hybrid pixel detector are depicted in Figure 2.25. A comprehensive overview about the original ATLAS pixel detector can be found in [ATL08].

### 2.3.1 The Insertable B-Layer: IBL

The upgrade of the ATLAS detector with an additional barrel layer of hybrid pixel detectors constitutes the first improvement of the tracking system for operation at the high luminosity LHC.

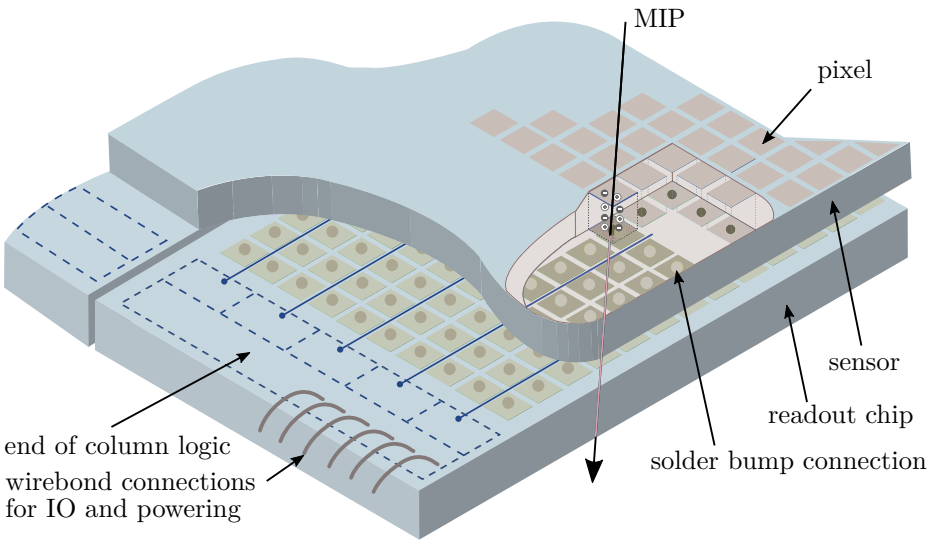


Figure 2.25: A hybrid pixel detector with square pixel that is hit by a minimum-ionizing particle (MIP). Based on [ise19].

This new layer is called Insertable B-Layer (IBL) and was installed 2014 in the center of the tracking detector between the existing pixel detector and a new beam pipe of smaller diameter. An additional layer with a reduced distance to the interaction point increases the precision of the impact parameter [KW16, p. 410], reduces the fake track probability induced by high pile-up events and therefore enhances vertex reconstruction and B-tagging performance [Tak16, 3f]. It also counteracts potential losses in the former innermost layer that is operated above its qualified radiation level. Figure 2.26 shows the layout of the IBL. It consists of 14 axial staves that are

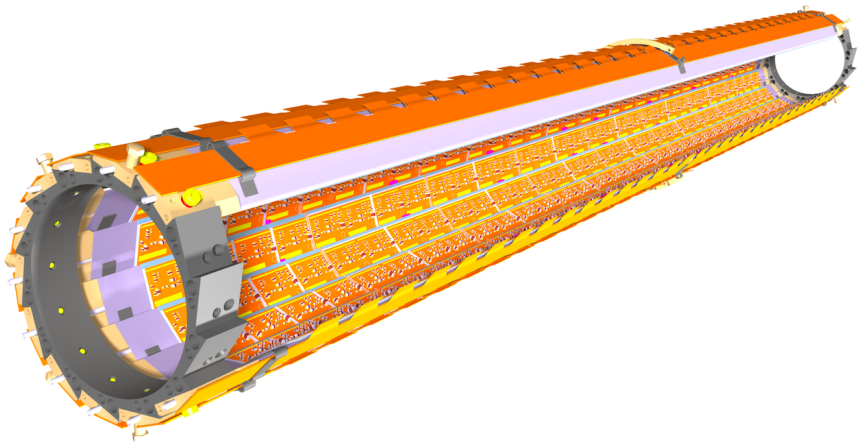

Figure 2.26: Layout of the ATLAS IBL. The detector modules are mounted on light-weight carbon fiber support-structures housing CO2 evaporative cooling tubes. ot all 14 staves are depicted. From [ATL08, p. 5].

tilted by 14° in $r - \phi$ with 20 % stave-to-stave overlap. In contrast to the initial pixel layers, no overlap in $z$-direction exists due to space constraints. Each stave contains 20 modules, 8 single chip modules on either ends with 3D sensors and 12 double-chip modules with planar sensors covering the central region. A single (or double) chip module is a functional unit consisting of a sensor, one (respectively two) readout chip(s), and one module flex directly glued to the detector. The flex provides the passive electronic components for signal termination and power filtering. Figure 2.27 shows the modules of the IBL project. Four single-chip or two double-chip modules

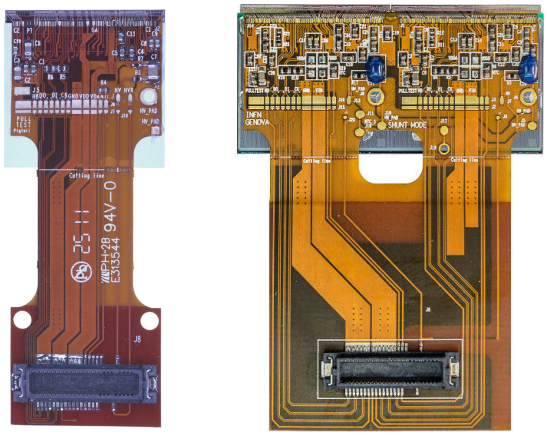

Figure 2.27: Modules of the ATLAS IBL. Single chip modules with 3D sensor (*left*) and double chip module with one double sized planar sensor connected to two readout chips (*right*).

form one power group sharing the same high voltage and low voltage power lines. During stave production the modules were connected with wire bonds to a multi-layer stave flex located at the stave back side, containing power, data acquisition, and configuration lines. With its reduced distance of only 3.3 cm to the interaction point, the IBL requires an improved radiation tolerance and a finer granularity. Therefore, the pixel size of the hybrid pixel detector in the IBL is reduced to 50 µm x 250 µm from 50 µm x 400 µm in the original pixel detector layers. With an integrated luminosity of 550 $\mathrm{fb}^{-1}$ that will be collected during IBL operation, the new layer has to sustain a fluence of 250 Mrad ionizing and $5 \times 10^{15}\,\mathrm{n_{eq}\,cm^{-2}}$ non-ionizing dose (including safety factors). The demanding requirements considering radiation hardness, material budged and space constrains required the development of a new hybrid pixel detector. This detector consist of a new readout chip and novel pixel sensors.

### The ATLAS FE-I4

The ATLAS Front-End I4 (short: FE-I4) is a pixel readout-chip designed in a radiation hard 130 nm CMOS process offered by IBM. It is optimized for high particle rates by fast signal shaping, digital time-walk correction, localized in-pixel buffers, and time multiplexed data output. With a dimension of 20.2 mm × 18.8 mm it is currently the largest chip used in a high-energy physics experiment. The active area constitutes a large fraction (89%) of the overall size. It contains a matrix of 26880 pixels arranged in an 80 × 336 array. Each Front-End pixel measures 50 µm × 250 µm and has an

ohmic connection to one sensor pixel. The Front-End pixels are divided into an analog and a digital section. A simplified schematic of the analog section is depicted in Figure 2.28. It comprises a

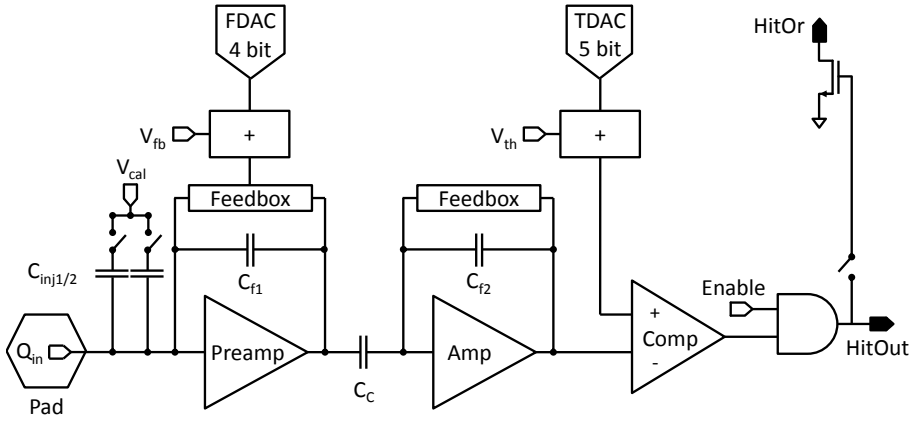


Figure 2.28: Analog pixel cell of the ATLAS FE-I4 consisting of two AC coupled charge sensitive amplifiers (*Preamp, Amp*), a comparator (*Comp*), a charge injection circuit ($V_{\text{cal}}$), shaping time and threshold tuning circuits ($V_{\text{fb}}$, *FDAC*; $V_{\text{th}}$, *TDAC*), an enable switch (*Enable*), and the HitBus signal (*HitOr*). The *HitOut* signal is further processed in the digital pixel cell that is not shown. Based on [Poh+15, p. 50].

two-staged AC-coupled charge sensitive amplifier (CSA) with adjustable shaping time for the first stage and an adjustable threshold for the discriminator that follows the second stage. Feedback and threshold DACs (*FDAC/TDAC*) present in each pixel allow fine tuning of the individual shaping times and detection thresholds. Per-pixel tuning is important to equalize the in-time efficiency during operation. In Section 5.3.2 the tuning procedure is depicted. Charge determination and time stamping is implemented in the ATLAS FE-I4 using the time-over-threshold technique (ToT) with less than 4-bit resolution. The leading edge and the time the charge signal is over the threshold are measured in counts of an externally supplied 40 MHz clock. This clock is provided by the readout system and synchronized to the bunch crossing frequency during operation at the LHC. The comparator output of each pixel (*HitOut*) can be logically ORed to form a hit bus (*HitOr*). Since the HitOr is an unclocked and asynchronous signal, it can be used for time-walk measurements and charge measurements with high resolution. An introduction to this method is given in Section 3.2.2. The readout chip also holds a charge-injection circuit for tuning and testing. It distributes a voltage step ($V_{\text{cal}}$) to selectable injection capacitors ($C_{\text{inj}_1}$, $C_{\text{inj}_2}$) present in each pixel. The charge injected by the circuitry is without calibration only coarsely known (few 10% error). A precise calibration procedure, including a discussion about the limitations of the charge-injection circuitry, is presented in Section 5.3.3. For powering, two stand-alone low-dropout voltage regulators are incorporated in the FE ([Gon13, p. 63]). They are used during IBL operation to generate the digital and analog supply voltage of 1.2 V and 1.5 V, respectively. [Poh15][Poh+15]

### The IBL pixel sensors

Main requirements for the IBL sensors are to be operational up to $5 \times 10^{15}\,\mathrm{n_{eq}\,cm^{-2}}$, a power dissipation below $200\,\mathrm{mW\,cm^{-2}}$ at $-15\,°\mathrm{C}$ working temperature, and slim inactive edges ($< 250\,\mu\mathrm{m}$). Slim inactive edges are needed to reduce the non-sensitive area between neighboring modules, since no overlap in $z$ is possible due to space constraints. Two silicon sensor technologies with different electrode configurations are used in the IBL: planar $n^+$-in-n and 3D $n^+$-in-p sensors (Table 2.2). The planar design is derived from the sensors employed in the original ATLAS pixel detector.

| Sensor technology | Planar $n^+$-in-n | 3D $n^+$-in-p |
|---|---|---|
| Bulk material | n-type, $2\,\mathrm{k\Omega\,cm} - 5\,\mathrm{k\Omega\,cm}$, float-zone | p-type, $10\,\mathrm{k\Omega\,cm} - 30\,\mathrm{k\Omega\,cm}$, float-zone |
| Electrode geometry | Segmented $n^+$-readout implantation with $p^+$ backside bias implantation | $n^+$ readout columns and $p^+$ biasing columns |
| Tile size | $18.6\,\mathrm{mm} \times 41.3\,\mathrm{mm}$ | $18.8\,\mathrm{mm} \times 20.5\,\mathrm{mm}$ |
| Thickness | $200\,\mu\mathrm{m}$ | $230\,\mu\mathrm{m}$ |
| Electrode distance | $200\,\mu\mathrm{m}$ (=thickness) | $67\,\mu\mathrm{m}$ |
| Bias voltage (begin/end-of-life) | $60\,\mathrm{V}/1000\,\mathrm{V}$ | $20\,\mathrm{V}/180\,\mathrm{V}$ |
| Manufacturer | CiS[8] | CNM[9]/FBK[10] |

Table 2.2: Properties of the two sensor technologies used in the IBL. [Poh15, p. 3][Wit13, p. 65]

$N^+$ readout implantations for electron collection are located in each pixel at the sensor surface with an inter-pixel gab of $20\,\mu\mathrm{m}$. The major advancement are slim inactive edges ($< 200\,\mu\mathrm{m}$) achieved by shifting the back-side guard rings underneath the opposing edge pixels and a reduction of the area occupied by the rings (Figure 2.29). Guard rings allow a controlled reduction of the sensor

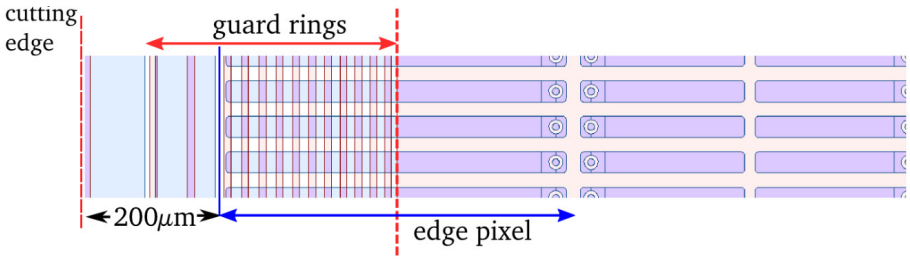


Figure 2.29: Edge design of the ATLAS IBL planar sensors. From [Col12].

bias-voltage to protect the readout chip and to prevent high electrical field strengths [Sch14, 82ff]. High electrical fields, above approximately $30\,\mathrm{V\,\mu m^{-1}}$, lead to impact ionization by free charge carriers creating secondary free charge carriers in an avalanche process. The consequential low ohmic path in the sensor can prevent sufficient sensor biasing.

[8] CiS Forschungsinstitut für Mikrosensorik und Photovoltaik GmbH, Erfurt, Germany
[9] Centro Nacional de Microelectronica (CNM), Barcelona, Spain
[10] Fondazione Brune Kessler (FBK), Trento, Italy

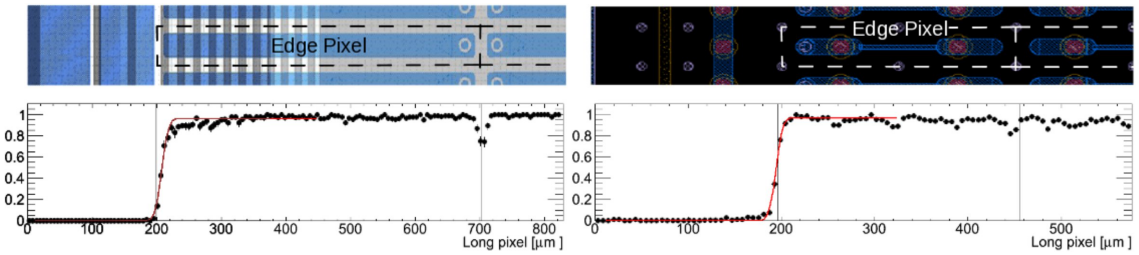


Figure 2.30: Detection efficiencies of planar (*left*) and 3D sensors (*right*). The edge efficiency is measured after an irradiation with $4 \times 10^{15}\,\mathrm{n_{eq}\,cm^{-2}}$ (*planar*) and $5 \times 10^{15}\,\mathrm{n_{eq}\,cm^{-2}}$ (*3D*). From [Col12, p. 35].

Many samples of the planar and 3D-sensor designs have been verified to sustain the required bias voltages as stated in Table 2.2. The efficiency of the slim edge layout was probed in test beams, as depicted in Figure 2.30. Both designs show high detection efficiencies already at approximately 200 µm from the sensor edge. The 3D-sensors, in contrast to the planar design, have their first application in high-energy physics. The main difference to the planar design is the geometry of the biasing- and readout electrodes. Readout electrodes are not situated on the detector surface but etched into the sensor bulk as columns of 6 µm radius by double sided Deep Reactive Ion Etching (DRIE). The distances between the electrodes can be made shorter than the sensor thickness (IBL design: 67 µm) leading to a much lower depletion voltage. The reduced drift distance of charge carriers decreases the charge collection time and therefore the charge trapping probability making the 3D concept very radiation hard [DW09]. A quantitative comparison of the charge-collection efficiency between IBL planar and 3D sensors after irradiations above $5 \times 10^{15}\,\mathrm{n_{eq}\,cm^{-2}}$, in anticipation of future pixel detector upgrades, is presented in Chapter 5. Two slightly different 3D designs from two manufacturers (CNM/FBK) are used for the IBL. In the CNM design, the columns are 210 µm long and isolated via p-stop/p-spray implantations on the $n^+/p^+$side.

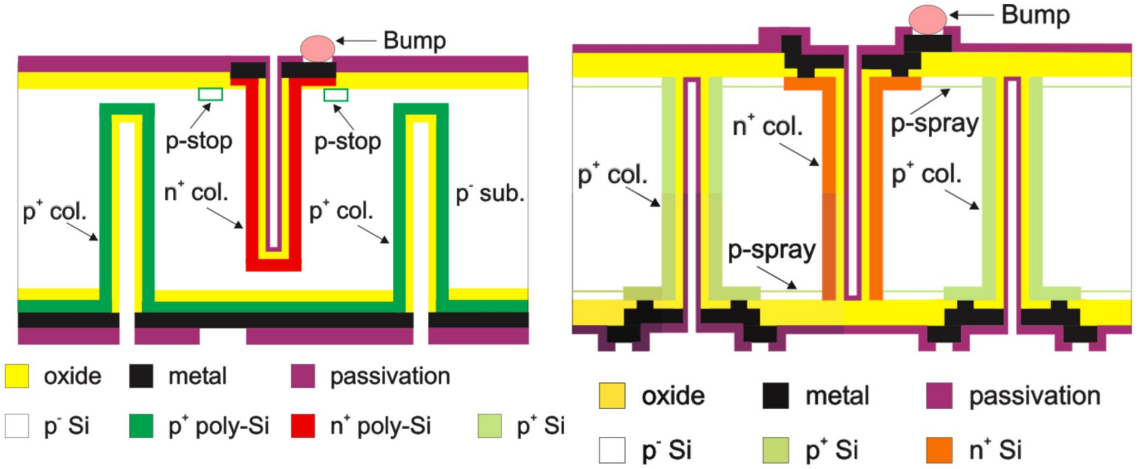


Figure 2.31: 3D sensor design from CNM (*left*) and FBK (*right*). [Col12, p. 17]

Whereas, the FBK design has electrodes that fully pass through the sensor bulk with p-spray isolation on both sides (Figure 2.31). In both designs each pixel has two n-readout electrodes and six p-type biasing electrodes shared with neighboring cells. A comprehensive overview showing the hit-detection efficiencies of highly irradiated devices can be found in [Col12].

# 3 Charge measurements with pixel detectors

Charge measurements are required for detector calibrations and the characterization of charge collection in pixel sensors. Generally, the charge deposition in the sensor from radioactive sources is preferred over a costly and complex test-beam at a particle accelerator (Chapter 4). However, to enable quantitative charge measurements, as in Chapter 5, the effect of multiple scattering and charge sharing in highly segmented sensors must be understood. This is studied in section Section 3.1 with a dedicated simulation. The influence of particle energies, setup- and analysis parameters on charge-spectra measurements with pixel detectors are explored.
In the second section of this chapter, methods for precise charge measurements with fast pixel detectors are introduced. The motivation is that, with increasing luminosity at high energy particle-physics experiments, faster readout electronics for pixel detectors are required. To cope with higher particle rates, shaping times of amplifiers are decreased and hit buffer sizes and output data rates are increased. These developments counteract charge resolution. Hit information with less charge information is preferred due to less buffer space and reduced data band width. Faster signals demand faster signal digitization, which in turn requires more power from an already tight power budged. Therefore, optimizing the charge resolution is a minor design goal. As a consequence, it is increasingly difficult to do sensor characterizations and detector calibrations with fast pixel-readout chips. Section 3.2 introduces two methods to overcome this issue. These methods are used for the measurements in chapter Chapter 5 and Chapter 6.

## 3.1 Simulation of charge measurements

Most charge measurements with MIPs presented in this study utilize a radioactive strontium source to measure charge spectra of single pixels. To understand single pixel charge-spectra from low energetic electron sources is not trivial. This often leads to omitted (e.g. [Teh+16, p. 3]) and questionable (e.g. [Per07, p. 883], [Rie+17, p. 5]) interpretations of charge spectra. Therefore, a simulation of a complete measurement setup, as used in Chapter 5, is created. Different cluster-size cuts, triggering, shielding, and beam collimation are simulated to understand the influence on the charge spectra. Additionally, the simulated results provide a reference for measurements and show that the often used assumption that a $^{90}$Sr-source give the charge spectrum of a MIP is a coarse approximation.

### 3.1.1 SourceSim: A GEANT4 based simulation

GEANT4 (**Ge**ometry **an**d **T**racking) is a C++ framework for the simulation of passage of particles through matter using Monte-Carlo methods (short: *MC*) [Ago+03] . In a Monte-Carlo simulation processes are described by sampling random numbers of the underlying probability distribution that describe these processes. The advantage is that a problem, which cannot be described analytically or consists of multiple complex and correlated processes, can be solved with a reasonable computation time. For example, for the description of energy loss the calculation of the interaction with each atom is not needed, but sampling from the energy-loss distribution (Section 2.1.1) is sufficient.

The probability distributions in GEANT4 are (semi-empirical) formulas describing physical processes. These process descriptions are only valid in a certain parameter space (energy range, particle type etc.) to maximize the accuracy - computation-time traded-off and are summarized in a comprehensive physics reference manual [Gea16a]. The careful selection of these processes (e.g. Bremsstrahlung, radioactive decay, ...) and process parameters (e.g. energy cut-off to avoid infrared divergence) is mandatory to describe real world experiments. Hence, the presented simulation *SourceSim* has been comprehensively qualified in Section 3.1.1 with real world data.

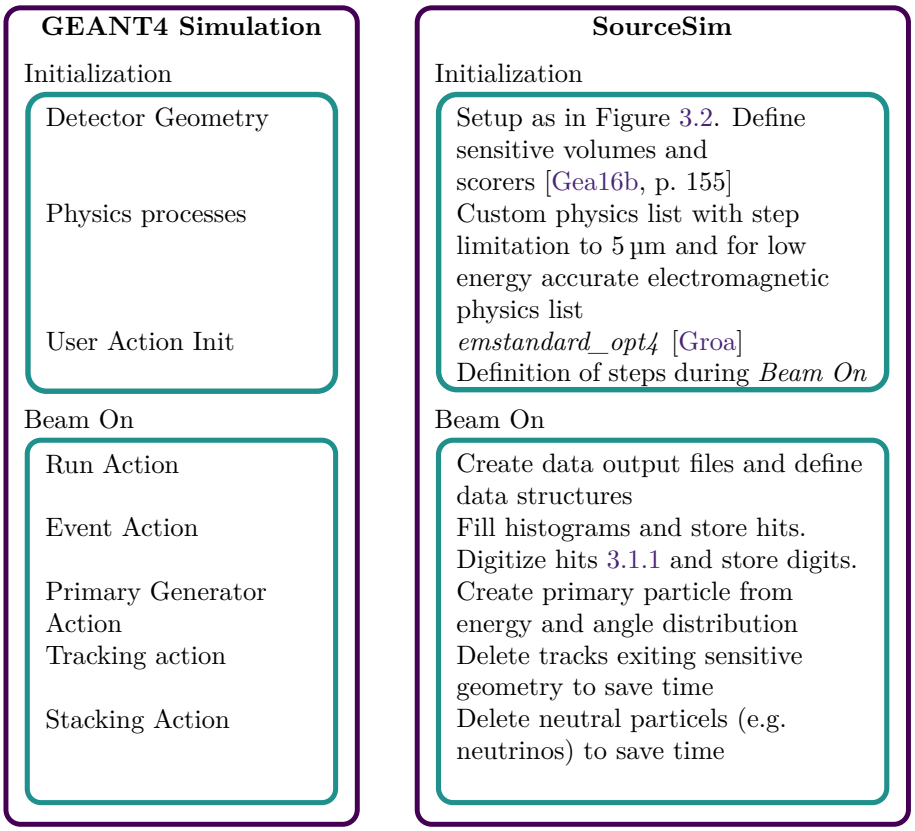


Figure 3.1: Sketch of important steps of a GEANT4 simulation (left) and the corresponding implementation in SourceSim (right).

### SourceSim

SourceSim is a software to simulate the response of pixel detectors when illuminated with particle sources like electrons from an accelerator or a radioactive $^{90}$Sr source. It is released as open-source software [Poh17] and follows the common structure of a GEANT4 simulation which consists of several repeating steps made programmatically accessible by class hooks [Gea16b, p. 4]. Most of these steps and their corresponding implementations of SourceSim are summarized in Figure 3.1. One run of the simulation is managed by a run manager, that initializes the geometry, physical processes and user defined actions at start-up. The geometry used in SourceSim is depicted in Figure 3.2. It consist of a *particle source*, a *source shield* to describe encapsulated radioactive sources, a two material *collimator*, the *planar detector*, a *trigger* volume and a *setup shield*. All materials and geometries are freely adjustable.

The smallest independent step of a run is an *event*, that corresponds to the generation of primary particles and the propagation through the geometry according to selected physics processes. Due to the independence of events, they can be calculated in parallel on multiple CPU cores leading to a simulation speed of 200 events/s – 10 000 events/s. User defined actions influence and store data at the different simulation steps within one event. The first step of an event is the creation of the primary particles. In case of this simulation the creation of an electron from a $^{90}$Sr source. Strontium disintegrates via Zirconium to Yttrium [Bé+06, p. 43]:

$$^{90}\mathrm{Sr} \xrightarrow[0.55\,\mathrm{MeV}]{28.8\,\mathrm{yr}} {}^{90}\mathrm{Z} \xrightarrow[2.28\,\mathrm{MeV}]{2.67\,\mathrm{d}} {}^{90}\mathrm{Y} \tag{3.1}$$

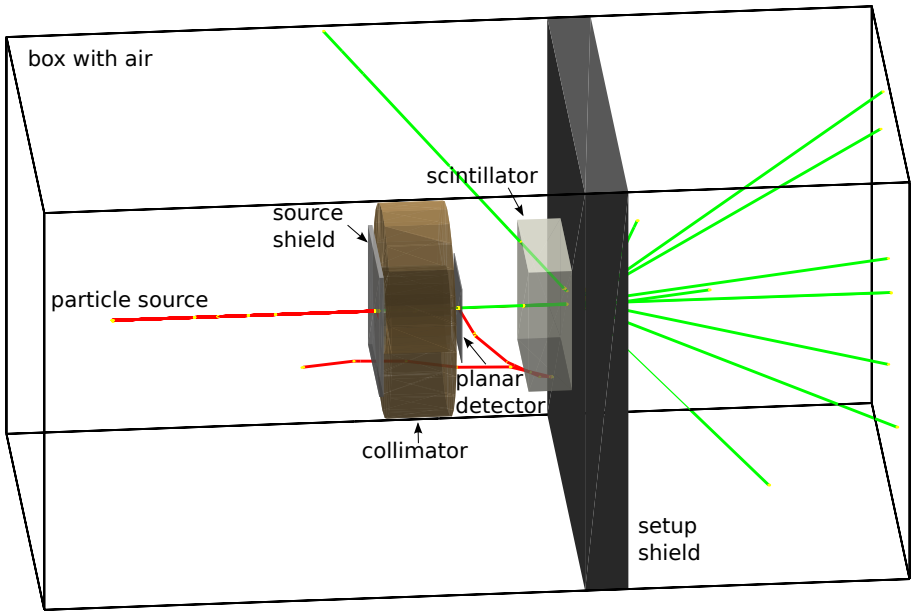


Figure 3.2: The simulated world of *SourceSim*. Negative charged tracks are red, photon tracks are green and locations of particle interactions (hits) are yellow.

The resulting energy spectrum consist of electrons from Strontium decay with a maximum energy of 0.55 MeV and of electrons from Yttrium decay with a maximum energy of 2.28 MeV. The simulation of radioactive decay is done only once due to high demand of computational time. The resulting energy spectrum is stored to enable consecutive simulations to sample electrons from this distribution. Additionally, the influence of a 1 mm source shield is simulated to describe the available encapsulated source (Figure 3.3). After creation of particles they are propagated in steps

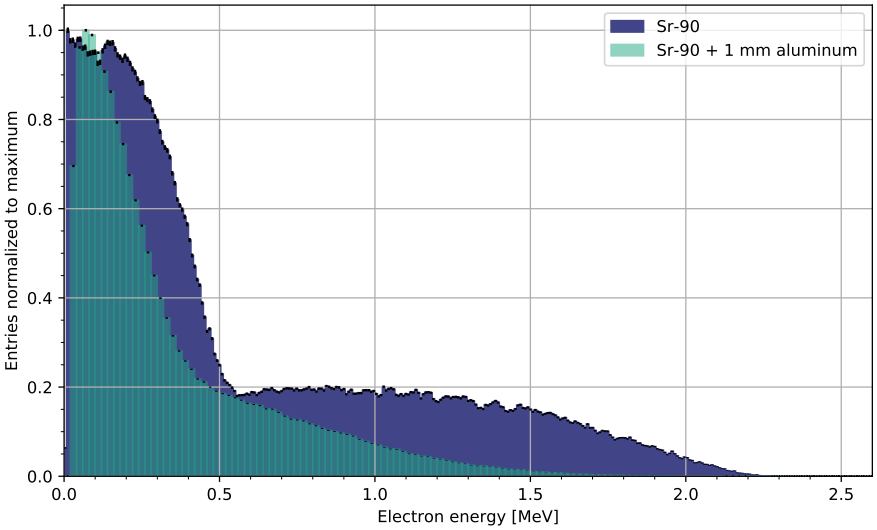


Figure 3.3: The energy spectrum of simulated $^{90}$Sr electron source with and without a 1 mm thick aluminium source shield.

through the simulated world. The step size is randomly sampled from the mean free paths $\lambda$ of all selected physics processes and the smallest step size defines the path length [Gea16a, p. 8]:

$$\lambda(E) = \frac{1}{\Sigma(E)} \tag{3.2}$$

with particle energy $E$ and the macroscopic cross section

$$\Sigma(E) = \sum_i n_i \cdot \sigma(Z_i, E) \tag{3.3}$$

where $\sigma(Z, E)$ is the total cross section per atom of a physics process and $i$ enumerates the different elements composing the material. Additional step size limitations are taken into account. For example, interactions are forced at material boundaries and maximum step lengths can be defined. Interactions with sensitive volumes (e.g. a sensor) are called *hits* and contain information like position, volume id, and energy deposit. Since GEANT4 uses a condensed multiple scattering algorithm, not all interactions create a hit in [Gea16a, p. 53] to save computational time. Values at sensitive volume boundaries are exact (e.g. total path-length and energy deposit), but locations of the multiple interactions within volumes are not. Especially within thin layers, like a silicon

detector, too few hits are created. Therefore, the maximum step size of the simulation was limited to 1 µm to approximate the almost continuous energy loss of a MIP better. At the end of an event all hits are stored to disk and *digitization* happens.

### Digitization

Digitization refers to the step where Monte-Carlo data is used to simulate the response of the measurement setup. The output are called *digits*. In *SourceSim* the digitization is the simulation of the response of a pixel detector to the localized energy deposits within the sensor volume. The calculated digits contain pixel index, event number, and charge information. Digitization is not part of the GEANT4 framework and is implemented in *SourceSim* in two consecutive steps (Figure 3.4). The first step is the digitization for a generic pixel detector and includes charge calculation, charge

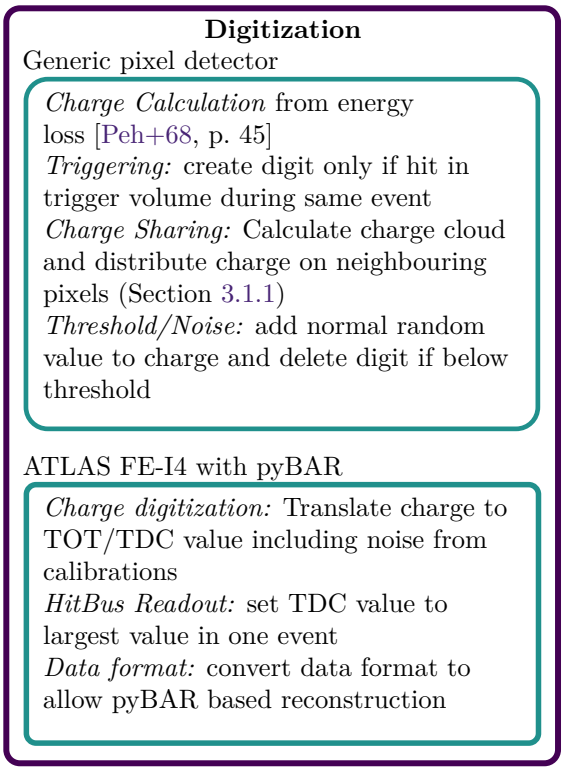


Figure 3.4: *SourceSim* digitization: Simulation of a pixel detector response in two steps. First: a generic digitization with charge sharing, noise and threshold. Second: A specific ATLAS FE-I4 digitization for ToT discretization.

sharing, triggering, threshold, and noise effects. The second digitization simulates the response of the ATLAS FE-I4 (Section 2.3.1) when readout using the readout system pyBAR (Section 3.2.1). It is implemented as a stand-alone Python script. The simulation of charge sharing needs to be accurate to be able to distinguish charge sharing (Section 2.1.5) from multiple scattering of the primary particle within the sensor volume (Section 2.1.1).

### Modeling charge sharing

To model charge sharing the charge-cloud evolution with time due to diffusion and repulsion has to be described. A simple ansatz is to use the seperate solutions of the continuity equation (Equation (2.51)) for diffusion (Equation (2.53)) and repulsion. The solution to the repulsion part is a sphere that confines the electrons and expands with time given by [Gat+87, p. 396]:

$$r_0 = \sqrt[3]{\frac{3\,\mu\,N\,e}{4\,\pi\,\varepsilon_s}\,t}$$

The charge density within the sphere is:

$$\rho(\vec{r}, t) = \frac{2\,\pi\,\varepsilon_s}{\mu\,t}(r_0^2 - r^2) \tag{3.4}$$

Both contributions are assumed to have Gaussian density distributions and the resulting charge cloud width is then calculated as the quadratic sum of the RMS of the two distributions [Gat+87, p. 397]. However, since repulsion depends on the charge density that decreases with time, this overestimates the contribution of repulsion. Therefore, a numerical solution to the continuity equation is implemented into *SourceSim*. The algorithm is introduced in [BH09, p. 510] and assumes a spherically symmetric Gaussian charge density:

$$\rho = \frac{Ne}{(2\pi\sigma(t)^2)} \exp\left(-\frac{r^2}{2\sigma(t)^2}\right)$$

with number of electrons $N$ and radius $r$. When inserting this charge density into the continuity equation, a calculation rule for the charge-cloud width $\sigma$ can be derived:

$$\frac{\partial\sigma(t)^2}{\partial t} = 2D + \frac{\mu Ne}{24\pi^{3/2}\epsilon_s\,\sigma(t)} \tag{3.5}$$

with diffusion constant $D$, permittivity of silicon $\epsilon_s$ and electron mobility $\mu$. For application of Equation (3.5), the charge-cloud distribution at $t = 0$ has to be known, but modeling the initial charge-cloud distribution is non-trivial. For the simulation of x-ray photon interactions, usually an effective spherical charge cloud at interaction is assumed (e.g. [God+09; You11]) to describe the ionization path of the short ranged secondary photoelectron [FGW77, p. 187]:

$$\sigma[\mu\text{m}] = 0.0044 \cdot E^{1.75}[\text{keV}] \tag{3.6}$$

With the photon energy $E$ in keV. But this approximation has limitations for energies above 10 keV as shown by comparisons to "exact" MC simulations in [XDB11, p. 191]. Above 10 keV the range of electrons in silicon is in the order of several µm [Ber+05] and an isotropic model cannot describe the directed electron path. Therefore, in *SourceSim* a range cut of 1 µm is set to allow simulation of high energetic x-ray sources and an initial charge-cloud sigma is defined by Equation (3.6) for each hit. Figure 3.5 shows the evolution of a normal distributed space charge in

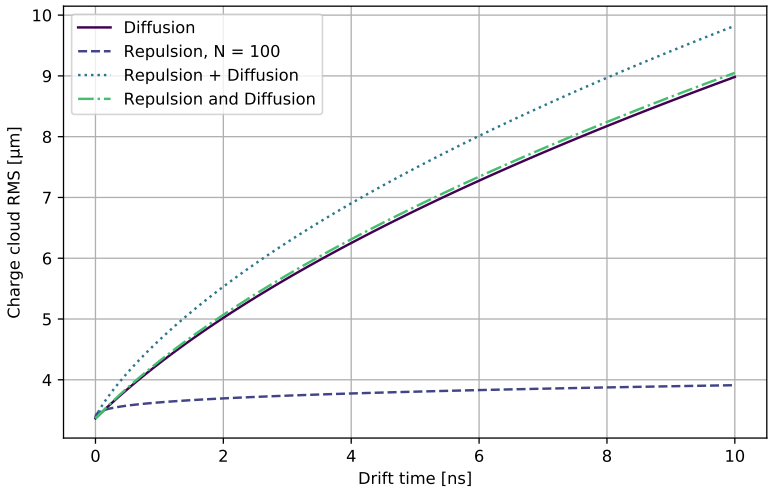


Figure 3.5: Charge-cloud evolution for a spherical normal distributed space charge. Four cases plotted: diffusion only, repulsion only, quadratic sum of both (*Rep. + Diff.*) and numerical solution to the continuity equation (*Rep. and Diff.*).

a silicon detector assuming an energy deposition of 5.9 keV, that corresponds to the most probable energy deposition of a $^{55}$Fe-source. The initial charge cloud is very small and repulsion is only dominant during the first 100 ps. The overestimation for the simple model can also be seen (*Rep. + Diff.*). The numerical solution is very similar to the solution of the continuity equation for diffusion alone. Especially, when considering that typical drift times are in the order of several ns. For the charge deposition of MIPs, where the initial charge density is even lower, it is sufficient to describe the charge-cloud evolution with diffusion only [Bel+83, p. 257]. Therefore, for the simulation of minimum-ionizing electrons diffusion only is considered. For the charge-cloud width as a function of the initial charge-cloud position in a planar sensor follows, as derived in Section 2.1.5,

$$\sigma(z)_{\substack{\text{n-bulk}\\\text{p-bulk}}} = d\sqrt{\frac{k_B\,T}{e\,V_{\text{dep}}}}\sqrt{\pm\ln\left(1 \pm \frac{2}{d}\frac{V_{\text{dep}}}{V \mp V_{\text{dep}}}z\right)} \tag{3.7}$$

Figure 3.6 shows the width for different drift distances in a fully depleted 200 µm sensor at different bias voltages and bulk resistivities. The charge-cloud width is in the order of a few µm and decreases to about 1 µm for parameters at the end of life time of an IBL sensor, under the simple assumption that full depletion is still possible ($V_{\text{bias}} = 1000\,\text{V}$, $V_{\text{depl}} = 900\,\text{V}$) and no drift velocity saturation exists. The calculated $\sigma(z)$ from Equation (3.7) is used in the simulation to calculate the relative charge deposited per pixel for each hit at position $x, y, z$ as derived in Equation (2.55):

$$Q_{\text{frac}}(x,y,z,a,b) = \frac{1}{4}\left(\text{erf}\left(\frac{x+\frac{a}{2}}{\sqrt{2}\,\sigma(z)}\right) - \text{erf}\left(\frac{x-\frac{a}{2}}{\sqrt{2}\,\sigma(z)}\right)\right)\cdot\left(\text{erf}\left(\frac{y+\frac{b}{2}}{\sqrt{2}\,\sigma(z)}\right) - \text{erf}\left(\frac{y-\frac{b}{2}}{\sqrt{2}\,\sigma(z)}\right)\right) \tag{3.8}$$

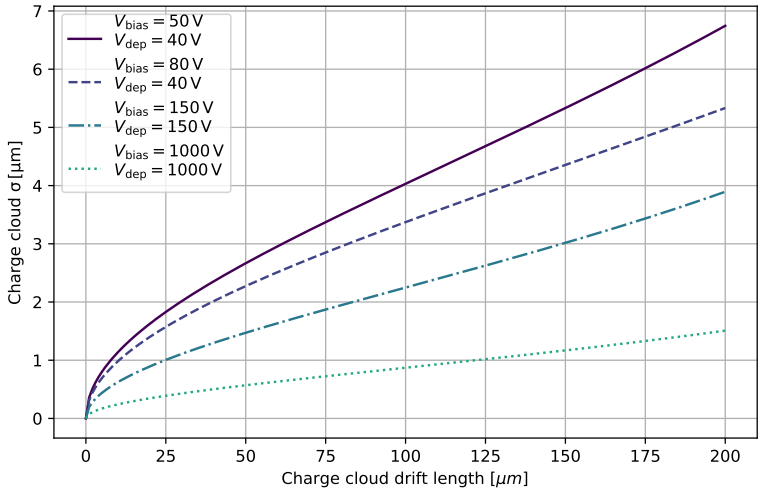


Figure 3.6: Charge-cloud width due to diffusion for different drift distances. A fully depleted 200 µm planar sensor is assumed, with different resistivities, depicted by their depletion voltage.

The pixel dimensions ($a$, $b$, sensor thickness ($d$)) are selectable parameters in *SourceSim*, as well as the temperature, bias voltage, and depletion voltage. The deposited charge per pixel for different drift lengths of the charge cloud can be calculated by integration of Equation (3.8) over the pixel area (Equation (2.57)). The result is shown in Figure 3.7 for ATLAS IBL pixels and for future ATLAS pixel geometries with smaller pixels. The average fraction of charge per pixel for a MIP

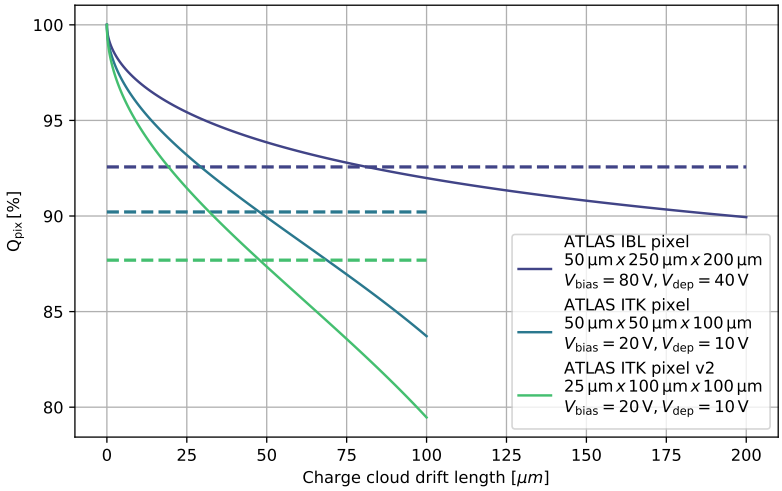


Figure 3.7: Charge per pixel for different geometries. A resistivity corresponding to a full-depletion voltage $V_{\text{dep}} = 40\,\text{V}$ at 200 µm and a bias voltage $V = 2 \cdot V_{\text{dep}}$ are assumed.

(dotted lines) can be calculated analytically, by integration of Equation (3.7) over $z = 0..d$, showing that the small pixel geometries have about 5 % less charge per pixel due to charge sharing for parameters corresponding to unirradiated sensors[1]. But generally charge sharing is small for ALTAS pixel geometries.

The output of the first digitization stage is used as input to the second stage where the response of the ATLAS FE-I4 including readout system is simulated. It is implemented as a data driven Monte Carlo simulation utilizing the per-pixel calibration data to describe the FE response. Figure 3.8 shows the calibration data (dots) for the charge given in ADC values (TOT/TDC). The corresponding response functions are derived as spline fits to the data on pixel level and are used to translate the simulated charge to the corresponding ADC value. The TDC error is sampled from a normal distribution with the measured width ($TDCerror$, Figure 3.8) and added to the calculated ADC values. The benefit of this implementation is that no (complex) description of the Front-End electronics is needed and behavior that is very difficult to model is automatically incorporated (e.g. noise that depends on the charge; Figure 3.8, light line). The simulation of the response is therefore "exact".

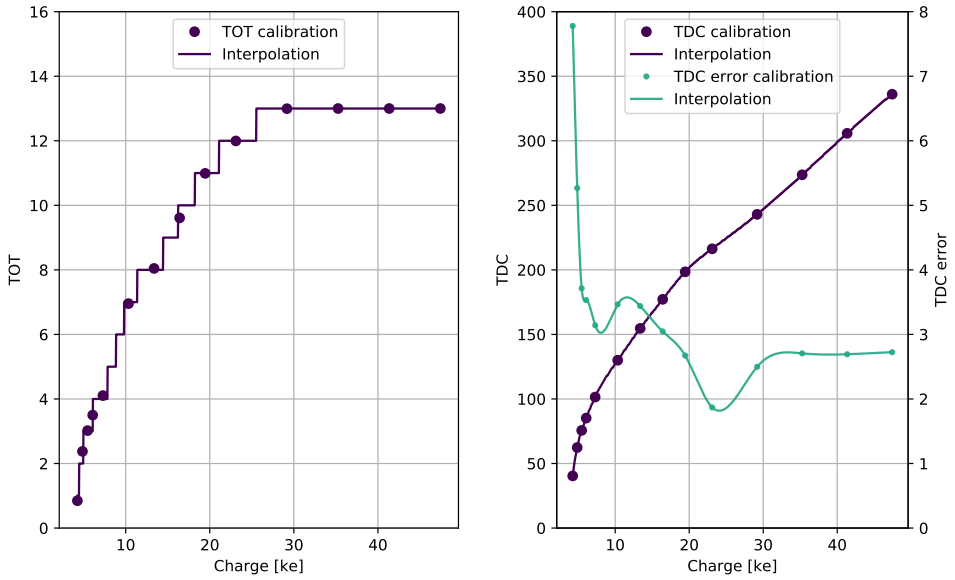


Figure 3.8: Measured transfer functions $TOT(charge)$ (left) and $TDC(charge)$ (right) of one example pixel (dots). Lines are the interpolated functions used in SourceSim.

### Qualification

The complexity and large parameter space of a GEANT4 simulation and the new implementation of a charge sharing model demand qualification with real world data. Therefore, the output of *SourceSim* is compared to published data as well as to ATLAS FE-I4 data. The literature data is

[1]The analytical expression can be found in Appendices.

provided within the GEANT4 framework as a benchmark for electromagnetic processes.

Scattering of low energetic electrons in thin layers is benchmarked by comparing the scattering angle of 15.6 MeV electrons in gold foils.

The energy deposition of low energetic electrons in thin silicon layers is verified by comparison to data from 1 MeV electrons traversing a 540 µm thick silicon sensor.The results agree considering that digitization of the sensor is missing. The new implementation of a charge sharing model is checked by comparison to data recorded in a 3.2 GeV electron beam with planar IBL modules (Section 2.3.1) with a sensor thickness of 200 µm and 250 µm. Figure 3.9 depicts the measured and simulated cluster size distributions. A cluster is a localized group of pixels, that detect the same

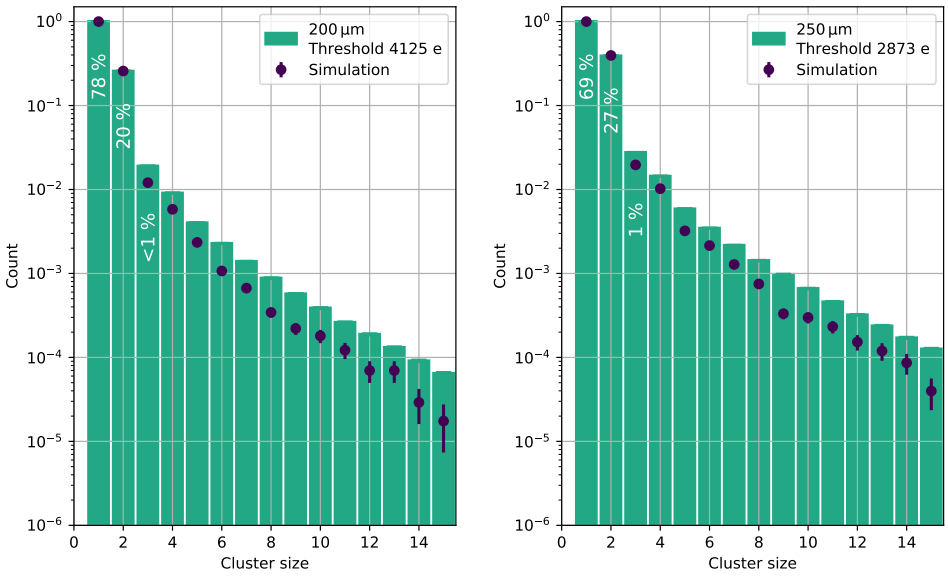


Figure 3.9: Measured and simulated cluster size distributions of a 200 µm (left) and a 250 µm (right) thick IBL planar sensor. The error bars depict the statistical error due to limited computational time restricting the number of simulated events. The threshold values during measurement and simulation are stated in the legend.

ionizing particle. Most abundant cluster sizes can be described quantitatively and larger, rare cluster sizes qualitatively. Large cluster with more than 4 pixels do not arise from charge sharing, but from delta electrons. The simulation of these does not seem to be exact and further investigation is needed to understand the discrepancy. Nevertheless, for the description of charge spectra this is negligible due to the rarity of delta electrons with long path lengths. This is also depicted by the successfull description of charge spectra in Figure 3.10 for two different cluster selections. The bump in the cluster-seed charge at about 10 keV due to charge sharing is reproduced well by the charge sharing model. It has to be stressed here that at no point a simulation parameter was adjusted to describe the measurement. Simulation and measurement are completely independent. One can conclude that *SourceSim* is capable of describing charge spectra of pixel detectors and the simulation results in the following Section 3.1.2 are meaningful.

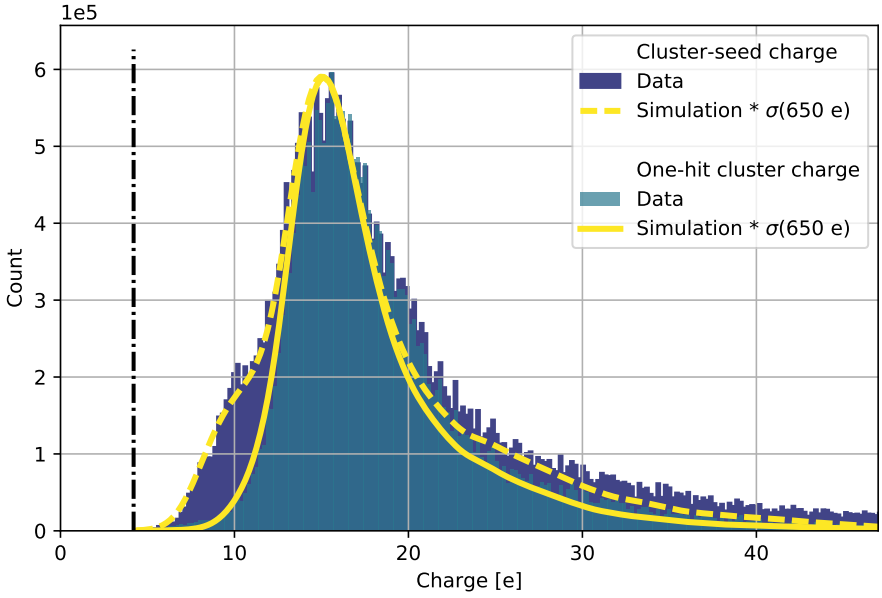


Figure 3.10: Measured and simulated charge distributions of 3.2 GeV electrons illuminating a 200 µm planar IBL pixel-sensor. The spectra show *one-hit cluster* charge and *seed cluster* charge. Simulated values are smoothed with a Gaussian kernel to suppress statistical fluctuations.

### 3.1.2 Charge spectra with $^{90}$Sr

Most electrons from $^{90}$Sr with an energy up to 2.28 MeV (Figure 3.3) are close to minimum-ionizing (Figure 2.1). Therefore, $^{90}$Sr is often treated as a MIP source. This is a valid approximation when looking at the average energy-deposit per path-length ($dE/dX$), the difference to an electron beam of several GeV is about 10 % only as shown in Figure 3.11b. But the deposited charge distribution of $^{90}$Sr is considerable broader with a higher most propable value (Figure 3.11c), due to the heavy scattering of the primary electrons in the sensor material increasing the path length (Figure 3.11a). Therefore, the deduction of sensor properties that rely on the energy deposit of low energetic electrons have a large systematic error due to the unknown path length. Generally, more charge is deposited for low energetic electrons in comparison to high energetic MIPs, but less charge per pixel due the transition of several pixel volumes by the primary electron. This leads to large cluster sizes and makes the measured charge spectra very depended on pixel geometry and cluster cuts (Figure 3.12). For the ATLAS IBL pixel geometry, it is not possible to determine a maximum in the charge distribution, that relates to the energy deposited, when histogramming charge of every pixel hit (Figure 3.12a, *dark blue*, measurement: Figure 7.1), a requirement for CCE studies as in Section 5.1. Simple single-pixel charge-measurements for CCE determination are therefore not feasible with $^{90}$Sr and data selection cuts on the cluster size mandatory. The best quantifiable peak is obtained for narrow distributions that minimize the Langau fit-error. Most narrow charge distributions are obtained when charge of all pixels is added up (Figure 3.12a, *cluster*

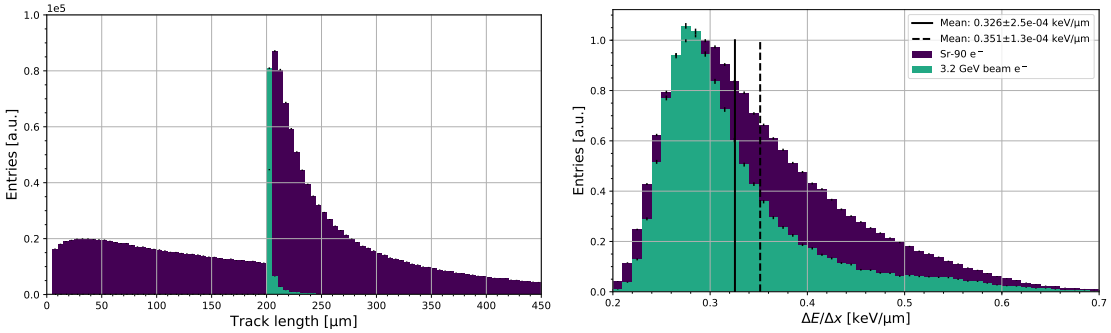


(a) (b)

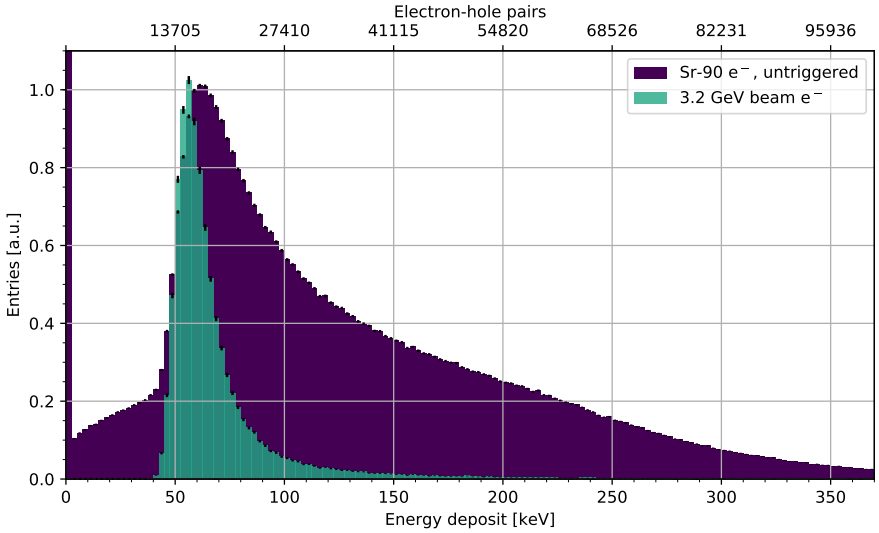


(c)

Figure 3.11: Path length (a), energy deposit per path length (b) and total energy deposit (c) of $^{90}$Sr electrons (*dark blue*) and 3.2 GeV electrons (*light green*) in a 200 µm silicon layer.

.

*charge*) or clusters with only one hit are selected (Figure 3.12a, *one-hit cluster-charge*). The usage of cluster-charge demands a good charge resolution for all channels, a premise often missing in prototype readout chips where only few channels have an accessible charge signal with high resolution. This is also the case for the ATLAS FE-I4, where one high resolution channel for all pixels is available via the *hit-bus* feature (Section 3.2.2). Since cluster-seed charge also suffers from charge sharing and creates artificial steps in the charge distribution for each cluster size (Figure 3.12a, *light blue*), the selection of *one-hit cluster* is often the best option. A way to further enhance the charge spectrum of $^{90}$Sr in terms of a more narrow and "Landau-like" distribution that can be described with a fit function is to select only electrons that traverse the sensor by adding a trigger behind the sensor. This removes stopped and backscattered electrons from the distribution (Figure 2.4). The charge spectra for triggered electrons is depicted in Figure 3.12b.

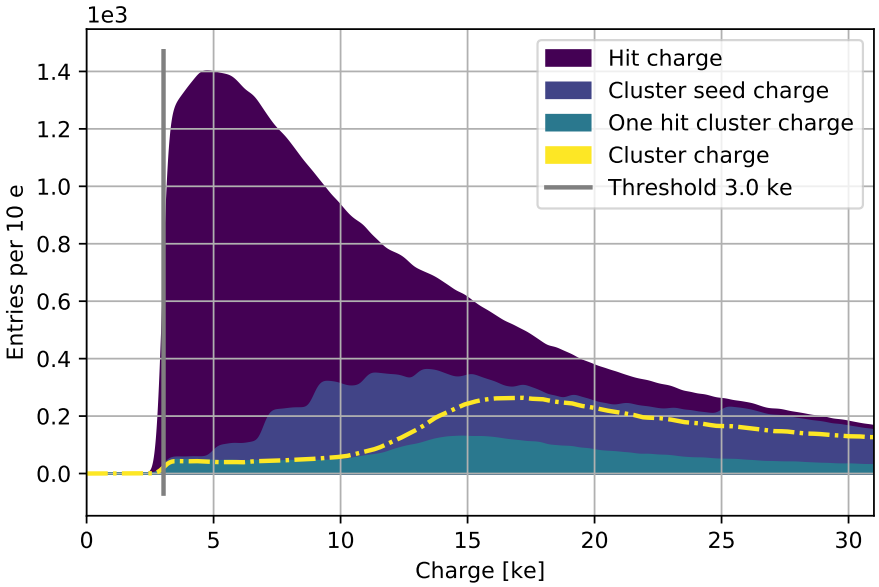


(a) untriggered

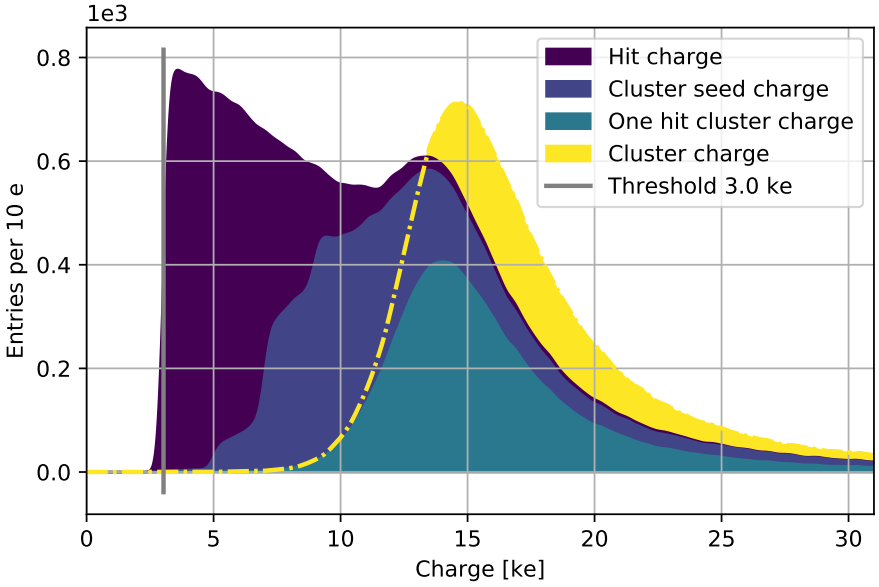


(b) triggered

Figure 3.12: Charge spectra of $^{90}$Sr electrons in a pixel detector for different cluster size cuts. Untriggered (a) and when using a trigger (b) to select traversing electrons. *SourceSim* simulation with planar ATLAS IBL pixel geometry. 3000 $e$ threshold and 200 $e$ noise.

.

The strong correlation between primary electron energy and scattering in the sensor makes charge spectra also dependent on the setup. Source encapsulation, opening angle of electrons, distance between source and sensor, and even the total material budged between sensor and trig-

ger influence the measured spectra. Therefore, the deduction of absolute sensor parameters like depletion depth and cross talk with less than 20 % error demands a very challenging simulation of the setup to deduce correction factors. Figure 3.13 shows the measured and simulated charge spectra for different cluster cuts for $^{90}$Sr in an planar ATLAS IBL pixel sensor. Despite varying

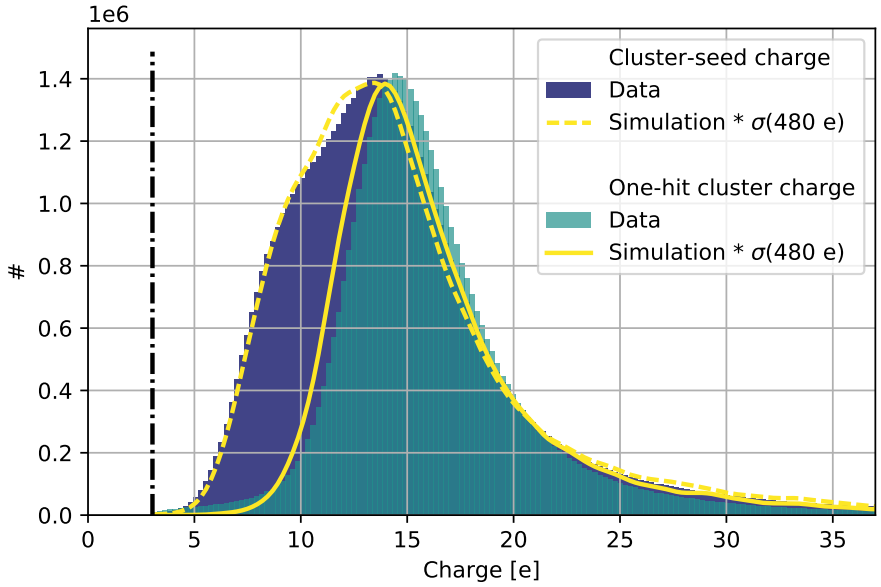


Figure 3.13: Measured and simulated charge distributions of $^{90}$Sr electrons illuminating a 200 µm planar IBL pixel-sensor. The spectra show one-hit cluster charge and seed hit charge. Simulated values are smoothed with a Gaussian kernel to suppress statistical fluctuations.

unknown parameters like electron opening angle and source-shield thickness to optimize the match between simulation and measurement only a qualitative description was possible. Consequently, absolute sensor quantities are not derived in this study with $^{90}$Sr, but solely with high energetic particle beams.

## 3.2 Methods for charge measurements

The ATLAS FE-I4 used for sensor characterizations in Section 5.2 is the successor of the ATLAS FE-I3, which has a return-to-baseline time for a MIP of $\sim$ 1 µs [ATL08, p. 10]. The charge digitization via the ToT-method with a 40 MHz clock results in approximately 100 different ADC values (*ToT-value*) to describe the charge spectrum of a MIP. For the FE-I4, the return-to-baseline time was reduced to about 200 ns [Gar+11, p. 5] to avoid single-pixel pile-up, while keeping the clock speed at 40 MHz. This also allowed for a reduction of the hit-charge information from an 8 to a 4-bit ADC value. Taking into account the ADC value coding to further reduce data bandwidth by incorporating *late-hit*, *no-hit*, and *big-hit* information [FEI12, p. 31] leaves 13 distinct ADC values to describe a charge spectrum with the first 3 values being redundant due to the steepness

of the $ToT(charge)$ transfer function (Figure 3.8, *left*). This leaves an insufficient amount of ADC values to describe charge spectra. As a result, a threshold offset above 1000 $e$ and a threshold gradient of 400 $e$ after tuning could not be identified before IBL production[2]. In this section two charge reconstruction methods that have been developed with the FE-I4 are introduced that do not rely on the charge digitization of the chip. Although these methods were developed for the ATLAS FE-I4, they can and have been applied for other pixel detectors (e.g. [Obe09, p. 80]).

### 3.2.1 pyBAR

The implementation of the charge reconstruction methods requires continuous raw-data taking, new measurement methods, and complex raw-data analysis. Hence, a new readout software called *pyBAR* (**B**onn **A**TLAS **R**eadout using **Py**thon, [JPa]) was developed within the scope of this study in collaboration with Jens Janssen. It is written in the high-level, interpreted programming-language Python and makes use of the scientific ecosystem of Python for data analysis, data visualization, and data storing (*SciPy*, [JOP+01]). The new charge recontruction methods called *Threshold-method* and *TDC-method*, as-well-as new chip calibration methods are part of the *pyBAR* software. More information about the readout system can be found in [Jan20].

### 3.2.2 Threshold- and TDC-Method

Figure 3.14 shows the common blocks of a charge digitization chain in a pixel detector as also present in the ATLAS FE-I4. The output of the comparator is a digital signal whose length corresponds to the time the charge signal $V_q$ is above a threshold voltage $V_{th}$. This time is called time-over-threshold (ToT). The ATLAS FE-I4 uses a constant current source in the feedback of the CSA leading to a signal shaping where the ToT-signal is in first order a linear function of the charge. The ToT-signal is discretized into multiple periods of the clock ($T$) with a TDC for further processing in the digital part (referred to as *ToT-value*). The discretization reduces the resolution

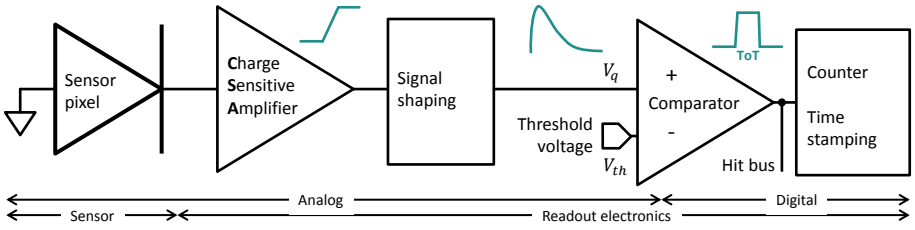


Figure 3.14: Common charge digitization chain of one pixel in a pixel detector. Consists of a sensor depicted as a diode, a CSA, a shaping stage, a comparator, and further digital logic.

[2]Measurement results and repercussions for IBL operation are discussed in Section 5.3.3

of the ToT-signal and is given by:

$$\begin{aligned} \mathrm{RMS}(T) &= \sqrt{\frac{1}{T}\int_0^T E(t,T)^2\,dt} \\ &= \sqrt{\frac{1}{T}\int_0^T t\,T - t^2\,dt} \\ &= \frac{T}{\sqrt{6}} \end{aligned} \tag{3.9}$$

with ToT-signal length $t$, clock cycle period $T$, and $0 \leq t \leq T$. The error $E(t,T)$ between continuous and discretized ToT-signal depends on the phase to the clock when the particle hits and the ToT-signal itself. Allowing an arbitrary phase, as present in measurements with radioactive sources, leads to the following quadratic error:

$$\begin{aligned} E(t,T)^2 &= E_l^2 \cdot \rho_l + E_r^2 \cdot \rho_r \\ &= t^2 \cdot \left(\frac{T-t}{T}\right) + (T-t)^2 \cdot \left(\frac{t}{T}\right) = t\,T - t^2 \end{aligned} \tag{3.10}$$

where $E_l/E_r$ are the two possible errors depending on the clock phase and $\rho_{l,r}$ the corresponding probabilities. Equation (3.10) shows that the error vanishes ($E = 0 \forall t = T, T \in \mathbb{N}$) for ToT-signals with a length of multiple periods $T$ and for ToT-signals between multiple periods ($t = (c+1/2)\,T \forall\, c \in \mathbb{N}$) the error is maximal. This is depicted in Figure 3.15. Therefore, the reduction

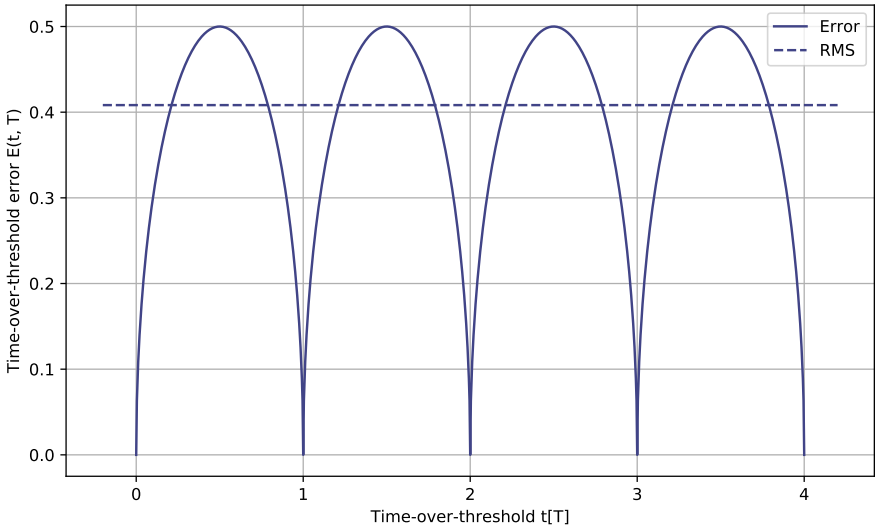


Figure 3.15: Time-over-threshold error due to discretization (Equation (3.10)) for different unclocked ToT-values. ToT-values are given in clock periods $T$ and RMS from Equation (3.9)

of the ToT-resolution to one value in Equation (3.9) should be taken with care. It does not reflect

the dependence on the time-over-threshold itself and the consequential systematic error in the charge reconstruction.

### TDC method

For the ATLAS-FE I4 the charge per discrete ToT-value is about $1.9\,\mathrm{k}e/ToT$ (Figure 3.8, *left*) in the charge range of interest ($8\,\mathrm{k}e - 23\,\mathrm{k}e$). Using Equation (3.9) with a clock period of 25 ns gives a charge resolution of about $800\,e$ with a maximum error of $950\,e$ (Equation (3.10)). Since this error is about one order larger than the electronic noise of an ATLAS FE-I4 module (Figure 5.14), decreasing the clock period significantly enhances charge resolution. This is the basic idea of the *TDC-method* where a FPGA based Time Digital Converter (TDC) is used to digitize the ToT-signal with a 16 times faster clock (640 MHz) decreasing the discretization error by the same factor. The ToT-signal is externally accessible via the *hit-bus* feature of the FE-I4. The *hit-bus* is a single ended, unclocked signal connecting the outputs of all pixel comparators (Figure 3.14). Since the *hit-bus* is a wired-OR, only the longest ToT-signal of a pixel cluster can be measured. The *hit-bus* is amplified on the single chip card and subsequently connected to an input of the FPGA via an open drain buffer for fast signal edge times [Eng14, 31f]. The TDC measurement is independent from the FE-I4 hit-data, demanding a data-stream correlation to assign the fast sampled ToT-signals to a hit. This correlation is realized in two steps. The first step is to assign TDC-values to events. Here one event corresponds to the hit-data recorded when one trigger is issued (e.g. from a scintillator). TDC-value correlation to an event is made possible by recording time differences between trigger- and TDC signals with the FPGA TDC module. Only when the TDC signal edge follows the trigger signal edge the TDC-value is accepted. Figure 3.16 shows some exemplary signals. A delay between trigger and TDC signal is expected due to time walk,

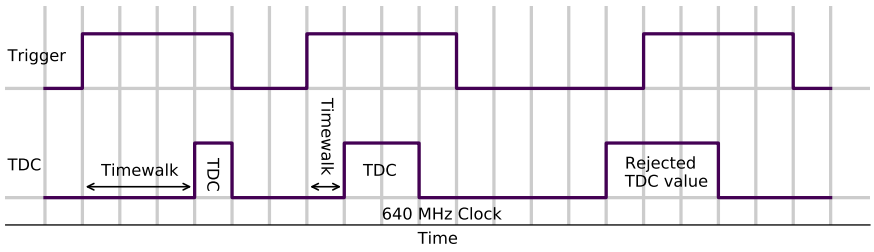


Figure 3.16: Trigger and TDC signal as seen by the FPGA TDC module. TDC-values not following a trigger signal are rejected.

which is for the FE-I4 in the order of a few ns to about 50 ns (Figure 6.13). The parallel record of trigger delays next to their corresponding TDC-value enables determination of time walk of the readout electronics in a table-top experiment. The knowledge of time walk is crucial to judge and tune the in-time efficiency of the detector. Time-walk measurements are depicted in Section 6.6.

Although a selection of valid TDC-values is possible in software by demanding a reasonable value for the time walk, measurements with $^{90}$Sr have shown that most ($> 99\,\%$) of the electrons do not hit pixel matrix *and* trigger volume, due to stuck and scattered electrons (Figure 2.4). This leads

to the record of many dispensable TDC-values, that can deplete data bandwidth of the readout system. Therefore, a filter is implemented in the FPGA firmware selecting only TDC-values with a preceding trigger.

The second step is the assignment of TDC-values to hits within on event. Since TDC signals of several pixels can overlap, an unambiguous assignment to a hit is only possible when just one pixel is hit. Consequently, solely *one-hit clusters* can be used. Hits with no cluster information due to their location next to disabled pixels or at the pixel matrix edge are discarded. Depending on the particle source these cuts lead to rejection of up to 90 % of the recorded data. Number of pixels and the hit rate per pixel have a large influence on the accepted events fraction. For a radioactive source measurement with a Poisson distributed hit rate per pixel $R$, the fraction of accepted events (*live time*) can be described by [Mül91, p. 543]:

$$\text{live-time} = \exp\left(-\tau R\right) \tag{3.11}$$

with dead-time per readout ($\tau$). Assuming reasonable values for the source activity (1 Hz – 1000 Hz per pixel) and dead-time (250 ns) when using the ATLAS FE-I4 with $^{90}$Sr leads to a *live-time* as depicted in Figure 3.17. Thus depending on the experiment it can be beneficial to only activate

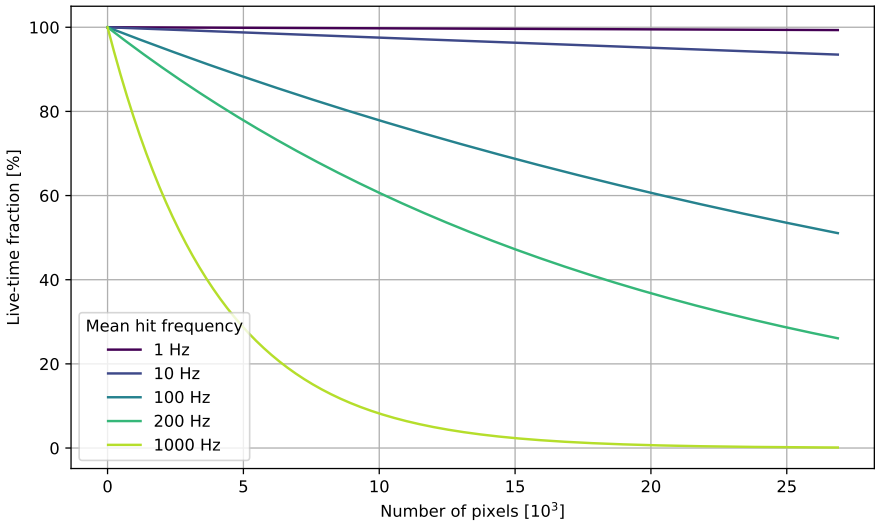


Figure 3.17: Live-time when using the TDC-method for different number of pixels and mean hit rates.

the hit-bus for a fraction of pixels.

The correct correlation of the data with the cuts mentioned above is checked by comparing the ToT-value as sampled by the Front-End and by the FPGA TDC. Figure 3.18 depicts the correlation when hit cuts are applied and for no cuts. The linear function shows a successful correlation for all selected hits ($b$). Despite the complexity of the TDC-method it allows to overcome the low charge resolution of the ATLAS FE-I4 (illustration in Figure 3.21) and opens up new applications.

One application is the BEAST experiment where the ATLAS FE-I4 is used for background radiation determination and the additional charge resolution helps distinguishing different particles types [Ahl16].

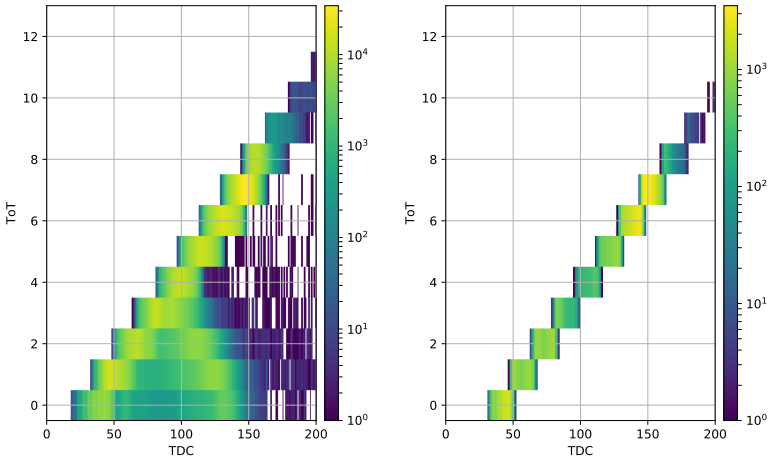


(a) No hit cuts (b) In-time hit from one-hit cluster

Figure 3.18: Time-over-threshold measured by the ATLAS FE-I4 (*y-axis*) and by the FPGA TDC (*x-axis*) for selected hits (b) and all hits (a). Unambiguous TDC-value assignment to a hit is possible when selecting in-time hits from one-hit cluster.

### Threshold method

The *threshold method* is well known for binary responding readout ASICS [Cam+05; Mik+01; Cam+94; Dab+00] and has been applied for the first time to the ATLAS FE-I4 [Poh+15]. The basic idea of the method is to use the adjustable threshold voltage ($V_{th}$, Figure 3.14) to change the hit detection threshold while measuring the hit rate of a particle source. This leads to a record of the integrated charge spectrum as depicted by *dots* in Figure 3.19. The integrated spectrum is differentiated to get the reconstructed spectrum (*triangles*) that represents the original charge spectrum (*dark line*) convoluted with a normal distribution. The standard deviation is given by the electronic noise. Differentiation of integrated spectra is mathematically not straightforward, since conventional finite-difference approximations greatly amplify the statistical fluctuations in the measured rate [Cha11, p. 1]. This is mitigated in two ways. Illuminated pixels are combined to increase the statistics and consequently decrease the statistical fluctuations and data is denoised before differentiation with smoothed spline curve fits of 3rd order [Die75; Die82]. The requirements for the threshold method to reconstruct a charge spectrum is a sufficiently large adjustable threshold range and a strict monotonicity for the charge signal amplitude ($V_q(q)$, Figure 3.14), meaning that the CSA does not go into saturation. This is the case for the ATLAS FE-I4 whose CSA does not saturate in the scan range of interest up to 35 k$e$ (Figure 5.17, right).

The threshold method only works when the change of the single pixel rate arises solely from the different threshold settings. Changes in the delivered particle rate have to be measured and

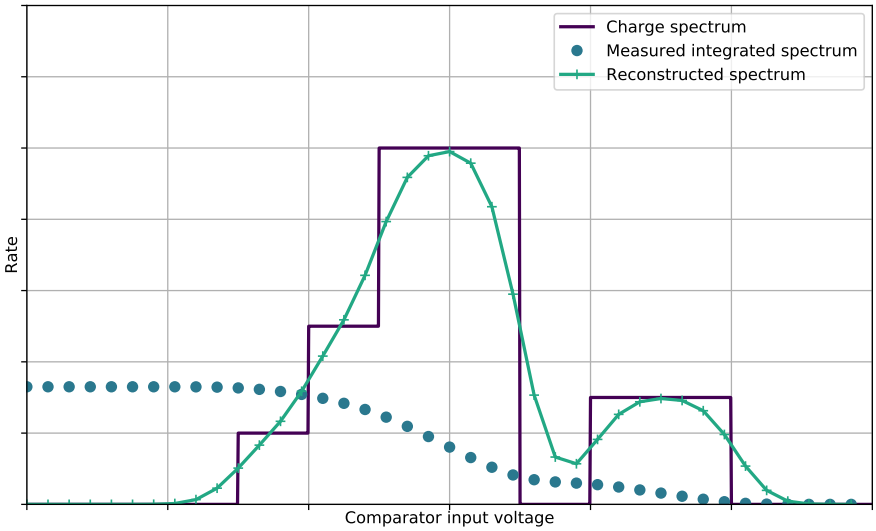


Figure 3.19: The threshold method illustrated by an arbitrary charge spectrum (*dark blue*). The measured integrated spectrum (*dots*), and the reconstructed spectrum (*light line*) are shown. The assumed electronic noise is half of one measurement step.

substracted [Poh+15, p. 51]. Additionally, with decreasing threshold it is more likely to see not only the seed pixel hit but also additional hits from its neighbors due to charge sharing (Section 3.1.1). This artificially increases the measured hit rate with lower thresholds. A solution is to count only

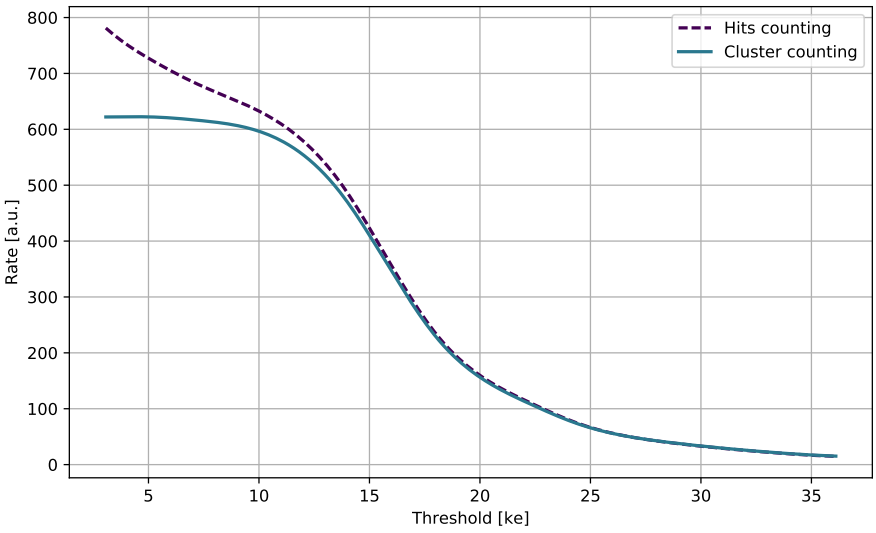


Figure 3.20: Measured rate for hit counting and cluster counting at different thresholds. ATLAS FE-I4 in a 3.2 GeV electron beam. Lower thresholds increase the cluster size leading to an increased hit count rate.

one hit per cluster, leading to particle counting instead of hit counting. The integrated single pixel charge spectrum before and after correction is depicted in Figure 3.20. The expected S-curve shape arising from the integrated Landau spectrum is seen if only one hit per cluster is used. The Threshold-method is the best method for single pixel charge measurements in terms of resolution (Figure 3.21), since it is limited by electronic noise only. The disadvantage is that it does not allow the assignment of the charge information to a single hit and demands permanent slow control communication to change the threshold.

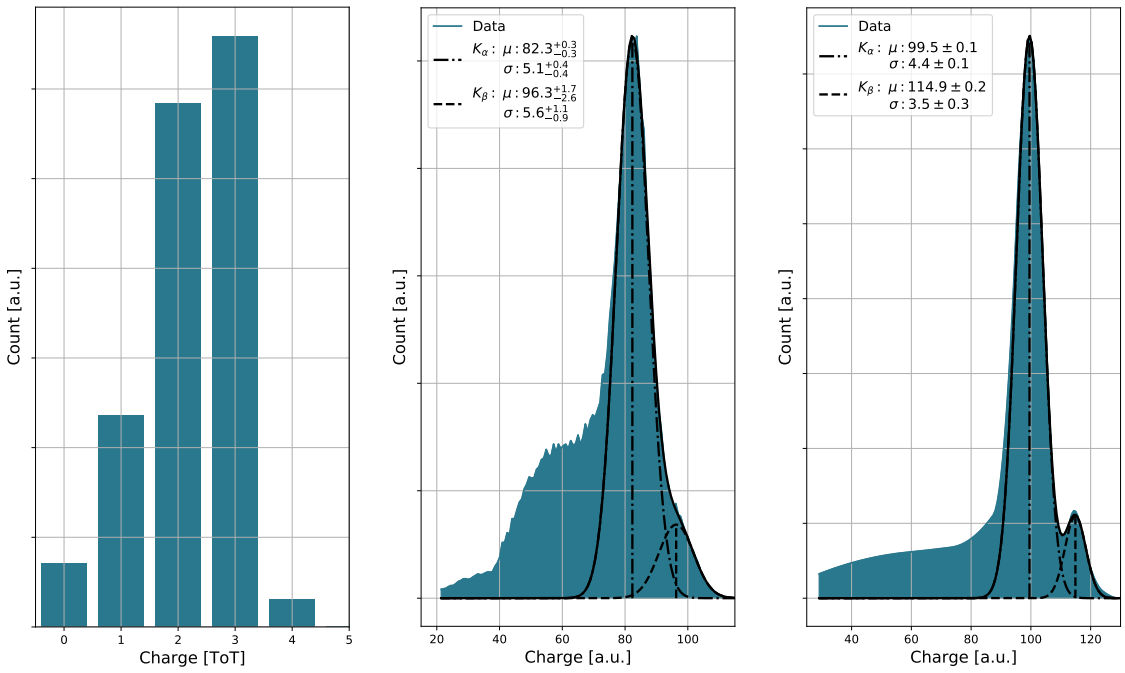


(a) FE-I4 ToT (b) TDC-method (c) Threshold-method

Figure 3.21: Charge spectra of a $^{109}$Cd $\gamma$-source. Measured with the ATLAS FE-I4 using the internal charge digitization (a), the TDC-method (b), and the Threshold-method (c).

# 4 Test-beam analysis

A *test-beam* is a minimum-ionizing particle-beam from a particle accelerator illuminating a detector under test (short: DUT). Test-beam campaigns allow for system tests, where conditions, as anticipated at the planned experiment, are simulated. Commonly varied parameters are track inclination angles, operational temperatures, timings of the trigger system, irradiation levels of electronics, readout-chip tunings, and sensor bias-settings. The influence of these parameters on quantities like hit efficiency and charge collection are investigated in a test-beam campaign. By the reconstruction of primary particle-tracks with particle telescopes, their position dependency can be measured. This information is then used to gain insight about the electrical field configuration in the sensor or the homogeneity of the per-pixel response after tuning.
A test-beam setup for particle track-reconstruction is complex and consists of multiple, independent planes of segmented tracking detectors. The readout systems of these detectors are synchronized by a central trigger system. Many hardware systems and software tools that are found in the ATLAS experiment for event based track reconstruction, can also be found in a smaller scale in a test-beam setup. Software tools for reconstructing tracks are needed and geometries of telescope setups have to be optimized to match beam conditions (such as beam momentum, track intensity). Additionally, data storage and fast data-quality check systems are required.
This chapter introduces a novel test-beam analysis software (*TBA*, Section 4.1), together with important analysis steps and -methods. Particular emphasis is put on the determination of the hit efficiency using telescope setups. A detailed analysis of the efficiency error depending on telescope and DUT parameters is presented in Section 4.2. The new software and error models are used in Chapter 6 to optimize the telescope setups and analysis parameters for the measurement of the hit-efficiency of passive CMOS-sensors.

## 4.1 Test-beam analysis software: TBA

A new test-beam analysis software called Test Beam Analysis (short: TBA) is developed and qualified within the scope of this study [Poh+]. The primary goal of the software is simplicity by design to allow an experimenter a fast, reliable, and comprehensible data analysis. The specific use case in this work is the determination of the hit efficiency of passive CMOS-sensors after irradiation, but TBA has been used for other test-beam data (e.g. [Jan17; Cai+19]). TBA enables quick data quality checks after data taking and in parts during data taking with an online-monitor [Poh]. Fast data analysis on sight is important to judge telescope alignment and usefulness of selected parameters (e.g. bias voltage, trigger delays) to allow optimized usage of valuable beam time. An exemplary

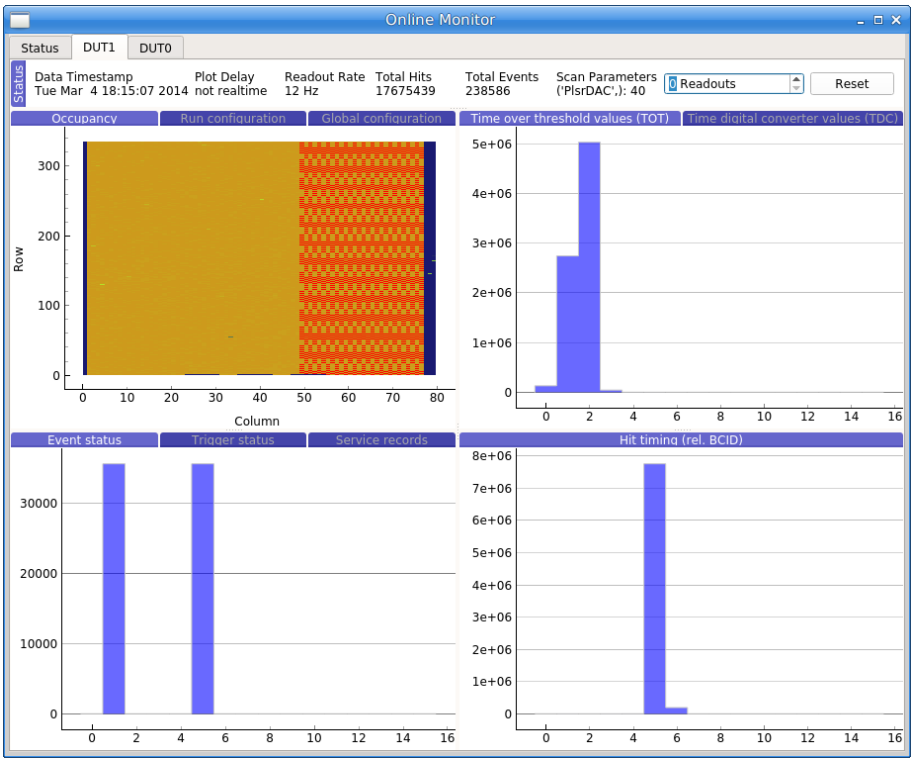


Figure 4.1: Graphical user interface of the online-monitor with ATLAS FE-I4 plugin. Real-time plotting of data from a threshold scan is depicted. *Top:* Readout system information, like actual scan parameter and readout frequency. *Bottom:* Four active plot windows show a 2D hit histogram (*top, left*), the recorded charge spectrum (*top, right*), a data quality histogram (*bottom, left*), and a hit time-stamps histogram with 25 ns bins (*bottom, right*).

output of the online monitor showing the data of an ATLAS-FE I4 is depicted in Figure 4.1. Simplicity of *TBA* is archived by choosing a modern, interpreted programming language (Python) with its well documented and tested scientific modules for data analysis (*SciPy* [JOP+01]). Complex relationships between software parts, a usual property of object-oriented frameworks, are deliberately omitted. TBA follows the procedural programming paradigm to map the sequential analysis steps onto multiple independent functions. This enables a user to understand an analysis step without reconstructing a complex context. The sequence of a full test-beam analysis is sketched in the following. Each function only requires the data output of the preceding function and the definition of the analysis parameters. Performance plots are created for each analysis step and a selection is depicted here. The steps are:

1. Hit table: Convert device specific data to the TBA hit data-format (table in HDF5-file [Grob]) containing: event number, hit position and charge.

2. Noisy pixel: Identify noisy pixels by comparing the occupancy of every pixel to its neighbors. A mask for noisy pixels is created.

3. Clustering: Combine hits of an event to cluster using the center-of-gravity algorithm. Do not create cluster containing noisy hits only.

4. Correlations: Correlate the cluster positions of all devices to the first device on event basis. Figure 4.2 shows the correlation histogram for the column direction of one plane.

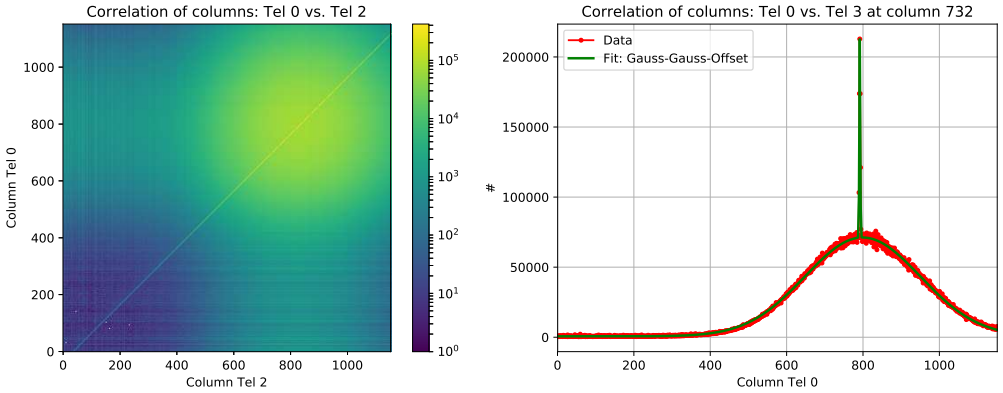


Figure 4.2: *Left:* Correlation histogram of the column position of a telescope plane against the column position another plane. *Right:* Fit of one slice of the correlation histogram to deduce the peak. From a linear fit of all peaks a pre-aligment is deduced. Plots created by *TBA*.

5. Pre-alignment: Deduce a linear function to describe the translation and rotation of the planes to the first plane by fitting the correlations. A fit of a slice of the correlation histogram is depicted in Figure 4.2 (*right*). Depending on the number of tracks per event the uncorrelated cluster positions follow the beam profile and are described by a Gaussian fit with offset.

6. Tracklets: Create tracklets by merging the cluster tables of each device on event basis into one table. Cluster positions are translated into a global coordinate system using the pre-alignment information.

7. Track finding: Find tracks by sorting the hit table in-place to the closest distance on event basis. This algorithm assumes perpendicular tracks on the planes which was the case for all measurements. The resulting table contains *track candidates*.

8. Alignment: Deduce a rotation and translation matrix for each plane from residuals, to create a global coordinate system. The residuals are created from linear track fits (see consecutive steps), but only on a subset of the track candidates to increase analysis speed.

9. Track fitting: Fit tracks with a $\chi^2$-minimization and create a track quality information per track, consisting of the number of clusters and the $\chi^2$ value. The available Kalman-filter track fitting [Die17, p. 51] is not used, since multiple scattering for the high energetic particle beam (120 GeV/c, Section 6.4.1) is negligible.

10. Track based analysis: Use the reconstructed tracks to deduce detector- and measurement characteristics. For example, localized charge-collection efficiency, hit detection efficiency and track resolution. The hit-efficiency measurement with a passive CMOS sensor is discussed in Section 6.5. The track resolution can be estimated from residuals. Residuals depict the difference between intersections of reconstructed tracks with the DUT plane and reconstructed DUT hit positions. They are a function of the pointing resolution of the telescope ($\sigma_{\text{pointing}}$), the track reconstruction capability of the software, the hit reconstruction algorithm, and the hit resolution of the pixel detector [Jan+16, p. 11]. Assuming a negligible contribution of the reconstruction software the measured residuals follow:

$$\sigma^2_{\text{residual}} = \sigma^2_{\text{hit}} + \sigma^2_{\text{pointing}}$$

Figure 4.3 shows the residuals measured on a Mimosa26 plane (Section 6.4.1) with 120 GeV pions after successful alignment. No offset is measured and the width of the Gaussian is below the binary hit resolution of one pixel ($18.4\,\mu\text{m}/\sqrt{12} = 5.3\,\mu\text{m}$) due to charge sharing. This result demonstrates a well working track reconstruction with TBA. The right plot shows the residuals of an ATLAS FE-I4 pixel in the short dimension (50 µm). The residuals are mainly given by the pixel pitch and thus the hit resolution of the detector. A large background can be seen due to many tracks reconstructed with the Mimosa26 planes (see Section 6.4.1) that are not correctly matched to this plane's hits. A detailed discussion about track matching of device with different integration times can be found in [Die17, p. 30].

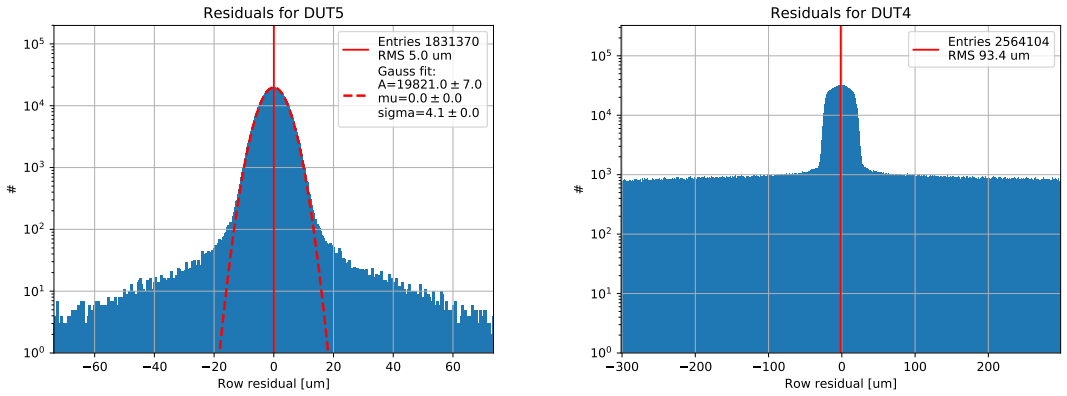


Figure 4.3: Residuals of tracks with a Mimosa26 plane (*left*) and an ATLAS FE-I4 plane (*right*). *Right:* the background larger than the pixel pitch of 50 µm arises from tracks that are associated to the wrong hit.

## 4.2 Hit efficiency-determination

The hit efficiency of a pixel detector is the probability to detect a charged particle track that traverses the sensitive detector volume. The efficiency is an important quantity for pixel detectors, since it defines the likelihood of correct track reconstruction from space points that are provided by multiple detector layers. For the pixel detector of the ATLAS experiment, an in-time hit efficiency of more than 97% at the end of life is required. The in-time efficiency is calculated from the number of detected hits with correctly assigned time stamps. These time stamps are multiples of 25 ns which is the bunch crossing frequency (40 MHz) of the LHC particle beam under nominal conditions. The time stamps are mandatory to assign hits to correct events. The determination of in-time efficiency can be separated into an efficiency measurement with a particle beam during a test-beam and a time-walk measurement relating the time of particle hit with the time of detection (Section 6.6). During test-beam the determination of the in-time efficiency is not straightforward, since the readout chip clock runs asynchronously with respect to the particle frequency. This is in contrast to the operation in the ATLAS detector where readout clocks are carefully synchronized to the constant bunch crossing frequency of the particle beam [Var00, p. 8]. The average hit efficiency is determined as the ratio of tracks seen by the sensitive sensor detector volume divided by the total number of tracks through the same volume. This ratio is calculated for each event individually. The errors in the efficiency determination are of statistical and systematic nature and are discussed in the following.

### 4.2.1 Statistical error

The probability to detect $k$ hits from $N$ tracks with true hit efficiency $\epsilon$ is given by the binomial distribution [Cas12, p. 2]:

$$P(k|\epsilon, N) = \frac{N!}{k!(N-k)!}\epsilon^k(1-\epsilon)^{N-k} \tag{4.1}$$

In order to construct the PDF of an estimator for the efficiency $\epsilon' = \frac{k}{N}$, given a measurement of $k$ hits out of $N$ tracks, Equation (4.1) can be inverted using Bayes' Theorem [Pat04, p. 4]:

$$P(\epsilon'|k, N) = \frac{\Gamma(N+2)}{\Gamma(k+1)\Gamma(N-k+1)}\epsilon'^k(1-\epsilon')^{N-k} \tag{4.2}$$

with the a priori assumption of a uniform efficiency $\epsilon \in [0, 1]$ and the gamma function $\Gamma(z) = \int_0^\infty x^{z-1}e^{-x}\,dx$. Equation (4.2) has its maximum at $\epsilon' = \frac{k}{N}$ and allows the estimation of confidence intervals. The common 1-$\sigma$ confidence interval $[\epsilon_-^{1\sigma}, \epsilon_+^{1\sigma}]$ is calculated as the shortest range where the integral of Equation (4.2) includes 68.3%:

$$\int_{\epsilon_-^{1\sigma}}^{\epsilon_+^{1\sigma}} P(\epsilon'|k, N)\,d\epsilon' = 0.683 \text{ with } |\epsilon_-^{1\sigma} - \epsilon_+^{1\sigma}| \stackrel{!}{=} \min \tag{4.3}$$

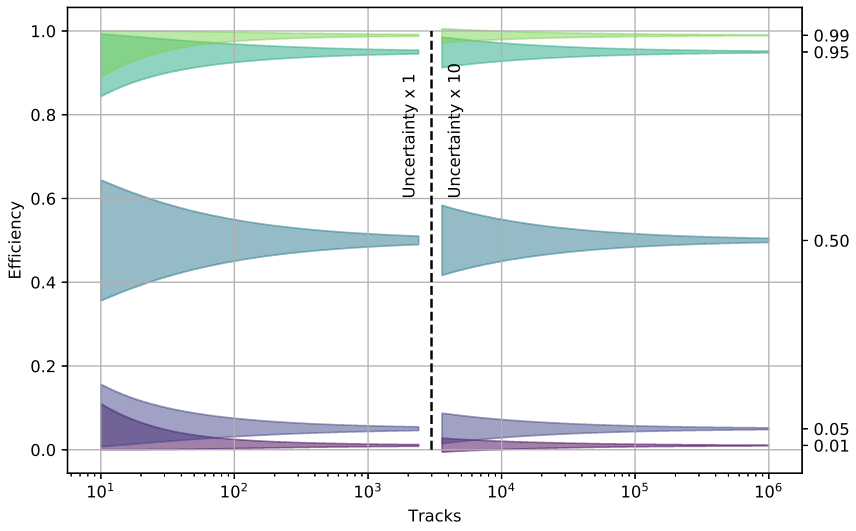


Figure 4.4: Statistical uncertainty of efficiency measurement for different sample sizes (*Tracks*). Areas give the $\pm 1$-$\sigma$ confidence interval (68.3%) for 5 curves depicting an efficiency of $1\%, 5\%, 50\%, 95\%$, and $99\%$. Errors are magnified by a factor of 10 at larger sample sizes for better presentation.

Figure 4.4 visualizes this interval for different numbers of total tracks and multiple efficiencies. The interval boundaries do not exceed the efficiency boundaries and decrease to values below 0.3 % for more than $1 \times 10^4$ tracks and an efficiency above 95 %. In one run it is common to record at least 1 million primary particles to simplify detector alignment. Assuming realistic values for the sensitive area of the detector under test (5 mm$^2$), a Gaussian beam spread of 5 mm, and a (pessimistic) low track reconstruction efficiency of 20 % leaves still more than $1 \times 10^5$ tracks for efficiency calculation. Confidence intervals for different sample sizes are summarized in Table 4.1 and are below 1 ‰ assuming more than $1 \times 10^5$ reconstructed tracks and usual efficiencies above 95 %. Consequently, the statistical error is often negligible and the error for the measured hit efficiency is mainly defined by systematic errors.

| **Tracks** | $10^2$ | $10^3$ | $10^4$ | $10^5$ |
|---|---|---|---|---|
| **Efficiency with uncertainty** | $50.00^{+4.95}_{-4.95}$ | $50.00^{+1.58}_{-1.58}$ | $50.00^{+0.50}_{-0.50}$ | $50.00^{+0.16}_{-0.16}$ |
| | $95.00^{+1.90}_{-2.50}$ | $95.00^{+0.66}_{-0.72}$ | $95.00^{+0.22}_{-0.22}$ | $95.00^{+0.07}_{-0.07}$ |
| | $98.00^{+1.12}_{-1.80}$ | $98.00^{+0.41}_{-0.48}$ | $98.00^{+0.14}_{-0.14}$ | $98.00^{+0.04}_{-0.04}$ |
| | $99.00^{+0.73}_{-1.47}$ | $99.00^{+0.28}_{-0.35}$ | $99.00^{+0.10}_{-0.10}$ | $99.00^{+0.03}_{-0.03}$ |
| | $99.90^{+0.10}_{-1.15}$ | $99.90^{+0.07}_{-0.15}$ | $99.90^{+0.03}_{-0.04}$ | $99.90^{+0.01}_{-0.01}$ |

Table 4.1: Statistical uncertainty of efficiency estimation for different quantities of reconstructed tracks and multiple efficiencies. Given as 68.3% confidence interval.

### 4.2.2 Systematic errors

The estimation of systematic errors for the DUT efficiency measured in a telescope setup is complex. Multiple effects can artificially increase and decrease the *measured* hits ($k_{\text{meas}}$) and the number of reconstructed tracks ($N_{\text{rec}}$) that are not related to the DUT efficiency ($\epsilon_{\text{dut}} = \frac{k}{N}$). The quantification of these errors is a major part of a test-beam analysis and involves many verification measurements and validation analyses. Additionally, cuts to data are applied during a test-beam analysis to minimize systematic effects and effectively increasing the data purity at the expense of the total number of tracks reconstructed. This is feasible since statistics is usually high enough (Section 4.2.1). The systematic effects changing the determined efficiency $\epsilon = \frac{k_{\text{meas}}}{N_{\text{rec}}}$ can be summarized into four categories as listed below. Special emphasis is put on the two categories that lead to a systematic overestimation of efficiency and analytical formulas are provided to quantify the overestimation.

1. **Increase $N_{\text{rec}}$:** The number of reconstructed tracks can be overestimated when fake tracks are build, leading to an underestimation of the DUT efficiency. The reasons for fake tracks are multifold:
   - Reconstructing multiple tracks from a few space points, provided by the telescope planes, is a combinatorical problem that can lead to the reconstruction of fake tracks. Since track densities are usually relatively low in a test-beam and the track angles are constant, this issue is negligible. Additionally, analysis cuts on the number of tracks per event, the minimum distance between hit-clusters to avoid track merging, and the track quality given by the $\chi^2$ of the track fit can effectively prevent fake tracks.
   - Fake tracks can be build from noise hits of telescope detector planes. Noise hits are identified and removed in the analysis by comparing pixel occupancies to their neighboring pixels. The probability of fake tracks can be largely reduced when many telescope planes are used and track building requires that most planes detect the track.
   - A low likelihood of assigning the tracks to the correct in-time DUT hit, can lead to additional tracks. This quantity is most challenging to optimize, especially when the telescope and DUT have distinct readout- and dead-times. The analysis cuts mentioned above are of no use, when timings between telescope and DUT are different. A common assessment of the time synchronization between telescope and DUT is the investigation of their position-correlation. The position-correlation is for example measured by the distance between track intersections and DUT hit-cluster (*residuals*, see Figure 4.3) and the position correlation between hit-clusters from DUT and telescope planes (*correlations*, see Figure 4.2). A way to avoid error-prone offline correlation the trigger veto time is to set to the dead-time of the slowest device in the measurement.
2. **Decrease $N_{\text{rec}}$:** The number of reconstructed tracks is reduced by the hit-detection efficiency of the telescope planes and the track building efficiency of the test beam analysis software. A reduction of the number of reconstructed tracks artificially *increases* the determined efficiency $\epsilon$, when in the same events hits of not reconstructed tracks are associated to other

track hits that are not detected by the DUT. The resulting efficiency can be expressed as a function of the number of reconstructed tracks per event $N_{\text{rec}}$:

$$\epsilon = \epsilon_{\text{dut}} + (1 - \epsilon_{\text{dut}}) \cdot P_{\text{sth}} \cdot P_{\text{rec.}}(N_{\text{rec}}) \cdot \frac{N_{\text{rec}}}{N_{\text{rec,tot}}}$$

with the track detection efficiency of the DUT $\epsilon_{\text{dut}}$ and the probability of detecting a substituting hit $P_{\text{sth}}$ from tracks that are not reconstructed. $P_{\text{rec.}}(N_{\text{rec}})$ is the probability to reconstruct exactly $N_{\text{rec}}$ tracks in the event and the last factor normalizes the overestimation of efficiency to the total number of reconstructed tracks.

The probability that a substituting hit is used for a track is given by the DUT efficiency itself and the probability $P_{\text{assoc}}$ that the hit is wrongly associated to the track. For the simple case that only one track is not reconstructed holds:

$$P_{\text{sth}} = \epsilon_{\text{dut}} P_{\text{assoc}}$$

When more than one track are not reconstructed follows:

$$\begin{aligned} P_{\text{sth}} &= \sum_{i=1}^{N_{\text{not rec}}} \binom{i}{N_{\text{not rec}}} (\epsilon_{\text{dut}} P_{\text{assoc}})^{N_{\text{not rec}}} (1 - \epsilon_{\text{dut}} P_{\text{assoc}})^{i - N_{\text{not rec}}} \\ &= 1 - (1 - \epsilon_{\text{dut}} P_{\text{assoc}})^{N_{\text{not rec}}} \\ &= 1 - (1 - \epsilon_{\text{dut}} P_{\text{assoc}})^{N - N_{\text{rec}}} \end{aligned}$$

Finally, the measured efficiency given $N_{\text{rec}}$ reconstructed tracks per event is:

$$\epsilon = \epsilon_{\text{dut}} + (1 - \epsilon_{\text{dut}}) \cdot \left(1 - (1 - \epsilon_{\text{dut}} P_{\text{assoc}})^{N - N_{\text{rec}}}\right) \cdot P_{\text{rec.}}(N_{\text{rec}}) \cdot \frac{N_{\text{rec}}}{N_{\text{rec,tot}}} \tag{4.4}$$

Several features can be seen when inspecting this result:

- Not reconstructed tracks always lead to an overestimation of the efficiency, except for the limiting cases of a fully efficient ($\epsilon_{\text{dut}} = 1$) or fully inefficient ($\epsilon_{\text{dut}} = 0$) device. For very high efficient devices ($\epsilon_{\text{dut}} \to 1$), the overestimation of efficiency from not reconstructed tracks is largely reduced.

- Reducing the number of tracks per event $N$ and consequently the number of not reconstructed tracks ($N_{\text{not rec}} = N - N_{\text{rec}} \to 0$) reduces the overestimation of efficiency. Unfortunately, the number of tracks is mainly an accelerator property and therefore rarely under control of the experimenter. But unfavorable beam conditions that produce coincident secondary particles, like a particle beam hitting the beam pipe, should be avoided.

- Decreasing the probability of having not reconstructed tracks reduces the overestimation of efficiency. In the optimal case, that all tracks are reconstructed the systematic

efficiency overestimation vanishes:

$$P_{\text{rec.}} = \begin{cases} 1 & \text{if } N_{\text{rec}} = N \\ 0 & \text{otherwise} \end{cases}$$

- Decreasing the probability of associating a hit of a not reconstructed track to another track ($P_{\text{assoc}}$) reduces the overestimation of efficiency.

The last two points are in control of the experimenter and can be optimized by proper choices for the experimental setup and analysis cuts. The probability $P_{\text{rec.}}(N_{\text{rec}} = 1)$ that a single track is reconstructed from telescope hits can be calculated from the efficiency of the telescope planes $\epsilon_{\text{plane}}$, the number of telescope planes $N_{\text{tel}}$, and the minimum number of hits $N_{\text{hit}}$ required in the analysis for track reconstruction:

$$P_{\text{rec.}}(N_{\text{rec}} = 1) = P_{\text{sof}} \cdot \sum_{k=N_{\text{hit}}}^{N_{\text{tel}}} B(k; N_{\text{tel}}, \epsilon_{\text{tel}}) = P_{\text{sof}} \cdot \sum_{k=N_{\text{hit}}}^{N_{\text{tel}}} \binom{N_{\text{tel}}}{k} \epsilon_{\text{plane}}^{k} (1 - \epsilon_{\text{plane}})^{N_{\text{tel}}-k}$$

with $B$ denoting the Binomial distribution:

$$\mathrm{B}(k; n, p) = \binom{n}{k} p^k (1-p)^{n-k}$$

and $P_{\text{sof}}$ the track reconstruction efficiency of the analysis software, that is considered independent of the number of tracks here. $P_{\text{sof}}$ is with common beam conditions (perpendicular tracks and low beam intensities) usually close to 1. For telescope setups with many and not fully efficient planes, it is beneficial to not require a hit in all planes during track reconstruction to reduce the number of not reconstructed tracks. For example a Mimosa26 telescope consists of $N_{\text{tel}} = 6$ planes and is usually operated with an efficiency of about $\epsilon_{\text{tel}} = 98\%$ [Die17, p. 50][Jan+16, p. 15]. Requiring a hit in all planes leads to 11% not reconstructed tracks, while less than 1% of the tracks are not reconstructed when requiring only 5 planes detecting the track.
The probability to reconstruct $N_{\text{rec}}$ out of $N$ tracks can be calculated from the single track reconstruction probability $P_{\text{rec.}}$ using again the Binomial distribution $B$:

$$P_{\text{rec.}}(N_{\text{rec}}) = B(N_{\text{rec}}, N, P_{\text{rec.}}) \tag{4.5}$$

The association probability $P_{\text{assoc}}$ between a track and a hit depends on the *association distance* $d$ applied during test beam analysis. Only hits with a distance smaller than the association distance are associated to the track. Since the track pointing and hit position resolutions are finite, an association distance larger 0 has to be chosen. But a too large association distance increases the probability $P_{\text{assoc}}$ of assigning wrong tracks to a hit. Therefore, the association distance must be carefully optimized with respect to beam, DUT, and telescope properties. When multiple scattering can be neglected and the telescope pointing

resolution is much smaller than the DUT pixel pitch, a common ansatz is to set the association distance to the (binary) hit resolution of the DUT. A maximum estimate for $P_{\text{assoc}}$ can be derived assuming a uniform, square beam of size $D$ with $d <= D$:

$$P_{\text{assoc}} = 1 - (1 - P_{\text{merge}})^{N_{\text{rec}}-1} \tag{4.6}$$

where $P_{\text{merge}}$ is the probability that two tracks are within the distance $d$:

$$P_{\text{merge}} = \left(1 - \left(1 - \frac{d}{D}\right)^2\right)^2 \tag{4.7}$$

Evidently the probability that a track is assigned to a wrong hit increases with the number of tracks $N_{\text{rec}}$ and the ratio of the association distance over the beam spread $\frac{d}{D}$.
The systematic overestimation of efficiency $\Delta\epsilon = \epsilon - \epsilon_{\text{dut}}$ due to not reconstructed tracks can be estimated from Equation (4.4) by summing over all numbers of reconstructed tracks:

$$\boxed{\Delta\epsilon = \sum_{N_{\text{rec}}=1}^{N-1} (1 - \epsilon_{\text{dut}}) \cdot \left(1 - (1 - \epsilon_{\text{dut}} P_{\text{assoc}})^{N - N_{\text{rec}}}\right) \frac{P_{\text{rec.}}(N_{\text{rec}}) N_{\text{rec}}}{N_{\text{rec,tot}}}} \tag{4.8}$$

with the expected number of reconstructed tracks per event:

$$N_{\text{rec,tot}} = P_{\text{rec.}}(N_{\text{rec}} = 1) \cdot N$$

Figure 4.5 shows the systematic overestimation of efficiency $\Delta\epsilon$ using Equation (4.8). The points with error bars depict exact values as reference from an independent Monte-Carlo-Simulation. A uniform, square beam is assumed and a telescope setup consisting of 6 planes with a plane efficiency of $\epsilon_{\text{plane}} = 98\,\%$. If not stated differently in the legend 2 tracks per event are used ($N = 2$), reconstructed tracks are assigned to any hit ($d = D \Rightarrow P_{\text{assoc}} = 1$), 6 hits are required for track reconstruction ($N_{\text{hit}} = 6$), and the track reconstruction efficiency of the software is set to 1. Figure 4.5 shows good agreement between the calculation and simulation for 2 track events over the whole efficiency range and a good description by Equation (4.8) for many track events and a DUT efficiency above 90 %. Even with this properly chosen setup consisting of high efficient telescope planes the overestimation of efficiency easily reaches a few percent. This makes the verification that a DUT efficiency of 97 % is reached, as required for the ATLAS pixel detector, challenging and illustrates the importance of proper analysis cuts. Cuts are applied in bottom two plot of Figure 4.5 leading to a reduction of the efficiency overestimation to less than a percent when only 5 telescope plane hits are required for track reconstruction (*left*) or the association distance is set to 10% of the beam width (*right*). When both cuts are used, the efficiency overestimation is always below 0.3 ‰.

3. **Increase $k_{\text{rec}}$:** The number of measured DUT hits can be increased by noise hits in the

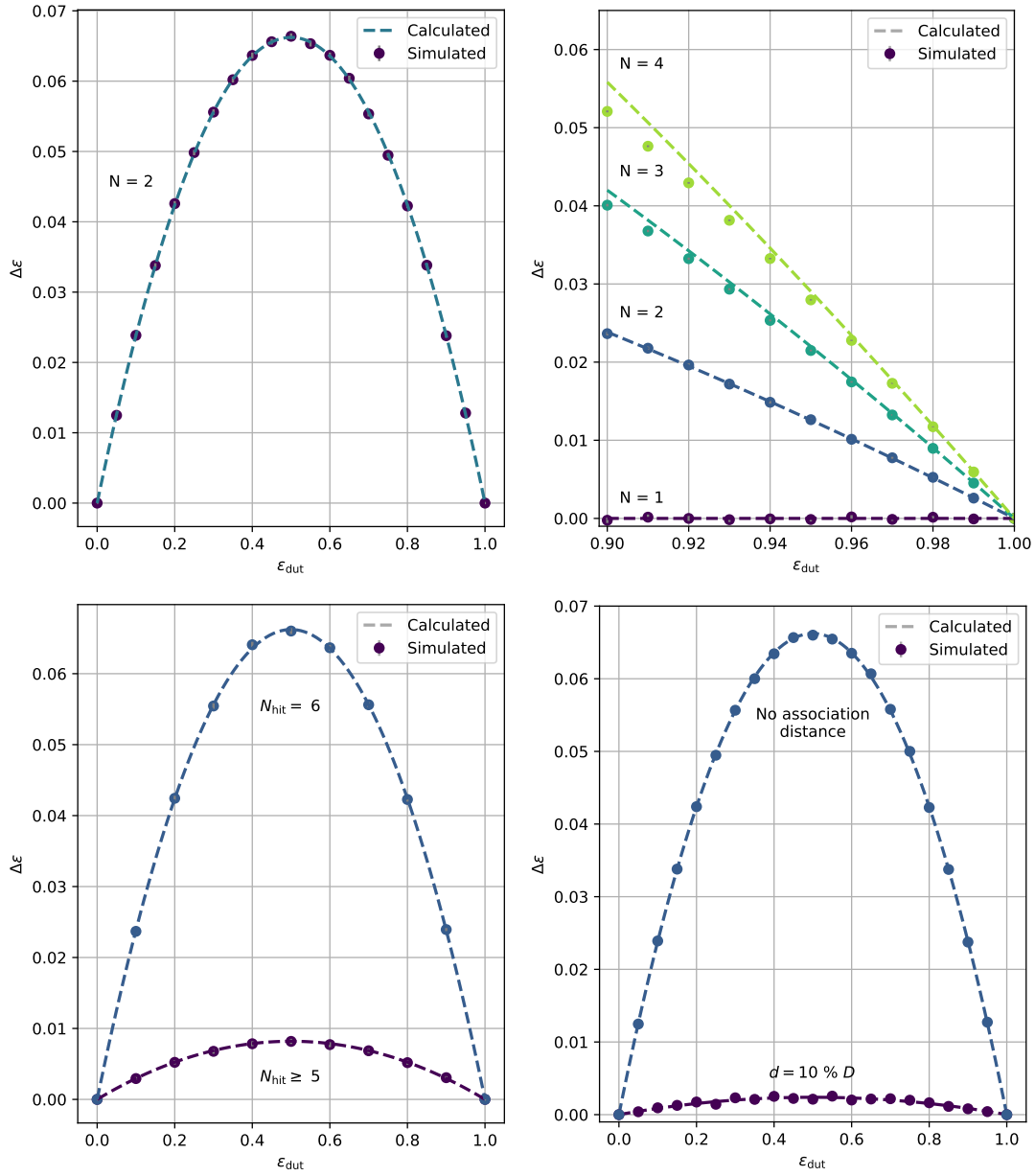


Figure 4.5: Systematic overestimation of the efficiency $\Delta\epsilon$ due to not reconstructed tracks as a function of the DUT efficiency $\epsilon_{\text{dut}}$. Lines are calculations using Equation (4.8) and points with error bars are corresponding values from simulation. Parameters are stated in text. *Top left:* Assuming 2 tracks per event. *Top right:* Assuming 1 to 4 tracks per event. *Bottom left:* Efficiency overestimation when requiring that all 6 telescope planes detect a hit for track reconstruction ($N_{\text{hit}} = 6$) or at least 5 telescope planes ($N_{\text{hit}} \geq 5$). *Bottom right:* Efficiency overestimation when using no association distance ($P_{\text{assoc}} = 1$) and when requiring that the hit to track distance $d$ is smaller than 10% of the beam width $D$, assuming a uniform, square beam.

DUT. This leads to an overestimation of efficiency, when a noise hits is assigned to a track whose hit is not detected by the DUT. In analogy to the derivation of Equation (4.8) follows for the systematic overestimation of efficiency:

$$\Delta\epsilon = (1 - \epsilon_{\text{dut}}) \cdot P_{\text{noise}} \tag{4.9}$$

$P_{\text{noise}}$ is the probability that a noise hit exists and is within association distance. It is assumed that the noise hit probability is independent of the DUT efficiency. For multi-track events no simple analytical formula could be found for $P_{\text{noise}}$ and the description becomes complex. A good maximum estimate is to assume only one track events:

$$P_{\text{noise}} = \sum_{i=1}^{N_{\text{pixel}}} B(i, n = N_{\text{pixel}}, p = P_{\text{occ}}) \cdot (1 - (1 - P_{\text{assoc}})^i) \tag{4.10}$$

The first factor is the Binomial distribution describing the probability of having $i$ noise hits in a DUT, that consists of $N_{\text{pixel}}$ pixels, while each pixel has the probability of $P_{\text{occ}}$ to create a noise hit in an event. This quantity is often referred to as *noise occupancy*. For the ATLAS pixel detector the noise occupancy is below $10^{-5}$, which translates to the detection of one noise hit per pixel when reading out 10000 events. The second factor in Equation (4.10) depicts the association probability of a track to any noise hit when having $i$ noise hits. An estimate of $P_{\text{assoc}}$ can be found using Equation (4.6) with $N_{\text{rec}} = 2$, describing a uniform, square beam profile with spread $D$ and an association distance of $d$:

$$P_{\text{assoc}} = \left(1 - \left(1 - \frac{d}{D}\right)^2\right)^2 \tag{4.11}$$

Several features can be identified in Equation (4.9) and Equation (4.10):

- In the existence of noise hits the measured efficiency is always systematically increased, except for the limiting case of a fully efficient device ($\epsilon_{\text{dut}} = 1$).
- Decreasing the noise hit probability ($P_{\text{occ}}$) decreases the efficiency overestimation. This can be done by an appropriate tuning of the device before measuring and by removing noise hits in the analysis.
- Decreasing the track to noise-hit association probability ($P_{\text{assoc}}$) decreases the efficiency overestimation. The parameter to optimize is the *association distance* $d$ (see Equation (4.11)).

Figure 4.6 depicts the systematic overestimation of efficiency due to noise hits for different noise occupancies and association distances assuming a pixel detector with 26880 pixels. The lines are calculated using Equation (4.9) and the point are reference values from a Monte-Carlo-Simulation. Even with a moderate noise occupancy of $10^{-4}$ the efficiency is heavily overestimated reaching a measured efficiency of above 90 % independent of the actual DUT efficiency. This shows that the noise occupancy must be checked for during data taking and

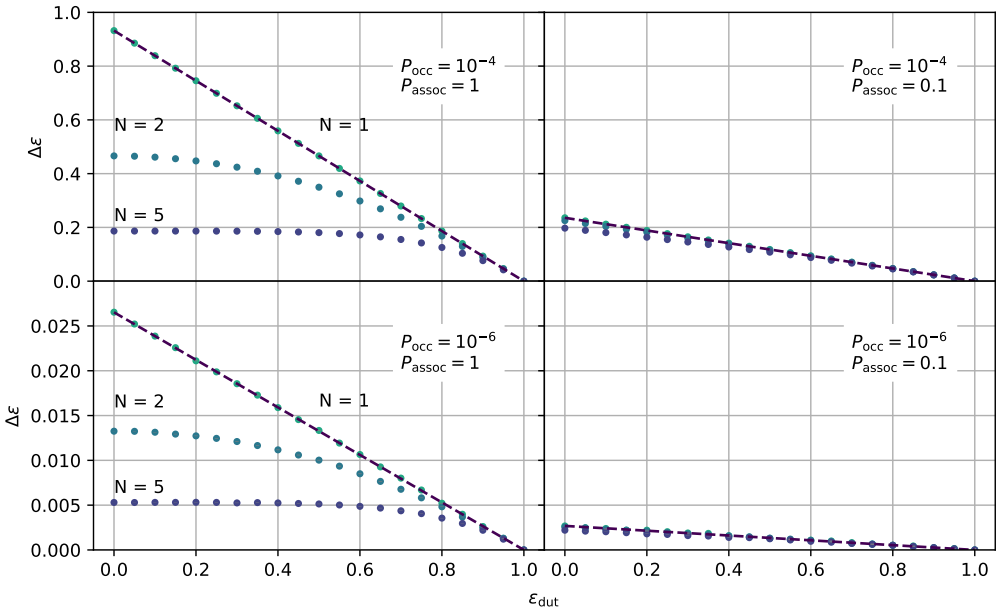


Figure 4.6: Systematic overestimation of the efficiency $\Delta\epsilon$ due to noise hits as a function of the DUT efficiency $\epsilon_{\text{dut}}$. The four plots depict curves for different values for the association probability $P_{\text{assoc}}$ and noise occupancy $P_{\text{occ}}$ assuming a pixel detector with 26880 pixels. Different *line colors* depict simulations for 1, 2, and 3 track events. The dotted lines are calculations for 1 track events using Equation (4.9).

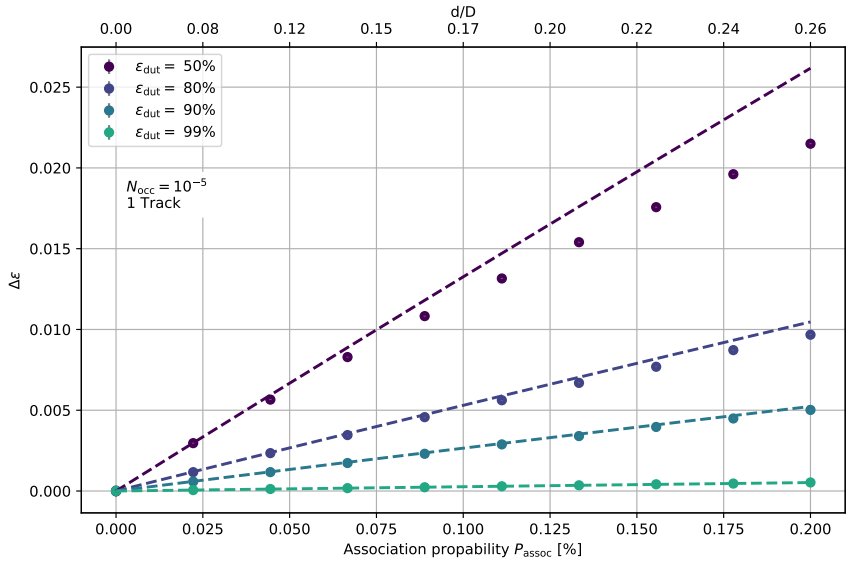


Figure 4.7: Overestimation of the efficiency $\Delta\epsilon$ due to noise hits as a function of the association probability. Multiple DUT efficiencies shown. The second x-axis shows the association distance to beam width ration, assuming a uniform and squared beam profile.

analysis and that a properly chosen association distance is mandatory. Already a reduction of the association probability to 10 % largely reduces the efficiency overestimation (Figure 4.6 *right*). The strong influence of association probability is depicted in Figure 4.7.

4. **Decrease $k_{\mathrm{rec}}$:** A reduction of measured DUT hits unrelated to the DUT efficiency is unlikely. The most common reason are large and undetected scattering angles of the particle track in a manner that the sensitive DUT part is not hit. Especially, at sensor edges and for large multiple scattering due to high material budged this effect can be observed. Solutions are better track fitting models that account for multiple scattering [PIM95; Kle12], an optimization of telescope planes positions [AFZ07], and the estimation of the mean efficiency from center pixels only.

# 5 Charge-collection efficiency of 3D- and planar sensors

This chapter compares the charge-collection efficiency of highly irradiated 3D- and planar silicon pixel-sensors. The Charge-collection efficiency after irradiation is a crucial parameter to assess the usability of a pixel sensor for high-energy physics. For this purpose, pixel detectors of the IBL project (Section 2.3.1) are irradiated with protons up to a fluence of $7 \times 10^{15}\,\mathrm{n_{eq}\,cm^{-2}}$ and examined at various sensor bias-voltages up to 1500 V (Section 5.4.2). The methods for charge measurements in Chapter 3 are used. Deficiencies in the charge measurement of the ATLAS FE-I4 are specifically addressed, as they not only impact the measurements presented here, but also the operation of the IBL in the ALTAS experiment (Section 5.3.3).

A minimal 2-parameter model is used to describe the measurements with a new simulation, that was developed for this study (Section 5.1). The simulation allows to investigate the influence of the depletion zone and the charge-carrier trapping on charge collection separately. Furthermore, it allows for the validation of the trapping model, as introduced in Section 2.2, at high fluences and complex field geometries of 3D-sensors (Section 5.4.4).

## 5.1 Simulation with Scarce

*Scarce* stands for **S**ilicon **C**h**ar**ge **C**ollection **E**fficiency and is a Python based software package to simulate the charge collection in irradiated silicon sensors with planar and 3D-electrode geometry. Simple analytical models exist to describe the Charge-Collection Efficiency (CCE) as a function of the drift distance (planar: [Tsu12, p. 55], 3D: [Da +08, p. 247]). Since full-depletion and saturated drift velocity of charge carriers are assumed, these models fall short of describing the dependence on bias voltage. For 3D-electrode geometries, in contrast to planar geometry (Equation (2.39)), no sufficient analytical solutions for the drift- and weighting-field are available, requiring a numerical solver for their calculation [Pie+07, p. 634]. Usually, a TCAD software is used to calculate the drift field and to simulate important sensor parameters like leakage current, capacitance, and CCE after irradiation. TCAD software packages also provide many adjustable models to describe effects like defect annealing, charge-carrier mobility, impact ionization, band-to-band tunneling etc. Great effort have been made within the RD 50 collaboration [RD5] and other groups to develop and tweak semi-empiric models for the description of relevant sensor parameters after high levels of irradiation, as described in Section 2.2. Numerous TCAD models exists (*Perugia* [Pet+06], *Proton* [Ebe13, p. 142], *Delhi* [Dal14]), each optimized for certain devices and specific parameters

like bulk material, particle type, and particle energy during irradiation. Consequently, these models lack generality. Additionally, they are only valid for the TCAD software they were developed for. A disadvantage of TCAD simulations is their demand of computational time making them unsuitable for multi-parameter optimizations and multi-electrode systems. Hence, the simulation domain is often restricted to one pixel or a part of one pixel.

*Scarce* is capable of fast simulations of planar and 3D pixel matrices. It is similar to existing open-source packages such as *Weightfield2* [Cen+15], *TRACS* [DC16], *Allpix2* [Spa+18], and *KDetSim* [KDe16], that either do not support 3D pixels or pixel matrices, were not available, have no irradiation model, or do not provide CCE information[1]. *Scarce* follows an as-simple-as-possible ansatz by reduction of the simulation to a 2D projection, neglecting charge-carrier repulsion, simplifying the detector response simulation, and using only 2 input parameters: the effective, homogeneous doping concentration and the trapping probability. Despite these simplifications, the measured charge-collection efficiency can be described as a function of the bias voltage (Section 5.4) with reasonable values for the two input parameters. The important parts of a *Scarce* simulation are introduced in the following.

### 5.1.1 Potentials and fields

Drift and weighting potentials are calculated by solving the 2 dimensional Laplace and Poisson equations (Equation (2.47), Equation (2.30)) on a discrete mesh.

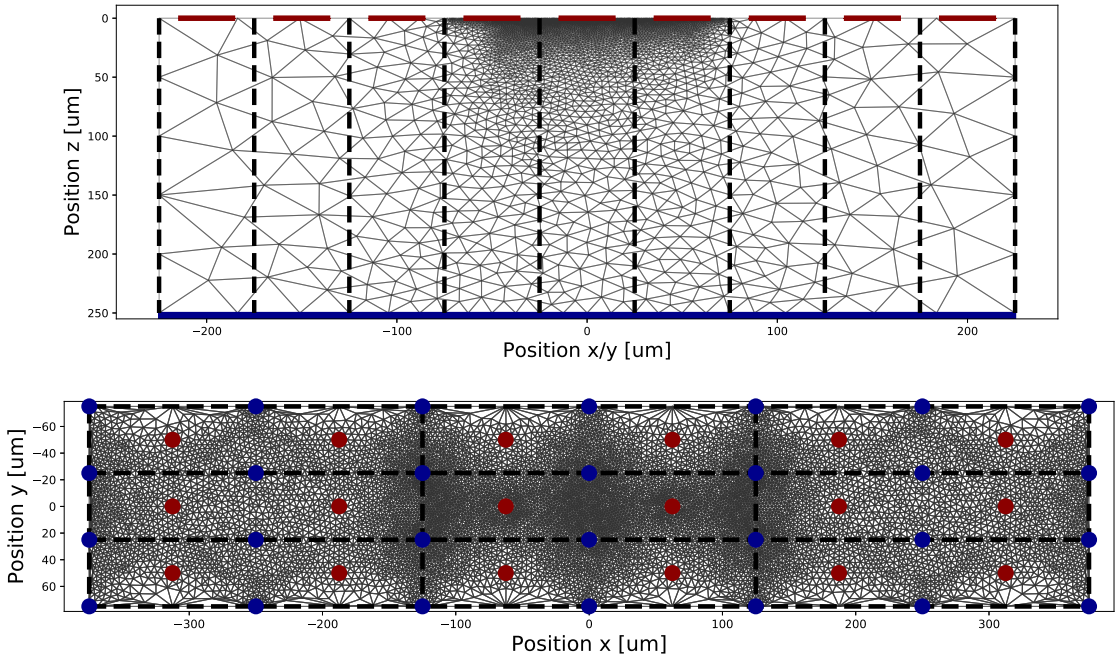


Figure 5.1: Simulation domain for planar (top) and 3D (bottom) pixel matrices with ALTAS IBL geometry. Mesh points reduced by one order of magnitude for better illustration.

[1] Partial package comparison in [Car+].

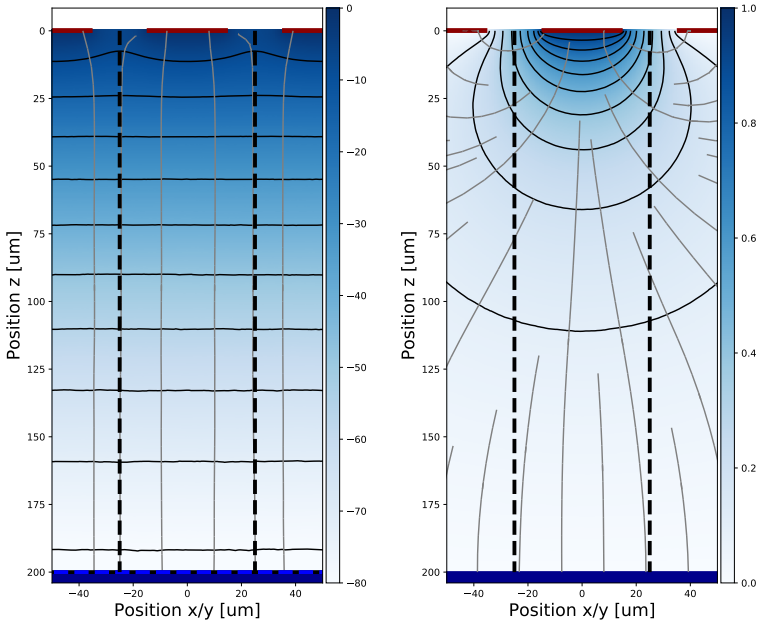


(a) Planar drift field (b) Planar weighting field

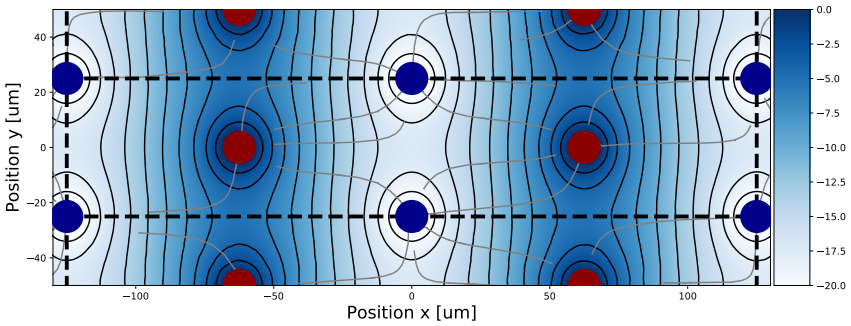


(c) 3D drift field

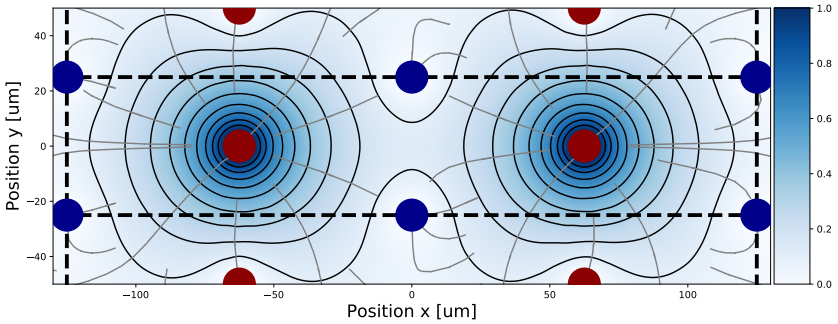


(d) 3D weighting field

Figure 5.2: Drift- and weighting field of a pixel within a pixel matrix. ATLAS IBL planar and 3D-silicon pixels are shown (*top/bottom*) with pixel boundaries (*dotted black line*), potentials in volt (*color gradient*), equipotential lines (*black*), and field lines (*gray*).

Boundary conditions are given by voltages at readout and bias electrodes and no boundary conditions are defined at simulated pixel-sides. Due to the symmetry from repeating bias and readout electrodes, it is possible to set boundary conditions for the drift field at pixel sides. However, for the weighting field such a symmetry does not exist. Therefore, additional pixels surrounding the simulated center pixel are defined. The minimum number of neighboring pixels is determined in a way that additional neighboring pixels do not change the calculated potentials at the center pixel. For the simulation of one ATLAS IBL 3D and planar pixel 8 neighboring pixels are sufficient. Figure 5.1 depicts the simulation domain used in *Scarce*. The mesh is generated by a mesh generator program (*gmsh* [GR09]) with increasing density at expected high-field gradients and at the center pixel to maximize accuracy. The resulting linear equation system is solved with a finite volume PDE solver (*fipy* [GWW09]). The fields are calculated from the negative gradient of the potential after smoothing with a bivariante cubic spline. The gradient is computed by central-difference approximation for interior mesh points and backward and forward central difference approximation at mesh boundaries. Figure 5.2 depicts calculated drift- and weighting potentials and fields in a planar and 3D pixel sensor matrix with ATLAS IBL geometry. The necessity of surrounding pixels for proper boundaries can be seen for the weighting potentials and fields that extend far into adjoining pixels. When the sensor bulk is not fully depleted, an additional boundary condition at the edge of the depletion zone is needed (Equation (2.39)). Since the depletion edge is not known apriori, an iterative solver is implemented. After calculating the drift potential with boundaries at the electrodes, an additional depletion zone boundary is defined at the minimum of the resulting potential. The potential is then re-calculated with the new boundary at the depletion edge. These

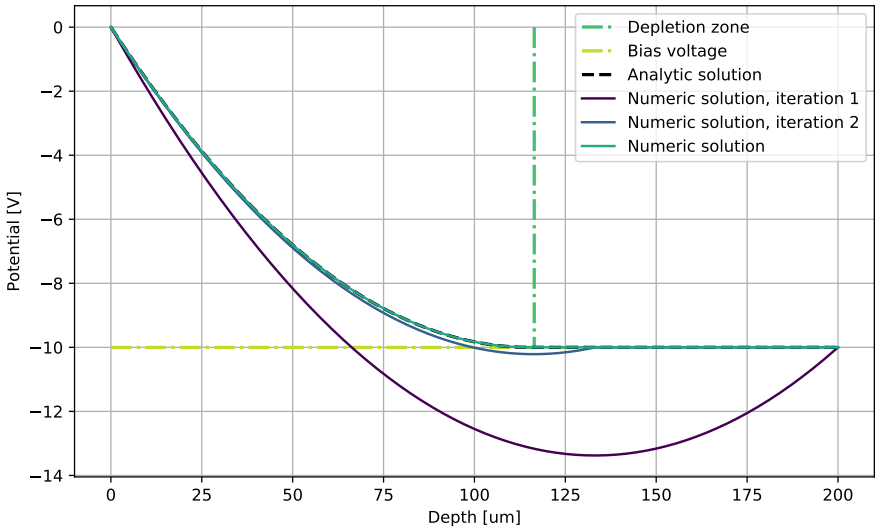


Figure 5.3: Potential of a not fully depleted planar pixel sensor with full fill factor. The parameters: 200 µm thickness, 30 V depletion voltage, 10 V bias voltage lead to a depletion depth of 116 µm (Equation (2.36)). The numerical solution matches the analytical solution (*black dotted*). The iteration steps illustrate the convergence to the solution.

steps are repeated until the minimum potential equals the bias potential. The method is depicted in Figure 5.3 for the 1D-potential of a planar pixel detector with full fill factor. In this example the numerical result matches the analytical solution (Equation (2.39)) after four iterations.

### 5.1.2 Signal simulation

The movement of electron-hole pairs is simulated using the free electron model, treating them as classic particles with effective masses and mobilities (Section 2.1.2). To increase simulation speed, not all electron-hole pairs are simulated but a sufficiently large number of so called *quasi-particles* ($\mathcal{O}(1000)$) is used to approximate results with negligible error (<1 %). The differential equation of movement:

$$\frac{d}{dt}\vec{x}_{e,h} = \vec{v}_{e,h} = \mu(\vec{E}(\vec{x}_{e,h}, T) \cdot \vec{E}(\vec{x}_{e,h}) \tag{5.1}$$

is numerically solved for each quasi-particle using *Explicit Forward Euler's Method* [But03, p. 45] with fixed time step and constant electric field approximation during one step. Alongside, the induced current and integrated charge from each quasi-particle is calculated using Ramo's Theorem (Section 2.46). This leads to the following set of equation that are updated for each time step $k$ and quasi-particle $n$ to calculate velocity, position, induced current $I$, and total induced charge $Q$ :

$$\vec{v}_{k+1,n} = \mu(\vec{E}(\vec{x}_{k,n})) \cdot \vec{E}(\vec{x}_{k,n}) + \vec{v}_d \tag{5.2}$$

$$\vec{x}_{k+1,n} = \vec{v}_{k,n}\,\Delta t \tag{5.3}$$

$$I_{k+1,n} = q_{k,n}\,\vec{E}_w(\vec{x}_{k,n})\,\vec{v}_{k,n} \tag{5.4}$$

$$Q_{k+1,n} = Q_{k,n} + I_{k+1,n}\Delta t \tag{5.5}$$

$$q_{k+1,n} = q_{k,n}\,e^{-\Delta t/\tau} \tag{5.6}$$

$\mu = \mu(\vec{E}, T)$ describes the mobility as introduced in Section 2.21, $\tau$ is the life-time of charge carriers reducing the drifting charge $q$ (Equation (2.79)), $\vec{E}_w$ the weighting field, and $\vec{v}_d$ the diffusion velocity. The fields at any position $\vec{x}$, that is usually not at a mesh point, are calculated from the numerical result (Section 5.1.1) as a 2D-spline interpolation. A contribution to the velocity due to diffusion ($\vec{v}_d$) is important for the simulation of charge collection of 3D-pixel detectors, due to low electric fields between electrodes in the form of a saddle, leading to unrealistic long drift times. Diffusion is implemented with an MC-method as introduced in [JH09, p. 1367]. Assuming that the e-h pair energy distribution follows the Boltzman distribution:

$$P(E) = \frac{1}{k_B T} \exp -E/(k_B T) \tag{5.7}$$

and using the relation between thermal energy and velocity ($1/2\,m_{\text{eff}}\,v^2 = 3/2\,k_B\,T$) one can

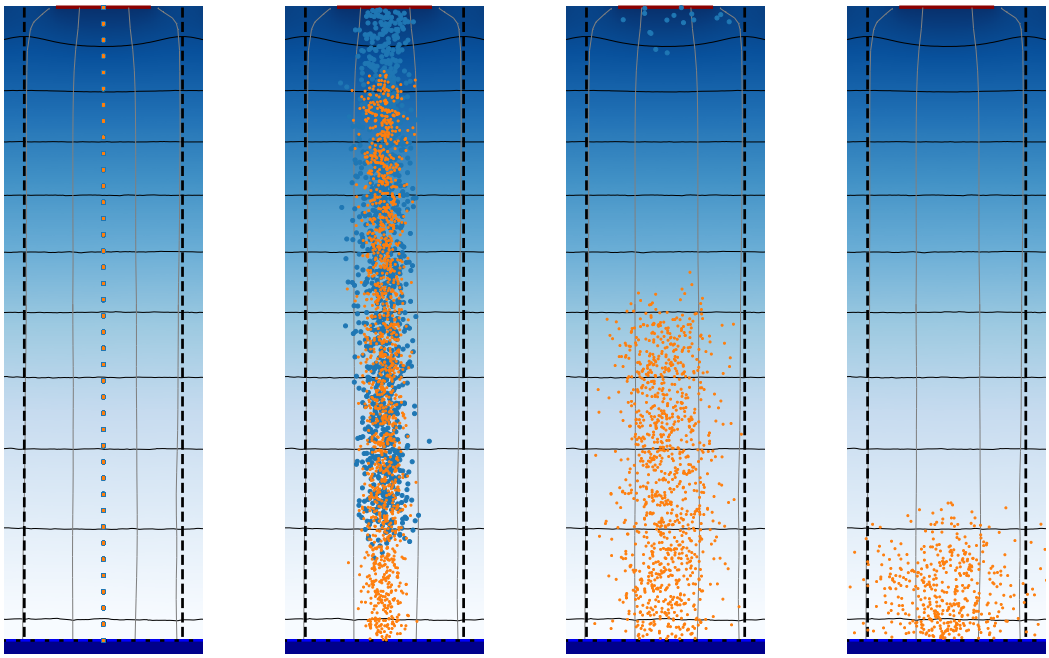


Figure 5.4: Movement of electron-hole pairs simulated with Scarce. The electrons are *blue circles* and the holes are *red circles*. At start ($t = 0\,\text{ns}$), 20 e-h pairs are created in the pixel center every 5 µm.

calculate the PDF for the particles velocity:

$$P(v) = P(E)\frac{dE}{dv} \tag{5.8}$$

$$= \frac{m_{\text{eff}}\, v}{k_B T} e^{-\frac{m_{\text{eff}}\, v^2}{2\, k_B T}} \tag{5.9}$$

with temperature $T$, Boltzmann constant $k_B$, and effective mass of the electron/hole ($m_{\text{eff}}$), that is assumed to be independent of the crystallographic orientation. At each time step $k$, a random diffusion velocity is calculated from a sample described by Equation (5.9) by means of *Inverse transform sampling* [Dev86, p. 27]:

$$U = \int_{-\infty}^{v} P(v)\, dv \tag{5.10}$$

$$= -e^{-\frac{m_{\text{eff}}\, v^2}{2\, k_B T}} + 1 \tag{5.11}$$

$$\Rightarrow v = \sqrt{-\frac{2\, k_B T}{m_{\text{eff}}} \ln(U)} \tag{5.12}$$

with a uniform random variable $U \in [0, 1[$. The velocity direction $\vec{n}$ in 2D is calculated from

another random variable $U \in [0, 1[$ with:

$$\vec{n} = \begin{pmatrix} \cos(2\pi U) \\ \sin(2\pi U) \end{pmatrix} \tag{5.13}$$

The evolution of e-h pairs in silicon with time, when diffusion and drift is included, is depicted in Figure 5.4. The time step $\Delta t$ has to be sufficiently small to approximate the solution to Equation (5.1) and was set to 1 ps for all simulations. The stability of the numerical solution is checked by verifying that for each e-h pair:

$$\int_0^{t_{\max}} q\,\mu\,\vec{E}_w \cdot \vec{E}\,dt = Q_{k_{\max},n} \in [0.99, 1.01]$$

holds, when trapping is deactivated. $k_{\max}$ is the time step where the electron and hole reach the electrode. Figure 5.5 shows the induced charge as a function of time for 3 electron-hole pairs at different starting positions in a planar sensor.

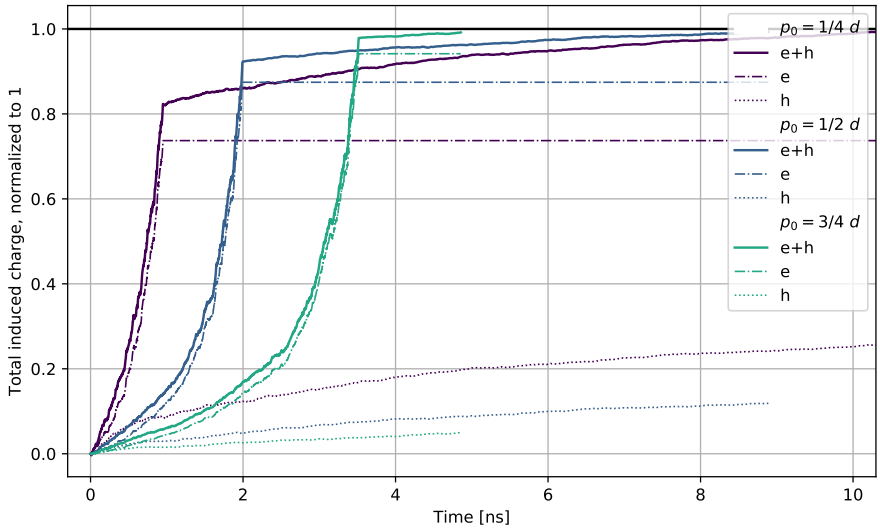


Figure 5.5: Induced charge from 3 electron-hole pairs drifting in an electric field. Planar ATLAS IBL electrode geometry, 200 µm thickness, p-type bulk. The start position of the *e-h* pairs is 1/4, 1/2, 3/4 of the thickness.

### 5.1.3 Charge-collection efficiency determination

The Charge-Collection Efficiency (CCE) is defined as the ratio between deposited charge in the sensor bulk and measured charge. Since readout electronics is modeled as an integrator, the measured charge corresponds to the induced charge (Figure 5.5). The induced charge is tracked as a function of time for each e-h pair and the total charge is defined as the value after all charge carriers have reached the electrodes. To allow examination of less efficient sensor areas, the total

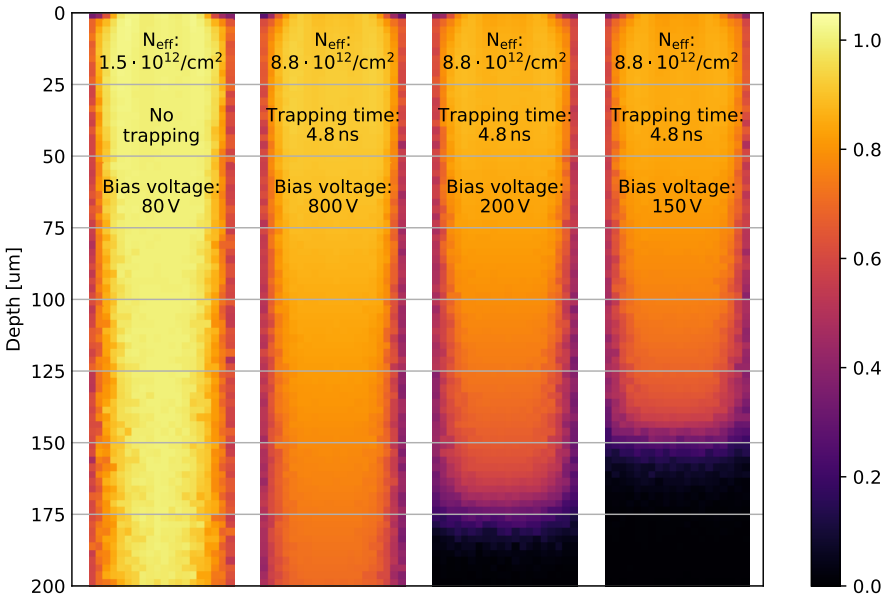


(a) Planar pixel, side view

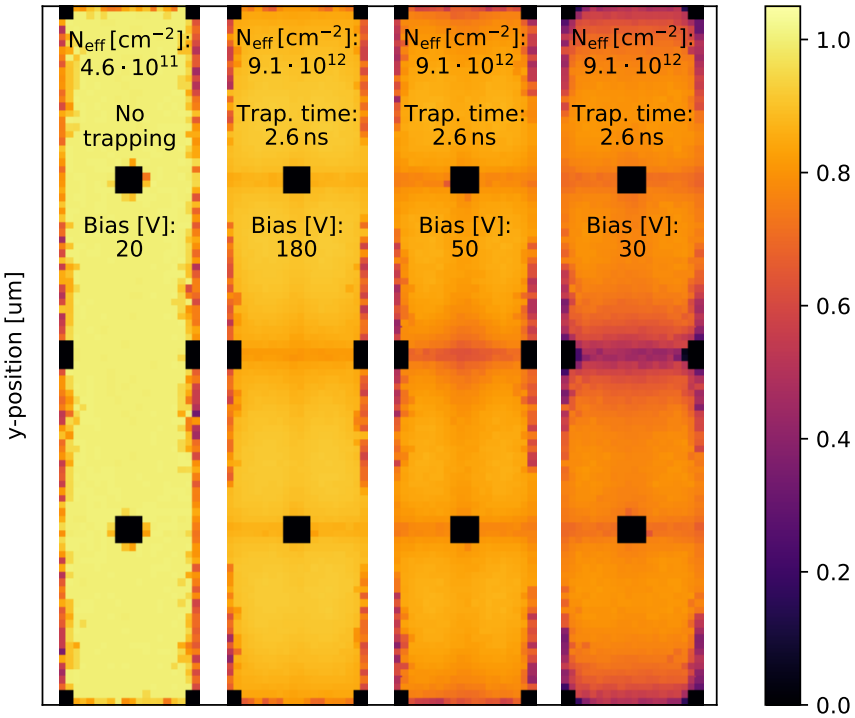


(b) 3D pixel, top view

Figure 5.6: Charge-collection efficiency maps for a planar n-in-p pixel sensor ($a$) and a 3D pixel sensor ($b$) with ATLAS IBL geometries. The left subplots show the CCE before irradiation. The other subplots depict the CCE at different bias voltages after an irradiation with $1 \times 10^{15}\,\mathrm{n_{eq}\,cm^{-2}}$. The corresponding parameters are given in the plot.

charge is stored as a function of the e-h pairs starting positions. For MIPs, the positions of charge deposition can be assumed to be uniformly distributed and independent of the sensor depth. Therefore, the e-h pairs created in *Scarce* are put on an equispaced grid. Figure 5.6 depicts simulated CCE of planar and 3D-pixel for different bulk resistivities, bias voltages, and trapping probabilities. The chosen parameters correspond to an irradiation with $1 \times 10^{15}\,\mathrm{n_{eq}\,cm^{-2}}$ as determined in Section 5.4.4. For the unirradiated case, one can see the influence of charge sharing, leading to CCE $\neq 1$ at pixel edges. Since diffusion is implemented as a random process (Equation (5.12)), multiple e-h pairs are simulated at each position to get the correct average CCE. The remaining statistical fluctuations explain the not completely smooth maps in Figure 5.6. A reasonable trade-off between simulation speed and accuracy is found when using 20 e-h pairs every 5 µm leading to a statistical error of a few percent. The change of the mean CCE due to irradiation is calculated in *Scarce* as the ratio of the total charge per pixel before and after irradiation. The normalized charge before irradiation is depicted in the leftmost sub-figure of Figure 5.6. After irradiation, the sensor bulk is not fully depleted anymore when too low bias is applied. This leads to a bulk volume that does not contribute to the charge signal. This can be seen in Figure 5.6(a) as *black* areas. The inefficient areas in the 3D-pixel plots are the locations of the bias and readout columns.

## 5.2 Measurement setup

Measurements of the charge-collection efficiency of IBL sensors with 3D and planar electrode configuration were realized in a climate chamber at room temperature (20 °C) and at −30 °C for irradiated devices. Post-irradiation cooling of sensors was necessary to prevent thermal runaway and to reduce leakage current for better signal- to-noise performance. Temperature and humidity were continuously monitored by several sensors close to the detector. A Strontium-90 electron source with an activity of about 23 MBq was used for charge deposition in the sensors. A fixed setup using a radioactive source was favored over a high-energy particle beam from a particle accelerator. This allowed better control of highly irradiated readout chips, temperature, and noise sources and enabled measurements with high statistics to do detailed studies of charge-collection

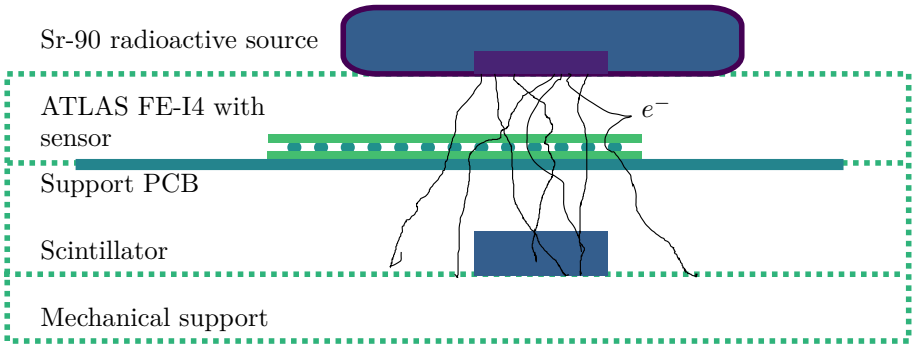


Figure 5.7: Simplified schematic of the measurement setup. Climate chamber, readout system, and power supplies are not shown.

efficiency with bias voltage. The setup includes a scaffold made of acrylic glass providing mounts for the radioactive source, scintillator, and the detector. This scaffold is mandatory to reproduce the exact positions of the different components, a requirement to allow comparative determination of CCE at different irradiation steps (Section 3.1.2). The setup, excluding readout system, cables, and power supplies, is depicted in Figure 5.7.

### 5.2.1 Detectors

This study is based on five different sensors (Table 5.1). Two planar pixel detectors with different thicknesses (200 µm, 250 µm) and three 3D pixel detectors with either columns fully passing the sensor bulk (*FBK*) or with about 40 µm distance to the sensor surfaces (*CNM*). Device P1 to D2 are similar to IBL modules (Section 2.3.1), except that all detectors are connected to a support PCB instead of a module flex (*single chip assembly*). Device D3 is a matrix of $12 \times 60$ 3D-FBK pixels, that are shorted by a metalization layer. Therefore, it is referred to as *3D-diode*. These devices are produced at wafer edges and were used for quality assurance during IBL production. In this study the 3D-diodes provide an independent measurement to spot calibration issues and other systematic errors, since a different readout is used and the charge measurement circuitry is not irradiated alongside with the sensor.

| **Device** | **Electrode config.** | **Irradiation** $[10^{15} n_{eq}\,cm^{-2}]$ | **Vendor** | **Thickness** [µm] | **Readout** | **Comment** |
|---|---|---|---|---|---|---|
| P1 | planar | 1; 5[2] | CiS | 200 | FE-I4B | Final IBL design |
| P2 | planar | 1; 7 | CiS | 250 | FE-I4A | |
| D1 | 3D | 1; 7 | CNM | 230 | FE-I4A | |
| D2 | 3D | 1; 5 | FBK | 230 | FE-I4A | |
| D3 | 3D | 1; 5[3] | FBK | 230 | Single channel CSA | Shorted pixel matrix |

Table 5.1: Devices used during measurements. Sensor properties summarized in Table 2.2. Some irradiation steps could not be measured (see *footnotes*).

### 5.2.2 Readout systems

The readout system is based on *USBpix2*-hardware [Bac+11, p. 37]. The system consists of 3 separate, electrically connected PCBs: a detector support PCB (*Single-Chip-Card*, short: *SCC*), an adapter PCB (*FE-I4 adapter card*), and a multi-purpose input-output PCB (*MIO 2*). The complete readout system, including low/high voltages and data connections, are depicted in Figure 5.8.

[2] Broken device due to transport failure.
[3] Insufficient signal-to-noise due to high leakage current.

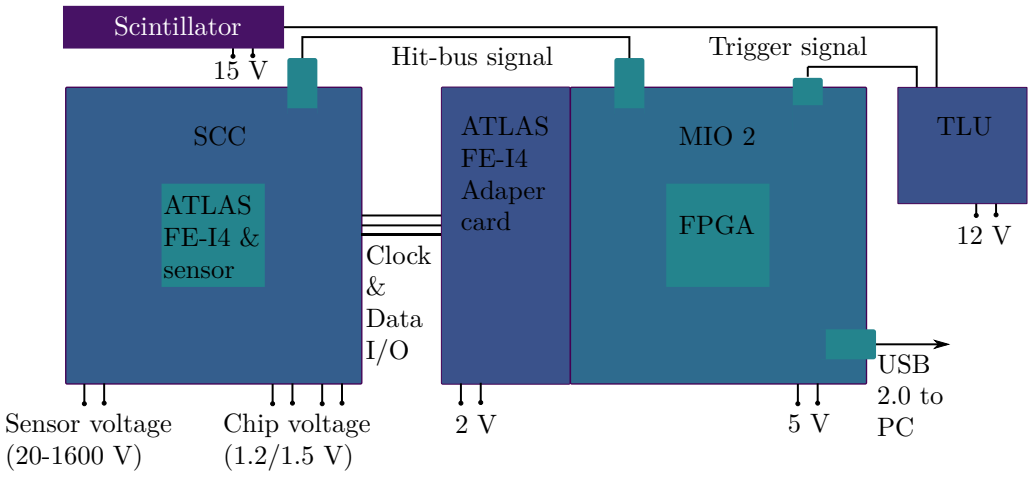


Figure 5.8: Readout system USBpix 2 with scintillator and Trigger-Logic-Unit (*TLU*). Only Single-Chip-Card (*SCC*), detector and scintillator are inside the climate chamber.

The detectors are fixed with thermally conductive glue to a 500 µm aluminum support that in turn is glued to the *SCC* (Figure 5.9). Although the aluminum support reduces the number of electrons reaching the trigger, it helps distributing heat to keep the sensor temperature below −20 °C during measurements. The FE-I4 is electrically connected to the support PCB with wire bonds. The PCB assumes functionality of the IBL module flex (e.g. signal termination, power filtering) and provides additional features for debugging and powering. To simplify the handling of highly irradiated chips and for better tunability at different temperatures, the build-in voltage regulators of the FE-I4 are not used during measurement. The voltages for the analog and digital part (1.5 V/1.2 V) are

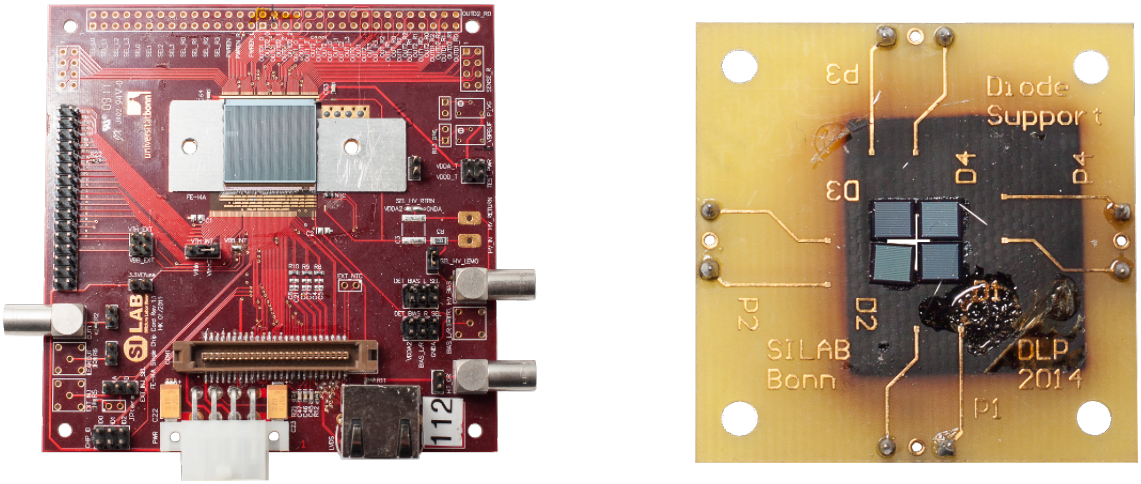


Figure 5.9: ATLAS IBL detector on a support card (*left*) and four 3D-diodes from IBL production (*right*). Both depict 3D FBK sensors, either full size or as smaller diodes with shorted pixels. Area of homogeneous irradiation with $2.5 \times 10^{15}\,\mathrm{cm}^{-2}$ protons is visible on the diode support PCB.

provided by external power supplies with sensed cables to compensate voltage drop.

The *MIO 2* houses an FPGA providing the FE clock and differential data input/-output lines for FE configuration and readout. A 2 MB block RAM is used to buffer the FE and TDC raw-data in a FIFO data structure. Data is transferred to the PC with a USB-2 interface. The single-ended *hit-bus* signal of the FE-I4 is connected through an open-drain buffer to the input-output board to allow charge measurements using the TDC-method (Section 3.2.2). A trigger is provided by a trigger-logic-unit (*TLU*, [Cus09; Cus07]) that discriminates the scintillator signal and creates a digital trigger signal. This signal is transmitted to the *MIO 2*, that in turn generates the trigger command for the FE. The FPGA modules and their corresponding Python drivers are defined in *basil*, a modular data-acquisition and system-testing framework [Sil]. The *FE-I4 adapter card* provides level shifters to interface the FPGA with the Front-End, that operate on different logic levels.

The 3D-diode readout is a standard chain for charge measurements consisting of a charge-sensitive-amplifier (CSA), a shaping-amplifier, and a multi-channel analog-digital-converter (MC-ADC). The readout chain is depicted in Figure 5.10. A custom made support PCB is used in a metal housing for shielding. The PCB supports 4 3D-diodes in close vicinity to simplify and speed up the irradiations with a particle beam. The support PCB can be seen in Figure 5.9. The devices

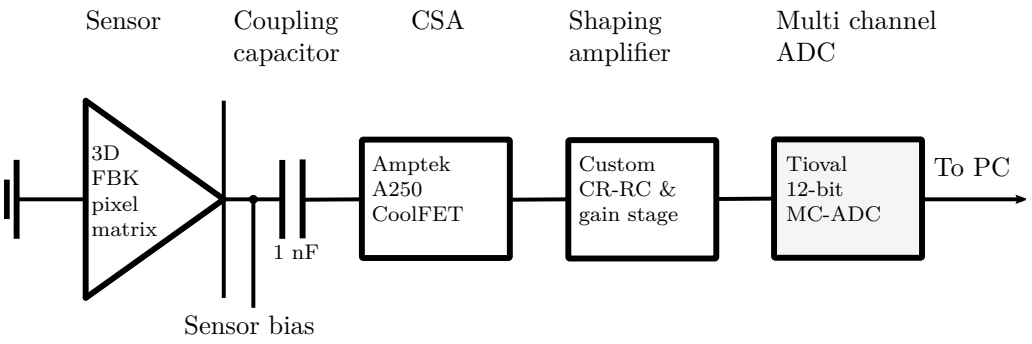


Figure 5.10: Readout system for 3D-diodes.

are wire bonded from both sides to connect the metal layers for biasing and readout columns. A commercial CSA is used (*Amptek A250CF CoolFET*, [Amp17]) that provides input-capacitance matching by selectable and cooled input transistors for better noise performance. The shaping amplifier is a custom made PCB with several operational amplifiers to implement programmable gain and CR-RC shaping stages. For fast pulse height digitization, a commercial multi-channel ADC with 12-bit resolution(*Toivel MC-ADC*, [Toi17]) is used, that provides an USB interface and software to record charge spectra with a PC. The 3D-diode setup (Figure 5.10) does not have a trigger, leading to less Landau-like and broader charge spectra as discussed in Section 3.1.2. But charge sharing is suppressed due to pixel shorting leading to the record of *cluster charge*. To mitigate contribution of partially depleted sensor areas at the sensor edge to the measured spectrum a collimator is used to focus illumination on the diode center.

## 5.3 Measurement procedures

### 5.3.1 Irradiation

The devices are irradiated in two consecutive steps to a fluence of $1 \times 10^{15}\,\mathrm{n_{eq}\,cm^{-2}}$ and $5 \times 10^{15}$ / $7 \times 10^{15}\,\mathrm{n_{eq}\,cm^{-2}}$ (Table 5.1). Irradiation takes place at the compact cyclotron accelerator of the Karlsruhe Institute of Technology (*KIT*) using an uncollimated proton beam with an energy of about 23 MeV at device position. During irradiation the devices are not biased and are kept in a cooling box with nitrogen atmosphere at −30 °C to avoid annealing. The box is moved with $115\,\mathrm{mm\,s^{-1}}$ to further mitigate heating up and to guarantee a homogeneous irradiation with the Gaussian distributed particle beam. Shipping and storing of irradiated devices is done below 0 °C, and the duration of device handling done at room temperature is kept below 3 h to prevent uncontrolled annealing. After each irradiation step the devices are annealed for 80 min at −60 °C [Mol99, p. 116], which is the accepted procedure. The proton fluence for each radiation step is set by beam current and irradiation time. After irradiation, the fluence is verified with activity measurements on $^{58}_{28}$Ni foils, that are attached to the devices during irradiation using the known production cross section of the nuclear reaction $^{58}_{28}\mathrm{Ni} \rightarrow {}^{57}_{28}\mathrm{Ni}$ ([Amj+14, p. 79],[Die03, p. 56]). The NIEL fluence for 23 MeV protons is calculated assuming a damage factor of 2. Determination of the absolute NIEL fluence is difficult, since it depends on the measurement error of the proton fluence from Ni-foil dosimetry (∼14 % [Die10, p. 8]]) and on the error of the damage factor itself. Although various measurements and simulations of the silicon damage factor for different particles and energies exist, they show a considerable spread. Figure 5.11 depicts damage factors from multiple publications in the energy range of interest. The generally assumed damage factor of $k = 2$ seems to be on

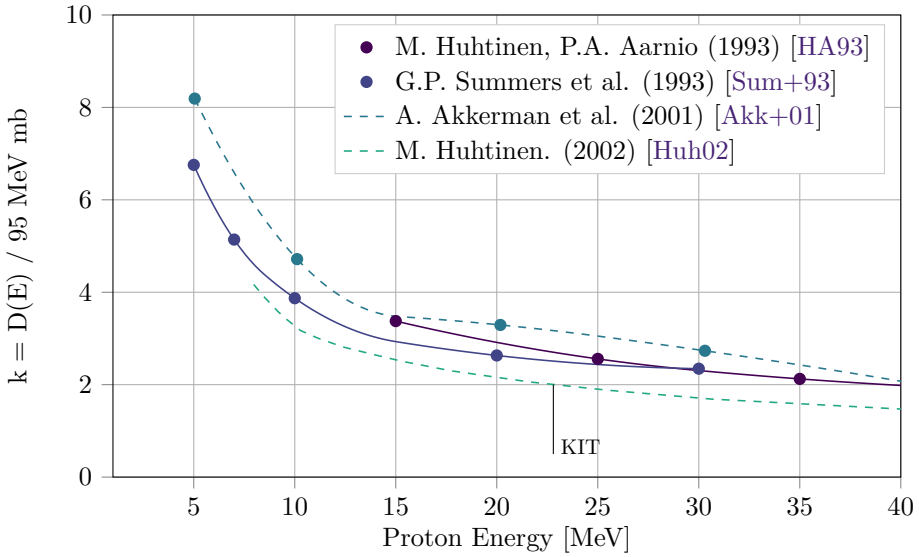


Figure 5.11: Determined damage factor of protons in silicon. Points are connected with a 2-nd order spline curve. Data partially taken from [VL00].

the lower end, almost all damage factors are larger. Recent measurements suggest a 10 % higher damage factor. However, in favor of comparability to other irradiation campaigns at KIT, the commonly considered damage factor of 2 is used. In general, it is assumed that the errors in the calibration constants lead to an uncertainty for the NIEL fluence up to 20 % [Ebe13, p. 56]. The irradiation steps for all devices are summarized in Table 5.2.

| **Device** | **1. Irradiation** $\text{Fluence}_{\text{tar./meas.}}$ $[10^{15}\text{n}_{\text{eq}}\,\text{cm}^{-2}]$ | **2. Irradiation** $\text{Fluence}_{\text{tar./meas.}}$ $[10^{15}\text{n}_{\text{eq}}\,\text{cm}^{-2}]$ | **Total fluence** $\text{Fluence}_{\text{tar./meas.}}$ $[10^{15}\text{n}_{\text{eq}}\,\text{cm}^{-2}]$ | **Total ionizing dose 1./2. irrad.** [Mrad] |
|---|---|---|---|---|
| P1 | 1 / 1 | 4 / 3.94 | 5 / 4.94 | 145 / 715 |
| P2 | 1 / 1 | 6 / 6 | 7 / 7 | 145 / 1015 |
| D1 | 1 / 1 | 6 / 6 | 7 / 7 | 145 / 1015 |
| D2 | 1 / 1 | 4 / 4.27 | 5 / 5.27 | 145 / 765 |
| D3 | 1 / 1 | 4 / 3.94 | 5 / 4.94 | 145 / 715 |

Table 5.2: Fluences of irradiation steps and total ionizing dose. Target fluence defined by beam current setting and illumination time. Measured fluence from Nickel-foil dosimetry. Damage factor $k = 2$ assumed. TID calculated with (5.14).

Irradiation with charged particles (especially at low energies) leads to a high ionizing-dose that change the behavior of transistors and potentially prevent detector operation after irradiation. For 23 MeV protons, the stopping power can be calculated from (2.1) and is 18.1 MeV cm$^2$ g$^{-1}$ ([Ber+05]). For the total ionizing dose (TID) follows after an irradiation with a proton fluence of $F_{\text{proton}}$:

$$\text{TID[Mrad]} = \frac{1}{k} \cdot F_{\text{proton}}[\text{cm}^{-2}] \cdot 18.1\,\text{MeV}\,\text{cm}^2\,\text{g}^{-1} \cdot 1.6022 \times 10^{-14}\,\text{J}\,\text{MeV}^{-1} \tag{5.14}$$

with damage factor $k$. The irradiated devices reach a dose of up to 1 Grad (Table 5.2), which is many times over the anticipated and qualified terminal dose of the ATLAS IBL pixel layer of 250 Mrad ([Cap+10, p. 84]).

### 5.3.2 Tuning

In general, tuning of a detector means changing settings with the intention to optimize certain behavior. For the ATLAS pixel detector, tuning is performed to ensure reliable and safe operation and to optimize and unify the in-time hit-detection efficiency. For the FE tuning, this mainly means changing the bias settings of amplifiers and voltages, thereby influencing power consumption, amplification gain, data bandwidth, detection threshold, and time walk. The goal for charge measurements, as presented in this chapter, is slightly different. Since spectra consists of data from multiple pixels, for increased statistics, an equalized pixel response to charge is also important. However, the main requirement is the optimization of the signal-to-noise ratio ($S/N$). The $S/N$ is most impacted by the threshold setting of the comparator and is set to $2500\,e - 3000\,e$ as suggested by measurements. Figure 5.12 shows the charge resolution determined by the width of the photo peak of multiple x-ray sources for low and high threshold settings. The detection threshold that is set for all devices ($\sim 3000\,e$) is still low enough to detect the Landau peak after irradia-

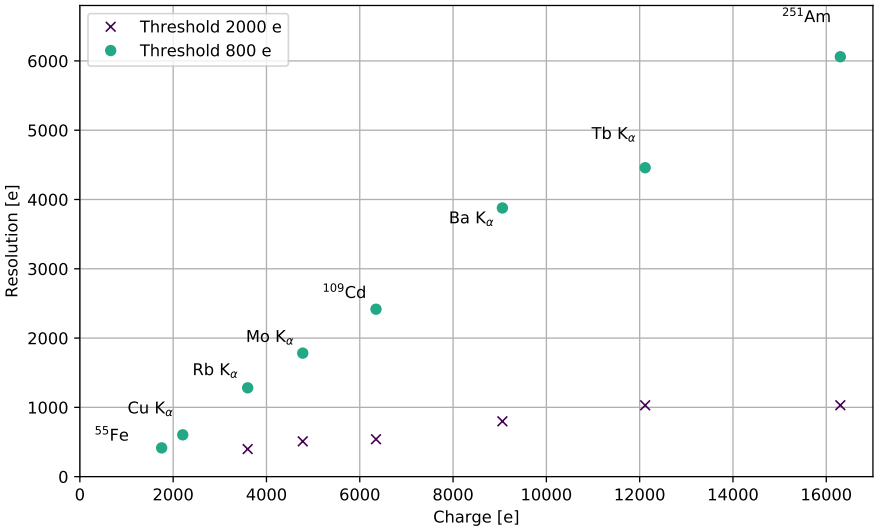


Figure 5.12: Charge resolution using the TDC-Method with the ATLAS FE-I4. High and low threshold tunings are depicted. The resolution is determined by the width ($\sigma$) of Gaussian fits to charge spectra from several X-ray sources. Data from [Eng14, p. 18].

tion. The charge resolution using the TDC-method is not defined by signal amplitude variations from electronic noise alone (as measured in a *threshold scan*, see Section 5.3.2), but is dominated by the transient behavior of the comparator of the ATLAS FE-I4 introducing a discrimination threshold dependent jitter. Additionally, a rather strong resolution dependence on the charge is observed (Figure 5.12) and has to be considered when analyzing spectra. For the charge range of interest, $4\,\mathrm{k}e - 23\,\mathrm{k}e$, the noise is $400\,e - 1000\,e$ and the $S/N$ of at least 10 sufficient.

To unify the response of pixels to charge the per-pixel threshold bias-DACs (TDAC) and feedback-current bias-DACs (FDAC) of the FE-I4 are adjusted. This mitigates gain and threshold variations between pixels due to statistical transistor mismatch. Threshold and gain variations before and after pixel-DAC tuning are depicted in Figure 5.13. Since even one noisy/stuck pixel renders the TDC-method impossible, noisy and stuck pixels are also identified and deactivated during chip tuning. Pixels are denoted as stuck, when the output of the comparator is always high. The reasons for stuck and noisy pixels are multifold: increased pixel leakage current after irradiation, inadequate bias settings of the analog pixel (e.g. [Bac14, p. 83]), and shortened pixels due to bump bonding. Especially, after irradiation, masking these pixels with a fraction of 1 % is important. Further, the *hit-bus* feature of pixels at sensor edge and adjacent to insensitive pixels is deactivated, to allow proper single-pixel cluster-size cuts as motivated in Section 3.1.2.

Additionally, all relevant and externally accessible analog biases of the ATLAS FE-I4 are checked and tuned at each irradiation step. After a TID of 1 Grad, several biasing circuitries in the analog part of device D1 are nonfunctional (e.g. *preamplifier bias*) and the bias voltages are provided by external power supplies to recover the analog amplification chain.

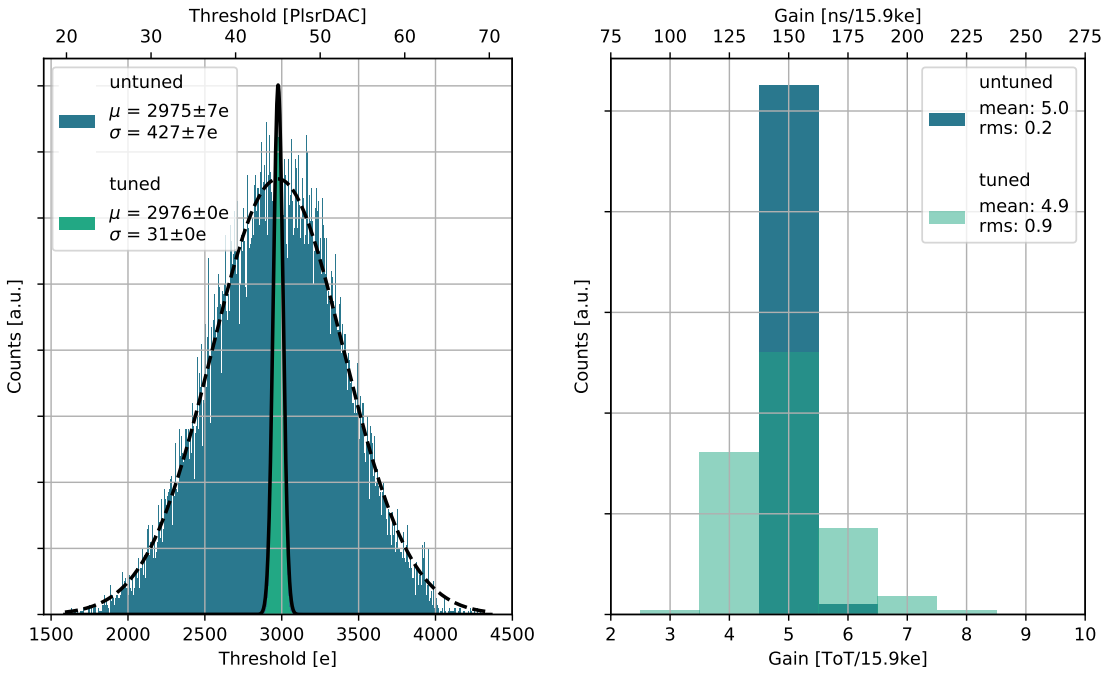


Figure 5.13: Threshold and gain tuning of the ATLAS FE-I4 pixel matrix. Distributions before (*dark*) and after tuning (*bright*) to 3000 $e$ and 150 ns/16 k$e$.

### Optimizing chip-tuning algorithms

The ATLAS FE-I4 is the largest readout chip in high-energy physics, to date, with 26880 pixels. Before operation, each pixel must be tuned using the internal injection circuitry. This circuitry creates a configurable voltage step over injection capacitors to inject a test charge. Existing tuning algorithms have been developed for the ATLAS FE-I3 with 2880 pixels only and show poor performance for its larger successor. A full-chip tuning (unifying per pixel threshold and gain to chosen values) takes several hours and motivates the implementation of the algorithms introduced here. In contrast to the FE-I3 ([Per+06, p. 7]), an auto-tune feature is not realized in the FE-I4, thereby demanding chip tuning in software. The new tuning algorithms reduce the full-chip tuning-time to about 5 min, allow application of the charge measurement methods introduced in Section 3.2, and were useful for the reduction of testing time in chip qualification tests during IBL production.

Since the injection circuitry can only be used for a limited number of pixels simultaneously, most time during tuning is spent changing pixel configurations (selection of injection capacitors, enable pixel readout). The underlying reason is leakage current in the transmission gates that select the injection capacitor in combination with a finite output impedance of the DAC driving the voltage of the charge-injection circuitry (PlsrDAC). This leads to a reduction of the voltage step. Consequently, the injected charge depends on the number of selected pixels. More information and measurements showing this relation can be found in [Bac14, p. 46]. The number of parallel injected

pixels is therefore limited to 112[4]. The mandatory consecutive injection leads to unavoidable delays when injecting charge into all pixels. Injecting charge several times into the pixels is termed *analog scan* and is used to verify the analog amplification chain and digital data handling for each channel.

| | **Threshold tuning** | **Gain tuning** | **New threshold tuning** | **New gain tuning** |
|---|---|---|---|---|
| **Runtime** | $\mathcal{O}(N_{\text{Thr.}} \cdot N_{\text{Ch.}})$ | $\mathcal{O}(N_{\text{Gain}})$ | $\mathcal{O}(\log N_{\text{Thr.}})$ | $\mathcal{O}(\log N_{\text{Gain}})$ |
| **ATLAS FE-I4 runtime** | $32 \cdot 100 = 3200$ | 16 | $\log_2(32)+1 = 6$ | $\log_2(16)+1 = 5$ |

Table 5.3: Runtimes of tuning algorithms. Comparison to new implementation utilizing a binary search algorithm (left vs. right). $N_{\text{Thr.}}/N_{\text{Gain}}$ is the number of threshold / gain setting and $N_{\text{Ch.}}$ the number of charge settings to record the charge response function (see. Figure 5.14). For the ATLAS FE-I4: $N_{\text{Thr.}} = 32$; $N_{\text{Gain}} = 16$; $N_{\text{Ch.}} = 100$.

Analogous to the big-$\mathcal{O}$ notation for runtime classification of computer algorithms, the runtime of previous and new tuning algorithms is analyzed. The runtime for the ATLAS FE-I4 is scaled to the number of analog scans as the smallest non-reducible time unit. Thus, $\mathcal{O}(1)$ is the time for one analog scan ($\approx$1 s). The differences between old and new tuning algrithms are depicted in Table 5.3 showing a decrease in runtime of at least one order. Previous tunings are implemented in a straight forward way: all DAC settings with their corresponding values are measured, a lookup table is created, and the setting with the value closest to the tuning value is selected. For the determination of threshold values during threshold tuning, a time-consuming *threshold scan* is used.

#### Threshold Scan

During a threshold scan, charge is injected below and above detection threshold to record the charge response function of each pixel. In an ideal circuitry with no noise, a step function can describe this function with the step at threshold position (Figure 5.14, *light dotted yellow*). Due to electronic noise with Gaussian distributed amplitudes, the response function smears out and is described by the CDF of the Gaussian distribution (Figure 5.14, *black line*):

$$R(q) = \frac{N_{\text{inj}}}{2}\left(1 + \text{erf}\left(\frac{q-\mu}{\sqrt{2}\sigma}\right)\right)$$

with number of injections $N_{\text{inj}}$. Fitting this function to data allows the determination of threshold ($\mu$) and noise ($\sigma$), whereby the threshold is the charge value with 50% hit detection-probability. Each sampling point of the response function is one analog scan and about 100 scans are used to sample the functions (Table 5.3, $N_{\text{char. sett.}}$) leading to 3200 analog scans for an ATLAS FE-I4

[4]Selecting every 3rd pixel of a double column (336 pixels). See Section 2.3.1.

threshold tuning.

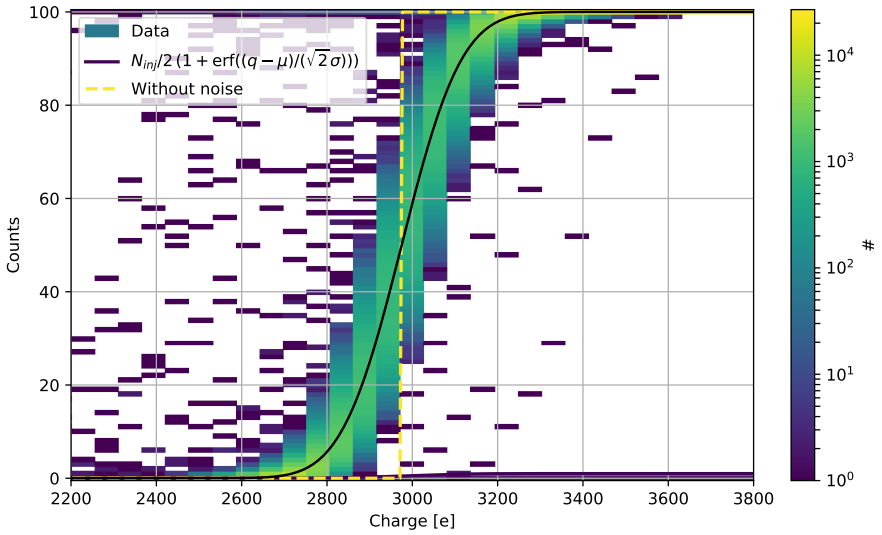


Figure 5.14: Detection probability for all pixels of an ATLAS FE-I4 determined with a threshold scan. Pixels are tuned to a threshold ($\mu$) of 2975 $e$ and have about 110 $e$ noise ($\sigma$). Overlay of the response curves of all pixels depicted as a heatmap. Theoretical curves are depicted for a system without electronic noise (*light dotted*) and with 110 $e$ noise (*dark line*). $N_{\mathrm{inj}} = 100$ injections per charge setting. Deviation from the theoretical curve occurs for less than 15 pixels (<1 ‰).

### New tuning algorithms

The new tuning algorithms utilize the fact that transfer functions of tuning-DACs are usually monotonous. This makes DAC-values sorted allowing for the application of the binary search algorithm [Knu98, p. 409]. In contrast to former tunings with linear complexity, binary search has logarithmic time complexity. During binary search, the middle element of sorted values is compared to the target value. If the value is too low, the lower half is discarded, otherwise the upper half is discarded. This procedure is recursively repeated and in each step half of the remaining values are eliminated. The recursion stops when only one element is left. When searching in values of a DAC, one can utilize that each DAC bit selects the remaining half to be searched. Thus, one starts at the MSB and selects for each iteration a lower bit and sets the bit depending if the measured value is above or below target value. The algorithm is illustrated in Figure 5.15 for a 4-bit threshold DAC. Convergence to the optimal value in a binary search is only ensured for exact searches. To ensure convergence to the closest value the best match is kept, compared to the converged value, and set if needed. For example, the converged value in Figure 5.15 is 3.2 k$e$, but the closest value is measured in the preceding step is 2.9 k$e$.

Besides a faster converging tuning algorithm, threshold-tuning time is further reduced using the fact that the detection probability at the given threshold is 50 %. Thus, the criterion during binary

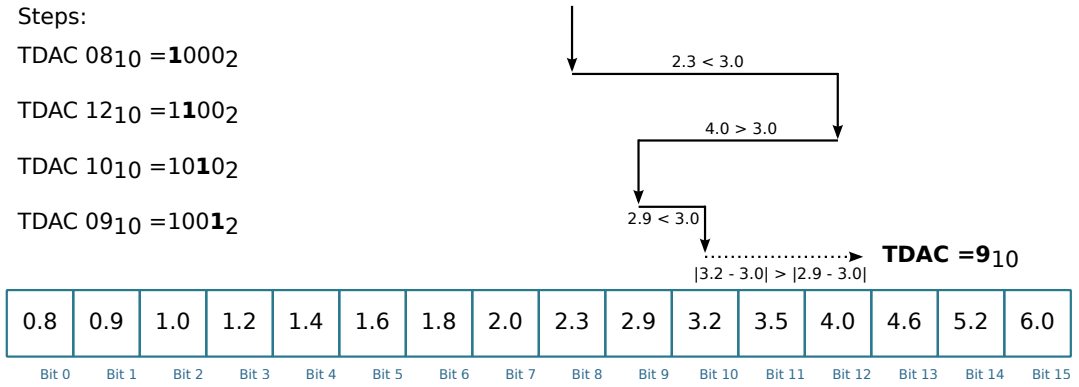


Figure 5.15: Example of a threshold tuning to 3 k$e$ using a binary search algorithm. A 4-bit threshold DAC (*TDAC*) is assumed implementing 16 different and sorted threshold values. Convergence to a non-optimal threshold setting is depicted (TDAC = 10).

search whether the threshold is too high or too low is a simple measurement of the hit-detection probability when injecting the charge of the threshold target value. A disadvantage of this method is an offset to the target threshold that occurs due to a finite step size of the charge-injection circuitry. For the ATLAS FE-I4, the step size of the *PlsrDAC* is about $\sim 60\,e\,\mathrm{DAC}^{-1}$ (Equation (5.15)), explaining the slight offset between threshold target value ($3000\,e$) and tuning result ($2975\,e$) in Figure 5.14. But a shift of the mean threshold that is much smaller than the electronics noise can be neglected here.

The tuning of the single channel amplifier for the 3D-diode comprises optimization of CR-RC shaper- and gain stages to maximize the signal-to-noise ratio. A shaping time of approximately 100 µs is selected for all measurements.

### 5.3.3 Calibration

Calibration of a detector setup is the determination of transfer functions to be able to relate settings and measured values to common units and theoretical expectations.

Calibration of the FE-I4 for charge measurements is divided into two distinct calibrations: calibration of the internal charge-injection circuitry and calibration of the per-pixel charge transfer-function.

#### Calibration of the charge-injection circuitry

The calibration of the internal charge-injection circuitry is needed to find an irradiation-independent quantity to scale the measured charge spectra of the sensors, since changes of the signal amplification due to TID in the FE is expected. By comparing the charge signal of the sensor, that is expected to decrease with irradiation, to the signal of the charge injection-circuitry such a scale is available. Nevertheless, changes in the injection circuitry itself with irradiation must be known and corrected for. The charge-injection circuitry of the ATLAS FE-I4 creates a voltage step over

capacitors ($C_{\text{inj}}$) present in each pixel to inject a charge $Q$:

$$Q = \Delta V(PlsrDAC) \cdot C_{\text{inj}} \tag{5.15}$$

Significant changes to the value of metal-oxide-metal capacitors with TID have not been observed and $C_{\text{inj}}$ is assumed constant here. The voltage $V$ for transistor switches located in each pixel is created in the end-of-column logic with a 12-bit DAC ($PlsrDAC$) and routed to each pixel. The linear transfer function of the PlsrDAC cannot be expected to be unaffected by TID (e.g. due to bias changes). The voltage transient $\Delta V(PlsrDAC)$ is therefore checked after each irradiation step. Measurements for device P2 are depicted in Figure 5.16, together with an example of a voltage transient measurement. PlsrDAC-calibrations of the other devices can be found in the Appendices. The variations with irradiation are found to be only approximately 5% for all devices.

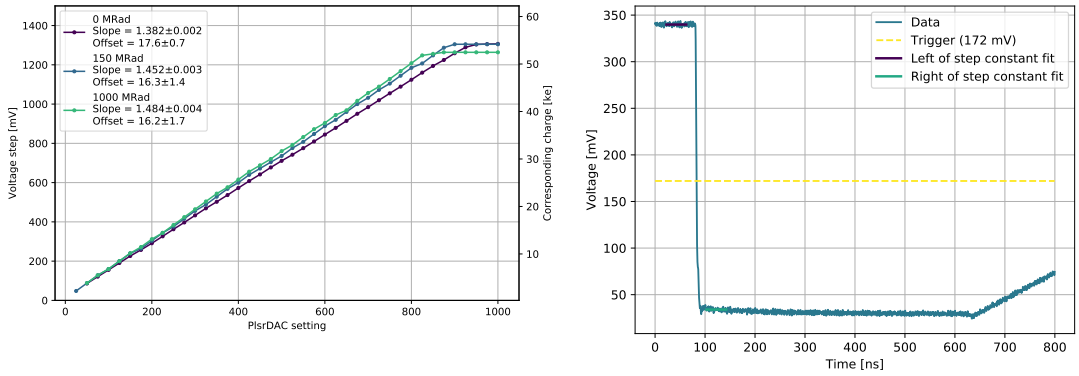


Figure 5.16: Left: Pulser DAC calibration of the charge-injection circuitry at different levels of irradiation. Device P2. Fit results of linear region stated in legend. Right: Example of a voltage step measurement.

### Per-pixel calibration

Sufficient statistics to determine the CCE requires the overlay of data from several thousand pixels. However, even after tuning, the response of pixels to charge differ. The time-over-threshold transfer functions are only similar at gain-tuning target-value (usually 16 k$e$) and disperse quickly. Additionally, an equalization of pixel thresholds at high thresholds is not possible anymore due to range limitations of the threshold DACs. Hence, for the application of charge reconstruction methods as introduced in Section 3.2.2, a per-pixel lookup-table is created. Example curves of threshold and time-over-threshold transfer functions for three pixels are depicted in Figure 5.17. Missing values are interpolated with 2nd order spline curves. A change of the TDC-calibration in the order of a few TDC-values, likely due to temperature differences, is frequently observed. Hence, the consistency of the calibration is always checked for a few pixels before and after source

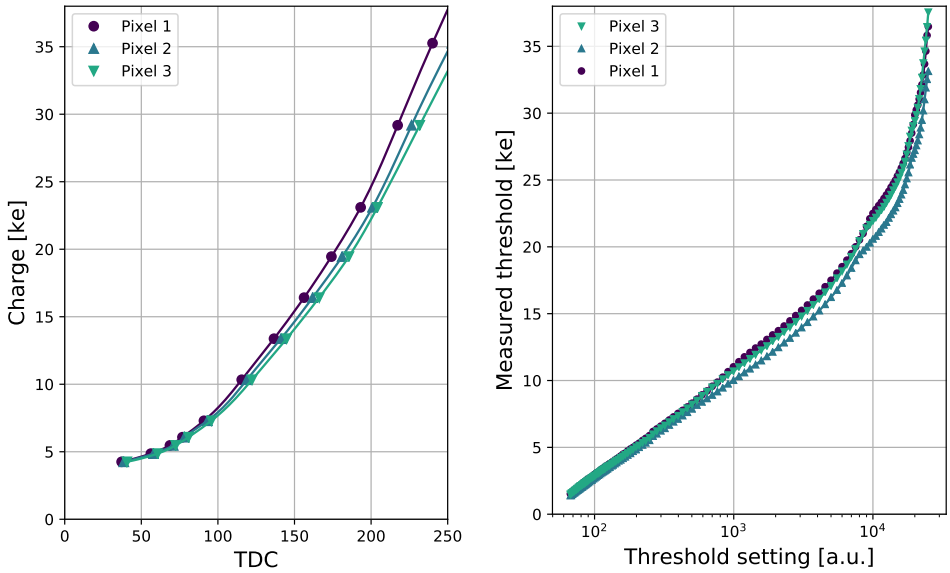


Figure 5.17: Per-pixel calibration illustrated by 3 example pixels for the TDC-method (*left*) and the Threshold-method (*right*).

measurement. If an offset $> 100\,e$ is observed the per-pixel calibration and source measurement are repeated.

#### Limitations of the charge-injection circuitry

To verify the measured transfer functions of the charge-injection circuitry and to determine the injection capacitor value (Equation (5.15)), multiple gamma sources are used on unirradiated sensors to deposit a known charge in the sensor bulk. Simulations with *SourceSim* validate the assumption that the full energy peaks of measured single-pixel charge-spectra correspond to the photo peak of the sources allowing absolute calibration of the injection circuitry. The reason is negligible charge sharing for the ATLAS IBL pixel geometry and large attenuation lengths ($> 1\,\text{mm}$) of the used gamma source photons ($^{109}$Cd to $^{241}$Am, $22\,\text{keV} - 60\,\text{keV}$, Figure 2.6).

Also, a difference between back- and front-side illumination is neither measured nor simulated. Consequently, the devices are backside illuminated to avoid attenuation by the readout chip for increased particle rates and measurement statistics. Figure 5.18 shows expected charge spectra of single-pixel clusters for multiple sources and two pixel geometries: a ATLAS IBL pixel geometry and a future small pixel geometry. The reconstructed peak positions are slightly below the photo peak positions with a maximum offset of less than $100\,e$. The assumption of negligible charge sharing is not valid anymore for small pixel geometries with reduced pixel-surface to sensor-thickness ratios and gamma sources like $^{55}$Fe depositing charge close to the sensor surface (few $10\,\mu\text{m}$). This can be seen at the bottom of Figure 5.18 for a hypothetical $300\,\mu\text{m}$ thick sensor with $50\,\mu\text{m} \times 50\,\mu\text{m}$ pixels. Due to longer drift lengths and smaller pixels, the photo peak smears out with a shoulder

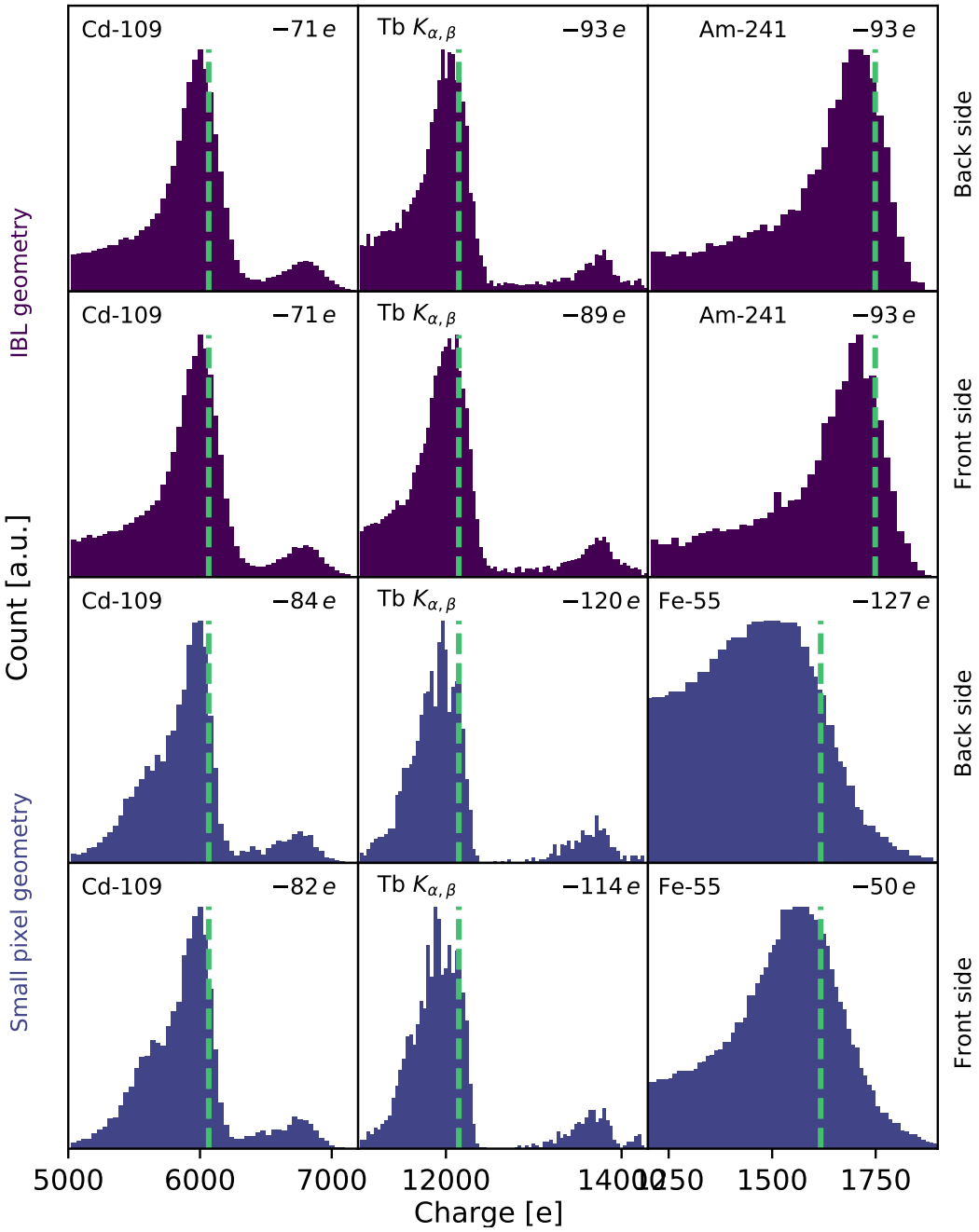


Figure 5.18: Charge spectra in silicon pixel detectors using single-pixel cluster. Multiple x-ray sources illuminating sensor front- and back-side. Photo peak from literature (*dotted line*) and offset to reconstructed photo peak depicted. Photo peak reconstructed by Gaussian fit (not shown). IBL planar pixel geometry: 50 µm x 250 µm x 200 µm (*top*) and small pixel geometry: 50 µm x 50 µm x 300 µm (*bottom*). *SourceSim* simulation.

to the left. Low energetic x-rays, when used for backside illumination, give a non Gaussian distribution with a difficult to determine peak position. For ATLAS IBL pixel geometry, this is not expected and simple Gauss fits to data are performed.

Calibration of the charge injection of device P1 with x-ray sources is depicted in Figure 5.19, which shows the voltage transient over the injection capacitor as a function of the expected photo peak energies from literature. The voltage transients are calculated from the per-pixel TDC calibration (Figure 5.17, *left*) relating the TDC value to a PlsrDAC value and the transfer function of

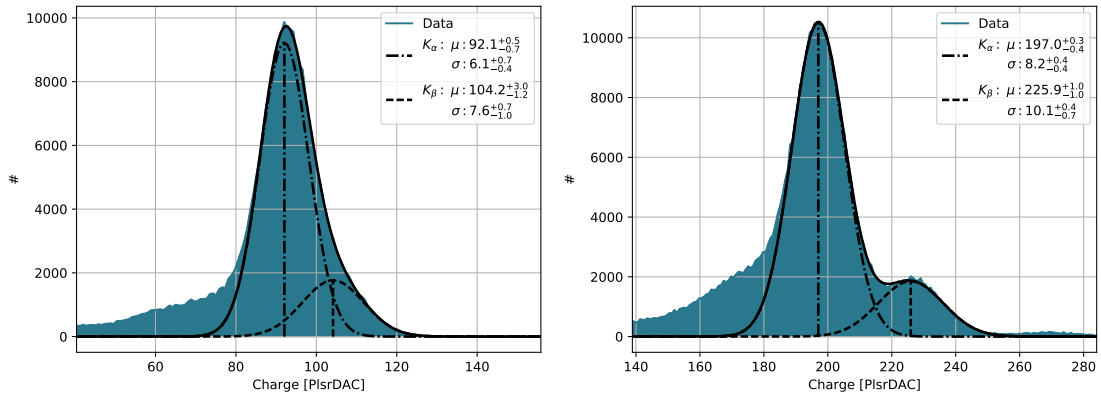


(a) $^{109}_{48}\mathrm{Cd} + ^{0}_{-1}\mathrm{e} \rightarrow ^{109}_{47}\mathrm{Ag} + \gamma(88\,\mathrm{keV})$ [Bé+16, p. 129] (b) Terbium [Des+03, p. 68]

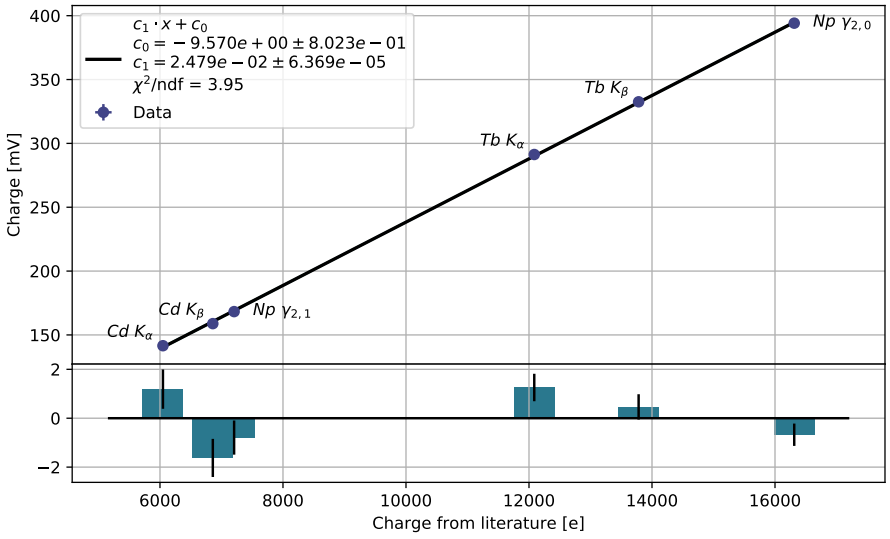


(c)

Figure 5.19: Calibration of the charge-injection circuitry with $\gamma$-sources. Device D1. *a,b:* Charge spectra of two sources with corresponding fits to K$\alpha$, K$\beta$ lines from X-ray fluorescence. TDC method with charge calculated in units of PlsrDAC from TDC(PlsrDAC) calibration. *c:* Full calibration (*top*) including offset to the line fit (*bottom*). Charge in electrons assuming 3.65 eV e-h$^{-1}$ and measured charge in mV using Equation (5.15). Errors from peak-fits and PlsrDAC calibration.

the PlsrDAC (Equation (5.15)):

$$dV(\text{PlsrDAC}(\text{TDC}_{\text{peak}})) \cdot \text{C}_{\text{inj}} = Q_{\text{lit}} \tag{5.16}$$

Each point is the maximum of the Gauss fit to the overlay of charge spectra from about 4000 pixels using a profile histogram (Figure 5.19, *top*). The difference to a straight line fit is depicted at the bottom. Since the TDC-calibration error and non-linearities in the PlsrDAC are not included (see Section 5.3.3) the offset cannot be explained by fit error alone, when judging goodness of the fit by reduced $\chi^2$. However, the measured maximum deviation of less than 100 $e$ is negligible for expected MPV values above 5 k$e$. From the slope, the value of the injection capacitor is determined and summarized in Table 5.4, together with the expected injection capacitor values measured during IBL production. The measured values are approximately 13 % larger than those determined dur-

| **Device** | P1 | P2 | D1 | D2 | Wafer probing |
|---|---|---|---|---|---|
| Capacitance | 6.67(2) fF | 7.41(2) fF | 6.46(2) fF | 6.62(2) fF | $(6.00 \pm 0.26)$ fF |

Table 5.4: Injection capacitor values determined with x-ray sources for all devices. Capacitance values with independent measurement on more than 3000 chips during IBL production for comparison.

ing IBL production. During production, the injection capacitor value is measured by charging and discharging a dedicated capacitor array, that is located in each chip. (Equation (6.1)). Due to unknown parasitic capacitances, that are only difficult to extract with post layout simulation, a large uncertainty can be expected. However, the relatively large offset of several 100 $e$ for the ATLAS FE-I4A at PlsrDAC=0 that increases to above 1000 $e$ for the final ATLAS IBL production version (ATLAS FE-I4B) is unexpected. The offset has been observed for all readout chips calibrated for charge measurements with x-ray sources ($> 10$, Figure 7.5), but an explanation could not be found. For ATLAS IBL operation, this has likely no consequences. The hit detection efficiency was verified to be sufficient at the end-of-life irradiation with an effective 2000 $e$ tuning ([Col12, p. 31]), a value also reachable with the internal charge-injection circuitry of the FE-I4B. The offset seems constant with TID, since charge spectra of an irradiated readout chip match the measurement with the single channel amplifier as presented in Section 5.4.3.

Another discrepancy exists when comparing charge deposition from gamma sources to the charge-injection circuitry: the charge injected into the pixels is a function of the column position in the pixel matrix. Two independent measurements show this behavior. One is the mean pixel threshold DAC value after threshold tuning, which shows a gradient (Figure 5.20, *top*). The other is a shift in the charge spectrum of a cadmium source as a function of column position using the threshold method (Section 3.2.2). The offset comes from the fact that per-pixel tuning and calibration use the charge-injection circuitry. The gradient was observed on all readout chips, but is with a maximum difference of about 400 $e$ relatively small. This effect was hidden during IBL qualification, since tuning and tuning verification measurements utilize the charge injection circuitry. Additionally, gamma source measurements do not reveal the gradient with the internal charge resolution of the ATLAS FE-I4. As a consequence, threshold tunings using the internal injection circuitry cannot

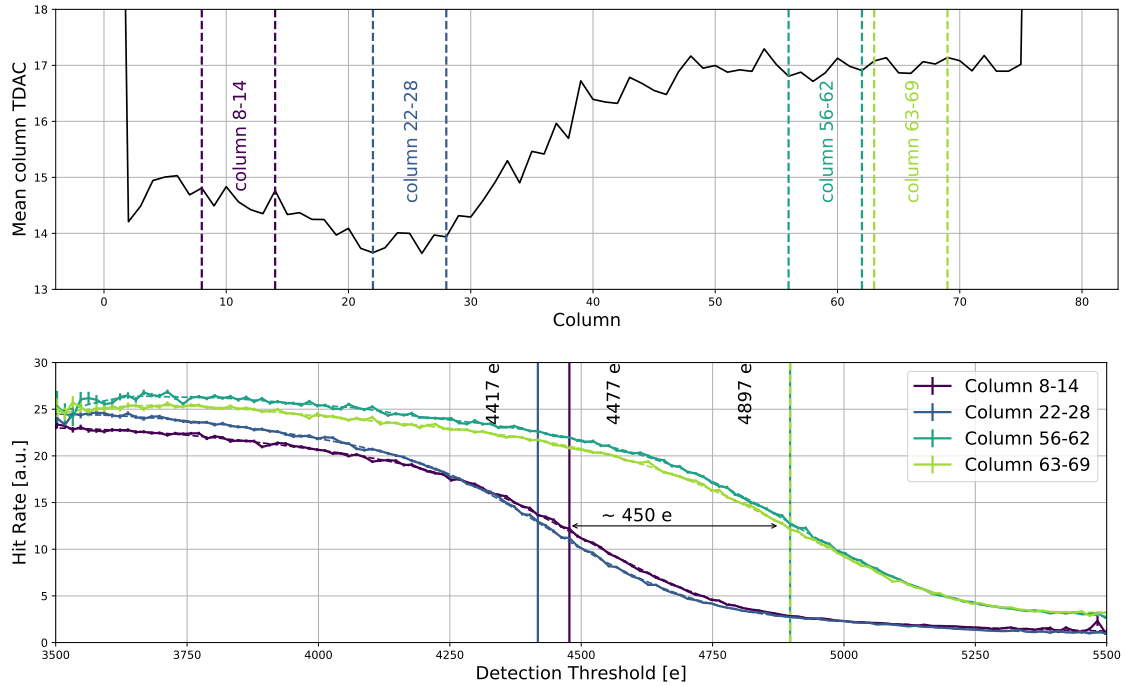


Figure 5.20: Two measurement showing the change of injected charge with column position using the internal charge-injection circuitry of the ATLAS FE-I4. Top: Threshold DAC distribution after threshold tuning with internal charge-injection circuitry. Bottom: Measured integrated single-pixel charge spectrum of a $^{109}$Cd $\gamma$-source after pixel calibration with internal charge injection circuitry.

reach an equalization below 400 $e$. Although this value exceeds the formulated requirement of the threshold tunability ($< 100\,e$, [Col12, p. 6]), it is unlikely to impact IBL performance, since a column dependent hit efficiency is never observed. The reason is a sufficient S/N for the 200 µm thick IBL sensors, even after end-of-life irradiation. Only for very thin sensors (50 µm), a column dependent hit efficiency is observed [Mac17]. The reason for the offset is likely the routing of the PlsrDAC voltage via metal lines to the pixels, introducing a position dependent impedance. A similar effect has been observed on other pixel chips [Mer10, p. 143]. This theory is supported by the fact that the PlsrDAC location is in column 26 where the injected charge is highest, and consequently, the TDAC distribution is lowest. Applying the voltage transient using an external pulser shows the same shift. However, a noise-based threshold tuning that does not use the charge-injection circuitry leads to no gradient in the TDAC distribution as one would expect (see [Jan20]). To not reduce charge resolution only the right part (column $> 65$) of the pixel matrix is used in this study, where the charge injected shows no column dependency.

## 5.4 Results

Collected charge and charge-collection efficiency strongly depend on the sensor bias-voltage, making the maximum applicable voltage an important property for sensors.

### 5.4.1 Leakage current of sensors

The leakage current as a function of the reverse bias voltage (*IV-curve*) is measured to determine the maximum operation voltage. Leakage current in silicon sensors consists mainly of thermal generation current and current from impact ionization [Lou+03, p. 81]. Thermal generation current shows a strong temperature dependency ($\propto T^2 \exp \frac{\text{const}}{T}$, Equation (2.75)), a linear dependency on irradiation (Equation (2.77)), and scales with the depletion volume. ($\propto \sqrt{V_{\text{bias}}}$, Equation (2.36) and Equation (2.76)). In an IV-curve, this can be seen as a steep rise for low depletion voltages until full-depletion is reached and the current saturates. The IV-curves of the planar sensors in Figure 5.21 follow this behavior. Additionally, the thinner 200 µm device shows an earlier saturation due to lower full-depletion voltage (*unirradiated curves*).

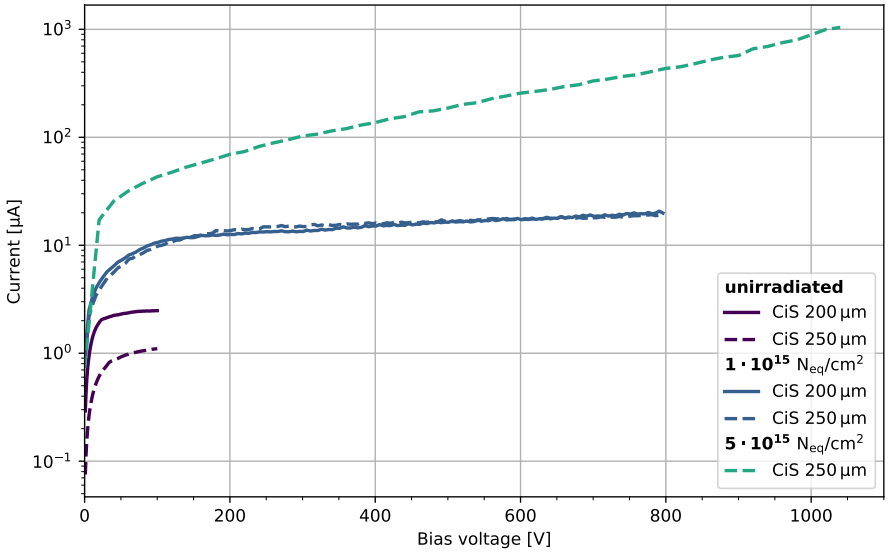


Figure 5.21: I-V curves of planar devices at different irradiation levels. Unirradiated measurements at room temperature and after irradiation at −30 °C after annealing. Front-End turned off during measurements except for measurement at $7 \times 10^{15}\,\text{n}_{\text{eq}}\,\text{cm}^{-2}$.

.

Localized impact ionization happens at strong electric fields ($\propto \exp(E)$, [Lou+03, p. 80]), where free electrons can gain enough energy to create secondary electrons. In an IV-curve this manifests as an additional exponential contribution. Impact ionization at high voltages can lead to a sudden increase of leakage current by orders of magnitudes. The corresponding voltage is called *breakdown voltage* and defines the maximum applicable voltage. Since electrical field strengths depend on doping profiles and geometry, the breakdown voltage varies between different sensor designs. For

example, the 3D-FBK design has a considerable lower breakdown voltage ($\sim 40\,\mathrm{V}$) than the CNM-3D design ($> 100\,\mathrm{V}$) due to pillars reaching the backside, creating field spikes between the $n$+-readout columns and the $p$-spray backside implantation [Bet+16, p. 10].

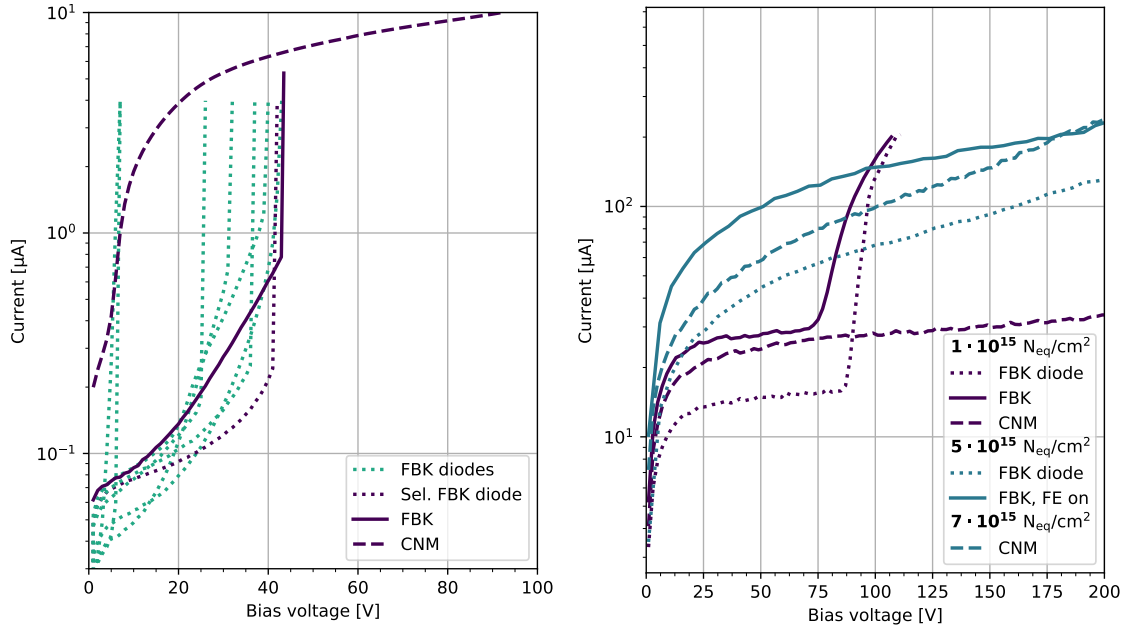


Figure 5.22: IV-curves of 3D-sensor devices. *Left:* Unirradiated devices at room temperature. Unused 3D-diodes depicted in light green and the selected 3D-FBK diode (D3) with a *dotted dark line*. Current of diodes scaled by the number of pixel to the FBK pixel matrix (*dark solid line*, (D2)). *Right:* IV-curves after irradiation to $1 \times 10^{15}\,\mathrm{n_{eq}\,cm^{-2}}$ – $7 \times 10^{15}\,\mathrm{n_{eq}\,cm^{-2}}$ measured at $-25\,^{\circ}\mathrm{C}$ – $-30\,^{\circ}\mathrm{C}$ after annealing. Front-End turned off during measurements except for FBK at $5 \times 10^{15}\,\mathrm{n_{eq}\,cm^{-2}}$.

But, even within the same sensor design, the breakdown voltage varies due to process variations. It is therefore an important qualification parameter during detector construction and defines mainly the production yield of a sensor. For IBL production, a minimum breakdown voltage of 40 volt for 3D devices is defined, a selection criterion also applied in this study. In general, 3D sensors show a lower yield than the planar sensors, which is attributed to the complexity of the process. This is also reflected in the measured IV-curves of the 3D-FBK diodes where only 2 of 12 tested 3D-diodes show a break down above 40 V. Figure 5.22 depicts 8 diode curves together with the selected device. The currents of the diodes are scaled by the number of pixels and show a comparable absolute leakage in comparison to the full-size 3D pixel matrix as expected.

For the planar sensors from CiS no breakdown is observed for voltage up to 1600 V. After irradiation the breakdown voltage usually increases. This can be seen for the FBK pixel sensors where the break down increases from 40 V when not irradiated to above 200 V after an irradiation to $5 \times 10^{15}\,\mathrm{n_{eq}\,cm^{-2}}$.

### 5.4.2 Determination of collected charge and charge-collection efficiency

Collected charge is determined by the most-probable-value (MPV) of the charge spectrum. The MPV is a more stable quantity for the average energy-loss due to fluctuations in the tail of the Landau distribution (Section 2.1.1). Single-pixel cluster-charge spectra are used following the reasoning in Section 3.1.2. Changes in the amplification chain caused by TID and increased leakage current from NIEL makes the noise vary at different irradiation levels. Therefore, it is important to deconvolve the spectrum by a function describing the noise. Otherwise higher noise would artificially lead to the determination of "more" collected charge. This is implemented by a deconvolution of the spectrum by a Gaussian with a sigma provided by the measured noise from TDC calibration (Figure 5.17) at MPV charge. The deconvoluted spectrum is fitted with a Langau, a convolution of a Landau and a Gauss function (Figure 5.23). The MPV of this

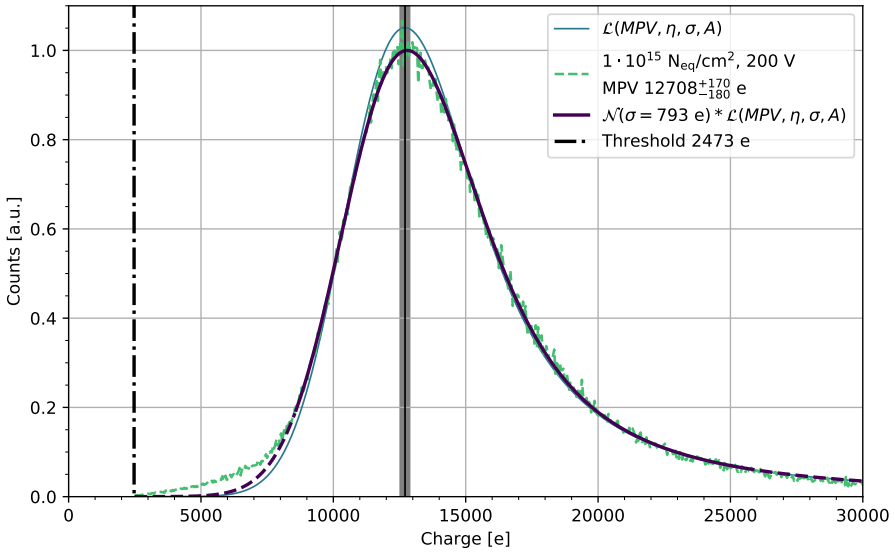


Figure 5.23: Langau $*$ Gauss fit to single-pixel cluster-charge spectrum of $^{90}$Sr electrons. Fit range depicted by solid dark line. Resulting Langau fit result after noise deconvolution is shown as a *solid light blue line*. Device D1 irradiated to $1 \times 10^{15}\,n_{eq}\,cm^{-2}$ at 200 V bias.

Langau defines the collected charge. The Gauss function is needed to better describe the measured charge spectra and smearing out of the Landau to lower values due to TDC calibration errors and charge sharing is expected (Section 2.1.1). Charge sharing and pixels that become noisy during long-term measurements (usually several hours) introduce an additional background to the spectrum. Thus, automatic fit range determination is implemented by maximizing the reduced $\chi^2$ while demanding a minimum range of MPV $\pm\, 5 \cdot \Delta$MPV. Fitting is done by $\chi^2$ minimization using the Minuit program package [JR75][CP]. The error of each bin with $N$ entries is assumed to have Poissonian fluctuations and set to $\sqrt{N}$. The numerical definition of the Landau function as introduced in [KS84] and used in common scientific program packages like CERN ROOT [BR97] and the GNU Scientific Library [Gou09] is ill-defined for the determination of the MPV fit error. In

this definition, the MPV is not an input parameter and influenced by two different parameters ($\mu$, $\eta$). Therefore, a new Python package is created (*pylandau*, [Poh16]) that uses as input the MPV for the position and $\eta$ for the distribution width. The package utilizes the same numerical definition as the packages mentioned above ($\mathcal{L}_{\text{orig}}$), but shifts the resulting Landau by changing $\mu$ to force the maximum at MPV. Additionally, the amplitude $A$ is scaled according to:

$$\max(\mathcal{L}_{\text{orig}}(\mu, \eta)) \stackrel{!}{=} \text{MPV} \rightarrow \mu_{\text{new}}$$
$$\mathcal{L}_{\text{new}}(\text{MPV}, \eta, A) = A \cdot \mathcal{L}_{\text{orig}}(\mu_{\text{new}}, \eta)$$

A gradient-less downhill-simplex algorithm numerically finds the maximum of the Landau [NM65]. An example of a fit to measured data is depicted in Figure 5.23. The MPV fit errors are determined using a numerical approach of the Minuit package (*Minos step*, [Jam06, p. 233]) to consider the non-linear errors introduced by the Landau function. The error for the MPV is defined as the distance from the minimum of the reduced $\chi^2$ contour at $\Delta\chi^2 = 1$. The contour is created by changing the MPV parameter and refitting the function while keeping MPV fixed and the other parameters ($A$, $\sigma$) free. This ensures that correlations among $A$ and $\sigma$ are considered. An example of a $\chi^2$ profile, determined for the MPV parameter, can be seen in Figure 5.24, together with the standard linear error-model leading to a parabola and symmetric errors.

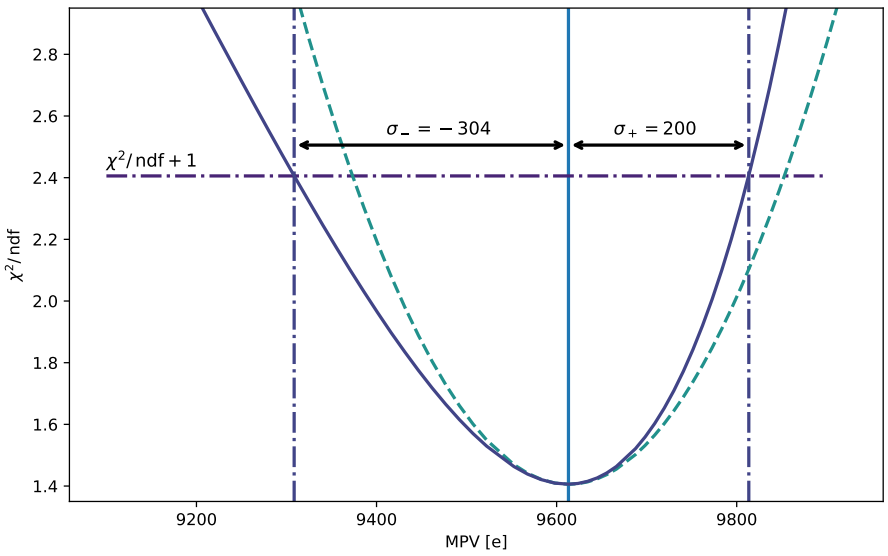


Figure 5.24: $\chi^2$/ndf contour for a Langau $*$ Gauss fit to a charge spectrum from $^{90}$Sr electrons. The dotted line shows the result assuming a linear error model leading to symmetric errors. The solid, dark curve shows the asymmetric errors calculated with a Minos step of the Minuit program package (see text).

### 5.4.3 Bias dependence of charge-collection efficiency

All devices with 3D and planar sensors (Table 5.2) are measured at multiple bias voltages below breakdown. Measurements are conducted at room temperature for unirradiated devices and at −30 °C after irradiation and annealing. The stated bias voltage is the voltage over the sensor, thus excluding the bias resistors. Errors are calculated from fit errors of the Landau function (Section 5.4.2) and the PlsrDAC calibration (Section 5.3.3). Figure 5.25 shows the CCE-curves for 3D sensors, determined as described in Section 5.4.2 and Figure 5.26 planar sensors. The

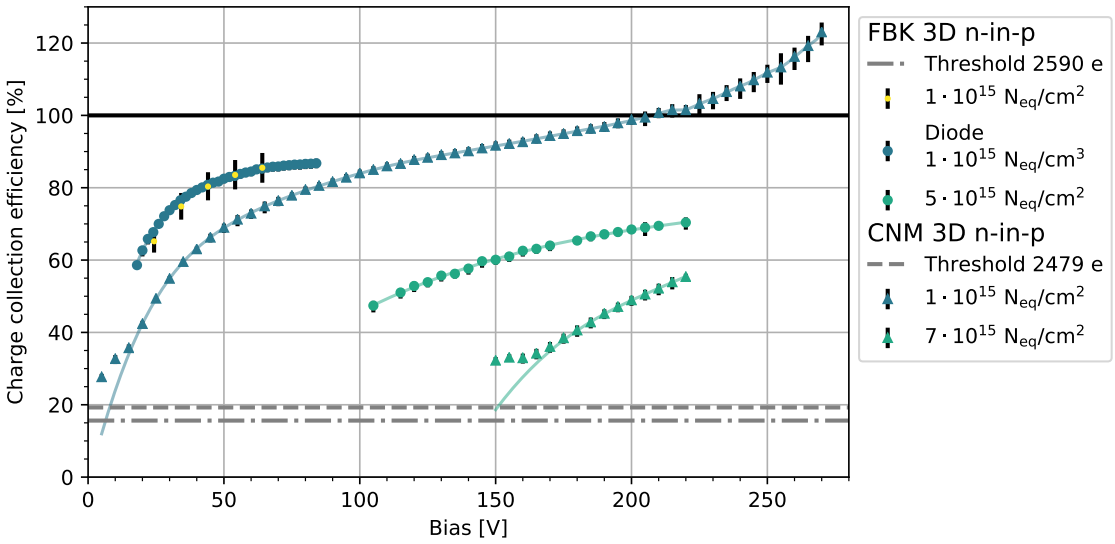


Figure 5.25: Charge-collection efficiency for 3D sensors as a function of bias voltage after different levels of irradiation (unirradiated, $1 \times 10^{15}\,\mathrm{n_{eq}\,cm^{-2}} - 7 \times 10^{15}\,\mathrm{n_{eq}\,cm^{-2}}$). Detailed explanation of curves are in text.

FBK diode and FBK pixel-matrix have very similar behavior, validating the calibration of the ATLAS FE-I4, even after irradiation (Section 5.3.3). The larger errors of the diode are mainly attributed to a broader Landau function, due to the missing trigger in the setup (see Figure 3.12). The hit detection threshold of the readout chip is about 2500 $e$ and given in percent of charge-collection efficiency. Close to the threshold, data points deviate from the smooth curve which is highlighted by a spline interpolation of $2^{\mathrm{nd}}$ degree. Here, the charge spectra can no longer be fully resolved. The maximum applied bias voltages of 75 V for FBK sensors is given by the sensor breakdown voltage. Due to the columns not fully passing through the sensor bulk in the CNM design, the CCE-curves are different to the FBK sensor. Additionally, the selected CNM device does not show breakdown at $1 \times 10^{15}\,\mathrm{n_{eq}\,cm^{-2}}$. For high bias voltages above 200 V, a charge-collection efficiency above 100 % is measured due to charge multiplication, a result comparable to measurements with strip detectors with similar 3D-column geometry [Koh+11, p. 1311]. Charge multiplication in 3D sensors occurs at high electric field regions (usually at readout columns). Since collected charge depends on the location of the particle hit, it is highly location dependent and introduces an inhomogeneity in the measured charge. Consequently, charge multiplication in

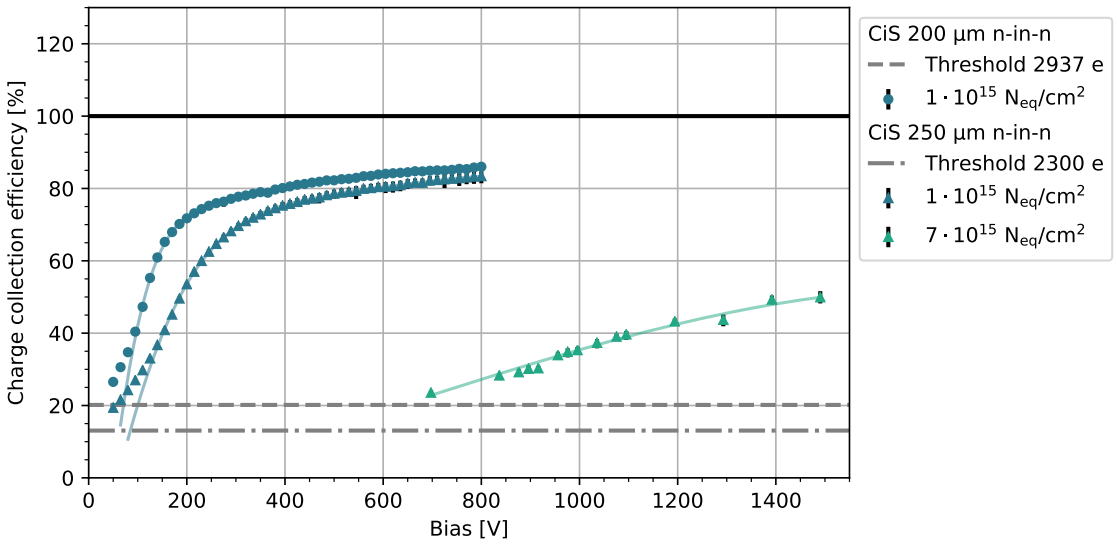


Figure 5.26: Charge-collection efficiency for planar sensors as a function of bias voltage after different levels of irradiation (unirradiated, $1 \times 10^{15}\,\mathrm{n_{eq}\,cm^{-2}} - 7 \times 10^{15}\,\mathrm{n_{eq}\,cm^{-2}}$).

3D-silicon sensors cannot be utilized to increase the hit-detection efficiency after irradiation. The location dependency can be measured using a high energetic particle beam to allow correlation of incident particle position with measured charge ([Rai+12, p. 1022]). The position dependency is also indirectly observed here by a broadening of the charge spectra, due to different levels of

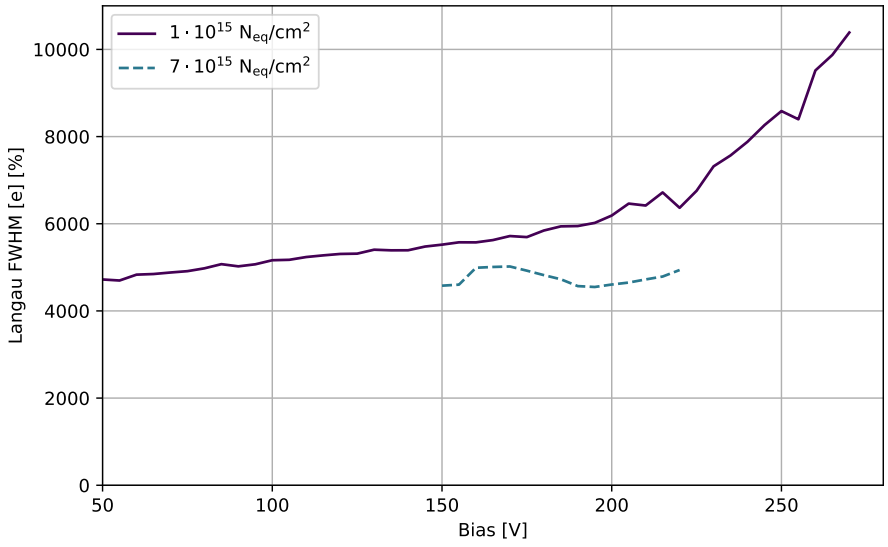


Figure 5.27: Full-width-half-maximum of Langau fits to charge spectra at different bias voltages. CNM-3D sensor after irradiation to $1 \times 10^{15}\,\mathrm{n_{eq}\,cm^{-2}}$ and $7 \times 10^{15}\,\mathrm{n_{eq}\,cm^{-2}}$. Charge multiplication increases distribution width at 200 V at $1 \times 10^{15}\,\mathrm{n_{eq}\,cm^{-2}}$.

charge multiplication. Figure 5.27 shows the FWHM of Landau spectra to increase significantly above 200 V where charge multiplication occurs. The broadening of the distribution also explains the increase of MPV fit-error in Figure 5.25. Partial charge multiplication artificially enhances the determined MPV and consequently the CCE and is unwanted. To exclude that the CCE-curves for other irradiation steps and devices are also affected, the consistency of the FWHM is checked (after noise subtraction) and no indication of charge multiplication is found. At $7 \times 10^{15}\,\mathrm{n_{eq}\,cm^{-2}}$ and the maximum tested bias voltage of 1500 V the efficiency reaches 50%.

### 5.4.4 Description with Scarce

The measurements presented in Section 5.4.3 are described with Scarce by optimizing the two input parameters: the charge-carrier lifetime $t_r$ and the effective doping concentration $N_{\mathrm{eff}}$. The n-type bulk of the planar sensors is treated as a p-type bulk due to type inversion, which occurs before the first irradiation step ($< 5 \times 10^{13}\,\mathrm{n_{eq}\,cm^{-2}}$). A minimization of the $\chi^2$ with fitting

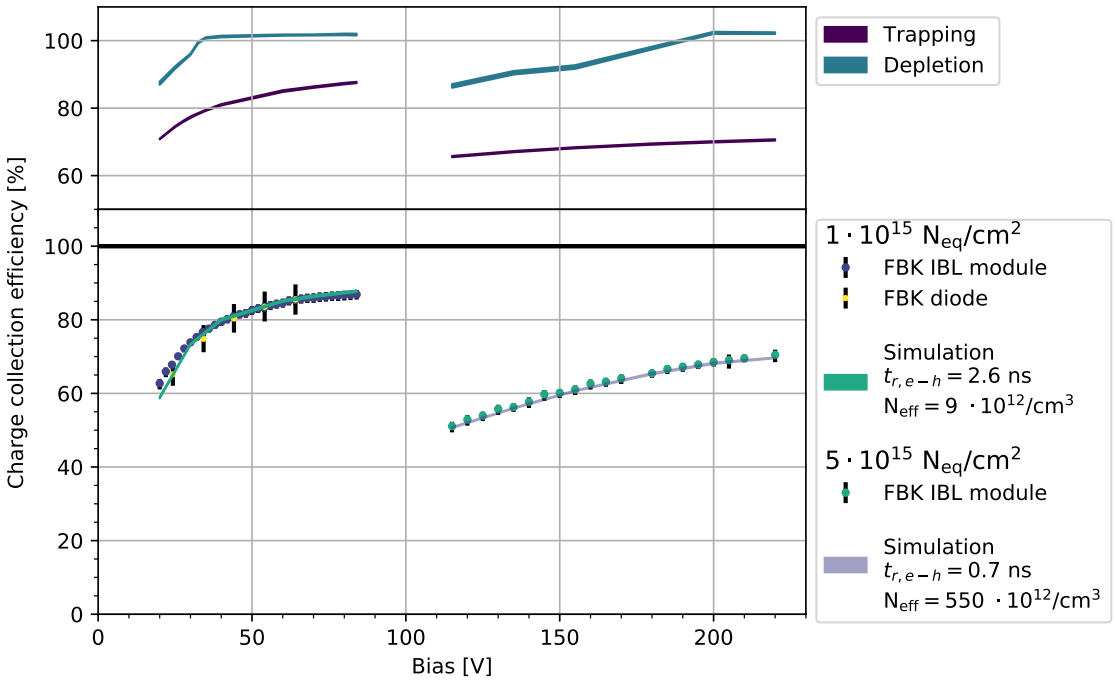


Figure 5.28: Simulation of measured charge-collection efficiency after irradiation for a 3D-FBK IBL sensor. *Top:* Influence of the bias voltage on charge-collection efficiency due to depletion (*bright*) and trapping (*dark*). *Bottom:* Measurements and simulated curves using parameters stated in legend. Width of curves are RMS values of multiple repetitions of the same simulation to depict simulation accuracy.

routines requires many simulations and is too demanding for the available computational power. Therefore, the optimization of input parameters is simplified to a discrete scan of the $\chi^2$ space, which is an easily parallelizable task. The optimization is performed on a computing cluster with

several hundred worker nodes provided by the Bonn Analysis Facility [18]. A minimum $\chi^2$ is found in two steps: a coarse search is performed first, with a step size of about $\Delta N_{\text{eff}} = 1 \times 10^{11}\,\text{cm}^{-3}$ and $\Delta t_r = 0.5\,\text{ns}$. Subsequently, a fine search is done after a step-size reduction of approximately one order of magnitude. The best estimated parameter values are used to evaluate the simulation accuracy by repeated simulations with these parameters. A small variation of about 2% RMS is identified due to diffusion simulation with limited numbers of quasi particles. Overlays of simulated curves to measurements are show in Figure 5.28 for the 3D-FBK sensor and in Figure 5.29 for planar sensors. The simulation accuracy is depicted as bands. Above the overlay are simulated

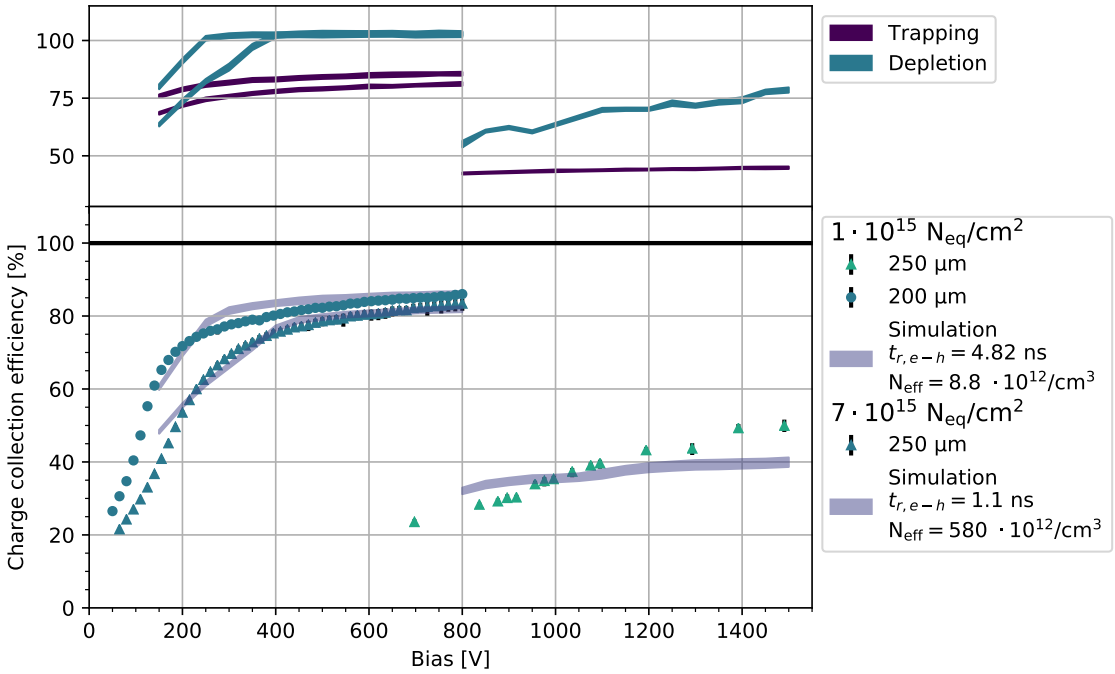


Figure 5.29: Simulation of the measured charge-collection efficiency after irradiation for a planar 250 µm IBL sensor. *Top:* Influence of the bias voltage on charge-collection efficiency due to depletion (*bright*) and trapping (*dark*). *Bottom:* Measurements and simulated curves using parameters given in legend. Width of curves are RMS values of multiple repetitions of the same simulation to depict simulation accuracy.

curves for two cases: charge-carrier trapping alone at full-depletion or partial depletion with no trapping. These curves allow to judge the influence of depletion and trapping on the charge-collection efficiency separately. For voltages before full-depletion, the increase of CCE is mainly affected by the depletion zone. The full-depletion voltage for the 3D-FBK diode is about 30 V and for the planar sensors 250 V and 380 V respectively at a fluence of $1 \times 10^{15}\,\text{n}_{\text{eq}}\,\text{cm}^{-2}$. The variation of depletion voltages is mainly a consequence of different electrode distances in the sensor designs (70 µm, 200 µm, 250 µm). At voltages above full-depletion, the CCE increases a few percent above 100%. The reason is faster charge collection due to higher bias voltages in comparison to the simulation for unirradiated sensors, which define the normalization. Faster charge collection

leads to less charge sharing (Section 2.1.5) and, as a result, to more charge per pixel. This effect is in the order of a few percent only and a comparable increase is observed in measurements with an unirradiated planar sensor. Faster charge collection is also the reason for an increasing charge-collection efficiency at voltages above full-depletion. Due to saturation of the charge-carrier velocity at high electrical fields (Figure 2.8), this influence disappears at high bias voltages leading to a less steep CCE curve. For irradiation above $5 \times 10^{15}\,\mathrm{n_{eq}\,cm^{-2}}$, a description with Scarce is not possible anymore. The strong increase of CCE in Figure 5.29 for the planar device at $7 \times 10^{15}\,\mathrm{n_{eq}\,cm^{-2}}$ cannot be explained with trapping and homogeneous effective doping concentration alone. Reasons are charge multiplication that becomes important at high electrical field strengths and is not implemented in Scarce and an inhomogeneous effective doping concentration leading to complex electrical field geometries (Section 2.2). To model the electrical field, measurements of its profile are needed. As a consequence, only simulations that describe the data are used in this study to extract an effective life-time of charge carriers and an effective doping concentration. The error on these values is assessed with the method introduced in Section 5.4.2. No refit is done when creating the $\chi^2$ contour of the parameter, but a simple minimum value calculation using the simulated parameter sets. An example is shown in Figure 5.30 for the parameters of the 3D-sensor after an irradiation with $5 \times 10^{15}\,\mathrm{n_{eq}\,cm^{-2}}$. The estimated values for all sensors and

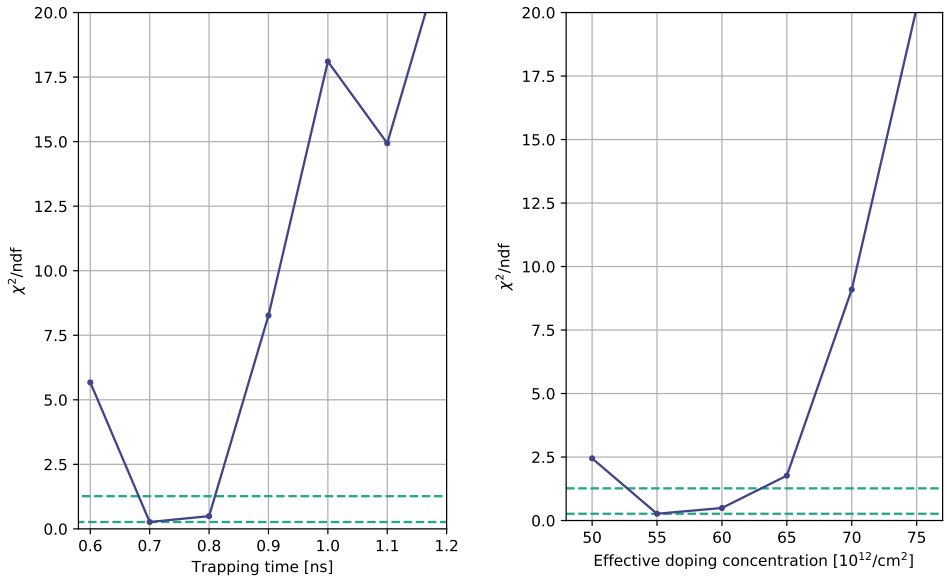


Figure 5.30: $\chi^2$/ndf contour from multiple simulations with Scarce. Data of the 3D-FBK sensor after an irradiation to $5 \times 10^{15}\,\mathrm{n_{eq}\,cm^{-2}}$. $\Delta\chi^2/\mathrm{ndf} = 1$ used for error estimation depicted as horizontal lines. *Left:* Contour for the trapping time. *Right:* Contour for the effective doping concentration.

irradiation steps are summarized in Table 5.5. The deduced life-times of charge carriers for 3D and planar devices do not agree within the errors, showing the limitations of this simulation using a minimum set of input parameters. In addition to the already mentioned uncertainty about the

| | Unirradiated | | $1 \times 10^{15}\,\mathrm{n_{eq}\,cm^{-2}}$ | | $5 \times 10^{15}\,\mathrm{n_{eq}\,cm^{-2}}$ | |
|---|---|---|---|---|---|---|
| | $t_r$ [ns] | $N_{\mathrm{eff}}$ [$10^{12}\mathrm{cm}^{-3}$] | $t_r$ [ns] | $N_{\mathrm{eff}}$ [$10^{12}\mathrm{cm}^{-3}$] | $t_r$ [ns] | $N_{\mathrm{eff}}$ [$10^{12}\mathrm{cm}^{-3}$] |
| Planar sensor | 0 | 1.48 | $4.8^{+0.1}_{-0.4}$ | $8.8^{+0.3}_{-0.8}$ | - | |
| 3D sensor | 0 | 0.46 | $2.9 \pm 0.4$ | $9.1 \pm 0.1$ | $0.75 \pm 0.08$ | $58 \pm 5$ |

Table 5.5: Effective life time of charge carriers and effective doping concentration for planar and 3D IBL-sensors at different irradiation levels. Extracted from measurements using the Scarce simulation.

electrical field and the missing charge-multiplication model, the assumption of equal trapping for electrons and holes and the reduction to a 2D simulation, introduces inaccuracies. To develop more realistic models, different measurements are needed on dedicated sensor test-structures that enable more direct measurements of trapping times and electric field profiles. For example, methods like the transient-current-technique that allows the deduction of the electrical field and trapping from measured velocity profiles of charge carriers. Or depletion-zone measurements using lasers that create charge at adjustable locations in the sensor bulk (E-TCT, two photon). Nevertheless, the determined trapping probabilities are in agreement with other independent measurements from literature, as depicted in the conclusions of Section 5.5.

## 5.5 Conclusion

The charge-collection efficiency depends on the gap between bias and read-out electrodes, as it affects the drift distance of charge carriers and the electric field strength. Due to similar effective doping concentrations of sensor materials after irradiation (Table 5.5), the measured depletion voltages of the planar and 3D-sensor designs at $1 \times 10^{15}\,\mathrm{n_{eq}\,cm^{-2}}$ can be well-described with the relation in Equation (2.36):

$$\text{depletion voltage} \propto (\text{electrode distance})^2$$

The measured values are summarized in Table 5.6. For planar sensors, the dependence of charge-collection efficiency at voltages below the full-depletion voltage is mainly given by the depletion width (Figure 5.29). This is not the case with 3D-sensors due to their in-homogeneous drift field (Figure 5.28). The maximum charge-collection efficiency at which the CCE curve saturates also depends on the electrode distance, as the charge-carrier mobility decreases at high electrical field strengths. However, the difference for the sensor designs studied is small (Table 5.6). After irradiation with $7 \times 10^{15}\,\mathrm{n_{eq}\,cm^{-2}}$, no saturation in charge-collection efficiency is observed. Additionally, the minimal 2-parameter model cannot describe the measurement data. These are indications of other, more complex effects, such as in-homogeneous space-charge (Figure 2.23) or charge-carrier multiplication. The maximum charge-collection efficiency between the 3D CNM sensor and the planar 250 µm CiS sensor are still comparable (55 % in Figure 5.25 vs. 50 % in Figure 5.26), even at such high-level irradiation. However, the significant difference in the sensor

| Sensor | Electrode distance | Full-depl. voltage | Max. charge-collection eff. |
|---|---|---|---|
| 3D FBK | $\sim 70\,\mu m$ | 30 V | 87 % |
| planar CiS | 200 µm | 250 V | 86 % |
| planar CiS | 250 µm | 380 V | 83 % |

Table 5.6: Sensor properties after an irradiation with $1 \times 10^{15}\,n_{eq}\,cm^{-2}$.

bias-voltages must be taken into account. The high bias voltage of 1500 V for the planar sensor is not practical in an experiment. For example, the maximum bias voltage in the IBL project is restricted to 1000 V (Table 2.2). Future sensors for the ATLAS pixel detector, that have guard rings on the readout side, will likely impose an even stricter limit on this value.
Another important aspect for the operation of sensors after irradiation is their power consumption, as it influences the cooling concept and thus the total material costs of the detector. The leakage current between the two sensor designs is defined by the generation current from radiation damage and is therefore comparable. However, a 3D-sensor that requires only one-sixth of the bias voltage of a planar sensor (220 V vs. 1500 V) also has only one-sixth of the power consumption. This is a major advantage of 3D-sensors and this advantage becomes increasingly important as luminosities at the LHC increase. Furthermore, the charge-collection efficiency of a 3D-sensor can be optimized by the column spacing, regardless of the sensor thickness, and therefore independent of the total charge and leakage current.

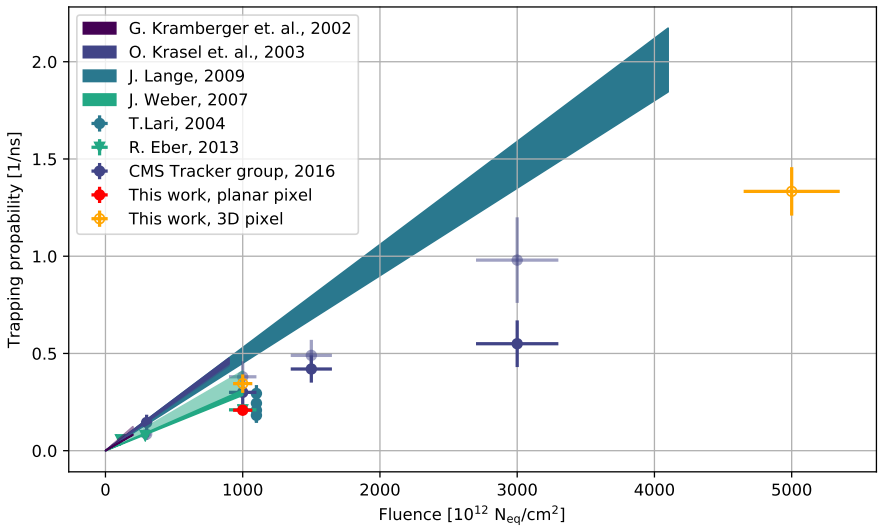


Figure 5.31: Trapping probabilities from multiple publications. Values determined separately for electrons and holes are distinguished using *dark* and *bright* colors. Areas are trapping probabilities measured with transient-current-technique published in [Kra+02a], [Kra+03], [Lan09], and [J W07]. The width of the area gives the $\pm\sigma$ confidence interval. Points are trapping probabilities from charge-collection efficiency measurements published in [Lar04], [Ebe13], and [Ada+16]. Values obtained in this study are highlighted in *red*.

For an irradiation up to $5 \times 10^{15}\,\mathrm{n_{eq}\,cm^{-2}}$, the description of measured data with the minimal 2-parameter model succeeds . The simple model of an effective trapping probability, which depends linearly on the fluence (Equation (2.79)), can be validated even at a high fluence of $5 \times 10^{15}\,\mathrm{n_{eq}\,cm^{-2}}$ and despite the complex electrical field profiles of 3D-sensors. The extracted trapping probabilities of free charge-carriers in silicon are summarized in Figure 5.31 along with already published values.

# 6 Passive CMOS-sensors

With the upgrade of the inner tracking detector of the ATLAS experiment, the surface covered by pixel detectors increases from less than $2\,\mathrm{m}^2$ at present ([ATL08, p. 39], [**Capeans:2010jnh**]) to approximately $14\,\mathrm{m}^2$ ([Col17, p. 12]). 3D-sensors are the preferred option for the innermost barrel layer of hybrid pixel detectors due to their radiation hardness and low power consumption, as presented in Chapter 5. Since only a relatively small area is attributed to the innermost layer, a complex production with relatively low yield is still feasible. For the remaining four barrel layers, different designs are investigated ranging from hybrid pixel detectors with ‚common' planar sensors or hybrid pixel detectors with active sensors that integrate the first amplification state to monolithic detectors where sensor and readout are located on the same silicon substrate [Hir+16; Per+17; Wer16]. Especially the outer layers with moderate requirements for the radiations hardness (layer $4/5 = 1 \times 10^{15}\,\mathrm{n_{eq}\,cm^{-2}} - 2 \times 10^{15}\,\mathrm{n_{eq}\,cm^{-2}}$ [Col16]) create a demand for new, large area concepts with cost-efficient designs that simplify production. Examples are monolithic CMOS detectors that do not need fine-pitch bump bonding and sensors using large p-type wafers [Unn+13] without the demanding double-sided process that has been the standard to date for the ATLAS pixel sensors [ATL08, p. 35]. With the increasing availability of high-voltage CMOS processes to small-market customers, another option becomes attractive: the utilization of a CMOS processing line to produce the sensor of a hybrid pixel detector. Since such a sensor does not incorporate any active components (transistors), they are termed: *passive* CMOS-sensors. The benefit of this approach is the utilization of cost-effective, high-throughput production lines with the ability to enhance the sensor design by CMOS-process features that are otherwise mostly not available:

- Multiple metal layers can be used to create a redistribution layer between readout pixels and sensor pixels to allow multi-chip modules without elongated inter-gap pixels.
- Metal-insulator-metal capacitors (*MIM*) can AC-couple the sensor-pixel to the readout-pixel that leakage current compensation in each readout-pixel is not mandatory simplifying its design.
- High-resistive polysilicon layers can be used for bias resistors connecting each sensor pixel to a bias grid. This allows for sensor qualification with IV curves before flip-chipping without the drawback of the common punch through implantations decreasing the hit efficiency.
- Low-resistive polysilicon layers for field plates can be used to increase the breakdown voltage.

Figure 6.1 depicts such a hypothetical device incorporating these benefits for a hybrid pixel detector module. To assess its feasibility for the future ATLAS pixel detector a prototypes of passive CMOS

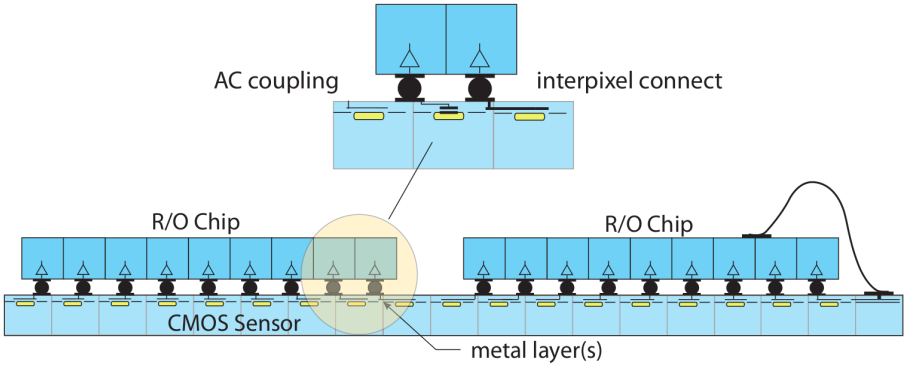


Figure 6.1: Hypothetical double-chip module using a passive CMOS sensor with AC-coupled pixels and pixel redistribution metal layer to prevent elongated gap pixels. From [GW18].

sensors were designed and are characterized here at irradiation levels as anticipated for the future outermost barrel pixel-layer.

## 6.1 Design

Multiple $n^+$-in-p pixel matrices and test structures in LFoundry 150 nm CMOS technology [LFo] have been produced to study break-down behavior, charge collection, pixel isolation, and hit efficiency before and after irradiation. The designs are produced on large 200 mm, high-resistive, Czochralski p-type wafers. The resistivity, as specified by the foundry, is nominally $4\,\mathrm{k\Omega\,cm} - 5\,\mathrm{k\Omega\,cm}$ and at least $2\,\mathrm{k\Omega\,cm}$. The passive CMOS submissions are shared with other active devices requiring a (more expensive) high-resolution mask set; a requirement to be relaxed for future dedicated sensor submissions. One of the produced designs is a $1.8\,\mathrm{mm} \times 4\,\mathrm{mm}$ pixel-sensor prototype with similar pixel geometry as the ATLAS IBL planar sensors (Section 2.3.1). The pixel matrix is depicted in Figure 6.2 and consists of $16 \times 36$ pixels with a pitch of $50\,\mu\mathrm{m} \times 250\,\mu\mathrm{m}$. Half of the pixels are AC-coupled with resistive bias. The other half is DC-coupled with a punch-through biasing structure to connect the pixel to a bias grid. A high-ohmic connection to a bias grid is needed to allow sensor qualification measurements (leakage current, breakdown voltage) before the flip-chip process [Wes+96, p. 227] and to define a fixed potential for the AC-coupled pixels. AC-coupling is archived with a 3.2 pF capacitor and a $15\,\mathrm{M\Omega}$ polysilicon resistor present in each pixel. The layers implementing the MIM capacitor (Figure 6.2, green) and the polysilicon resistor are chosen as large as possible. The n-implantation for charge collection in each pixel measures $30\,\mu\mathrm{m} \times 230\,\mu\mathrm{m}$ with $20\,\mu\mathrm{m}$ gap to the neighboring n-implantations. A $4\,\mu\mathrm{m}$ p-stop grid is located between the pixels to ensure n-implantation isolation after irradiation. It is implemented below (contactable) field plates made of a low-resistive polysilicon layer with the intention to flatten field spikes after irradiation, thus enhancing break down behavior [Hem18]. Two outermost columns have varying charge-collection node widths ($15\,\mu\mathrm{m} - 30\,\mu\mathrm{m}$, Figure 6.2 *right*). These columns allow the investigation of the influences of the fill factor on hit efficiency and input capacitance (Section 6.3). The *fill factor* defines the area fraction taken by the charge-collection node to the total surface area.

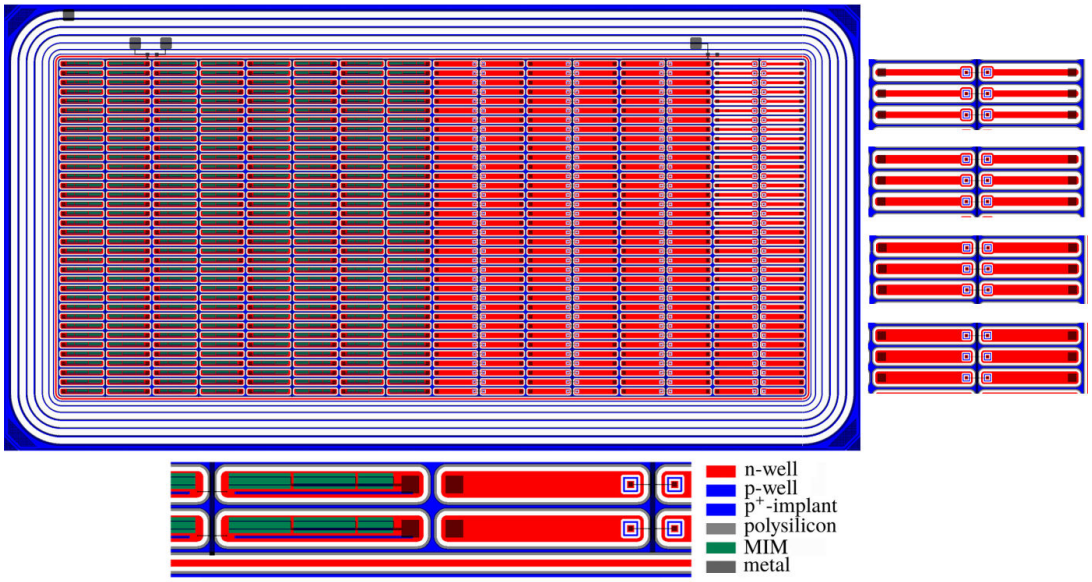


Figure 6.2: Sensor matrix with 576 pixels surrounded by one n-well ring and subsequently 7 p-type guard rings (*top*). The *bottom* shows 4 edge pixels with bump pads. *Left:* pair of AC-coupled pixels with a large area fraction filled by *MIM* layers providing capacitive coupling; *right:* pair of DC-coupled pixels containing dedicated implants for punch through biasing (bias dots). *Right*: edge columns of DC-coupled pixels with varying n-implantation widths (15 µm – 30 µm). [Poh+17]

The matrix is surrounded by an n-implantation to restrict the active volume of the edge pixels followed by seven p-implantation guard rings to bring down the high voltage that is applied from the backside. The pixel sensors have been thinned to 300 µm by LFoundry and to 100 µm by Ion Beam Services in France [IBS]. Subsequently, their backside is processed with a p-implantation and metalization layer. Thinning to 100 µm was done in a TAIKO process [DIS] where the outer edge of the wafer is left unground to create a self-sustainable wafer that simplifies handling during production. [Poh+17]

## 6.2 Leakage current and maximum bias voltage

The breakdown voltage defines the maximum applicable reverse bias voltage to create the depletion region (Section 2.37) that contributes to the charge signal. The breakdown-voltage value and distribution are a function of the sensor design and process variations. The variations mainly define the yield during production. To access these variations current curves as a function of bias are measured for 114 passive CMOS sensors located on one wafer half with 300 µm thickness. The bias grid is connected with needles using a wafer probe-station and the metalized backside is contacted with the probe-station chuck. The current-voltage curves show very similar characteristics, as depicted in Figure 6.3, with a break down voltage above 100 V for all sensors measured. This creates a sufficient depletion depth of about 130 µm assuming the minimum resistivity of 2 kΩ cm.

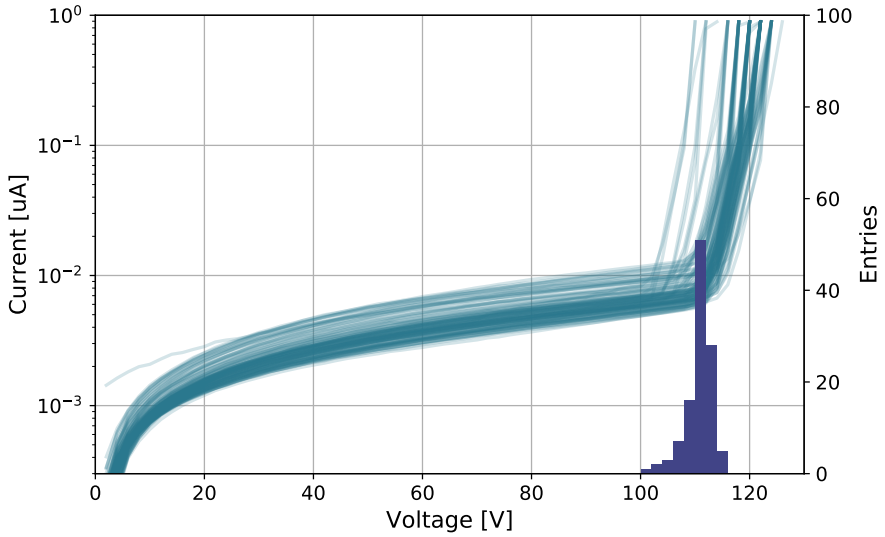


Figure 6.3: Current voltage characteristics of 113 passive CMOS sensor. Measured on a 300 µm wafer. The histogram depicts the break down voltages.

Only one sensor showed a short between the high-voltage contacts due to a production error, as recognized by visual inspection (Figure 6.4a). The break down location before flip-chip is identified on 5 different sensors via electron-emission spectroscopy to be located at the bias dots of the DC-coupled pixels (Figure 6.4b). After bump bonding of the sensor to the ATLAS FE-I4 the break down voltage changes severely. Three out of 10 sensors show a higher break down at about 160 V while the remaining sensors break down below 10 V or exhibit ohmic behavior. The reason is likely an ohmic connection of the sensor edge to the front-end via bump bonds. This issue is expected

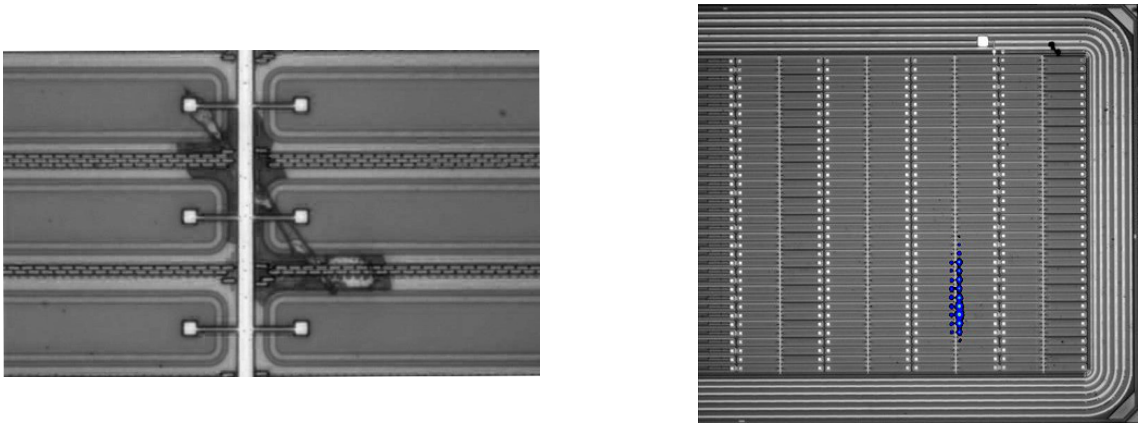

Figure 6.4: Pictures of the pixel matrix with DC-coupled pixels. *Left:* Processing error below the bias grid metalization creating a short between bias voltage and ground. *Right:* Picture with overlay from Electron Emission Spectroscopy showing the break down to be located at the bias dots (measurement by Julie Segal).

for sensors that do not fully cover the front-end and can be mitigated by electrical insulation of the sensor edge with glue, a step that is not done for these prototypes. An inherent process problem for LFoundry sensor designs can be excluded, since the IV curves return to normal after de-soldering and similar monolithic designs do not show early break down. IV-curves after flip chip for a 300 µm thick sensor before and after irradiation are depicted in Figure 6.5a. The initial

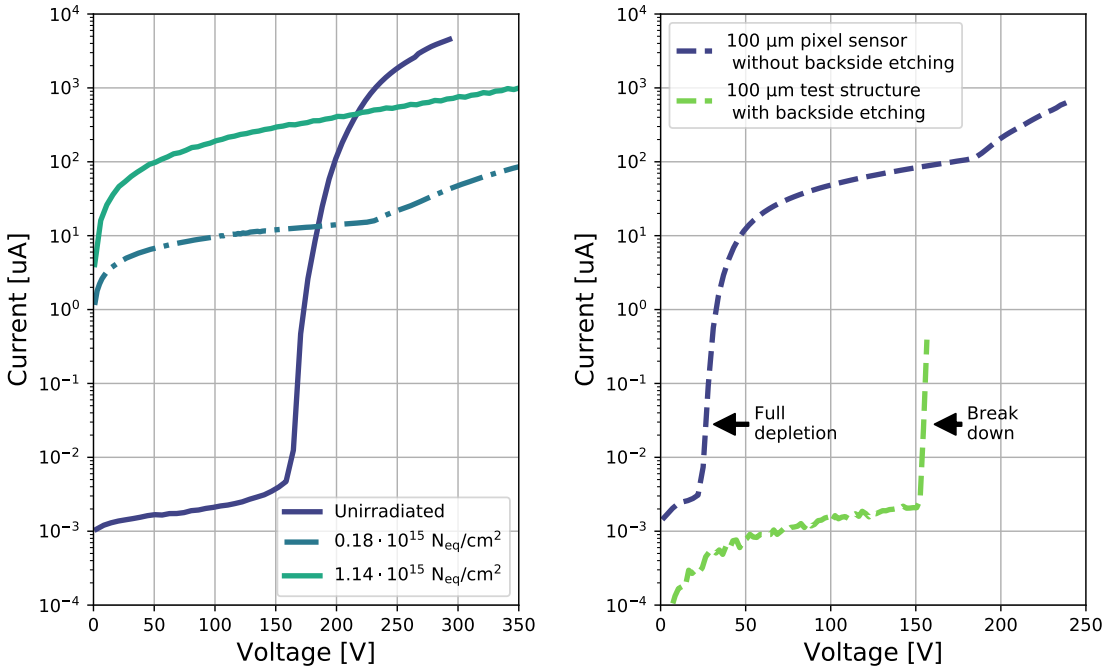


Figure 6.5: Current voltage curves of LFoundry passive CMOS sensor prototypes after flip-chip to the ATLAS FE-I4. *Left:* Current at different levels of irradiation. Scaled to room temperature. *Right:* Comparison between a flip chipped 100 µm sensor without backside etching to a 100 µm pixel matrix with backside etching.

break down voltage increases after irradiation and no breakdown is measured for voltages in excess of 700 V after $1.1 \times 10^{15}\,\mathrm{n_{eq}\,cm^{-2}}$. The 100 µm thin device exhibits an increased leakage current at 23 V. This corresponds to the voltage when full-depletion is reached assuming a reasonable resistivity of 5.5 kΩ cm (see Figure 6.15). The reason is a missing etching step after backside grinding leaving a layer of damaged silicon. This effect has been reported before (e.g. [Oki+15]) and can be mitigated with an additional etching step after backside grinding. Figure 6.5b shows the successful mitigation of the abnormal leakage when comparing the passive sensor to a similar test structure that is treated with plasma etching. The excess leakage renders operation of the sensor at full-depletion impossible due to an increased noise hits-rate. Therefore, all results presented in this chapter are for not fully depleted passive CMOS sensors. For charge collection and hit-efficiency studies this is a worst-case scenario; pixel sensors are usually operated at voltages in excess of the full-depletion voltage, especially at moderate irradiation levels or when using thin devices.

## 6.3 Capacitance and noise

The capacitance at the input of the CSA of the pixel readout-chip decreases gain ($g \sim \frac{1}{C_{\text{in}}}$ [Hav14, p. 14]) and increases electronics noise ($\sigma_{\text{ENC}} \sim \sqrt{C_{\text{in}}}$ [Kar10, p. 103]) and rise time ($\tau_r \sim C_{\text{in}}$ [Kar10, p. 19]) of the charge signal. It is therefore an important parameter to consider and minimize when designing a pixel detector. The main contribution to the input capacitance is attributed to the sensor capacitance $C_{\text{d}}$ which in turn is primarily given by the geometry of the readout implantation (area and perimeter with respect to total pixel area). For ALTAS IBL planar geometries the sensor capacitance is dominated by the inter-pixel capacitance, followed by the capacitance towards the sensor backplane and towards the readout chip [Hav+13, p. 87]. The inter-pixel capacitance depends linearly on the ratio of the readout implantation-width to pixel-pitch [Gor+01, p. 72]. To investigate the change of sensor capacitance with different ratios for 50 µm × 250 µm pixels a dedicated test structure in LFoundry process with multiple pixel geometries was designed. Capacitance measurements are performed using a charge-pump circuit located on the same structure. The circuit switches a voltage between $V_{\text{in}}$ and GND with a fixed frequency $f$ to periodically charge and discharge the sensor capacitance $C_{\text{d}}$. For frequencies low enough to fully charge and discharge the capacitance, one can determine its value with an average DC-current measurement ($\bar{i}$) using an ampere-meter:

$$C_{\text{d}} = \frac{Q}{V_{\text{in}}} = \frac{\int_0^T i(t)\,dt}{V_{\text{in}}} = \frac{\frac{1}{T}\int_0^T i(t)\,dt}{f\,V_{\text{in}}} = \frac{\bar{i}}{f\,V_{\text{in}}} \tag{6.1}$$

Figure 6.6 depicts measured capacitance of two pixel-geometries that are also realized in the passive CMOS sensor. When applying a bias voltage in excess of 100 V, the passive CMOS pixel with IBL

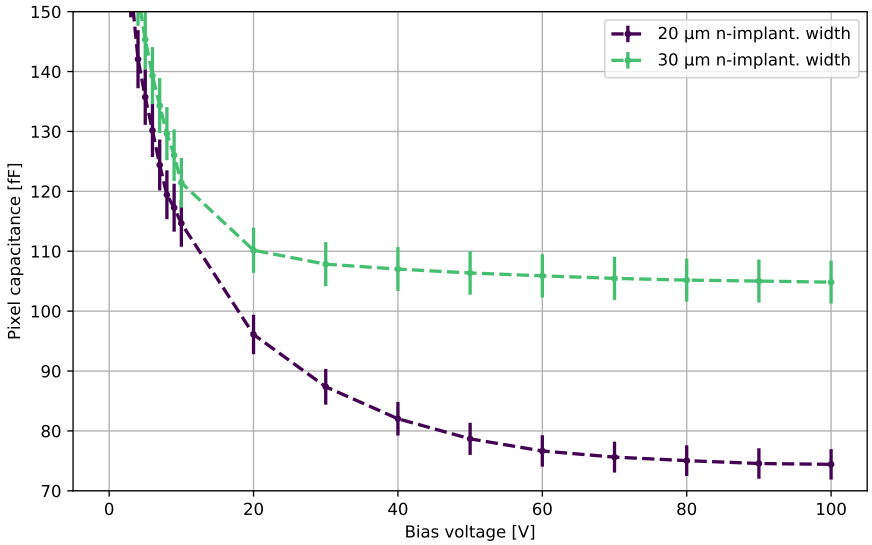


Figure 6.6: Capacitance of DC-coupled pixels with varying readout implantation widths. Measured on dedicated test structure with pixel geometries as in Figure 6.2. Data from [Loe17].

planar pixel geometry (width/pitch = 30 µm/50 µm) has a capacitance of about 105 fF, a value similar to the measured capacitances of ATLAS IBL sensors (110 fF [Hav+13, p. 86]). The pixel with reduced width-to-pitch ratio (20 µm/50 µm) shows a significant reduction of the capacitance to 75 fF. The consequential, unfavorable reduction of the hit efficiency due to the smaller fill-factor is discussed in Section 6.5. Figure 6.7 shows the electronic noise of the ATLAS FE-I4 with the passive

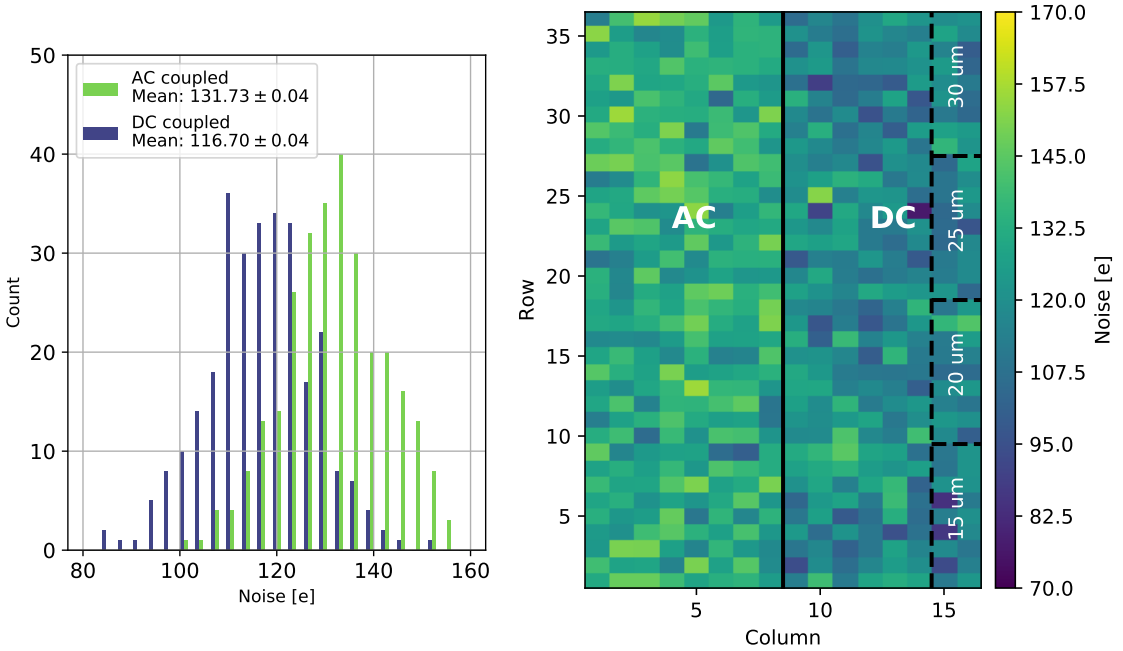


Figure 6.7: Electronic noise of a pixel detector with passive CMOS sensor in LFoundry technology and ATLAS FE-I4 readout chip. *Left:* Histogram of per pixel noise for AC- and DC-coupled pixels. *Right:* Noise values of pixels in the array with markers depicting the different pixel flavors (coupling and fill factor).

CMOS sensor measured with a threshold scan (Section 5.3.2). The optimization of the FE-I4 to an input capacitance above 100 fF and the relatively large gain and noise variation at pixel level prevent the observation of reduced noise for pixels geometries with reduced capacitance (Figure 6.7*b*). However, a relatively large difference (132 $e$ vs 117 $e$) is observed between AC- and DC coupled pixels. The reason are likely additional parasitic capacitances by the layers implementing the bias resistor and MIM capacitor for AC-coupling. Their values have not been optimized and are chosen as large as possible given the area constrains (C=3.2 pF, R=15 MΩ). These values are subject to optimization in future submission to reduce the additional capacitance. Nevertheless, a noise value of 132 $e$ is still below the measured noise when using a 3D-sensor (140 $e$). Since the sensor capacitance and noise values of 3D- and planar sensors are well-known and the noise dependence on input capacitance is strictly monotone, the capacitance of AC-coupled pixels can be estimated to be below 170 fF [Kar10, p. 102]. Table 6.1 summarizes noise and capacitance values for the passive CMOS pixels in comparison to ATLAS IBL pixel sensors.

| Sensor | Capacitance [fF] | Noise [$e$] |
|---|---|---|
| Pass. CMOS, DC pixel, small n-implant. | 75 fF | 115 $e$ |
| Pass. CMOS, DC pixel | 105 fF | 115 $e$ |
| Pass. CMOS, AC pixel | $< 170$ fF | 130 $e$ |
| ATLAS IBL planar | 110 fF | 120 $e$ |
| ATLAS IBL 3D | 170 fF | 140 $e$ |

Table 6.1: Noise and input capacitance of passive CMOS pixels with AC- and DC-coupling in comparison to ATLAS IBL pixel sensors when read out with the ATLAS FE-I4. IBL sensors capacitance values from measurements in [Hav+13] with about 5 fF uncertainty. Noise values from threshold scan measurement (Section 5.3.2) with 5 % error. The input capacitance of AC-coupled pixels is maximum estimated from noise.

## 6.4 Particle-telescope setups

To investigate the hit detection-efficiency of pixel detectors with passive CMOS-sensors several test-beam measurements (Chapter 4) are conducted. Two different telescope setups with distinct advantages are used in these measurements.

### 6.4.1 Mimosa26 telescope

A high-resolution telescope (*EUDET* [Rub12]) consisting off six Mimosa26 pixel detectors and one ATLAS FE-I4 time-reference plane is utilized for the test-beam at the SPS located at CERN. The small pixels of the Mimosa26 planes (18.4 µm × 18.4 µm), in combination with a high energetic pion beam (120 GeV/c [H600]) with negligible multiple scattering, lead to a high pointing resolution $< 3$ µm [Jan+16]. However, due to a slow rolling shutter readout with a frame time of 115.2 µs the reconstructed tracks lack precise time-stamping information for unambiguous assignment to *DUT* hits. Although an ATLAS FE-I4 time-reference plane is used to reduce the probability of

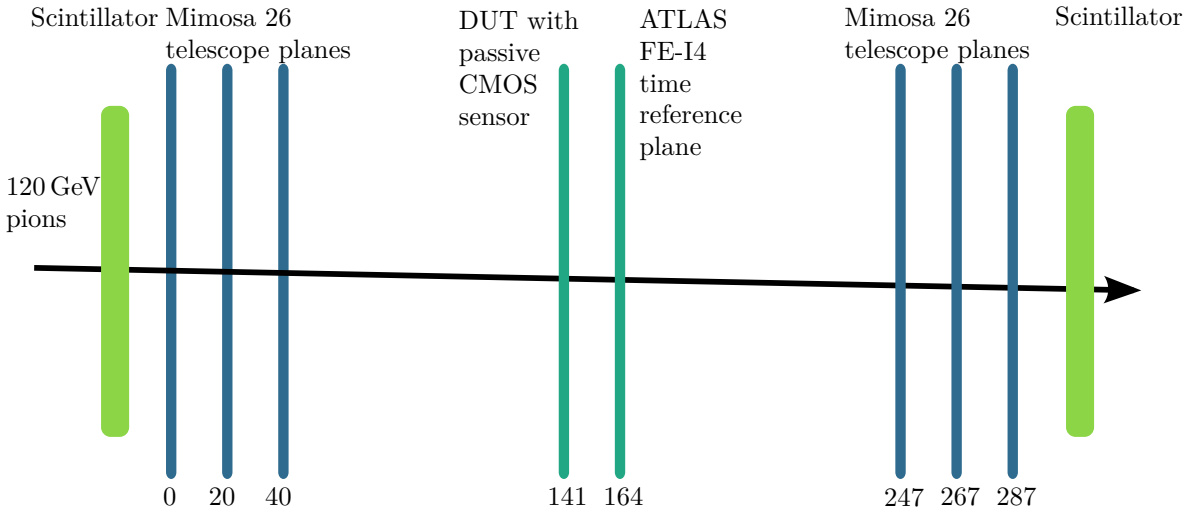


Figure 6.8: High-resolution *EUDET* telescope setup with time-reference plane and DUT with passive CMOS sensor. Z-positions of planes in mm and approximately to scale.

wrong assignment, the probability is still too high to measure the hit efficiency with small error ($< 1\%$). Each track with a wrong time stamp decreases artificially the determined *DUT* hit efficiency (Section 4.2). The telescope setup with the device under test is shown in Figure 6.8.

### 6.4.2 ATLAS FE-I4 telescope

The other telescope is a custom-made, fast FE-I4 based telescope consisting of two planes of ATLAS IBL planar pixel detectors (Section 2.3.1). The advantage of this telescope is a very high probability of track detection ($\gg 99\%$), a low probability of building fake tracks due to a negligible amount of noise hits ($\ll 1$ noise hits per pixel per $1 \cdot 10^6$ events), and a time stamp with 25 ns precision. This leads to a small systematic error in the efficiency determination, as discussed in Section 4.2.2. Additionally, the integration time per trigger (400 ns) of the telescope planes matches the integration time of the passive CMOS sensor device. This simplifies track assignment to DUT hits. The disadvantage of this telescope are large pixels (up to 250 µm in one dimension) leading to a poor pointing resolution of up to 200 µm.

According to the capabilities of the two telescopes, the high-resolution telescope is used to measure the relative hit efficiency with sub-pixel resolution and the fast telescope to determine the absolute hit efficiency with small error. The fast telescope is used at the Electron Stretcher Accelerator (*ELSA*) in Bonn, where electrons with a rate up to 625 MHz are available [Heu+16, p. 4]. The low energy (2.5 GeV – 3.2 GeV) leading to multiple scattering and poor pointing resolution is of no concern for the absolute hit efficiency. A central readout signal (*trigger*) for the telescopes and *DUT* is created from scintillators, when they are hit in coincidence. The trigger command is created by a trigger-logic-unit (TLU, Section 5.2.2) when all devices signal readiness for trigger acceptance (*trigger veto*). The minimum delay between two triggers is set to about 15 µs for the fast telescope and about $2 \times 115.2$ µs for the high-resolution telescope corresponding to the readout time of two frames. The trigger-logic-unit also creates a trigger identifier that is embedded into the data streams and used for offline event correlation between the devices.

## 6.5 Hit efficiency

The mean efficiency of pixel detector modules with 100 µm and 300 µm thin LFoundry passive CMOS sensors is measured in 4 test beams at ELSA using a 2.5 GeV – 3.2 GeV electron beam. The average hit efficiency is determined as the ratio of tracks seen by the sensitive sensor volume divided by the total number of tracks through the same volume. This ratio is calculated for each event individually. One event combines the hits recorded within the integration time of 400 ns. Figure 6.9 shows the time of hit detection within one event with 25 ns binning. Only two bins are expected due to the random phase between time stamping clock and particle hit. A larger time windows is measured here due to jitter in the trigger generation of the readout system requiring the selection of a relatively large time window of 400 ns. Figure 6.10 summarizes the efficiencies for different bias voltages and levels of irradiation (unirradiated, $1.8 \times 10^{14}\,\mathrm{n_{eq}\,cm^{-2}}$, $1.14 \times 10^{15}\,\mathrm{n_{eq}\,cm^{-2}}$). Each

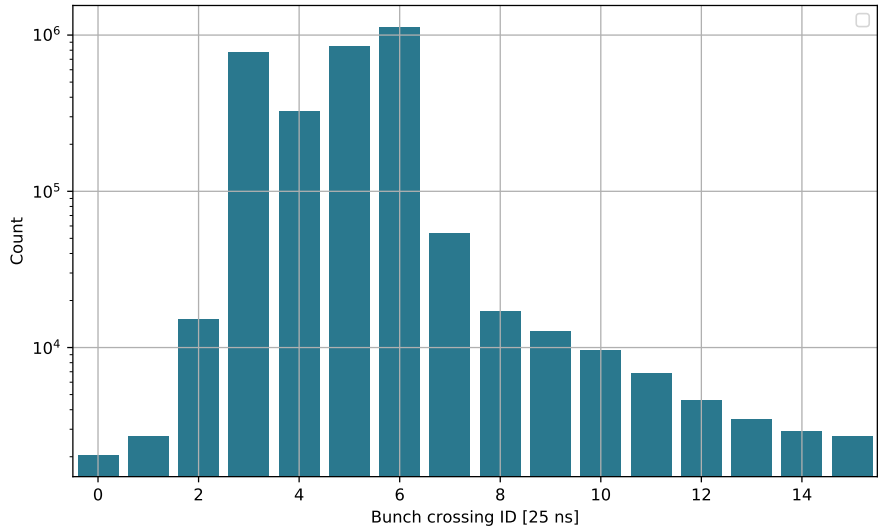


Figure 6.9: Time of hit recording for events with 400 ns readout window. Triggering with scintillator and TLU (see Section 5.2.2). Time stamps with 25 ns width. ATLAS FE-I4 with LFoundry passive CMOS sensor in a 2.5 GeV electron particle beam.

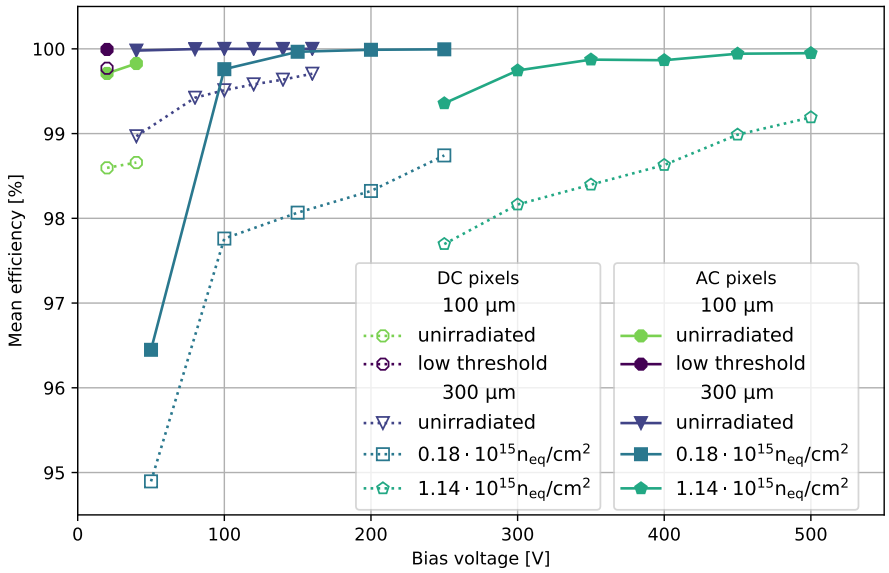


Figure 6.10: Mean efficiency of LFoundry passive CMOS sensors as a function of bias voltage. Readout with the ATLAS FE-I4 chip at a charge detection threshold of about 3000 $e$ and 1500 $e$ (*low threshold*). 3 levels of irradiation are depicted (unirradiated, $1.8 \times 10^{14}$ $n_{eq}$ $cm^{-2}$, $1.14 \times 10^{15}$ $n_{eq}$ $cm^{-2}$). A 100 µm and 300 µm thin sensor is used and the efficiency is shown for AC-coupled (*solid curves*) and DC-coupled (*dotted curves*) curves separately. Based on [Poh+17].

point is determined according to the analysis as summarized in Section 4.1. For the efficiency calculation at least $10^5$ electron tracks are used that intersect with at least 35 sensor pixels located in the center. The detection threshold is set to about 3000 $e$ for the modules with 300 µm sensor and 1500 $e$ for the 100 µm sensor modules. The track association distance is with 500 µm chosen relatively large due to the coarse pointing resolution of the ATLAS FE-I4 telescope in x-direction. The uncertainty of the efficiency is calculated as depicted in Section 4.2 and is below 1 ‰. Repeated measurements with the same parameters validate a very small error. Efficiency values are reproducible with sub per mille deviations. The difference between AC- and DC-coupled pixels is about 1 % after irradiation. This can be attributed to the punch-through implantation to the bias grid, creating a competing charge collection node. The inefficient area at the bias dots is visible in the in-pixel efficiency map (Figure 6.11). The AC-coupled pixels that use a resistor to connect

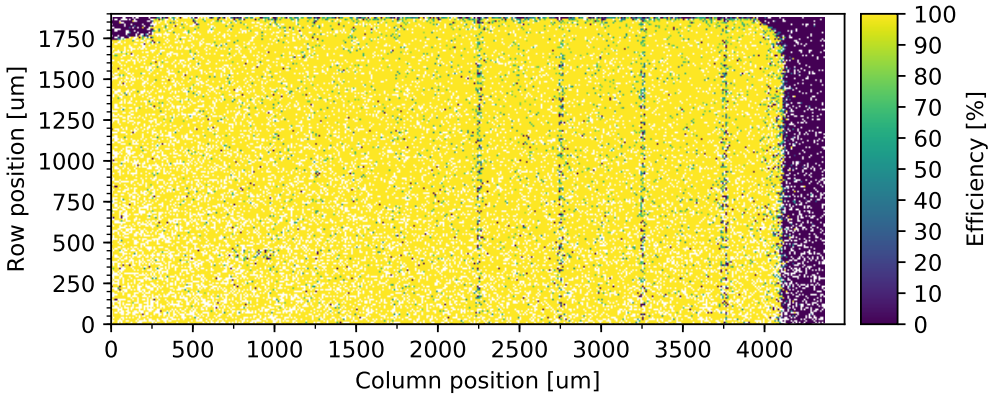


Figure 6.11: Hit efficiency of an LFoundry passive CMOS sensors readout with the ATLAS FE-I4 at a charge detection threshold of about 3000 $e$. Two disabled pixels (*top, left*) and the sensor edge (*right*) are visible. Areas where efficiency determination is not possible due to low statistics are white. From [Poh+17].

to the bias grid do not show this efficiency drop and are fully efficient before irradiation (100 %). Resistor biasing is therefore a promising feature available for CMOS sensors; especially for future sensors with smaller pixels where a punch-through implantation would constitute an even larger fraction to the total sensitive area. Another investigation, in view of smaller pixels for future pixel detectors, is the variation of the readout implantation width. Although the sensor capacitance per pixel is reduced for small pixel designs, the total capacitance per area, a main driver for the overall power consumption, increases. The archived reduction of the sensor capacitance for the passive CMOS sensor with smaller readout implantation is about 30 %, as discussed in Section 6.3. The corresponding reduction of the hit efficiency, due to low field regions between pixels, is measured in a test beam and shown in Figure 6.12. The results show that the efficiency reduction after irradiation of the low-capacitance pixel-design is only approximately 1 % when applying sufficient bias. This makes it an interesting option. However, a performance enhancement for the overall pixel-detector design in terms of power consumption, timing, and noise can only be expected if the readout chip is optimized for smaller input capacitances. This is currently not foreseen.

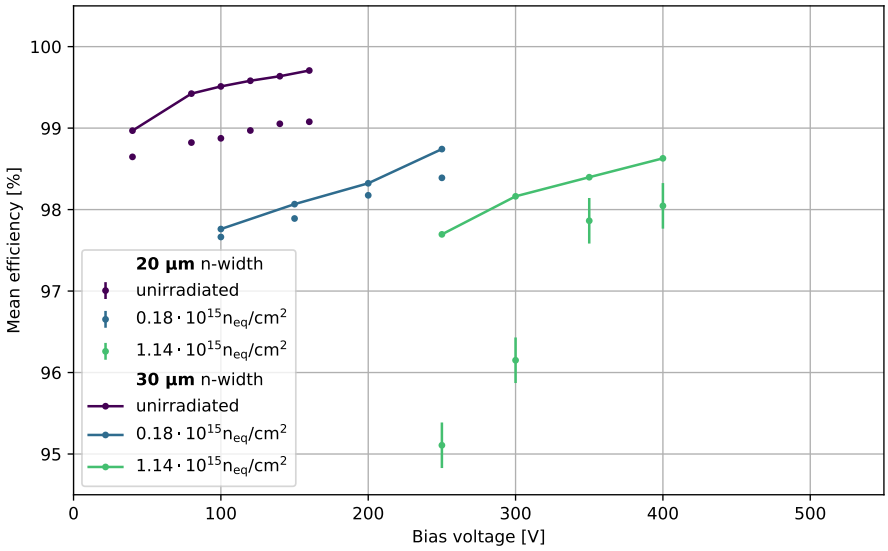


Figure 6.12: Average efficiency of DC-coupled pixels with different n-implantation widths at multiple levels of irradiation (unirradiated, $1.8 \times 10^{14}\,\mathrm{n_{eq}\,cm^{-2}}$, $1.14 \times 10^{15}\,\mathrm{n_{eq}\,cm^{-2}}$). LFoundry passive CMOS sensor with ATLAS FE-I4 readout. Due to coarse pointing resolution of the telsecope and small area of test pixel the error are relatively large.

## 6.6 Time-walk

The time interval between charge deposition and detection is called hit delay. It is given by the drift time of the charge carriers in the sensor and the delays in the charge amplification chain (amplifier, shaper, discriminator). Constant delays are irrelevant since they only add to the overall latency. However, varying delays should be below the bunch crossing time of 25 ns to allow hit assignment to the corresponding event. The hit-delay variation between a minimum charge deposition (defined by the detection threshold) and maximum charge deposition is called *time walk*. For ATLAS IBL modules, the main contribution to the time walk comes from the finite signal rise-time of the charge signal. This rise-time is given by bandwidth and slew-rate limitations from signal amplification, -shaping, and -discrimination.

For the ATLAS FE-I4 large time-walk differences between chips are observed (15 ns – 45 ns), when using the standard settings for pre-amplifier, amplifier, and comparator biases. When comparing the time-walk between a module with LFoundry passive CMOS-sensor and a module with 3D-sensor, one observes insignificant differences that can be explained by chip bias variations. The comparison is depicted in Figure 6.13. Since LFoundry sensor capacitances do not exceed the ones of IBL sensors( Section 6.3), an influence on the rise-time from the sensor capacitance ($\tau_r \propto C_\mathrm{d}$, [Kar10, p. 19]) is also not expected .

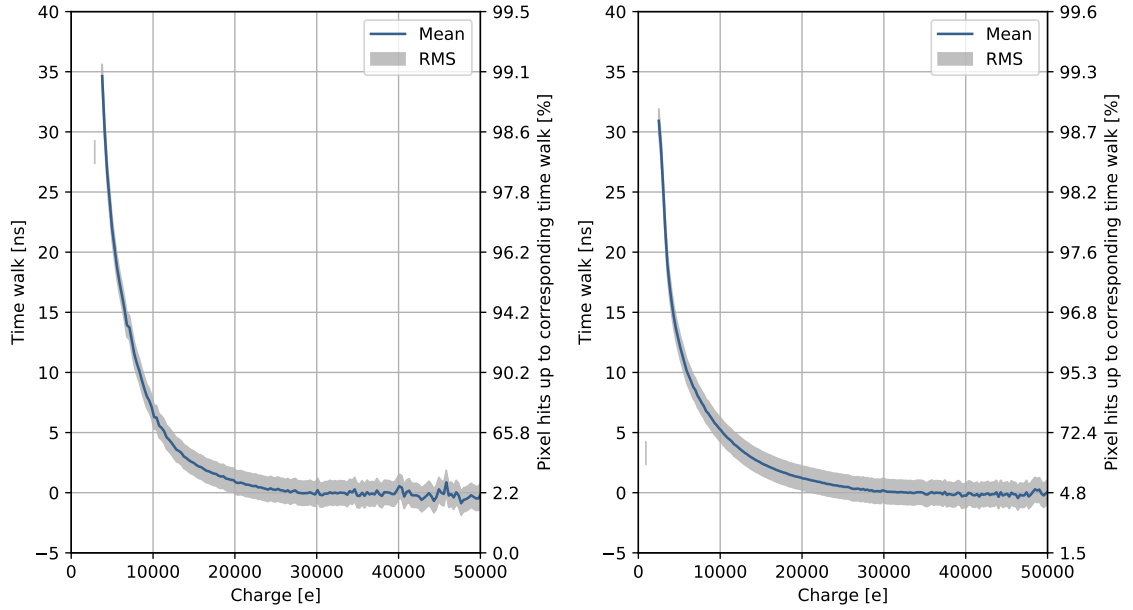


(a) 300 µm LFoundry passive CMOS sensor

(b) ATLAS IBL FBK 3D sensor, D2

Figure 6.13: Time-walk measured with electrons from a $^{90}$Sr source and the ATLAS FE-I4. Mean time-walk of many pixels are plotted with pixel to pixel variation (*RMS*). The right axis depicts the number of hits up to the given time-walk using the single pixel charge spectrum of the $^{90}$Sr electrons.

## 6.7 Charge-collection efficiency and bulk resistivity

Traditionally, silicon sensors are fabricated on wafers made by the Float Zone crystal growth technique; a technique that allows good impurity control to archive high-resistive silicon substrates [Här+05]. Only in the last years cheaper high-resistive Czochralski (CZ) wafers became available for large scale sensor designs that can reach several 1000 Ω cm. Since the usage of high-resistive CZ-wafers for pixel sensors in high irradiation environments is a novelty, detailed investigation of the resistivity development with irradiation have been carried out [Man+17][Li+05]. For the passive CMOS sensor, it is of interest to verify the specified resistivity ($> 2\,\mathrm{k\Omega\,cm}$) to ensure a sufficient depletion depth given the bias voltage before break down ($d \propto \sqrt{(V \cdot \rho)}$, Equation (2.37)). Especially, before irradiation where the break down voltage is relatively low (160 V, Figure 6.5). Therefore, multiple charge spectra are recorded with an unirradiated 300 µm sensor at different bias voltages using a 3.2 GeV electron beam (Figure 6.14). The charge is measured using the TDC-method (Section 3.2.2) after calibrating the readout chip with multiple x-ray sources[1]. For 3.2 GeV electrons the most probable energy-loss in 200 µm silicon is $260\,\mathrm{eV\,\mu m^{-1}}$, as extracted with SourceSim (Section 3.1.2). This value is also validated by measurement in Section 3.1.2 assuming $3.65\,\mathrm{eV\,e\text{-}h^{-1}}$ (Figure 3.10). For the most probable number of e-h pairs per path length follows $71\,\mathrm{e\text{-}h\,\mu m^{-1}}$, a value comparable to measurements in [MPS11, p. 9]. Assuming that the detected

[1] Procedure described in Section 5.3.3

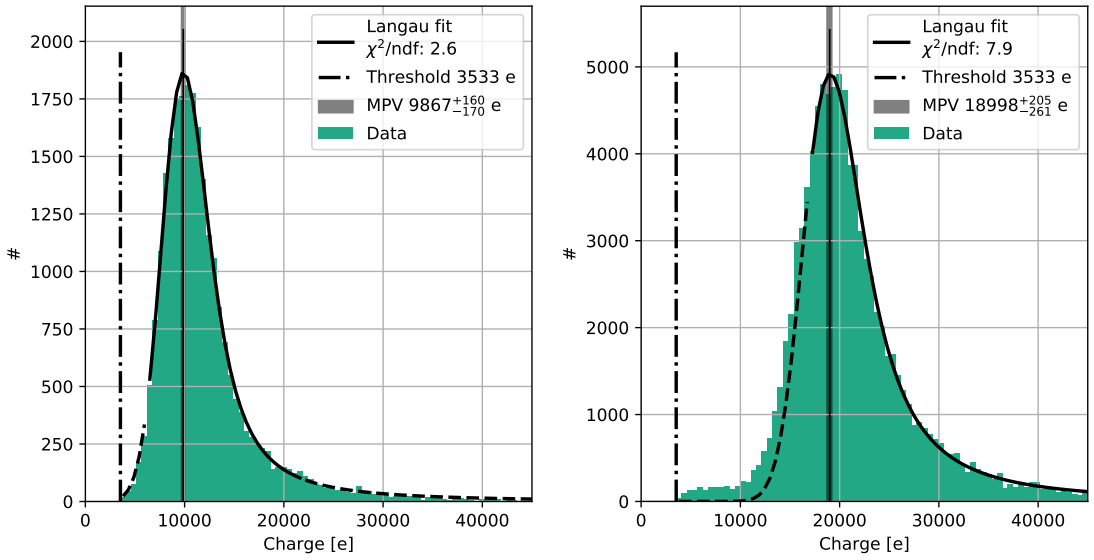


(a) 40 V (b) 160 V

Figure 6.14: Charge spectra of a 300 µm passive CMOS sensor at different bias voltages. 3.2 GeV electron beam and single-hit clusters are selected.

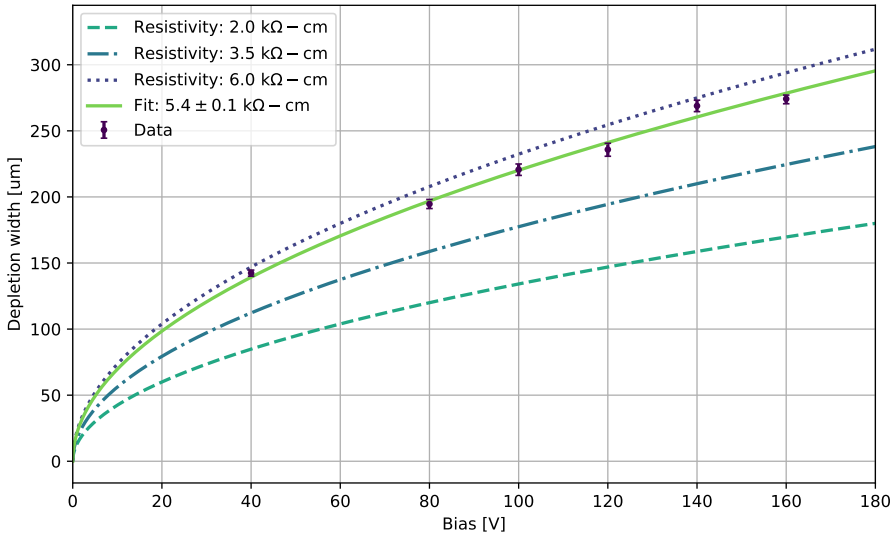


Figure 6.15: Depletion depth as a function of bias voltage. Depletion calculated from measured charge spectra. Expected curves (*dotted lines*) for different bulk resistivities and fit to data (*solid line*) depicted.

charge signal consists only of drifting charge carriers from the depletion region, due to the fast shaping of the ATLAS FE-I4 CSA, one can calculate the depletion depth as a function of bias voltage from the charge spectra. The result is depicted in Figure 6.15 together with theoretical

curves for different p-type wafer resistivities. The fitted resistivity of $(5.4 \pm 0.1)\,\mathrm{k\Omega\,cm}$ matches the foundry specifications (at least $2\,\mathrm{k\Omega\,cm}$, typical $4\,\mathrm{k\Omega\,cm} - 5\,\mathrm{k\Omega\,cm}$).

## 6.8 Conclusion

Prototypes of pixel sensors using the LFoundry CMOS process with 100 µm and 300 µm thickness are characterized and compared to the planar pixel-sensors of the ATLAS experiment (Section 6.1). Important sensor parameters such as capacitance (Section 6.3), charge collection (Section 6.7) and detection efficiency (Section 6.5) are similar or even slightly better. Necessary improvements have been identified for the low breakdown voltage before irradiation (160 V, Figure 6.5) and the higher input capacitance of the AC-coupling schema (Section 6.3). Various pixel designs that are possible through the CMOS process, such as AC-coupling and resistor biasing, as-well-as variations of the readout implantation, have been studied in view of optimizations for sensor capacity and charge-collection efficiency. An increased detection efficiency of approximately 1 % for resistor biasing could be observed. Due to the absence of the usual punch-though implantation, the efficiency before irradiation is at the maximum (100%, Figure 6.10). The possibility to connect the pixels to a bias grid for testing, without a punch-though implantation, is especially beneficial for future small pixel designs. A reduction in sensor capacity by 30 % was measured for designs with varying fill-factor and a concomitant reduction in detection efficiency of approximately 1 %. In addition, important lessons for the sensor processing steps, such as the need for backside etching and edge passivation for small prototypes, were learned. Driven by the promising results presented here, further prototypes have already been studied. Designs with higher breakdown voltage before irradiation, in excess of 300 V, were identified ([Coq18], [Man+18, p. 128]). In addition, a dedicated full-size sensor was designed for the qualification process of sensors for the future ATLAS pixel detector. It incorporates smaller 50 µm x 50 µm pixels and will cover an area of up to 4 readout-chip using reticle stitching.

# 7 Summary

The upgrade of the Large Hadron Collider in 2025 will open a new luminosity domain for collider experiments in high-energy physics. Over a period of about 12 years $3000\,\mathrm{fb}^{-1}$ will be collected, imposing challenging requirements for the future tracking detectors. Especially, the layers of the pixel detectors that are closest to the interaction point, will experience exceptional damage from radiation ($1.5 \times 10^{16}\,\mathrm{n_{eq}\,cm^{-2}}$, 7700 kGy). Therefore, new radiation tolerant sensors and readout electronics are developed and improvements of radiation-damage models for new sensor designs and high radiation levels are of importance.

In this study, 3D- and novel passive-CMOS silicon sensors were characterized after irradiation. They were investigated using the readout chip of the latest upgrade of the ATLAS pixel detector, the ATLAS FE-I4. Alongside, models and methods for charge-collection and efficiency determination with pixel detectors, before and after irradiation, were developed. The TDC-method enabled charge-collection efficiency measurements of sensors using the ATLAS FE-I4 with unprecedented resolution. A new simulation based on a minimal 2-parameter model successfully describes charge collection in silicon up to a fluence of $5 \times 10^{15}\,\mathrm{n_{eq}\,cm^{-2}}$. The crucial dependence of charge-collection on bias voltage for planar sensors of different thicknesses, as-well-as 3D sensors is reproduced by the simulation. The extracted life-time of charge-carriers in silicon at $5 \times 10^{15}\,\mathrm{n_{eq}\,cm^{-2}}$ is $0.75 \pm 0.08$ ns and is compatible with published values at lower levels of irradiation. At $7 \times 10^{15}\,\mathrm{n_{eq}\,cm^{-2}}$, 3D sensors demonstrate a charge-collection efficiency of 55%, similar to the 250 µm planar sensor with 50%. However, only a fraction of the bias voltage is required for the 3D sensor (220 V vs. 1500 V). Consequently, only 15% of the power consumption is needed, which is an important requirement for the future innermost layer of pixel detectors in the ATLAS experiment. With a small area attributed to this layer, 3D sensors are a promising option, despite their complex production. For the outer layers of the future pixel detector, where a large area has to be covered, a novel planar sensor using a CMOS process was characterized. The sensor was produced using the LFoundry 150 nm process and incorporates DC- and AC-coupled pixels. In comparison to planar sensors of the actual ATLAS pixel detector, the passive CMOS sensor displayed equal performance under irradiation up to $1.1 \times 10^{15}\,\mathrm{n_{eq}\,cm^{-2}}$. The capacitance of DC-coupled pixels (105 fF) corresponds to the capacitance of ATLAS planar sensors. The detection efficiency after irradiation exceeds 99% at 500 V bias. Additionally, AC-coupling of pixels to the readout, a feature available in the CMOS process, was evaluated. The resistor biasing in these pixels increases the efficiency by approximately 1% over the common punch-through biasing of ATLAS planar sensors. Especially, for future small-pixel designs this is beneficial. The option of a passive CMOS sensor for the future ATLAS pixel detector is currently pursued and a full-size prototype, with an area covering up to four readout chips, will be available in the near future.

# Appendices

### Charge fraction per planar pixel

The following shows the deviation of the average charge fraction in one pixel as a function of the planar pixel geometry ($a$, $b$, $d$) for a MIP in an n-/p-type sensor bulk. The result is validated with numerical integration. A simple Taylor series expansion could not be found.

$$
\begin{aligned}
Q_{\mathrm{pix}}(a,b,d) &= \frac{1}{d}\int_0^d \overline{Q}_{\mathrm{frac}}(a,b,\sigma(z))\,dz \\
&\underset{(2.57)}{=} \frac{1}{d}\int_0^d \frac{1}{ab}\left(a-\sqrt{\frac{2}{\pi}}\sigma(z)\right)\left(b-\sqrt{\frac{2}{\pi}}\sigma(z)\right)\,dz \\
&= 1-\sqrt{\frac{2}{\pi}}\frac{a+b}{a\,b\,d}\underbrace{\int_0^d \sigma(z)\,dz}_{*}+\frac{2}{\pi}\frac{1}{a\,b\,d}\underbrace{\int_0^d \sigma(z)^2\,dz}_{**} \\
&= 1 \\
&\quad -\sqrt{\frac{2}{\pi}}\frac{a+b}{a\,b}\frac{d\,C_0}{4\,C_1}\left(\mp\sqrt{\pi}(1\mp C_1)\,{}^{\mathrm{erfi}}_{\mathrm{erf}}\left(\sqrt{C_2}\right)+2(C_1\pm 1)\sqrt{C_2}\right) \\
&\quad \mp\frac{2}{\pi}\frac{1}{a\,b}\frac{d^2\,C_0^2}{2}\left(2\mp C_2-\frac{C_2}{C_1}\right)
\end{aligned}
$$

with

$$
\begin{aligned}
C_0 &= \sqrt{\frac{k_B\,T}{e\,V_{\mathrm{dep}}}} \\
C_1 &= \frac{V_{\mathrm{dep}}}{V} \\
C_2 &= \ln\left(\frac{1+C_1}{1-C_1}\right)
\end{aligned}
$$

using *:

$$\int_0^d \sigma(z) \underset{(2.60)}{=} d\sqrt{\frac{k_B\,T}{e\,V_{\text{dep}}}} \int_0^d \sqrt{\pm \ln\left(1 \pm \frac{2}{d}\frac{V_{\text{dep}}}{V \mp V_{\text{dep}}} z\right)}\, dz$$

$$\underset{\substack{C_0=\sqrt{\frac{k_B\,T}{e\,V_{\text{dep}}}} \\ C_i=\frac{2}{d}\frac{V_{\text{dep}}}{V\mp V_{\text{dep}}}}}{=} d\,C_0 \int_0^d \sqrt{\pm \ln\left(1 \pm C_i\, z\right)}\, dz$$

$$= d\,C_0 \frac{1}{2\,C_i}\left(\mp\sqrt{\pi}\,\underset{\text{erf}}{\text{erfi}}\left(\sqrt{\pm \ln\left(1 \pm C_i\, d\right)}\right) + 2\left(C_i\, d \pm 1\right)\sqrt{\pm \ln\left(1 \pm C_i\, d\right)}\right)$$

$$\underset{\substack{C_1=\frac{V_{\text{dep}}}{V} \\ C_2=\ln\left(\frac{1+C_1}{1-C_1}\right)}}{=} \frac{d^2\,C_0}{4\,C_1}\left(\mp\sqrt{\pi}(1 \mp C_1)\,\underset{\text{erf}}{\text{erfi}}\left(\sqrt{C_2}\right) + 2(C_1 \pm 1)\sqrt{C_2}\right)$$

**:

$$\int_0^d \sigma(z)^2 \underset{(2.60)}{=} \pm d^2 \frac{k_B\,T}{e\,V_{\text{dep}}} \int_0^d \ln\left(1 \pm \frac{2}{d}\frac{V_{\text{dep}}}{V \mp V_{\text{dep}}} z\right)\, dz$$

$$\underset{\substack{C_0=\sqrt{\frac{k_B\,T}{e\,V_{\text{dep}}}} \\ C_i=\frac{2}{d}\frac{V_{\text{dep}}}{V\mp V_{\text{dep}}}}}{=} \pm d^2\,C_0^2 \int_0^d \ln\left(1 \pm C_i\, z\right)\, dz$$

$$= \mp d^2\,C_0^2\left(d + \left(d \pm \frac{1}{C_i}\right)\ln\left(\frac{1}{1 \pm C_i\, d}\right)\right)$$

$$\underset{\substack{C_1=\frac{V_{\text{dep}}}{V} \\ C_2=\ln\left(\frac{1+C_1}{1-C_1}\right)}}{=} \mp\frac{d^3\,C_0^2}{2}\left(2 \mp C_2 - \frac{C_2}{C_1}\right)$$

### Deposited charge of $^{90}$Sr electrons

Figure 7.1 depicts the measured charge deposited by $^{90}$Sr electrons in one ATLAS IBL pixel. No Landau distribution can be seen due to heavy scattering of primary electrons.

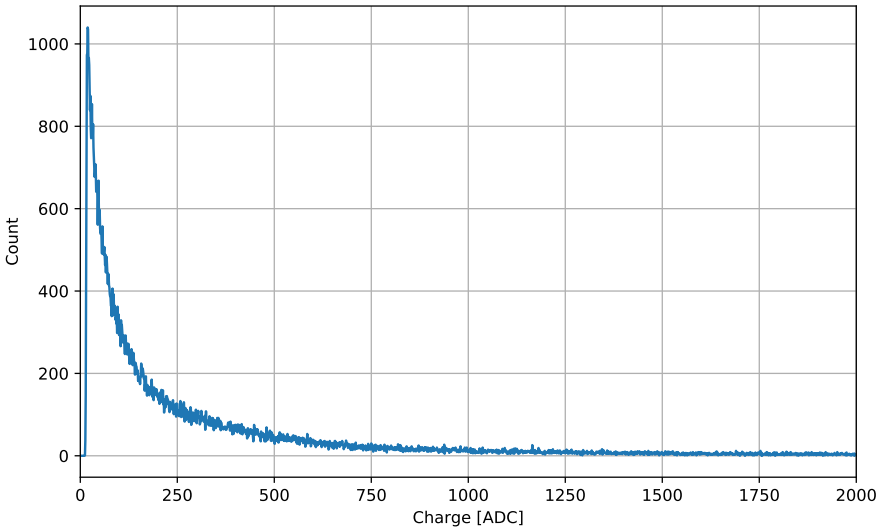


Figure 7.1: Deposited charge of $^{90}$Sr electrons in one ATLAS IBL 3D pixel. Measured with a single channel CSA setup without trigger (Section 5.2.2). The noise floor and the signal spectrum overlap and no peak is visible.

### Detector calibrations

Detector calibrations not mentioned in text are listed here for reason of completeness.

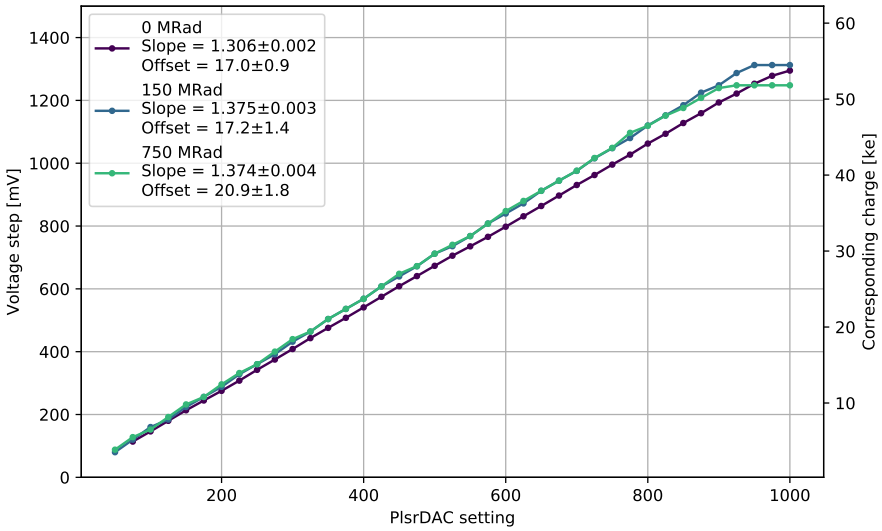


Figure 7.2: Pulser DAC calibration of the charge-injection circuitry at different levels of irradiation. Pixel detector with 3D-FBK sensor (Device D2, Table 5.1). Results of linear fits to linear region in legend.

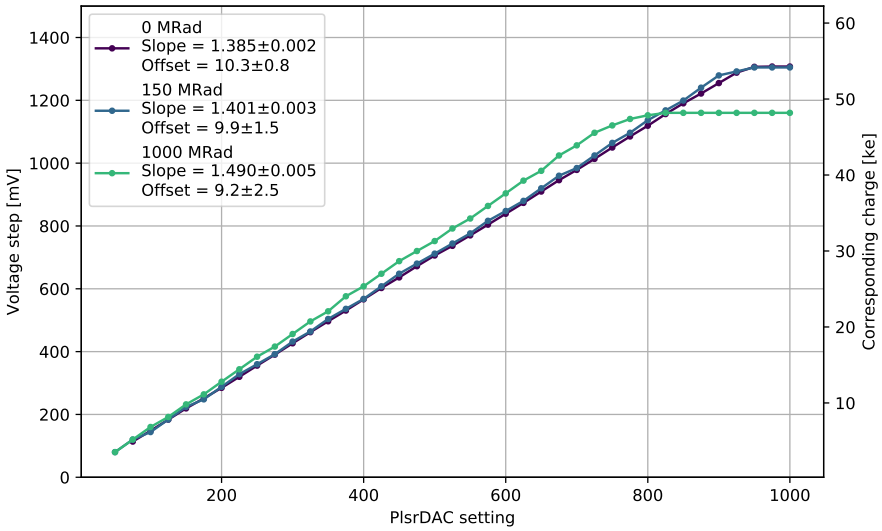


Figure 7.3: Pulser DAC calibration of the charge injection circuitry at different levels of irradiation. Pixel detector with 3D-CNM sensor (Device D1, Table 5.1). Results of linear fits to linear region in legend.

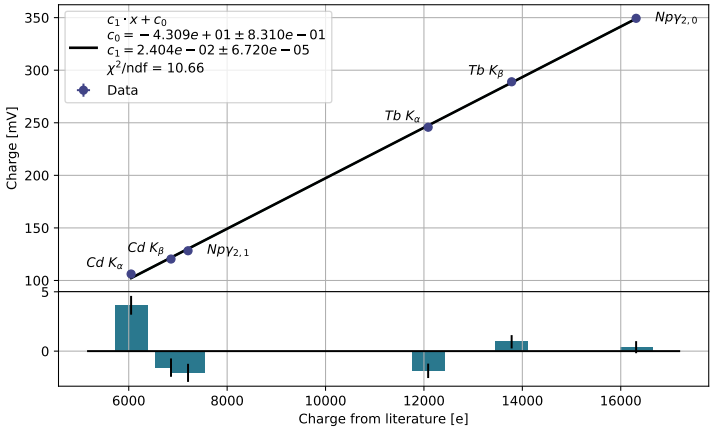


(a) Device P1

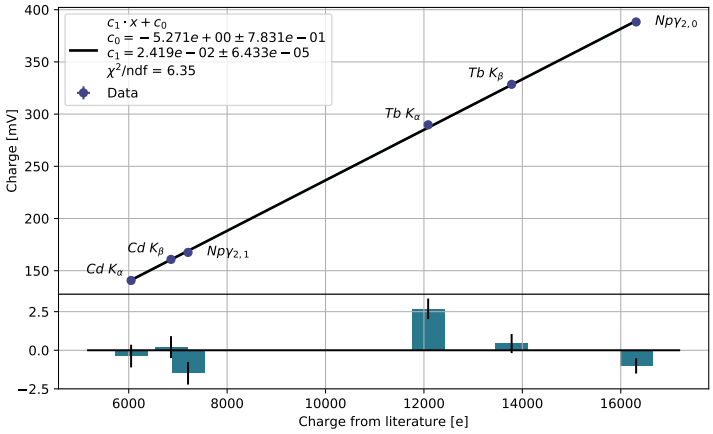


(b) Device P2

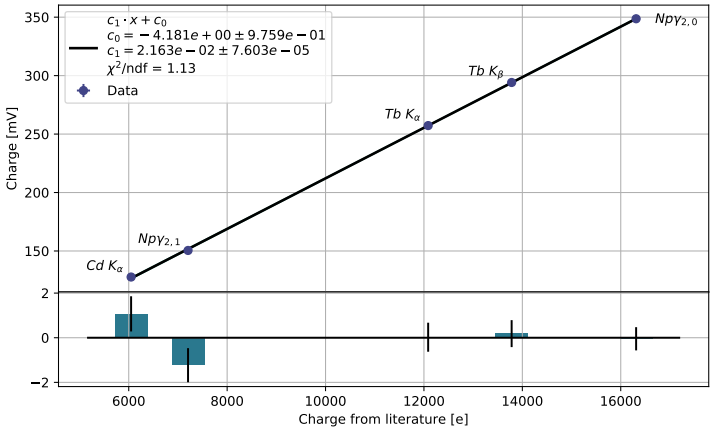


(c) Device D2

Figure 7.4: Calibration of the charge-injection circuitry with $\gamma$-sources. Calibration (*top*) including offset to the line fit (*bottom*). Charge in electrons assuming 3.65 eV e-h$^{-1}$ and measured charge in mV using Equation (5.15). Errors from peak-fits and PlsrDAC calibration.

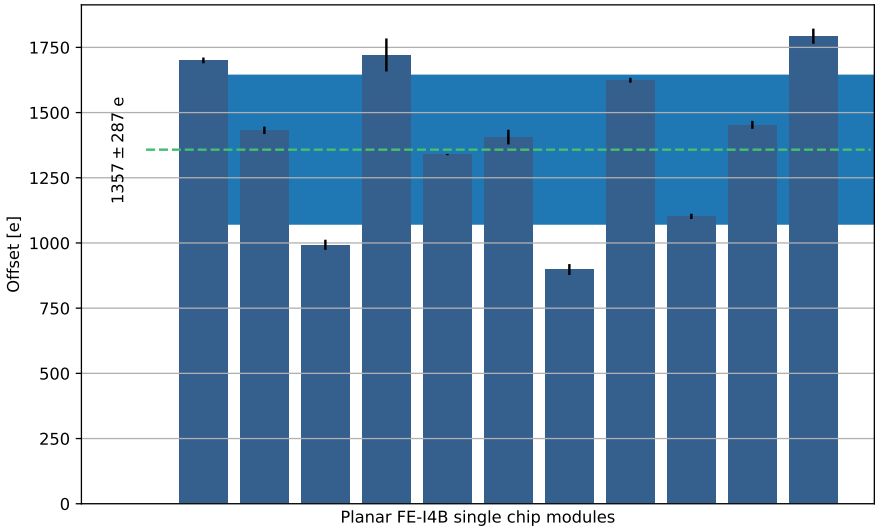


Figure 7.5: Offset of the internal charge-injection circuitry after calibration with multiple x-ray sources. ATLAS IBL like single planar modules with ATLAS FE-I4B.

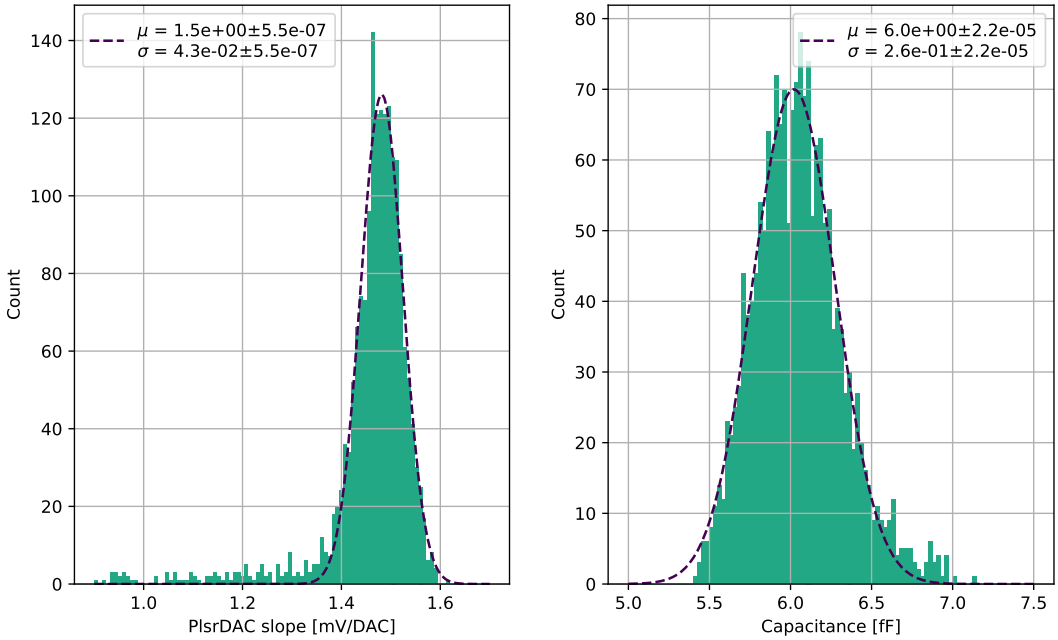


Figure 7.6: Distribution of calibration constants of the internal charge-injection circuitry of the ATLAS FE-I4B. Values determined from chip qualification tests at wafer level using a probestation during ATLAS IBL production. Only qualified chips (1821) shown.

**Simulation parameters**

| **Parameter** | **IBL sensor** | **Small pixel sensor** |
|---|---|---|
| Software | SourceSim | |
| Temperature | 330 K | |
| E-h pair energy | 3.65 eV | |
| Pixel geometry | 50 µm × 250 µm x 200 µm | 50 µm x 50 µm x 300 µm |
| Threshold | 3000 $e$ | 600 $e$ |
| Noise | 120 $e$ | 70 $e$ |
| Depletion voltage | 45 V | 100 V |
| Bias voltage | 80 V | 120 V |
| Sensor bulk | n-type | p-type |

Table 7.1: Simulation parameters for x-ray charge spectra.

| | |
|---|---|
| Sensor type | planar |
| Electrodes | n+ readout |
| Bulk type | p-type |
| Eff. doping concentration | $1.45 \times 10^{12}\,\mathrm{cm}^{-3}$ |
| Thickness | 200 µm |
| Bias voltage | 80 V |
| Pixel pitch | 50 µm |
| Readout electrode pitch | 30 µm |

Table 7.2: Sensor parameters for Scarce simulation of induced charge.

# Glossary

*ADC* Analog digital converter. 100

*CCE* Charge-Collection Efficiency. 63, 89, 90, 95–98, 108, 118, 120–122

*CDF* Cumulative distribution function.. 105

*CSA* Charge Sensitive Amplifier. 49, 67, 71, 100, 132, 140, 147

*DAC* Digital Analog converter. 49, 103–108, 112, 113, 148

*DUT* Device Under Test.. 75, 81, 135

*FDAC* Feeback current DAC of the ATLAS FE-I4 to adjust gain at pixel level (time-over-threshold per charge).. 103

*FE* Front-End, here: Synonym for the ALTAS FE-I4 pixel readout chip.. 48, 49, 100, 102, 107

*FIFO* First In First Out, storage element. 100

*FPGA* Field Programmable Gate Array. 69, 100

*FWHM* Full-Width-Half-Maximum.. 120

*IBL* Insertable B-Layer. 9, 30, 47–51, 63, 67, 89–92, 95–99, 104, 109, 110, 112, 113, 115, 120, 121, 124

*Langau* Convolution of the Landau and a Gaussian distribution function.. 13, 15, 63, 116, 119

*LHC* Large Hadron Collider. 1, 3–6, 34, 45, 46, 49, 79, 124

*MC* Monte Carlo: method to model behavior of a process by using random numbers of the probability density function describing this process. 93

*MIP* Minimum-ionizing particle. 12, 13, 19, 27–29, 32, 47, 53, 57, 59, 60, 63, 66, 97, 145

*MPV* Most-probable-value. 12, 13, 112, 116, 117, 120

*MSB* Most-significant-bit. 106

*NIEL* Non-ionizing energy-loss. 101, 102, 116

*PC* Personal Computer. 100

*PCB* Printed Circuit Board. 98–100

*PDE* Partial Differential Equation. 92

*PDF* Probability Density Function. 79, 94

*PlsrDAC* Injection voltage DAC of the internal charge injection circuitry. 104, 111–113, 118

*Python* High-level programming language for general-purpose programming [Fou]. 57, 67, 76, 89, 100

*RAM* Random Access Memory. 100

*RMS* Root Mean Square. 58, 120, 121

*TBA* Test Beam Analysis. [Poh+]. 75, 76, 78

*TCAD* Technology Computer Aided Design. 89, 90

*TDAC* Threshold DAC to adjust the threshold at pixel level. 103, 113

*TDC* Time Digital Converter. 67, 69, 70, 100, 111, 116

*TID* Total-ionizing-dose. 102, 103, 107, 108, 112, 116

*TLU* Trigger Logic Unit. [Cus09; Cus07]. 136

*ToT* Time-over-Threshold. 49, 67

*USB* Universal Serial Bus. 100

# Acronyms

$D$ diffusion constant. 29

$V_{\text{dep}}$ full-depletion voltage. 32

$\epsilon_s$ permittivity of silicon. 21, 43

$a$ pixel pitch in x. 30, 60, 145

$b$ pixel pitch in y. 30, 60, 145

$d$ sensor thickness. 32, 60, 145

$e$ elementary charge. 43

# Bibliography


[18] *Bonn Analysis Facility*. 2018. URL: https://wiki.physik.uni-bonn.de/computing/UserGuides/index.php/Main_Page.

[Ada+16] W. Adam et al. "Trapping in proton irradiated p + -n-n + silicon sensors at fluences anticipated at the HL-LHC outer tracker". In: *JINST* 11.04 (2016), P04023. URL: http://stacks.iop.org/1748-0221/11/i=04/a=P04023.

[AFZ07] P.Niezurawski A.F.Zarnecki. *EUDET Telescope Geometry and Resolution Studies*. Tech. rep. DESY, 2007. URL: https://www.eudet.org/e26/e27/e295/eudet-report-2007-01.pdf.

[Ago+03] S. Agostinelli et al. "Geant4-a simulation toolkit". In: *Nucl. Inst. and Meth. A* 506.3 (2003), pp. 250–303. DOI: 10.1016/S0168-9002(03)01368-8.

[Ahl16] Patrick Ahlburg. "Development of a FE-I4-based module for radiation monitoring with BEAST II during the commissioning phase of the Belle II detector". MA thesis. University of Bonn, Nov. 2016.

[Akk+01] A Akkerman et al. "Updated NIEL calculations for estimating the damage induced by particles and $\gamma$-rays in Si and GaAs". In: *Radiat. Phys. Chem.* 62.4 (2001), pp. 301–310. DOI: https://doi.org/10.1016/S0969-806X(01)00207-9.

[Amj+14] N. Amjed et al. "Activation cross-sections of proton induced reactions on natural Ni up to 65 MeV". In: *Appl. Radiat. Isot.* 92.Cmplete (2014), pp. 73–84.

[Amp17] Amptek. *CoolFET Charge Sensitive Amplifier Specifications*. Amptek. 2017. URL: http://amptek.com/pdf/coolfet.pdf.

[Apo+00] J Apostolakis et al. "An implementation of ionisation energy loss in very thin absorbers for the GEANT4 simulation package". In: *Nucl. Inst. and Meth. A* 453.3 (2000), pp. 597–605. DOI: https://doi.org/10.1016/S0168-9002(00)00457-5.

[ATLa] ATLAS collaboration. *ATLAS experiment public results*. URL: https://twiki.cern.ch/twiki/bin/view/AtlasPublic/LuminosityPublicResultsRun2.

[ATLb] ATLAS collaboration. *Radiation Simulation Public Results*. URL: https://twiki.cern.ch/twiki/bin/view/AtlasPublic/RadiationSimulationPublicResults.

[ATL08] ATLAS Pixel Collaboration. "ATLAS pixel detector electronics and sensors". In: *JINST* 3 (2008), P07007. DOI: 10.1088/1748-0221/3/07/P07007.

[Bac+11] M. Backhaus et al. "Development of a versatile and modular test system for ATLAS hybrid pixel detectors". In: *Nucl. Inst. and Meth. A* 650 (2011), pp. 37–40. DOI: 10.1016/j.nima.2010.12.087.

[Bac14] Malte Backhaus. "High bandwidth pixel detector modules for the ATLAS Insertable B-Layer". Dissertation. Universität Bonn, 2014. URL: http://hss.ulb.uni-bonn.de/2014/3507/3507.htm.

[Bak+87] J. F. Bak et al. "Large Departures from Landau Distributions for High-Energy Particles transversing thin Si and Ge Detectors". In: *Nucl. Phys. B* 288 (1987), p. 681.

[Bé+06] M.-M. Bé et al. *Table of Radionuclides*. Vol. 3. Monographie BIPM-5. France: BIPM, 2006. URL: http://www.bipm.org/utils/common/pdf/monographieRI/Monographie_BIPM-5_Tables_Vol3.pdf.

[Bé+16] M.-M. Bé et al. *Table of Radionuclides*. Vol. 8. Monographie BIPM-5. France: BIPM, 2016. URL: http://www.bipm.org/utils/common/pdf/monographieRI/Monographie_BIPM-5_Tables_Vol8.pdf.

[Bea+99] L. Beattie et al. "Carrier lifetimes in heavily irradiated silicon diodes". In: *Nucl. Inst. and Meth. A* 421.3 (1999), pp. 502–511. DOI: https://doi.org/10.1016/S0168-9002(98)01229-7.

[Bel+83] E. Belau et al. "Charge Collection in Silicon Strip Detectors". In: *Nucl. Inst. and Meth.* 214 (1983), p. 253. DOI: 10.1016/0167-5087(83)90591-4.

[Ben+04] Michael Benedikt et al. *LHC Design Report*. CERN Yellow Reports: Monographs. Geneva: CERN, 2004. DOI: 10.5170/CERN-2004-003-V-3.

[Ben+17] Mathieu Benoit et al. *Modeling Radiation Damage Effects for Pixel Sensors in the ATLAS Detector*. Tech. rep. ATL-COM-INDET-2017-011. Geneva: CERN, Mar. 2017. URL: https://cds.cern.ch/record/2255825.

[Ber+] M. J. Berger et al. *XCOM: Photon Cross Sections Database (interactive)*. URL: http://physics.nist.gov/PhysRefData/Xcom/Text/XCOM.html.

[Ber+05] M.J. Berger et al. *ESTAR, PSTAR, and ASTAR: Computer Programs for Calculating Stopping-Power and Range Tables for Electrons, Protons, and Helium Ions*. online database. Version 2.0.1. 2005. URL: https://physics.nist.gov/PhysRefData/Star/Text/intro.html.

[Bet+16] G.-F. Dalla Betta et al. "Investigation of leakage current and breakdown voltage in irradiated double-sided 3D silicon sensors". In: *JINST* 11.09 (2016), P09006. URL: http://stacks.iop.org/1748-0221/11/i=09/a=P09006.

[BGK14] H. Bichsel, D.E. Groom, and S.R. Klein. "Passage of particles through matter". In: *[Oli+14]* (2014), p. 398.

[BH09] Mathieu Benoit and L.A. Hamel. "Simulation of charge collection processes in semiconductor CdZnTe gamma-ray detectors". In: *Nucl. Inst. and Meth. A* 606.3 (2009), pp. 508–516. DOI: 10.1016/j.nima.2009.04.019.

[Bic88] H. Bichsel. “Straggling in thin silicon detectors”. In: *Rev. Mod. Phys.* 60, No. 3 (1988), p. 663. DOI: 10.1103/RevModPhys.60.663.

[BR97] R. Brun and F. Rademakers. “ROOT: An object oriented data analysis framework”. In: *Nucl. Instrum. Meth.* A389 (1997), pp. 81–86. DOI: 10.1016/S0168-9002(97)00048-X.

[But03] J. C. Butcher. *Numerical Methods for Ordinary Differential Equations*. 2nd. J. Wiley, 2003. DOI: 10.1007/978-0-85729-148-6.

[Cai+19] I. Caicedo et al. “The Monopix chips: Depleted monolithic active pixel sensors with a column-drain read-out architecture for the ATLAS Inner Tracker upgrade”. In: *PIXEL 2018*. Taiwan, 2019. arXiv: 1902.03679 [physics.ins-det].

[Cam+05] F. Campabadal et al. “Beam tests of ATLAS SCT silicon strip detector modules”. In: *Nucl. Inst. and Meth. A* 538.1 (2005), pp. 384–407. DOI: 10.1016/j.nima.2004.08.133.

[Cam+94] M. Campbell et al. “Development of a pixel readout chip compatible with large area coverage”. In: *Nucl. Inst. and Meth. A* 342.1 (1994), pp. 52–58. DOI: 10.1016/0168-9002(94)91410-9.

[Cap+10] M Capeans et al. *ATLAS Insertable B-Layer Technical Design Report*. Tech. rep. CERN-LHCC-2010-013. ATLAS-TDR-19. Sept. 2010. URL: https://cds.cern.ch/record/1291633.

[Car+] N. Cartiglia et al. “Comparison of different non-commercial detector simulation packages”. 27th RD50 Workshop presentation. URL: https://indico.cern.ch/event/456679/contributions/1126330/.

[Cas12] D Casadei. “Estimating the selection efficiency”. In: *JINST* 7.08 (2012), P08021. URL: http://stacks.iop.org/1748-0221/7/i=08/a=P08021.

[Cen+15] Francesca Cenna et al. “Weightfield2: A fast simulator for silicon and diamond solid state detector”. In: *Nucl. Inst. and Meth. A* 796 (2015). RESMDD14 Proceedings, pp. 149–153. DOI: 10.1016/j.nima.2015.04.015.

[Cha11] Rick Chartrand. “Numerical Differentiation of Noisy, Nonsmooth Data”. In: *ISRN Applied Mathematics* 2011 (2011), p. 11. DOI: 10.5402/2011/164564.

[Chi+05] V. Chiochia et al. “Simulation of heavily irradiated silicon pixel sensors and comparison with test beam measurements”. In: *IEEE Trans. Nucl. Sci.* 52.4 (Aug. 2005), pp. 1067–1075. DOI: 10.1109/TNS.2005.852748.

[Chi13] A Chilingarov. “Temperature dependence of the current generated in Si bulk”. In: *JINST* 8.10 (2013), P10003. URL: http://stacks.iop.org/1748-0221/8/i=10/a=P10003.

[Col12] ATLAS IBL Collaboration. “Prototype ATLAS IBL Modules using the FE-I4A Front-End Readout Chip”. In: *JINST* (2012), P11010. DOI: 10.1088/1748-0221/7/11/P11010.

[col14] The ATLAS collaboration. *Radiation background studies for the Phase II inner tracker upgrade*. Tech. rep. ATL-UPGRADE-PUB-2014-003. Geneva: CERN, Sept. 2014. URL: https://cds.cern.ch/record/1753332.

[Col16] ATLAS Collaboration. *Expected fluence after 3000fb-1 for the extended@4 layout*. ATLAS Public result. Oct. 2016. URL: https://atlas.web.cern.ch/Atlas/GROUPS/PHYSICS/PLOTS/ITK-2016-002/.

[Col17] ATLAS Collaboration. *Technical Design Report for the ATLAS Inner Tracker Pixel Detector*. Tech. rep. CERN-LHCC-2017-021. ATLAS-TDR-030. Geneva: CERN, Sept. 2017. URL: https://cds.cern.ch/record/2285585.

[Coq18] Daniel Coquelin. "Characterization of a small pixel LFoundry Sensor with the FE65-P2 Readout System". MA thesis. University of Bonn, 2018.

[CP] LHC Computing and Grid Project. *Re-implementation of MINUIT in an object-oriented way using C++*. URL: http://lcgapp.cern.ch/project/cls/work-packages/mathlibs/minuit/index.html.

[Cus07] D. Cussans. "A Trigger/Timing Logic Unit for ILC Test-beams". In: *TWEPP* (Sept. 2007). Workshop, pp. 420–422. DOI: 10.5170/CERN-2007-007.420.

[Cus09] D. Cussans. *Description of the JRA1 Trigger Logic Unit (TLU), v0.2c*. Tech. rep. DESY, 2009. URL: http://www.eudet.org/e26/e28/e42441/e57298/EUDET-MEMO-2009-04.pdf.

[CW51] J. J. L. Chen and S. D. Warshaw. "The Energy Loss of Electrons Passing through Matter". In: *Phys. Rev.* 84 (2 Oct. 1951), pp. 355–361. DOI: 10.1103/PhysRev.84.355.

[Da +08] C. Da Via et al. "Radiation hardness properties of full-3D active edge silicon sensors". In: *Nucl. Inst. and Meth. A* 587 (2008), pp. 243–249. DOI: 10.1016/j.nima.2007.12.027.

[Dab+00] W. Dabrowski et al. "Design and performance of the ABCD chip for the binary readout of silicon strip detectors in the ATLAS semiconductor tracker". In: *IEEE Trans. Nucl. Sci.* 47.6 (Dec. 2000), pp. 1843–1850. DOI: 10.1109/23.914457.

[Dal14] R. Dalal. "Simulation of Irradiated Detectors". In: *VERTEX*. 2014. URL: https://pos.sissa.it/cgi-bin/reader/contribution.cgi?id=227/030.

[DC16] Alvaro Diez and Pablo de Castro. *TRACS: Transient Current Simulator*. Software repository. Aug. 2016. URL: https://github.com/IFCA-HEP/TRACS.

[Des+03] Richard D. Deslattes et al. "X-ray transition energies: new approach to a comprehensive evaluation". In: *Rev. Mod. Phys.* 75 (1 Jan. 2003), pp. 35–99. DOI: 10.1103/RevModPhys.75.35.

[Dev86] Luc Devroye. *Non-uniform random variate generation*. 1st ed. Springer, 1986. DOI: 10.1007/978-1-4613-8643-8.

[Die03] Alexander Dierlamm. “Studies on the Radiation Hardness of Silicon Sensors”. PhD thesis. Karlsruhe U., 2003. URL: http://ekp-invenio.physik.uni-karlsruhe.de/record/45039.

[Die10] Alexander Dierlamm. *Proton Irradiation in Karlsruhe*. Presentation. 16th RD50 Workshop. June 2010. URL: https://indico.cern.ch/event/86625/contributions/2103519/.

[Die17] Yannick Dieter. “Setup and Characterization of the Test Beam Area for Pixel Detector Tests at ELSA”. MA thesis. University of Bonn, Sept. 2017.

[Die75] P. Dierckx. “An algorithm for smoothing, differentiation and integration of experimental data using spline functions”. In: *J. Comput. Appl. Math.* 1.3 (1975), pp. 165–184. DOI: 10.1016/0771-050X(75)90034-0.

[Die82] Paul Dierckx. “A Fast Algorithm for Smoothing Data on a Rectangular Grid While Using Spline Functions”. In: *SINUM* 19.6 (1982), pp. 1286–1304. URL: http://www.jstor.org/stable/2157211.

[DIS] DISCO. *DISCO*. https://www.disco.co.jp/eg/solution/library/taiko.html.

[DW09] C. DaVia and S.J. Watts. “The geometrical dependence of radiation hardness in planar and 3D silicon detectors”. In: *Nucl. Inst. and Meth. A* 603.3 (2009), pp. 319–324. DOI: https://doi.org/10.1016/j.nima.2009.02.030.

[EB08] Lyndon Evans and Philip Bryant. “LHC Machine”. In: *JINST* 3.08 (Aug. 2008), S08001–S08001. DOI: 10.1088/1748-0221/3/08/s08001.

[Ebe13] Robert Eber. “Untersuchung neuartiger Sensorkonzepte und Entwicklung eines effektiven Modells der Strahlenschädigung für die Simulation hochbestrahlter Silizium-Teilchendetektoren”. Dr. KIT, 2013. URL: https://ekp-invenio.physik.uni-karlsruhe.de/record/48328.

[Eng14] Mario Engel. “Spektroskopiemessungen mit dem ATLAS FE-I4 mit planarem n-in-n Silizumsensor”. Bachelor Thesis, University of Bonn. Sept. 2014.

[ER65] F. E. Emery and T. A. Rabson. “Average Energy Expended Per Ionized Electron-Hole Pair in Silicon and Germanium as a Function of Temperature”. In: *Phys. Rev.* 140 (6A Dec. 1965), A2089–A2093. DOI: 10.1103/PhysRev.140.A2089.

[EVL02] V Eremin, E Verbitskaya, and Z Li. “The origin of double peak electric field distribution in heavily irradiated silicon detectors”. In: *Nucl. Inst. and Meth. A* 476.3 (2002). RESMDD Proceedings, pp. 556–564. DOI: https://doi.org/10.1016/S0168-9002(01)01642-4.

[FEI12] FE-I4 Collaboration. *The FE-I4B Integrated Circuit Guide*. 2.3. Dec. 2012. URL: https://indico.cern.ch/event/261840/contributions/1594374/attachments/462649/641213/FE-I4B_V2.3.pdf.

[FGW77] H.-J. Fitting, H. Glaefeke, and W. Wild. "Electron penetration and energy transfer in solid targets". In: *Phys. stat. sol* 43.1 (Sept. 1977), pp. 185–190. DOI: 10.1002/pssa.2210430119.

[Fou] Python Software Foundation. *Python Language Reference, version 2.7 and version 3.6*. URL: https://www.python.org/.

[G+17] Apollinari G. et al. *High-Luminosity Large Hadron Collider (HL-LHC): Technical Design Report V. 0.1*. CERN Yellow Reports: Monographs. Geneva: CERN, 2017. DOI: 10.23731/CYRM-2017-004.

[GA00] Fabiola Gianotti and Monica Pepe Altarelli. "Precision physics at the LHC". In: *Nuclear Physics B - Proceedings Supplements* 89.1 (2000). Loops and Legs in Quantum Field Theory, pp. 177–189. DOI: https://doi.org/10.1016/S0920-5632(00)00841-0.

[Gar+11] M. Garcia-Sciveres et al. "The FE-I4 pixel readout integrated circuit". In: *Nucl. Inst. and Meth. A* 636 (2011), p. 155. DOI: 10.1016/j.nima.2010.04.101.

[Gat+87] E. Gatti et al. "Dynamics of Electrons in Drift Detectors". In: *Nucl. Inst. and Meth. A* 253 (1987), pp. 393–399. DOI: 10.1016/0168-9002(87)90522-5.

[Gea16a] Geant4 Collaboration. *Physics Reference Manual Version 10.3*. Dec. 2016. URL: http://geant4.web.cern.ch/geant4/support/userdocuments.shtml.

[Gea16b] Geant4 Collaboration. *User's Guide for Application Developers Version 10.3*. Dec. 2016. URL: http://geant4.web.cern.ch/geant4/support/userdocuments.shtml.

[GMS01] D.E. Groom, N.V. Mokhov, and S.I. Striganov. "Muon stopping power and range tables 10-MeV to 100-TeV". In: *Atom. Data Nucl. Data Tabl.* 78 (2001), pp. 183–356. DOI: 10.1006/adnd.2001.0861.

[God+09] Godet, O. et al. "Modelling the spectral response of the Swift-XRT CCD camera: experience learnt from in-flight calibration". In: *A&A* 494.2 (2009), pp. 775–797. DOI: 10.1051/0004-6361:200811157.

[Gon13] Laura Gonella. *Low mass hybrid pixel detectors for the high luminosity LHC upgrade*. Presented 23 Sep 2013. Nov. 2013. URL: https://cds.cern.ch/record/1633150.

[Gor+01] Grant Gorfine et al. "Silicon pixel capacitance". In: *Nucl. Inst. and Meth. A* 465.1 (2001). SPD2000, pp. 70–76. DOI: https://doi.org/10.1016/S0168-9002(01)00348-5.

[Gor15] I.V. Gorelov. "A leakage current-based measurement of the radiation damage in the ATLAS Pixel Detector". In: *JINST* 10.04 (2015), p. C04024. URL: http://stacks.iop.org/1748-0221/10/i=04/a=C04024.

[Gou09] Brian Gough. *GNU Scientific Library Reference Manual - Third Edition*. 3rd. Network Theory Ltd., 2009. URL: http://www.gnu.org/software/gsl/.

[GR09] Christophe Geuzaine and Jean-François Remacle. “Gmsh: A 3-D finite element mesh generator with built-in pre- and post-processing facilities”. In: *Int. J. Numer. Methods. Eng.* 79.11 (2009), pp. 1309–1331. DOI: 10.1002/nme.2579.

[Groa] Electromagnetic Standard Physics Working Group. URL: http://geant4.cern.ch/collaboration/working_groups/electromagnetic/index.shtml.

[Grob] The HDF Group. *HDF5: a data model, library, and file format for storing and managing data.* URL: https://support.hdfgroup.org/HDF5/.

[GW18] Maurice Garcia-Sciveres and Norbert Wermes. “A review of advances in pixel detectors for experiments with high rate and radiation”. In: *Reports on Progress in Physics* (2018). DOI: 10.1088/1361-6633/aab064.

[GWW09] Jonathan E. Guyer, Daniel Wheeler, and James A. Warren. “FiPy: Partial Differential Equations with Python”. In: *Comput. Sci. Eng.* 11.3 (2009), pp. 6–15. DOI: 10.1109/MCSE.2009.52.

[H600] H6. *Manual for H6 Beamline Users.* Version 3.0. May 2000. URL: http://sba.web.cern.ch/sba/BeamsAndAreas/h6/H6manual.pdf.

[HA93] M. Huhtinen and P.A. Aarnio. “Pion induced displacement damage in silicon devices”. In: *Nucl. Inst. and Meth. A* 335.3 (1993), pp. 580–582. DOI: https://doi.org/10.1016/0168-9002(93)91246-J.

[Ham01] C. Hamaguchi. *Basic Semiconductor Physics.* Physics and astronomy online library. Springer, 2001. DOI: 10.1007/978-3-642-03303-2.

[Han+83] S. Hancock et al. “Energy loss and energy straggling of protons and pions in the momentum range 0.7 to 115 GeV/c”. In: *Phys. Rev. A* 28 (2 Aug. 1983), pp. 615–620. DOI: 10.1103/PhysRevA.28.615.

[Här+05] J. Härkönen et al. “Particle detectors made of high-resistivity Czochralski silicon”. In: *Nucl. Inst. and Meth. A* 541.1 (2005). Development and Application of Semiconductor Tracking Detectors, pp. 202–207. DOI: https://doi.org/10.1016/j.nima.2005.01.057.

[Har17] Frank Hartmann. “Evolution of Silicon Sensor Technology in Particle Physics”. In: *Springer Tracts Mod. Phys.* 275 (2017). DOI: 10.1007/978-3-319-64436-3.

[Hav+13] Miroslav Havránek et al. “Measurement of pixel sensor capacitances with sub-femtofarad precision”. In: *Nucl. Inst. and Meth. A* 714 (2013), pp. 83–89. DOI: https://doi.org/10.1016/j.nima.2013.02.038.

[Hav14] Miroslav Havránek. “Development of pixel front-end electronics using advanced deep submicron CMOS technologies”. Dissertation. Universität Bonn, 2014. URL: http://hss.ulb.uni-bonn.de/2014/3787/3787.htm.

[He01] Z. He. “Review of the Shockley-Ramo theorem and its application in semiconductor gamma-ray detectors”. In: *Nucl. Inst. and Meth. A* 463 (2001), p. 250. DOI: 10.1016/S0168-9002(01)00223-6.

[Hem18] T. Hemperek. "Exploration of advanced CMOS technologies for new pixel detector concepts in High Energy Physics". Dissertation. Universität Bonn, 2018.

[Heu+16] N. Heurich et al. "The New External Beamline for Detector Tests at ELSA". In: *IPAC*. Korea, 2016, THPOY002. DOI: 10.18429/JACoW-IPAC2016-THPOY002.

[HGD93] B.L. Henke, E.M. Gullikson, and J.C. Davis. "X-Ray Interactions: Photoabsorption, Scattering, Transmission, and Reflection at E = 50-30,000 eV, Z = 1-92". In: *Atomic Data and Nuclear Data Tables* 54.2 (1993), pp. 181–342. DOI: 10.1006/adnd.1993.1013.

[Hir+16] Toko Hirono et al. "CMOS pixel sensors on high resistive substrate for high-rate, high-radiation environments". In: *Nucl. Inst. and Meth. A* 831 (2016). Hiroshima Proceedings, pp. 94–98. DOI: https://doi.org/10.1016/j.nima.2016.01.088.

[Hir17] Toko Hirono. *Charge cloud width measurement by backside illumination of a 100 um sensor. Private Communication.* 2017.

[Huh02] M. Huhtinen. "Simulation of non-ionising energy loss and defect formation in silicon". In: *Nucl. Inst. and Meth. A* 491.1 (2002), pp. 194–215. DOI: 10.1016/S0168-9002(02)01227-5.

[IBS] IBS. URL: ttp://www.ion-beam-services.com/.

[ise19] iserundschmidt, science event agency, private communication. *Hybrid pixel detector picture*. 2019. URL: http://www.iserundschmidt.de/.

[J W07] R. Klingenberg J. Weber. "Free Charge Carriers Trapping Properties in Neutron-Irradiated DOFZ Silicon Pad Detectors". In: *IEEE Trans. Nucl. Sci.* 54.6 (Dec. 2007), pp. 2701–2705. DOI: 10.1109/TNS.2007.910855.

[Jac+77] C. Jacoboni et al. "A review of some charge transport properties of Silicon". In: *Solid-State Electronics* 20 (1977), pp. 77–89. DOI: 10.1016/0038-1101(77)90054-5.

[Jam06] Frederick James. *Statistical methods in experimental physics*. 2nd ed. World Scientific, 2006. DOI: 10.1142/6096.

[Jan+16] Hendrik Jansen et al. "Performance of the EUDET-type beam telescopes". In: *EPJ Tech. Instrum.* 3.1 (Oct. 2016), p. 7. DOI: 10.1140/epjti/s40485-016-0033-2.

[Jan17] J. Janssen. "Test beam results of ATLAS DBM pCVD diamond detectors using a novel threshold tuning method". In: *JINST* 12.03 (Mar. 2017), pp. C03072–C03072. DOI: 10.1088/1748-0221/12/03/c03072.

[Jan20] Jens Janssen. "working title: a diamont beam monitor for the ATLAS pixel detector upgrade". to be published. Dissertation. Universität Bonn, 2020.

[JH09] M. Jeong and M. D. Hammig. "The Atomistic Simulation of Thermal Diffusion and Coulomb Drift in Semiconductor Detectors". In: *IEEE Trans. Nucl. Sci.* 56.3 (June 2009), pp. 1364–1371. DOI: 10.1109/TNS.2009.2021426.

[JOP+01] Eric Jones, Travis Oliphant, Pearu Peterson, et al. *SciPy: Open source scientific tools for Python*. 2001. URL: http://www.scipy.org/.

[JPa] Jens Janssen, David-Leon Pohl, and et. al. *Software package* pyBAR*, versatile readout and test system for the ATLAS FE-I4(A/B) pixel readout chip*. https://github.com/SiLab-Bonn/pyBAR.

[JR75] F. James and M. Roos. "Minuit - a system for function minimization and analysis of the parameter errors and correlations". In: *Comput. Phys. Commun.* 10.6 (1975), pp. 343–367. DOI: https://doi.org/10.1016/0010-4655(75)90039-9.

[Kar10] Michael Athanassios Karagounis. "Analog Integrated CMOS Circuits for the Readout and Powering of Highly Segmented Detectors in Particle Physics Applications". Dissertation. Fernuniversitätt in Hagen, 2010. URL: https://ub-deposit.fernuni-hagen.de/receive/mir_mods_00000029.

[KDe16] KDetSim developers. *KDetSim-A simple way to simulate detectors. A ROOT based library for calculation of fields and signals in semiconductor devices*. Project Webpage. Jan. 2016. URL: http://www-f9.ijs.si/~gregor/KDetSim/.

[Kle12] Claus Kleinwort. "General broken lines as advanced track fitting method". In: *Nucl. Inst. and Meth. A* 673 (2012), pp. 107–110. DOI: https://doi.org/10.1016/j.nima.2012.01.024.

[KLF93] H.W. Kraner, Z. Li, and E. Fretwurst. "The use of the signal current pulse shape to study the internal electric field profile and trapping effects in neutron damaged silicon detectors". In: *Nucl. Inst. and Meth. A* 326.1 (1993), pp. 350–356. DOI: 10.1016/0168-9002(93)90376-S.

[Knu98] Donald Ervin Knuth. *The art of computer programming, vol.3: Sorting and Searching*. 2nd ed. Vol. 3. Pearson Education, 1998.

[Koh+11] M. Kohler et al. "Beam Test Measurements With Planar and 3D Silicon Strip Detectors Irradiated to sLHC Fluences". In: *IEEE Trans. Nucl. Sci.* 58.3 (June 2011), pp. 1308–1314. DOI: 10.1109/TNS.2011.2126598.

[Kra+02a] G. Kramberger et al. "Effective trapping time of electrons and holes in different silicon materials irradiated with neutrons, protons and pions". In: *Nucl. Inst. and Meth. A* 481 (2002), pp. 297–305.

[Kra+02b] G Kramberger et al. "Determination of effective trapping times for electrons and holes in irradiated silicon". In: *Nucl. Inst. and Meth. A* 476.3 (2002). RESMDD Proceedings, pp. 645–651. DOI: https://doi.org/10.1016/S0168-9002(01)01653-9.

[Kra+03] O. Krasel et al. "Measurement of trapping time constants in proton-irradiated silicon pad detectors". In: *IEEE Nucl. Sci. Symp.* Vol. 1. Oct. 2003, 439–443 Vol.1. DOI: 10.1109/NSSMIC.2003.1352079.

[Kra+09] G. Kramberger et al. “Performance of silicon pad detectors after mixed irradiations with neutrons and fast charged hadrons”. In: *Nucl. Inst. and Meth. A* 609.2 (2009), pp. 142–148. DOI: https://doi.org/10.1016/j.nima.2009.08.030.

[Kra+12] G Kramberger et al. “Determination of detrapping times in semiconductor detectors”. In: *JINST* 7.04 (2012), P04006. URL: http://stacks.iop.org/1748-0221/7/i=04/a=P04006.

[Kra11] G. Kramberger. *Solid State Detectors for High Radiation Environments*. Ed. by C. W. Fabjan and H. Schopper. Vol. 21B2. Elementary Particles of Landolt-Börnstein. Springer-Verlag Berlin Heidelberg, 2011. DOI: 10.1007/978-3-642-14142-3_7.

[KS84] K.S. Kölbig and B. Schorr. “A Program Package for the Landau Distribution”. In: *Comput. Phys. Commun.* 31 (1984). (Erratum: Comput. Phys. Commun. 178 (2008), S. 972), pp. 97–111. DOI: 10.1016/0010-4655(84)90085-7,10.1016/j.cpc.2008.03.002.

[KW16] H. Kolanoski and N. Wermes. *Teilchendetektoren: Grundlagen und Anwendungen*. Berlin, Heidelberg, New York: Springer, 2016. DOI: 10.1007/978-3-662-45350-6_1.

[Lan09] Jorn Lange. “Radiation damage in proton-irradiated epitaxial silicon detectors”. MA thesis. Hamburg U., 2009. DOI: 10.3204/DESY-THESIS-2009-022.

[Lan44] L.D. Landau. “On the energy loss of fast particles by ionization”. In: *J. Phys. (USSR)* 8 (1944), p. 201. DOI: 10.1016/C2013-0-01806-3.

[Lar04] T. Lari. “Measurement of trapping time constants in irradiated DOFZ silicon with test beam data”. In: *Nucl. Inst. and Meth. A* 518.1 (2004). Frontier Detectors for Frontier Physics: Proceedin, pp. 349–351. DOI: https://doi.org/10.1016/j.nima.2003.11.019.

[LD91] Gerald R. Lynch and Orin I. Dahl. “Approximations to multiple Coulomb scattering”. In: *Nucl. Inst. and Meth.* 58.1 (1991), pp. 6–10. DOI: https://doi.org/10.1016/0168-583X(91)95671-Y.

[Leo94] R.W. Leo. *Techniques for Nuclear and Particle Physics Experiments*. 2nd edition. Berlin–Heidelberg–New York: Springer, 1994.

[LFo] LFoundry. *LFoundry, a SMIC owned Company*. http://www.lfoundry.com/en/technology.

[Li+05] Z. Li et al. “Gamma radiation induced space charge sign inversion and re-inversion in p-type MCZ Si detectors and in proton-irradiated n-type MCZ Si detectors”. In: *Nucl. Inst. and Meth. A* 552.1 (2005). RESMDD Proceedings, pp. 34–42. DOI: https://doi.org/10.1016/j.nima.2005.06.003.

[Lin03] G. Lindstrom. “Radiation damage in silicon detectors”. In: *Nucl. Inst. and Meth. A* 512 (2003), pp. 30–43. DOI: 10.1016/S0168-9002(03)01874-6.

[Loe17] Maximilian Loepke. “Kapazitätsmessung von CMOS-Pixelstrukturen”. Bachelor Thesis. Aug. 2017.

[Lou+03] N. V. Loukianova et al. “Leakage current modeling of test structures for characterization of dark current in CMOS image sensors”. In: *IEEE Trans. Electron Devices* 50.1 (Jan. 2003), pp. 77–83. DOI: 10.1109/TED.2002.807249.

[Lut96] G. Lutz. “Effects of deep level defects in semiconductor detectors”. In: *Nucl. Inst. and Meth. A* 377.2 (1996). Proceedings, pp. 234–243. DOI: 10.1016/0168-9002(96)00025-3.

[Mac17] Anna Macchiolo. “FEI4 Threshold Study”. presentation. Nov. 2017.

[Man+17] I. Mandić et al. “Neutron irradiation test of depleted CMOS pixel detector prototypes”. In: *JINST* 12.02 (2017), P02021. URL: http://stacks.iop.org/1748-0221/12/i=02/a=P02021.

[Man+18] I. Mandić et al. “Charge-collection properties of irradiated depleted CMOS pixel test structures”. In: *Nucl. Inst. and Meth. A* 903 (2018), pp. 126–133. DOI: 10.1016/j.nima.2018.06.062.

[MCK03] R.S. Muller, M. Chan, and T.I. Kamins. *Device Electronics For Integrated Circuits, 3Rd Ed.* Wiley India Pvt. Limited, 2003.

[Mer10] Marius Mertens. “Der PANDA Mikro Vertex Detektor: Entwicklung eines Labormesssystems, Simulation der MVD-Betriebsparameter sowie Untersuchungen zur Auflösung der Breite des Ds0*(2317)”. PhD thesis. FZ Jülich: Ruhr Universität Bochum, 2010. URL: https://panda.gsi.de/oldwww/db/thesesDB/MM14-101119_diss.pdf.

[Mik+01] B. Mikulec et al. “Characterisation of a single photon counting pixel system for imaging of low-contrast objects”. In: *Nucl. Inst. and Meth. A* 458.1 (2001). Proceedings, pp. 352–359. DOI: 10.1016/S0168-9002(00)01037-8.

[Mol+02] M Moll et al. “Relation between microscopic defects and macroscopic changes in silicon detector properties after hadron irradiation”. In: *Nuclear Instruments and Methods in Physics Research Section B: Beam Interactions with Materials and Atoms* 186.1 (2002), pp. 100–110. DOI: https://doi.org/10.1016/S0168-583X(01)00866-7.

[Mol18] M. Moll. “Displacement Damage in Silicon Detectors for High Energy Physics”. In: *IEEE Trans. Nucl. Sci.* 65.8 (Aug. 2018), pp. 1561–1582. DOI: 10.1109/TNS.2018.2819506.

[Mol47] G. Moliere. “Theorie der Streuung schneller geladener Teilchen I. Einzelstreuung am abgeschirmten Coulomb-Feld”. In: *Z. Naturforsch.* A2 (1947), p. 133. URL: http://zfn.mpdl.mpg.de/data/Reihe_A/2/ZNA-1947-2a-0133.pdf.

[Mol48] G. Moliere. “Theorie der Streuung schneller geladener Teilchen II. Mehrfach- und Vielfachstreuung”. In: *Z. Naturforsch.* A3 (1948), p. 78. URL: http://zfn.mpdl.mpg.de/data/Reihe_A/3/ZNA-1948-3a-0078.pdf.

[Mol99] Michael Moll. “Radiation damage in silicon particle detectors: Microscopic defects and macroscopic properties”. PhD thesis. Hamburg U., 1999. URL: http://www-library.desy.de/cgi-bin/showprep.pl?desy-thesis99-040.

[MPS11] S Meroli, D Passeri, and L Servoli. "Energy loss measurement for charged particles in very thin silicon layers". In: *JINST* 6.06 (2011), P06013. URL: http://stacks.iop.org/1748-0221/6/i=06/a=P06013.

[Mül91] Jörg W. Müller. "Generalized dead times". In: *Nucl. Inst. and Meth. A* 301.3 (1991), pp. 543–551. DOI: https://doi.org/10.1016/0168-9002(91)90021-H.

[NM65] J. A. Nelder and R. Mead. "A Simplex Method for Function Minimization". In: *Comput. J.* 7.4 (1965), pp. 308–313. DOI: 10.1093/comjnl/7.4.308.

[Obe09] Theresa Obermann. "Performance evaluation of a fully depleted monolithic pixel detector chip in 150 nm CMOS technology". PhD-Thesis. Universität Bonn, 2009. URL: http://hss.ulb.uni-bonn.de/2017/4778/4778.htm.

[Oki+15] Masao Okihara et al. "Lapis SOI Pixel Process". In: *SOIPIX proceedings*. 2015. URL: https://inspirehep.net/record/1405139/files/arXiv:1511.05224.pdf. arXiv: 1511.05224 [physics.ins-det].

[Oli+14] K.A. Olive et al. "Review of Particle Physics (RPP)". In: *Chin. Phys.* C38 (2014). An updated RPP is published every 2 years. The online access to the current and previous issues is available from http://pdg.lbl.gov/, p. 090001. DOI: 10.1088/1674-1137/38/9/090001.

[Pat04] Marc Paterno. "Calculating efficiencies and their uncertainties". In: (2004). URL: http://inspirehep.net/record/669498.

[Peh+68] R.H. Pehl et al. "Accurate determination of the ionization energy in semiconductor detectors". In: *Nucl. Inst. and Meth.* 59.1 (1968), pp. 45–55. DOI: 10.1016/0029-554X(68)90342-X.

[Peq08a] Joao Pequenao. "Computer generated image of the whole ATLAS detector". Mar. 2008. URL: https://cds.cern.ch/record/1095924.

[Peq08b] Joao Pequenao. "Event Cross Section in a computer generated image of the ATLAS detector." Mar. 2008. URL: https://cds.cern.ch/record/1096081.

[Per+06] I. Perić et al. "The FEI3 readout chip for the ATLAS pixel detector". In: *Nucl. Inst. and Meth. A* 565 (2006), pp. 178–187. DOI: 10.1016/j.nima.2006.05.032.

[Per+17] I. Perić et al. "Status of HVCMOS developments for ATLAS". In: *JINST* 12.02 (2017), p. C02030. URL: http://stacks.iop.org/1748-0221/12/i=02/a=C02030.

[Per07] Ivan Perić. "A novel monolithic pixelated particle detector implemented in high-voltage CMOS technology". In: *Nucl. Inst. and Meth. A* 582.3 (2007). VERTEX 2006, pp. 876–885. DOI: 10.1016/j.nima.2007.07.115.

[Pet+06] M. Petasecca et al. "Numerical Simulation of Radiation Damage Effects in p-Type and n-Type FZ Silicon Detectors". In: *IEEE Trans. Nucl. Sci.* 53.5 (Oct. 2006), pp. 2971–2976. DOI: 10.1109/TNS.2006.881910.

[Pie+07] Claudio Piemonte et al. “Study of the signal formation in single-type column 3D silicon detectors”. In: *Nucl. Inst. and Meth. A* 579.2 (2007). Hiroshima Proceedings, pp. 633–637. DOI: 10.1016/j.nima.2007.05.261.

[PIM95] M. Pentia, G. Iorgovan, and A. Mihul. “Multiple scattering error propagation in particle track reconstruction”. In: *Rom. J. Phys.* 40 (1995), pp. 181–191. arXiv: hep-ex/9406006 [hep-ex].

[Poh] David-Leon Pohl. *A generic online monitor showing real-time plots from independent data acquisition systems*. URL: https://github.com/SiLab-Bonn/online_monitor.

[Poh+] David-Leon Pohl et al. *A powerful and adaptable analysis software in Python for beam test data*. https://github.com/SiLab-Bonn/testbeam_analysis. URL: https://github.com/SiLab-Bonn/testbeam_analysis.

[Poh+15] David-Leon Pohl et al. “Obtaining spectroscopic information with the ATLAS FE-I4 pixel readout chip”. In: *Nucl. Inst. and Meth. A* 788.Supplement C (2015), pp. 49–53. DOI: doi.org/10.1016/j.nima.2015.03.067.

[Poh+17] D.-L. Pohl et al. “Radiation hard pixel sensors using high-resistive wafers in a 150 nm CMOS processing line”. In: *JINST* 12.06 (2017), P06020. URL: http://stacks.iop.org/1748-0221/12/i=06/a=P06020.

[Poh10] Thomas Pohlsen. “Charge collection and space charge distribution in neutron-irradiated epitaxial silicon detectors”. PhD thesis. Hamburg U., 2010. DOI: 10.3204/DESY-THESIS-2010-013.

[Poh15] David-Leon Pohl. “Overview of the ATLAS Insertable B-Layer (IBL) Project”. In: *PoS* RD13 (2015), p. 012. DOI: doi.org/10.22323/1.189.0012.

[Poh16] David-Leon Pohl. *Software package* pyLandau. https://github.com/SiLab-Bonn/pyLandau. 2016. URL: https://github.com/SiLab-Bonn/pylandau.

[Poh17] D.-L. Pohl. *A GEANT4 based simulation to describe the response of pixel detectors illuminated by particles sources.* Aug. 2017. URL: https://github.com/DavidLP/SourceSim.

[Rai+12] Aaron Mac Raighne et al. “Characterisation of Glasgow/CNM Double-Sided 3D Sensors”. In: *Phys. Procedia* 37 (2012). TIPP Proceedings, pp. 1016–1023. DOI: https://doi.org/10.1016/j.phpro.2012.02.445.

[Ram39] S. Ramo. “Currents Induced by Electron Motion”. In: *Proceedings of the I.R.E* 27 (1939), pp. 584–585. DOI: 10.1109/JRPROC.1939.228757.

[RD5] RD50 Collaboration. *CERN webpage*. https://rd50.web.cern.ch/rd50/.

[Rie+17] C. Riegel et al. “Radiation hardness and timing studies of a monolithic TowerJazz pixel design for the new ATLAS Inner Tracker”. In: *JINST* 12.01 (2017), p. C01015. URL: http://stacks.iop.org/1748-0221/12/i=01/a=C01015.

[Rub12] I. Rubinskiy. "An EUDET/AIDA Pixel Beam Telescope for Detector Development". In: *Physics Procedia* 37 (2012). TIPP Proceedings, pp. 923–931. DOI: https://doi.org/10.1016/j.phpro.2012.02.434.

[SBS84] R.M. Sternheimer, M.J. Berger, and S.M. Seltzer. "Density effect for the ionization loss of charged particles in various substances". In: *Atom. Data Nucl. Data* 30.2 (1984), pp. 261–271. DOI: 10.1016/0092-640X(84)90002-0.

[Sch+00] F. Scholze et al. "Determination of the electron–hole pair creation energy for semiconductors from the spectral responsivity of photodiodes". In: *Nucl. Inst. and Meth. A* 439.2 (2000), pp. 208–215. DOI: https://doi.org/10.1016/S0168-9002(99)00937-7.

[Sch14] Jörn Schwandt. *Radiation Hard Silicon Pixel Sensor for X-ray Science*. Sept. 2014. URL: http://www.iexp.uni-hamburg.de/groups/pd/contents/index/index-199.html.

[Sch97] D. K. Schroder. "Carrier lifetimes in silicon". In: *IEEE Trans. Electron Devices* 44.1 (Jan. 1997), pp. 160–170. DOI: 10.1109/16.554806.

[SHS04] Bernhard Schnizer, Thomas Heubrandtner, and Gunther Schweitzer. "Simple models for RPC weighting fields and potentials". In: *Nucl. Inst. and Meth. A* 535.1 (2004). VCI Proceedings, pp. 554–557. DOI: https://doi.org/10.1016/j.nima.2004.07.186.

[Sil] Silab. *Software package* basil*, modular data acquisition system and system testing framework in Python*. https://github.com/SiLab-Bonn/basil.

[SL12] S.M. Sze and M.K. Lee. *Semiconductor Devices, Physics and Technology*. Wiley, 2012.

[SM 06] Kwok K. Ng S.M. Sze. "p-n Junctions". In: *Physics of Semiconductor Devices*. Wiley-Blackwell, 2006. Chap. 2, pp. 77–133. eprint: https://onlinelibrary.wiley.com/doi/pdf/10.1002/9780470068328.ch2. DOI: 10.1002/9780470068328.ch2.

[SN07] S.M. Sze and K.K. Ng. *Physics of Semiconductor Devices (3rd ed.)* Wiley, 2007. DOI: 10.1002/0470068329.

[Spa+18] S. Spannagel et al. "Allpix2: A modular simulation framework for silicon detectors". In: *Nucl. Inst. and Meth. A* 901 (2018), pp. 164–172. DOI: https://doi.org/10.1016/j.nima.2018.06.020.

[SR52] W. Shockley and W. T. Read. "Statistics of the Recombinations of Holes and Electrons". In: *Phys. Rev.* 87 (5 Sept. 1952), pp. 835–842. DOI: 10.1103/PhysRev.87.835.

[Sum+93] G. P. Summers et al. "Damage correlations in semiconductors exposed to gamma, electron and proton radiations". In: *IEEE Trans. Nucl. Sci.* 40.6 (Dec. 1993), pp. 1372–1379. DOI: 10.1109/23.273529.

[Tak16] Yosuke Takubo. *ATLAS IBL operational experience*. Tech. rep. ATL-INDET-PROC-2016-012. Geneva: CERN, Nov. 2016. DOI: 10.22323/1.287.0004.

[Tan+18] M. Tanabashi et al. "Review of Particle Physics". In: *Phys. Rev. D* 98 (3 Aug. 2018), p. 030001. DOI: 10.1103/PhysRevD.98.030001.

[Teh+16] N. Alipour Tehrani et al. “Capacitively coupled hybrid pixel assemblies for the CLIC vertex detector”. In: *Nucl. Inst. and Meth. A* 823 (2016), pp. 1–8. DOI: 10.1016/j.nima.2016.03.072.

[Toi17] Toival. *Toival ADC/MCA*. Toival. Nov. 2017. URL: http://www.toivel.com/alalog-digital-converter.php.

[TS67] P.A. Tove and W. Seibt. “Plasma effects in semiconductor detectors”. In: *Nuclear Instruments and Methods* 51.2 (1967), pp. 261–269. DOI: https://doi.org/10.1016/0029-554X(67)90012-2.

[Tsu12] Jieh-Wen Tsung. “Diamond and Silicon Pixel Detectors in High Radiation Environments”. PhD thesis. University of Bonn, 2012. URL: https://inspirehep.net/record/1231025.

[Unn+13] Y. Unno et al. “Development of novel n+-in-p Silicon Planar Pixel Sensors for HL-LHC”. In: *Nucl. Inst. and Meth. A* 699 (2013). Hiroshima Proceedings, pp. 72–77. DOI: 10.1016/j.nima.2012.04.061.

[Var00] J Varela. *Timing and synchronization in the LHC experiments*. Tech. rep. CMS-CR-2000-012. Geneva: CERN, 2000. URL: http://cds.cern.ch/record/478248.

[VL00] A. Vasilescu and G. Lindstroem. *Displacement damage in Silicon*. on-line compilation. Aug. 2000. URL: https://rd50.web.cern.ch/rd50/NIEL/default.html.

[Wer16] N. Wermes. “Depleted CMOS pixels for LHC proton-proton experiments”. In: *Nucl. Inst. and Meth. A* A824 (2016), pp. 483–486. DOI: 10.1016/j.nima.2015.09.038.

[Wes+96] Trond I. Westgaard et al. “Radiation hardness of punch-through and FET biased silicon microstrip detectors”. In: *Nucl. Inst. and Meth. A* 377.2 (1996). Proceedings, pp. 429–434. DOI: https://doi.org/10.1016/0168-9002(96)00216-1.

[Wit13] Tobias Wittig. “Slim edge studies, design and quality control of planar ATLAS IBL pixel sensors”. Presented 08 May 2013. PhD thesis. 2013. DOI: 10.17877/DE290R-5402.

[XDB11] Cheng Xu, Mats Danielsson, and Hans Bornefalk. “Validity of spherical approximations of initial charge cloud shape in silicon detectors”. In: *Nucl. Inst. and Meth. A* 648.Supplement 1 (2011), S190–S193. DOI: https://doi.org/10.1016/j.nima.2010.11.173.

[You11] Hazem Yousef. “Energy Dependent Charge Spread Function in a Dedicated Synchrotron Beam PnCCD Detector”. PhD thesis. Universität Siegen, 2011. URL: http://dokumentix.ub.uni-siegen.de/opus/volltexte/2011/550/.